

Ultrafast Photochromic Reactions of Structurally Modified Furylfulgides and a Bridged Azobenzene

Dissertation

zur Erlangung des Doktorgrades
der Mathematisch-Naturwissenschaftlichen Fakultät
der Christian-Albrechts-Universität zu Kiel

vorgelegt von

Dipl.-Chem. Ron Siewertsen

aus Kiel

Institut für Physikalische Chemie
der Christian-Albrechts-Universität zu Kiel

Kiel, im März 2011

Referent: Prof. Dr. F. Temps
Koreferent: Prof. Dr. B. Hartke

Tag der mündlichen Prüfung: 17. Mai 2011
Zum Druck genehmigt: 17. Mai 2011

gez. Prof. Dr. rer. nat. L. Kipp, Dekan

Hiermit erkläre ich an Eides Statt, dass die vorliegende Abhandlung – abgesehen von der Beratung durch meinen Betreuer Herrn Prof. Dr. F. Temps – nach Inhalt und Form meine eigene Arbeit ist.

Diese Arbeit hat weder in Auszügen noch in ganzer Form einer anderen Stelle im Rahmen eines Prüfungsverfahrens vorgelegen. Sie wurde in ihrer Gesamtheit nicht veröffentlicht und auch nicht zur Veröffentlichung eingereicht.

Die Arbeit ist unter Einhaltung der Regeln guter wissenschaftlicher Praxis der Deutschen Forschungsgemeinschaft entstanden.

Ron Siewertsen

Abstract

In this Thesis, the effect of structural modifications on the ultrafast dynamics and photochemical properties of furylfulgides and azobenzenes, as two important classes of photochromic switches, was investigated by femtosecond time-resolved transient absorption spectroscopy (fsTAS). The parent compound of the furylfulgides (MeF) was systematically modified by steric and electronic effects with a bulky isopropyl substituent (iPrF) or by intramolecular bridging (7rF) at the hexatriene/cyclohexadiene chromophore and by benzannulation of the furyl ring (MeBF), respectively. The second task was the investigation of the photo-induced isomerization of a highly constrained bridged azobenzene derivative (brAB), which can be regarded as a new improved class of azobenzenes.

For the four furylfulgides the excited-state reaction pathways of the photochromic $E \rightleftharpoons C$ ring closure and opening reaction and the unwanted $E \rightleftharpoons Z$ isomerization were investigated. The steric effects in iPrF and 7rF caused an inhibition of the $E \rightarrow Z$ channel and a selective increase of the ring closure quantum yield, while electronic effects selectively improved the ring opening efficiency. The $E \rightarrow C$ pathway was found to be accelerated for iPrF and 7rF by a factor of ≈ 2 with time constants of $\tau = 0.05$ ps compared to MeF and MeBF with $\tau \approx 0.12$ ps. Kinetic competition of the reaction pathways was found to improve the $E \rightarrow C$ efficiency of sterically restrained fulgides. The $E \rightarrow Z$ channel was only observed for MeF and MeBF with $\tau \approx 0.34$ ps. Furthermore, the $E \rightarrow Z$ isomerization was found to be a conformer-specific reaction, depending on the population of two E -conformers (E_α and E_β) in their electronic ground states. With E -7rF, a pure E_α -fulgide could be studied for the first time. The new compound was specially designed for this purpose.

The excited-state $C \rightarrow E$ ring opening reaction was strongly influenced by the electronic effects. For MeF, iPrF and 7rF virtually identical barrierless sub-picosecond excited-state dynamics could be observed, only slightly affected by steric modifications. For MeBF significantly increased excited-state lifetimes of $\tau = 16.9$ ps could be observed, which is ≈ 25 times longer than for MeF. Excited-state energy barriers along a non-reactive excited-state pathway are a plausible hypothesis to explain the increased photochemical efficiency.

The diazocine derivative brAB possesses strongly improved photochromic properties compared with normal azobenzene (AB), such as spectrally separated S_1 ($n\pi^*$) absorption bands and considerable higher $E \rightarrow Z$ and $Z \rightarrow E$ isomerization quantum yields. Due to the steric constraints, the Z -isomer is the thermodynamically stable form. The reasons for the improved properties of brAB could be elucidated by fsTAS and quantum chemical calculations. For the $Z \rightarrow E$ and the $E \rightarrow Z$ reactions, ultrafast excited-state dynamics with $\tau = 70$ fs and $\tau < 50$ fs and sub-picosecond isomerization times of $\tau = 0.27$ ps and 0.32 ps were observed, respectively. The accelerated and more efficient photoreactions could be explained by a pre-orientation of the CNNC dihedral angle and inhibition of ineffective reaction channels of AB.

Kurzfassung

In der vorliegenden Dissertation wurde der Einfluss struktureller Modifikationen zweier wichtiger Klassen molekularer Schalter auf deren photodynamische und -chemische Eigenschaften mittels Femtosekunden-zeitaufgelöster transientser Absorptionsspektroskopie (fsTAS) untersucht. Die Stammverbindung der untersuchten Furylfulgide (MeF) wurde durch sterische Beschränkungen (iPrF und 7rF) an ihrem Hexatrien/Cyclohexadien-Chromophor oder elektronisch durch Benzanellierung des Furylrings (MeBF) modifiziert. Aus der Klasse der Azobenzole (AB) wurde das durch eine Ethylenbrücke stark sterisch beschränkte Diazozinderivat brAB untersucht, das als Stammverbindung einer neuen Klasse molekularer Schalter betrachtet werden kann.

Für die vier Furylfulgide wurden die erwünschte photochrome $E \rightleftharpoons C$ -Ringschluss- und Ringöffnungsreaktion und die $E \rightleftharpoons Z$ -Nebenreaktionen untersucht. Sterische Effekte bewirkten eine Unterdrückung der $E \rightarrow Z$ -Reaktion und eine selektive Erhöhung der Ringschlussquantenausbeute ($\phi_{E \rightarrow C}$), während elektronische Effekte selektiv eine Erhöhung von $\phi_{C \rightarrow E}$ bewirkten. iPrF und 7rF zeigten eine beschleunigte $E \rightarrow C$ -Reaktion mit Zeitkonstanten von $\tau = 0.05$ ps im Vergleich zu MeF und MeBF ($\tau \approx 0.12$ ps). Der $E \rightarrow Z$ -Kanal konnte nur für MeF und MeBF beobachtet werden ($\tau \approx 0.34$ ps). Es konnte weiterhin gezeigt werden, dass die $E \rightarrow Z$ -Isomerisierung eine konformerspezifische Reaktion ist, die von dem Populationsverhältnis zweier E -Konformere (E_α und E_β) abhängt. Mit E -7rF wurde erstmals ein reines E_α -Fulgid entwickelt und untersucht.

Die Dynamik der $C \rightarrow E$ -Reaktionen zeigte eine starke Beeinflussung durch elektronische Effekte. Während für MeF, iPrF und 7rF unabhängig von sterischen Effekten eine direkte, barrierefreie Dynamik auf der Subpikosekunden-Zeitskala festgestellt wurde, konnte für C -MeBF eine bis zu 25-mal langsamere Dynamik ($\tau = 16.9$ ps) beobachtet werden. Dies wurde durch das Auftreten von Energiebarrieren im angeregten Zustand entlang eines unreaktiven Deaktivierungspfads interpretiert und erklärt die Erhöhung von $\phi_{C \rightarrow E}$.

Das verbrückte AB-Derivat brAB weist im Vergleich zu AB deutlich verbesserte photochemische Eigenschaften auf. Hierzu gehören spektral getrennte S_1 ($n\pi^*$)-Absorptionsbanden der beiden Isomere und deutlich erhöhte $E \rightarrow Z$ - und $Z \rightarrow E$ -Quantenausbeuten. Durch die Ringspannung im E -Isomer ist das Z -Isomer die thermodynamisch stabile Form. Die Ursache der außerordentlichen Eigenschaften von brAB konnten mittels fsTAS und mit quantenchemischen Rechnungen aufgeklärt werden. Für die $Z \rightarrow E$ - und die $E \rightarrow Z$ -Photoreaktion wurde ein ultraschnelles Verlassen der Franck-Condon Region mit $\tau = 70$ fs für die Z - und $\tau < 50$ fs für die E -Form sowie Subpikosekunden-Isomerisierungszeiten von $\tau = 0.27$ ps und $\tau = 0.32$ ps gemessen. Die im Vergleich zu AB deutlich schnellere Dynamik und die erhöhten Quantenausbeuten konnten durch eine sterisch bedingte Vororientierung des CNNC-Torsionswinkel und durch die Beschränkung von ineffektiven Reaktionskanälen von AB erklärt werden.

Contents

1	Introduction	1
1.1	Elementary Photophysical and Photochemical Processes in Organic Molecules	5
1.2	Fulgides as Photochromic Switches	11
1.2.1	Applications of Fulgides and Related Systems	12
1.2.2	Effects of Structural Modifications	16
1.2.3	Conformeric Forms of <i>E</i> -Fulgides and their Thermal Equilibration .	20
1.2.4	Reaction Mechanism and Photo-Induced Dynamics of Fulgides . . .	21
1.2.5	Investigated Furylfulgides and Aims of this Thesis	23
1.3	Azobenzenes as Photochromic Switches	25
1.3.1	Applications of Azobenzenes	27
1.3.2	Reaction Mechanism and Photo-Induced Dynamics of Azobenzenes	30
1.3.3	Investigated Azobenzene Derivative and Aims of this Thesis	33
	References	35
2	Experimental Methods	45
2.1	The Principle of Femtosecond Time-Resolved Transient Absorption Spectroscopy	45
2.2	Femtosecond Transient Absorption Setup	46
2.2.1	Optical Pathway for White Light Probe Generation	47
2.2.2	Optical Pathway for the NOPA Pump Pulses	51
2.2.3	Data Acquisition	54
2.3	Experimental Artifacts in fs Time-Resolved Transient Absorption Spectroscopy	55
2.4	Data Analysis	59
	References	63
3	Parallel Ultrafast <i>E-C</i> Ring Closure and <i>E-Z</i> Isomerisation in a Photochromic Furylfulgide Studied by Femtosecond Time-Resolved Spectroscopy	65
3.1	Introduction	67
3.2	Methods	70
3.3	Results	72
3.4	Discussion	78
3.5	Conclusions	84
	References	87
	Supporting Information	89

4	Tuning of Switching Properties and Excited-State Dynamics of Fulgides by Structural Modifications	99
4.1	Introduction	101
4.2	Experimental	104
4.3	Results	105
4.4	Discussion	110
4.5	Conclusions	116
	References	119
5	Electronic and Steric Effects on the Photo-Induced $C \rightarrow E$ Ring-Opening of Structurally Modified Furylfulgides	123
5.1	Introduction	125
5.2	Experimental Details	128
5.3	Results	128
5.4	Discussion	135
5.5	Conclusion	139
	References	141
6	Ultrafast $Z \rightarrow E$ Photoisomerisation of Structurally Modified Furylfulgides	143
6.1	Introduction	145
6.2	Experimental	148
6.3	Results	149
6.4	Discussion	154
6.5	Conclusion	157
	References	159
7	Photochromism of Rotation-Hindered Furylfulgides Influenced by Steric Modifications	161
7.1	Introduction	163
7.2	Results and Discussion	165
7.3	Conclusion	173
7.4	Experimental	174
	References	181
	Supporting Information	183
8	Highly Efficient Reversible $Z \rightleftharpoons E$ Photoisomerization of a Bridged Azobenzene with Visible Light through Resolved $S_1(n\pi^*)$ Absorption Bands	191
8.1	Reprint of the Publication	193

References	197
Supporting Information	199
Additional Results	207
9 Superior $Z \rightarrow E$ and $E \rightarrow Z$ photoswitching dynamics of dihydrodibenzodiazocine, a bridged azobenzene, by $S_1(n\pi^*)$ excitation at $\lambda = 387$ and 490 nm	209
9.1 Introduction	211
9.2 Experimental and computational methods	213
9.3 Results	215
9.4 Discussion	223
9.5 Conclusions	228
References	231
Supporting Information	235
10 Summary	239
Acknowledgment	245
Curriculum Vitae	247

1 Introduction

Photochemical molecular switches undergo reversible transformations between two isomers upon irradiation by ultraviolet (UV) or visible (VIS) light. The time scale of those reactions is now known to be governed by vibrational periods and occurs on the femtosecond (fs) to picosecond (ps) range. For photochromic switches, the reaction is accompanied by a change of the UV/VIS absorption spectra, which allows for a wavelength specific excitation and transformation between the two species. As an immediate consequence of the structural change of the molecule, several physicochemical properties such as color, free volume, density, dielectric constant, refractive index, π -conjugation, redox potential, and even magnetic properties may change during photoisomerization. Depending on the switchable molecular properties, applications such as high-density optical data storage^[1-7], tiny photon-driven machines that convert light into mechanical motion^[8-10], photoregulation of biomolecules,^[11-16] and innovative photoresponsive surfaces^[17-19] have already been demonstrated. Multi-dimensional applications like two-photon 3D data storage systems^[5-7] already allow for data storage capacities of 1 Terabyte (TB) on a photochromic dye-doped polymer-based disc with 120 mm diameter, which is higher by a factor of ≈ 40 than current commercial optical storage technology. Conventional Blu-Ray discs with the same diameter are currently available with ≈ 25 GB storage capacity. These super-high density storage devices require highly optimized photochemical switches with high photoisomerization quantum yields, well separated absorption spectra of the photochromic isomers, high photochemical fatigue, rapid response and excellent thermal stability.

Important classes of photochromic switches which fulfill the above mentioned criteria are fulgides and fulgimides,^[6,20,21] diarylethenes,^[3,22] spiropyrans,^[3,23,24] and azobenzene (AB) derivatives^[3,8,25-27] (see Fig. 1.1). Their photoisomerization reactions, which are based on the molecular structure, can be divided into two major categories: Electrocyclic ring closure/opening and *trans/cis* (*E/Z*) photoisomerization. The photochromism of fulgides and fulgimides, diarylethenes and spiropyrans is based on a photo-induced reversible electrocyclization. The closed forms of fulgides, fulgimides and diarylethenes show an absorption band in the VIS spectral range, while the open isomers exhibit their first absorption band at significantly shorter wavelengths. Upon excitation in the respective first absorption bands, the molecules undergo reversible photoisomerization between their two forms. Spiropyrans, on the other hand, are subject to a photo-induced heterolytic bond cleavage on excitation with UV light, which leads to the amphoteric ionic structure of merocyanine with an onset of absorbance in the VIS region. The merocyanine can be

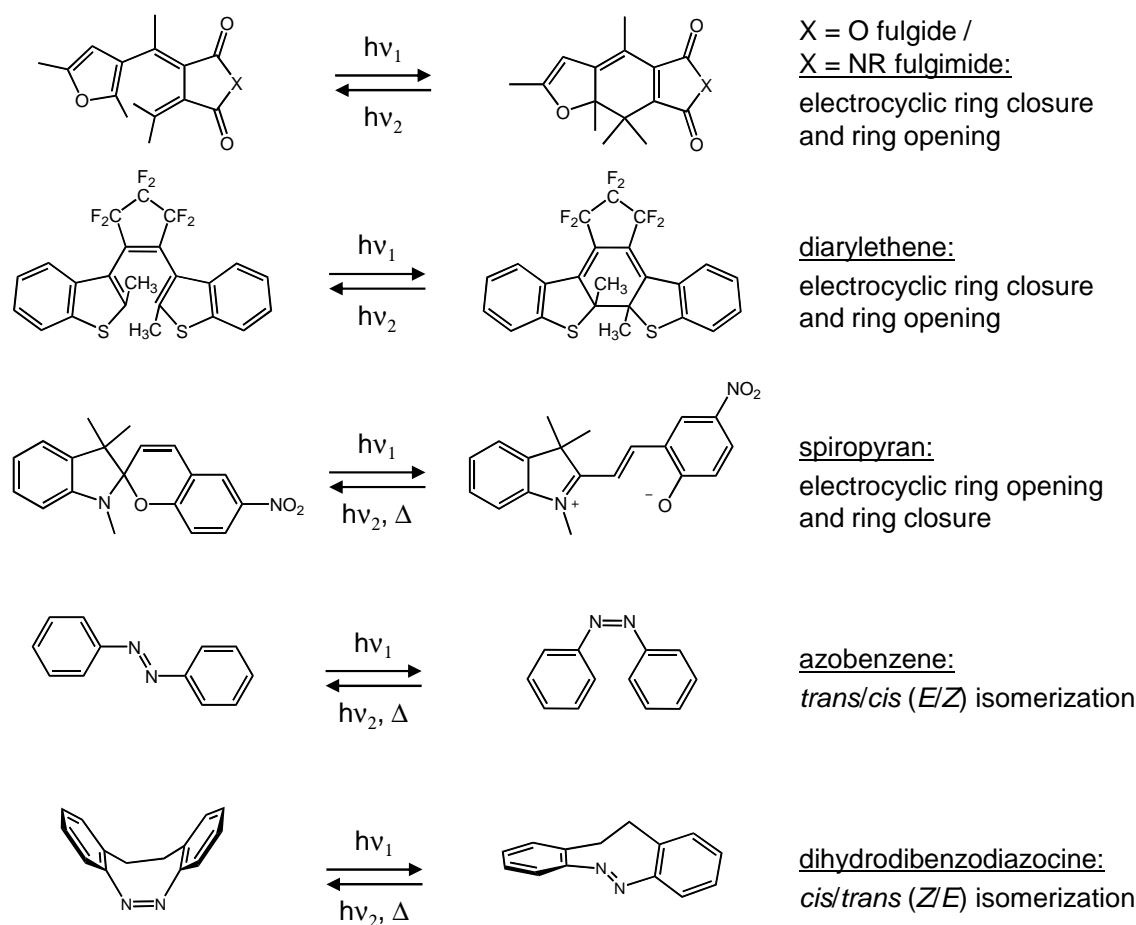


Figure 1.1: Important classes of photochromic switches and their photochemical and thermal isomerization reactions.

switched back to the closed form by irradiation in the VIS or by thermal energy (heat). As mentioned above, the respective isomers of fulgides and fulgimides, diarylethenes and spiropyrans differ strongly in their UV/VIS absorption and fluorescence spectra, thus they can be used, e.g., as optical memory storage media. The poor thermal stability of merocyanine, however, limits the application of spiropyran in this field.

For applications requiring a large change in geometry or dipole moment, ABs are usually the first choice.^[8,25,27] Azobenzenes show a photochemically induced *trans/cis (E/Z)* isomerization accompanied by large-amplitude structural and dipole moment changes between the elongated *E*- and more compact *Z*-form. The *E*-form of AB is the thermodynamic stable isomer, whereas the *Z*-form undergoes thermally and photochemically induced *Z* \rightarrow *E* isomerization. The AB derivative dihydrodibenzodiazocine possesses superior photochromic properties compared to AB,^[26,28] and therefore may become the parent molecule of a new class of photochromic switches.

Regarding the efficiency and photostability of light-driven molecular switches, fast reaction times are essential. Photo-excited organic molecules very easily undergo unwanted

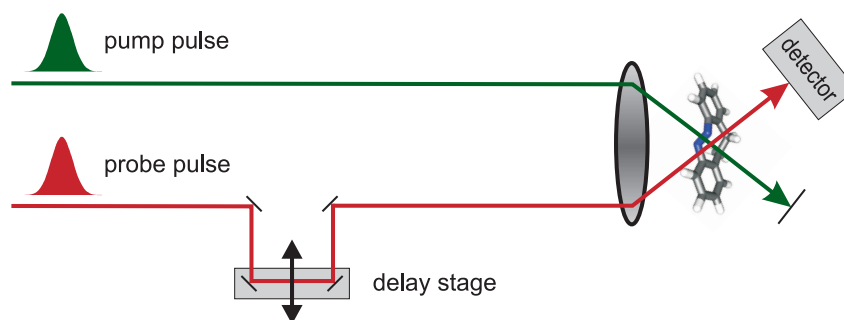


Figure 1.2: Principle of the pump-probe technique.

side reactions, quenching processes with other molecules, and radiative or non-radiative transitions. It is not astonishing therefore that the isomerization reactions of the most promising photochromic compounds such as azobenzenes, fulgides and diarylethenes happen on the very fast femtosecond time scale. On this fundamental time scale, the movement of atoms in a molecule takes place. Side reactions are minimized, because only few molecular degrees of freedom are involved in the photoreaction.

One of the key challenges of today's photochemistry is the detailed analysis and consequently the improvement of photochromic switches regarding their excited-state pathways and the influences of internal or external parameters on the excited-state dynamics. The mechanism of reactive and non-reactive transformations of molecules is determined by the entering region and the topography of the excited electronic potential energy surfaces (PESs). Detailed understanding of molecular dynamics at the atomic level in terms of motion on excited electronic PESs will allow for purposive improvement of photochromic properties.

Femtosecond time-resolved spectroscopy, based on the generation of ultrashort laser pulses and the pump-probe technique, is the key technology for studying ultrafast excited-state dynamics. The pump-probe technique, depicted in Fig. 1.2, enables us to detect ultrafast molecular events in real time. The laser output from a fs laser system is divided into a pump and a probe beam, which both are spatially and temporally overlapped in the sample. A variation of the temporal delay between the pump and probe pulses is achieved by an optical delay stage. Using this setup, the time-dependencies of the changes induced in the sample by the pump pulse can be monitored by the probe pulse at different delay times between pump and probe. A powerful method for studying the detailed dynamics of photoisomerization reactions is fs time-resolved absorption spectroscopy (fsTAS), which allows for monitoring the vibronic transformations from the initial photo-excited states of the molecules all the way to the equilibrated final products.

Since the 1990s, passively mode-locked solid-state lasers provide high-quality ultrashort laser pulses. Especially titanium-sapphire (Ti:Sa) lasers with a typical pulse length of

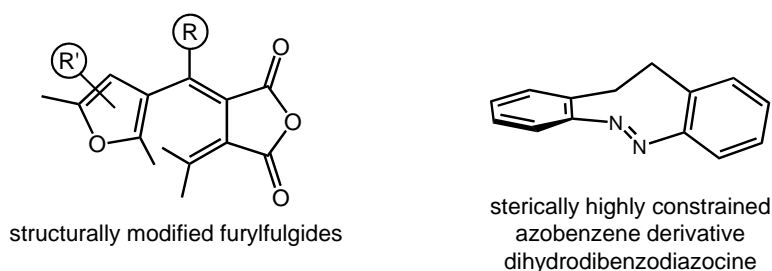


Figure 1.3: Structures of the two classes of photochromic switches investigated in this Thesis. Left: Furylfulgides, right: Dihydrodibenzodiazocine.

100 – 200 fs have become the work horses in ultrafast spectroscopy. Ultrashort laser pulses in combination with the pump/probe technique led to the development of femtochemistry and femtobiology. A. H. Zewail is one of the pioneers in this field and was honored with the Nobel Prize for Chemistry in 1999.^[29]

The present Thesis deals with the ultrafast photo-induced reaction dynamics of structurally modified furylfulgides and a sterically highly restrained azobenzene-related photochromic diazocine molecule (see Fig. 1.3). Azobenzenes are ideal candidates for the design of functional surfaces^[18,30] and molecular machines or manipulators.^[10,31] Fulgides are photochromic switches with high application potential for high density data storage^[5,6] and far-field fluorescence nanoscopy.^[32–36] The investigation of the relations between structure, static photochemical properties, and ultrafast dynamics opens the possibility of improving fulgides and azobenzenes as photochromic switches for applications. Of particular interest are the effects of modifications of the excited-state topography and the control of excited-state pathways by chemical modifications.

The following Section 1.1 of this Introduction will first present a summary of the elementary photophysical and photochemical processes in large organic molecules. In particular, different possible vibronic deactivation processes are discussed which might compete with the desired photochemical reactions. The photochemical processes are classified according to the point of transfer from the photo-excited PES to the electronic ground state and the conical intersection (CI) as important photochemical funnel is described.

Section 1.2 thereafter gives a survey of the available literature on the class of photochromic furylfulgide switches, which are in one of the two foci of this Thesis. Examples of promising applications of fulgides in optical data storage taken from literature will be shown in order to illustrate their relevance. A summary of structural modifications that led to the outstanding photochemical properties of modern fulgides will be given followed by a summary of publications dealing with the ultrafast dynamics of fulgides and related systems during the last years. In the last part of Section 1.2, the pursued strategy of the

structural modifications of the investigated fulgides will be explained.

In Section 1.3 an overview will be given of the available literature of photochromic AB switches, which are in the second focus of this Thesis. Application examples of ABs used for a photoswitchable restriction enzyme, functionalization of surfaces, and for a light-driven motor system are summarized. Different isomerization mechanisms of AB are discussed on the basis of fs time-resolved spectroscopy from literature. These results led to the idea of the investigated dihydrodibenzodiazocine molecule as an improved azobenzene-based molecular switch.

The following Chapter 2 describes the experimental setup used for the present research and the data analysis.

Chapters 3-7 discuss the obtained results for the investigated furylfulgides. Chapters 8-9 are dealing with the results for the azobenzene-related diazocine. Chapter 10 finally gives a summary of the work performed for this Thesis.

1.1 Elementary Photophysical and Photochemical Processes in Organic Molecules

The photoexcitation of a molecule is followed by photophysical or photochemical processes. Photophysical processes are radiative or radiationless transitions between electronic states without a change in chemical structure of the molecule,^[37,38] primary photochemical processes yield a photoproduct that is structurally different from the initially photo-excited reactant. As photophysical processes only lead back to the reactant, they consequently lower the photochemical efficiency. A desired photochemical reaction will only predominate, if the photochemical process is faster than the fastest competing photophysical process. The photochemical efficiency is described by the reaction quantum yield.

The main photophysical processes can be visualized in the Jablonski diagram^[39] shown in Fig. 1.4. At the beginning of a photophysical process stands the absorption of a photon and population of vibrational states of the excited electronic state (S_1) with the same multiplicity as the initial state (S_0) according to the selection rules for vibronic transitions and the Franck-Condon (FC) principle. The excess energy with respect to the excited-state minimum can be distributed to other vibrational modes of the molecule on a fs time scale via internal vibrational energy redistribution (IVR, $10^{-13} - 10^{-9}$ s).¹ For molecules in solution, excess energy can also be transferred to the environment, which leads to vibrational energy transfer (VET, 10^{-11} s) and thus eventually to the vibrational ground state of the respective electronic state.

Internal conversion (IC, 10^{-14} to $> 10^{-9}$ s) is a radiationless process that allows for

¹Typical time scales for the processes are given in parentheses.

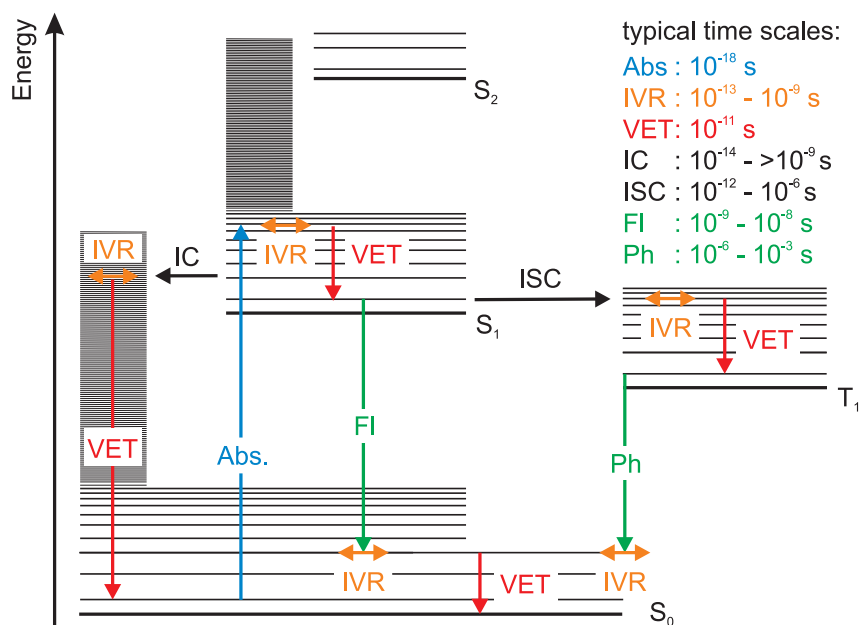


Figure 1.4: Schematic illustration of the photophysical processes after vibronic excitation in a molecule (Jablonski diagram). Electronic states are depicted as thick horizontal lines, vibrational states are represented by thin horizontal lines. Abs.: Absorption; IVR: Internal Vibrational Energy Redistribution, VET: Vibrational Energy Transfer; IC: Internal Conversion; ISC: Intersystem Crossing; Fl: Fluorescence; Ph: Phosphorescence.

electronic deactivation into highly excited vibrational levels of a lower-lying electronic state without a change in multiplicity. On the other hand, a non-radiative transition from a photo-excited singlet state to a triplet state (or reverse) is called intersystem crossing (ISC, 10^{-12} – 10^{-6} s). Because ISC is a spin-forbidden process, it is slower than IC. According to Fermi’s Golden Rule, the time scale of IC strongly depends on the coupling matrix element squared of the two involved electronic states and the density of (acceptor) states. It can be very fast (10^{-14} s) for small energy gaps.

In addition to the non-radiative electronic deactivation, luminescence can also lead back to the electronic ground state. In particular, the excess energy is released by spontaneous emission of radiation. According to Kasha’s rule,^[40] luminescence generally occurs from the lowest electronically excited state of a given multiplicity, because it is usually slower than IC and VET from higher states. The process is called fluorescence (10^{-9} – 10^{-8} s) for singlet-singlet transitions and phosphorescence for triplet-singlet transitions. Phosphorescence shows lifetimes of the order of milliseconds up to minutes or even hours.

The concept of potential energy surfaces (PESs) derived from the Born-Oppenheimer separation/approximation allows for the visualization of molecular photochemical reactions as a movement of the excited wavepacket in the $(3N - 6)$ -dimensional space of the internal nuclei coordinates. The FC point is the initial position on the excited PES. Förster *et al.* established a classification of photochemical reactions according to the point, where the

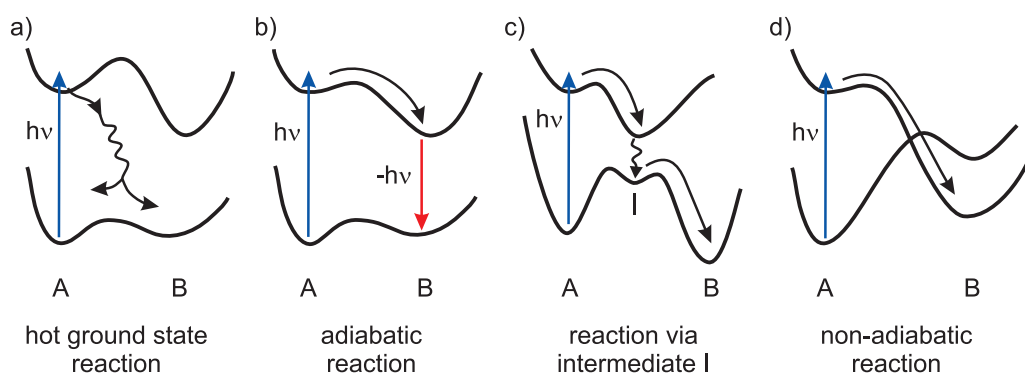


Figure 1.5: Classification of photoreactions according to the point of transfer from the photo-excited PES to the electronic ground state.

molecule is transferred from the photo-excited PES to the electronic ground state of the product (see Fig. 1.5).^[38,41] For the hot ground-state reaction (Fig. 1.5a), the transition point is structurally similar to the FC point and might be a minimum on the excited PES. The reaction $A \rightarrow B$ in the electronic ground state is driven by the excess energy the molecule possesses after IC from the transition point into highly excited vibrational states in the electronic ground state. The lifetime of the vibrationally hot electronic ground state molecules can be predicted by unimolecular rate theory (Rice–Ramsperger–Kassel–Marcus (RRKM) theory and its variants).^[42–44] As the VET of molecules in solution proceeds very fast (on a ps time scale), the hot ground-state reaction competes rarely with VET and the photochemical efficiency of hot ground-state reactions is generally low. If the chemical reaction proceeds on the excited PES as depicted in Fig. 1.5b, the process is called an adiabatic reaction. Adiabatic reactions are common in triplet states, where competing photophysical processes are slow. Singlet state adiabatic reactions may be processes with only minor structural changes with low energy barriers such as proton transfer reactions.^[45] The adiabatic reaction needs not be followed by radiative electronic deactivation as depicted in Fig. 1.5b, other deactivation mechanisms are also possible. For example, the deactivation may proceed via an unstable intermediate in the ground state as depicted in Fig. 1.5c.

Photochemical reactions may also proceed directly from the excited state to the electronic ground state via a non-adiabatic (or diabatic) reaction as shown in Fig. 1.5d. This direct photoreaction to the product proceeds via geometries at which the involved PESs cross at a conical intersection (CI) or nearly cross by avoided crossing. CIs result from non-adiabatic vibronic coupling terms, which are neglected in the standard, adiabatic Born–Oppenheimer approach of the description of PESs. When two electronic states become isoenergetic, the coupling terms cannot be neglected for two states of the same multiplicity. Two conditions must be fulfilled for a CI which requires at least two independently variable nuclear coordinates: (i) The energy of the diabatic states must be degenerate. (ii) The

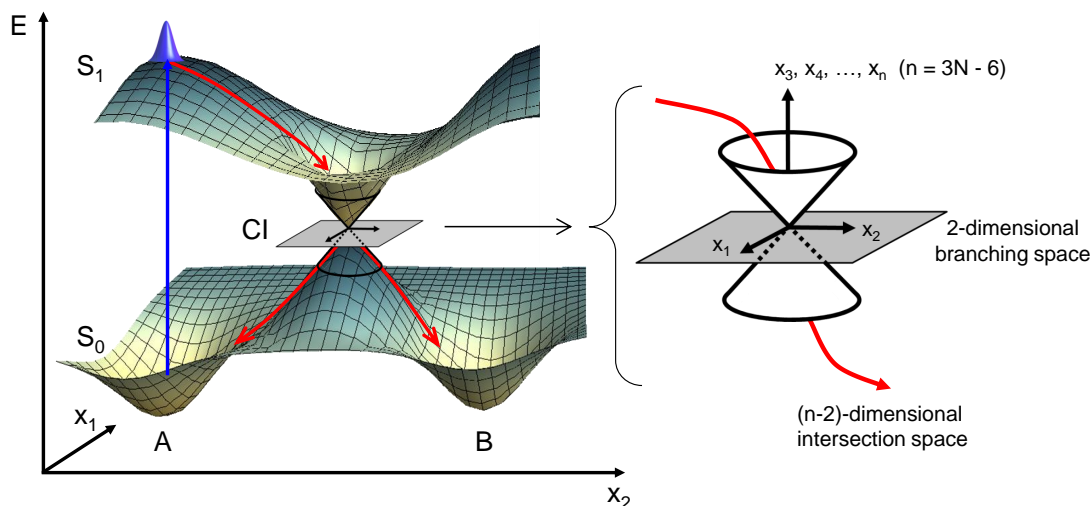


Figure 1.6: Left: Two-dimensional sketch of PESs along the coordinates x_1 and x_2 which span the branching plane for the crossing of two states with the same multiplicity for a polyatomic molecule. Right: Expanded view of the conical intersection (CI) region.

coupling terms must not lead to an avoided crossing.^[37,38]

In the case of a diatomic molecule with a one-dimensional space of internal nuclear coordinates, there is one degree of freedom to fulfill the two conditions. This leads to a strict non-crossing rule for diatomic molecules. For polyatomic molecules, PESs may cross in a $(3N - 8)$ -dimensional subspace of the $(3N - 6)$ -dimensional nuclear coordinate space and CIs are possible for each point of the intersection space. In Fig. 1.6 a CI between two states of the same multiplicity is sketched. The coordinates x_1 and x_2 span the 2D branching plane. The shape of the PESs in the vicinity of the CI has the form of a double cone. Movement along x_1 and x_2 lifts the degeneracy, while movement in the remaining $3N - 8$ directions (x_3, x_4, \dots, x_n) remains degenerate. The result is a conical intersection hyperseam in $3N - 8$ dimensional coordinate space.

CIs are involved in most fast (sub-picosecond) photochemical reactions. They act as photochemical funnels between electronic states and allow for very fast and efficient reactions with low photochemical fatigue. The topography of the excited-state PES and the FC point on this surface determine the accessibility of the CI and strongly influence the photochemical properties of molecular switches. Modification of the PES by chemical modifications of photochromic switches and systematic investigations of the molecular dynamics with femtosecond time-resolved spectroscopy therefore provide high potential for the improvement of switching properties of molecular devices.

The photonic economics of the light-driven processes are determined by their quantum yields. The photoisomerization quantum yield ϕ determines the number n_x of a photochemical event divided by the number of photons n_p that were absorbed by the reactant

of interest. For example, the photochemical process



has the isomerization quantum yield

$$\phi_{AB} = \frac{n_{AB}}{n_p} \quad (2)$$

with values of $0 \leq \phi_{AB} \leq 1$. In an extension of Kasha's rule, reaction quantum yields should be independent of the excitation wavelength, but there are several examples where this is not the case (see Section 1.2 and 1.3 below).

As photophysical processes often compete with the desired photochemical reactions, they lower the reaction quantum yields. Photoisomerization via a CI is fast enough to compete with fast photophysical processes and thus can lead to efficient photoreactions with high isomerization quantum yields, determined by the branching ratio at the CI to the reactant and the product electronic ground state (see Fig. 1.6).

As this Thesis deals with the investigation and optimization of photochromic switches, the determination of their isomerization quantum yields is essential. The experimental method for the determination of isomerization quantum yields depends on the number of possible photochemical and thermal reactions of the investigated molecule and will be detailed where appropriate.

1.2 Fulgides as Photochromic Switches

Furylfulgides are an important class of photochromic switches which undergo photo-induced and thermally irreversible $E \rightarrow C$ ring closing and reverse $C \rightarrow E$ ring opening. Both are six-electron electrocyclic reactions between the colorless, open E -isomer and the colored, closed C -isomer as shown in Fig. 1.7. An additional photochemical $E \rightarrow Z$ isomerization at the $C^4 - C^5$ double bond as an unwanted side reaction can compete with the desired photochromic $E \rightarrow C$ pathway and leads to a colorless, non-cyclizable Z -form.

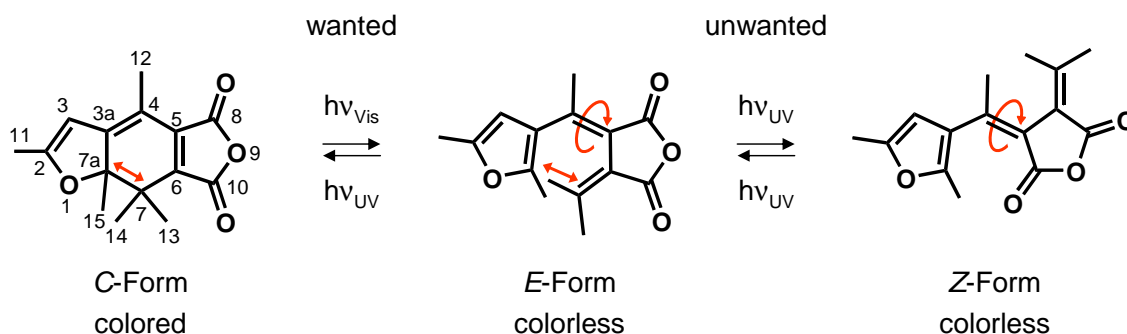


Figure 1.7: Photoisomerization reactions of furylfulgides. The atom numbering is indicated for the C -form.

The stationary UV/VIS absorption spectra of the three isomers are shown in Fig. 1.8. They display the excellent photochromic properties of this molecule, as the absorption bands of the C - and the E -isomer are well separated. The open E - and Z -isomer absorb only in the UV spectral range, with maxima of their first bands at $\lambda = 335$ and 350 nm, respectively. The closed C -isomer shows a strong absorption band in the VIS range, centered at $\lambda = 470$ nm. The weak absorption of the C -isomer around 365 nm in combination with high absorption of the Z -isomer allows for the formation of a photostationary state

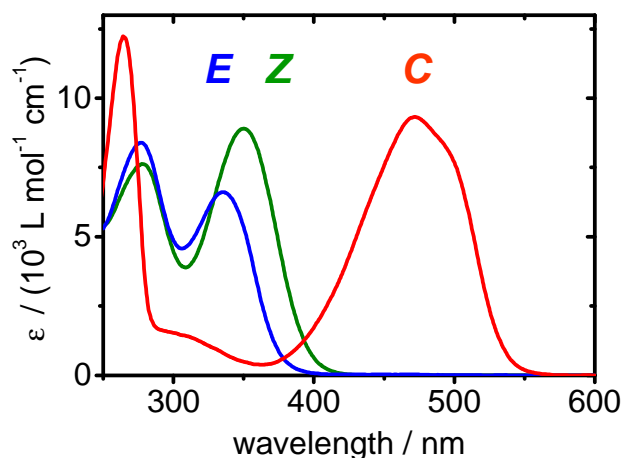


Figure 1.8: Stationary UV/VIS absorption spectra spectra of the three isomers of a furylfulgide in n -hexane.

(PSS) with $E \rightarrow C$ conversion of $\approx 95\%$ and an amount of only $\approx 1\%$ of the Z -isomer in toluene.^[46] The C -isomer can be switched quantitatively to the E -form by irradiation around $\lambda = 470$ nm.

The photochromic properties of fulgides are very sensitive to structural modifications. A lot of synthetic work has been performed within the last two decades in order to tune their switching properties by structural modifications, which enabled several applications of fulgides and related systems as summarized in the following.

1.2.1 Applications of Fulgides and Related Systems

Fulgides are widely used photochromic switches in various applications, such as molecular memories,^[4,6,20,47] photo-control of enzyme activity,^[11] photo-modulation of optical materials,^[48–50] photo-induced liquid crystal phase changes,^[51,52] photo-switching of electron and energy transfer processes or fluorescence modulation.^[53–55] One of the most promising applications for fulgides is high density data storage. Two examples from the literature will be presented in order to illustrate the requirements on modern fulgides and their derivatives.

Rath *et al.* presented the preparation of organic nanodots containing photoswitchable fulgide molecules by dewetting of thin precursor films on topographically structured substrates.^[47] Two-dimensional periodic topographic templates containing cylindric holes with diameters of $d = 50 - 400$ nm were used. A phenyl-thiophen-fulgide (PTF, see Fig. 1.9) was used as molecular device that can be switched between the closed C -isomer (state 1) and the open E -isomer (state 0) by irradiation at $\lambda = 350$ nm and 515 nm, respectively. The isomeric state of the fulgide was detected by monitoring the intense fluorescence emitted from the C -isomer after excitation at 515 nm. Information could be written and read out using a confocal fluorescence microscope. The regular arrangement of the dots allowed for the individual calculation of each dot position from period and orientation of the pattern with very high optical resolution. The authors reported that a theoretical storage density of 74 Gbit/in² would be possible, which is higher by a factor of ≈ 5 than the optical storage technology used in a Blu-Ray Disc. The major problem of

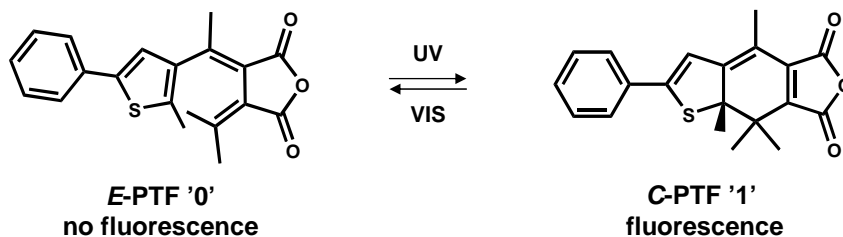


Figure 1.9: Structures of the C - and the E -phenyl-thiophen-fulgide (PTF). PTF excited at VIS wavelength emits fluorescence in the C -form only (for details see text).

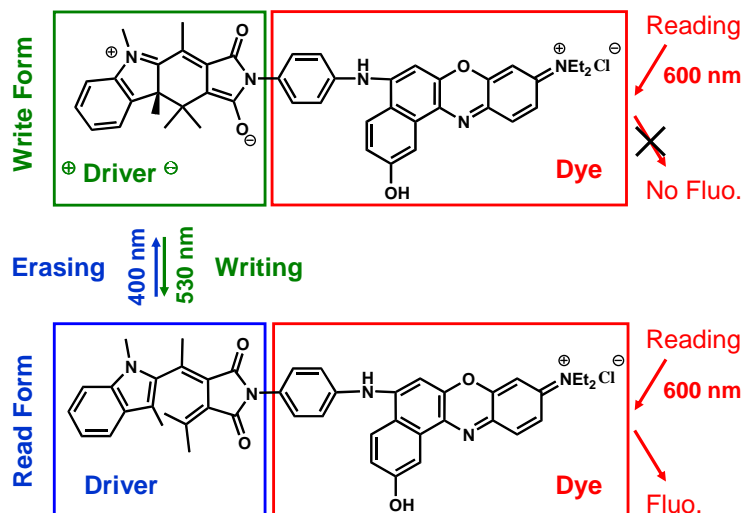


Figure 1.10: Fulgimide based photochromic switch (driver) attached to a fluorescence dye. The driver can be switched between the read and the write form with light of different wavelengths. The dye is excited at a longer wavelength to emit fluorescence when the driver is in the read form only. A write, read and erase process with nondestructive readout is possible.

this system is the destructive readout, because switching and fluorescence excitation occur at the same excitation wavelength.

Dvornikov *et al.* solved the problem of destructive readout using a fulgimide-based photochromic switch (“driver”) attached to an intensely fluorescing benzo-phenoxazine dye (see Fig. 1.10a).^[6,21] The fulgimide can be transferred between the open *E*-form (“read form”) and the closed *C*-form (“write form”). The dye component shows an intense absorption band at longer wavelengths compared to the “write” or “read” forms of the fulgimide, and emission of the dye only occurs, when the driver is in the *E*-form. The separation of the absorption spectra of the “dye” from both fulgimide isomers opens the possibility for a rewritable optical storage device with non-destructive readout.

Dvornikov *et al.* already developed the first 1 TB data storage device in the form of a removable “Write Once - Read Many” (WORM) disc. Briefly, a photoacid generator (PAG) and a dye precursor (DP) were dispersed in a polymer host (a 120 mm-diameter disk, thickness 1.2 mm). Two-photon absorption at 532 nm leads to a photochemical reaction that creates an acid. The photo-generated acid reacts with the DP and a strongly fluorescing dye is formed, which absorbs around 630 nm region and emits around 670 nm. A single-beam two-photon recording (532 nm) and one-photon readout (630 nm) system was developed by Walker *et al.*, which allows for the technical applications (see Fig. 1.11). The two-photon write process allows for 3D-data storage within different layers of the disc, since this nonlinear process only occurs inside the tight focus of the lens.^[5-7] This opens the possibility for storing data in hundreds of layers in one DVD-type disk by moving the focal position of the writing beam. The recorded data can be read by one-photon

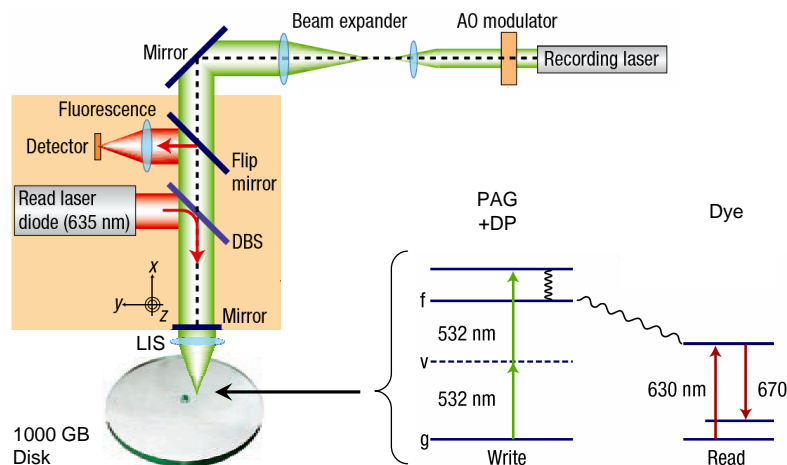


Figure 1.11: Schematic single-beam two-photon recording system to write and read 1 Tbyte of data in a DVD-type disk. Two-photon excitation for the writing process and collinear one-photon readout with a confocal architecture enables 3D-data writing and reading. DBS: dichroic beam splitter; LIS: liquid immersion system (= objective lens); AO: acousto optic modulator. Bottom right: Writing process via two-photon excitation of the photoacid generator (PAG, write) and formation of the “read” dye; v: virtual state; f: final state. Figure adapted by permission from Macmillan Publishers Ltd: Nature Photonics, Walker *et al.*^[5], copyright 2008.

induced fluorescence after excitation at 630 nm, whereupon a confocal architecture reduces crosstalk between the layers.^[6] A comparable setup would be adaptable for the use of the fulgimide-based photochromic switch shown in Fig. 1.10a)^[6] in order to realize a “Write Many - Read Many” fulgimide-based data storage device with comparable capacity.

The fast technical developments of applications require highly effective molecular devices with optimized “standard” photochemical properties like high photoisomerization quantum yields, separation of the absorption bands of photochromic isomers, and low photochemical fatigue. Furthermore, the requirements on photochromic switches increase, hence advanced properties like high two-photon absorption cross sections or the ability to record and read polarization and spectral information in order to enable multi-dimensional data storage systems have to be optimized.^[7]

Photochromic switches such as fulgides, diarylethenes and spiropyrans also offer high application potential for far-field fluorescence nanoscopy.^[32–34,56,57] When they are attached to a suitable organic donor fluorophore^[20–23,47,58,59], the fluorescence can be reversibly switched on and off on irradiation at different wavelengths (see, e.g., Figs. 1.9 and 1.10). They can therefore be used as fluorescence markers, tagging the structures of interest, such as proteins, cellular cytoskeleton or biomolecular structures.

The resolution of conventional optical fluorescence microscopes using visible light is limited due to diffraction to approximately 200 nm in the imaging plane.^[60] However, in order to monitor the activity of biological molecules within cells to determine their function, higher optical resolution under ambient conditions is required. Breaking the

resolution limit of optical fluorescence microscopes using visible light could be achieved by Stimulated Emission Depletion (STED) microscopy.^[32-34] Briefly, a specially formed (doughnut-shaped) STED beam is spatially overlapped with the excitation beam at the sample. The STED beam preferentially quenches the fluorescence of the photo-excited markers at the outer edge of the excitation spot, but not in the center. This reduces the fluorescence spot to ≈ 20 nm and allows for resolving structures below the diffraction limit by scanning the sample on a x - y grid.

The use of photoswitchable fluorophores in this field led to the development of new high-resolution wide field fluorescence imaging techniques, such as photoactivated localization microscopy (PALM)^[61,62] or stochastic optical reconstruction microscopy (STORM)^[63-65], and direct STORM (dSTORM).^[35,66] High-resolution wide field techniques use photoswitchable fluorophores tagged to the structure of interest in order to disperse spatial information of the fluorophores in the time domain by repeated activation, localization, and deactivation of the fluorophores. For each activation process, only a few molecules are stochastically converted to the emitting state with a density of active fluorophores less than one in a diffraction-limited region by appropriate adjustment of the irradiation intensity. By photoexcitation of the active fluorophores their positions can be obtained from an image of diffraction-limited fluorescence spots of these molecules - the point-spread functions (PSFs) - detected with a charge-coupled device (CCD) camera. If the density of activated molecules was larger, like in conventional fluorescence microscopy, their PSFs would overlap in the resulting image and the single molecules could not be localized individually. After the read out of the CCD camera, the fluorophores are switched to their inactive state and the procedure is repeated. This results in a large number of images that are analyzed individually. The localization procedure of single fluorophores within one image is based on the statistical fit of the PSFs with two-dimensional Gaussian functions. The error of the fitted position is $\sigma_{x,y} = s/(N^{1/2})$, where s is the standard deviation of a Gaussian (≈ 200 nm for light of wavelength $\lambda = 500$ nm) and N is the total number of detected photons.^[67,68] The structure of the sample can be reconstructed below the diffraction limit from the determined single molecule positions in all frames. Single-molecule localization with nanometer precision has already been reported.^[69-71]

The development of new photochromic switches for improved fluorescence imaging and for the tracking of the target structures are of fundamental importance. Furthermore, environmental effects caused by attaching the photochromic switch to the target structure might influence the switching efficiency. Therefore, the influence of steric restraints on photochromic switches as studied in this Thesis might be important for further applications of the investigated fulgides as fluorescence markers.

1.2.2 Effects of Structural Modifications

The photochemical properties of fulgides vary with structural modifications, which can be nicely seen in the historical development of this class of molecules. Fulgides are derivatives of dimethylene succinic anhydride **1** shown in Fig. 1.12. They can undergo photo-induced *cis/trans* isomerizations at the two methyldiene double bonds only, but the products are identical with the reactants. The attachment of an aryl substituent at one methyldiene double bond in **2** (Fig. 1.12) generates photochromic behavior due to a possible electrocyclic $E \rightarrow C$ ring closure of the hexatriene (HT) unit, which changes the conjugated π -system and therefore the absorption behavior. The photochemical properties of these first fulgides synthesized by Stobbe in the early 20th century^[72–74] were far from ideal. The conversion ratio of the ring closure reaction was quite low because of insufficient spectral separation of the absorption bands. Moreover, the *C*-form showed a thermal back reaction to the open form and photochemical degradation due to hydrogen transfer reactions. Heller *et al.* tuned the absorption spectra of the *C*-form by the use of a heteroaromatic aryl group at the methyldiene double bond (see, e.g., **3** in Fig. 1.12), which led to well separated absorption bands between the photochromic isomers.^[75] Furthermore, the replacement of the hydrogen atoms at C^{7a} and C^2 by methyl groups prevented the disrotatory thermal ring opening reaction of the closed *C*-form and reduced the photochemical degradation.^[76,77] As mentioned above, the furylfulgide (FF) **3** shown in Fig. 1.12 can undergo photochemical $E \rightleftharpoons Z$ isomerization at the $C^4 - C^5$ and the $C^6 - C^7$ methyldiene double bonds leading to the unwanted *Z*-form and to an undesired deactivation process that lowers the isomerization quantum yields, respectively. In the following, the ring closure and ring opening reaction will be denoted as the $E \rightleftharpoons C$ ($C^7 = C^{7a}$) reaction (or $E \rightleftharpoons C$ reaction for short), the $E \rightleftharpoons Z$ isomerization of the $C^4 = C^5$ ethylenic group will be referred to as the $E \rightleftharpoons Z$ ($C^4 = C^5$) reaction (or $E \rightleftharpoons Z$ reaction for short), and the $E \rightleftharpoons Z$ isomerization of the $C^6 = C^7$ isopropenylic double bond will be referred to as $E \rightleftharpoons Z$ ($C^6 = C^7$) deactivation (or deactivation for short).

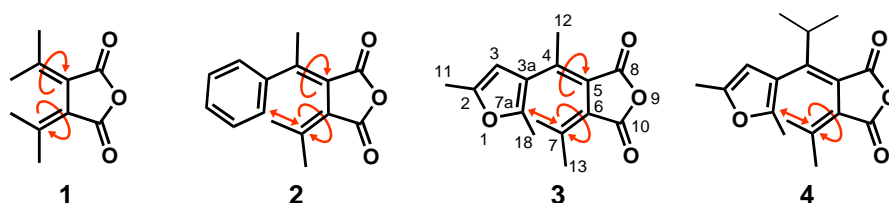
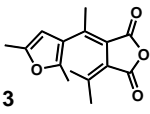
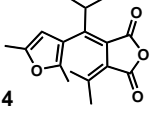
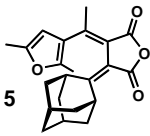
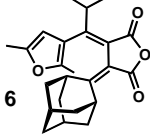
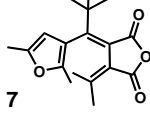
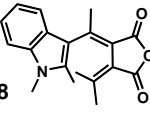
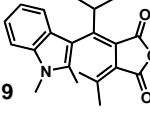
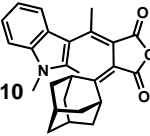
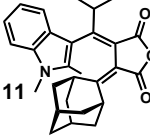
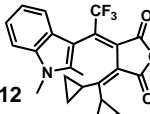


Figure 1.12: Development of furylfulgide switches: Structural modifications of dimethylene succinic anhydride **1** led to the photochromic phenylfulgide **2**, and the related but thermally stable furylfulgide **3**. The inhibition of the unwanted $E \rightarrow Z$ isomerization at the $C^4 - C^5$ double bond was realized in **4**.

Table 1.1: Effect of structural modification on the isomerization quantum yields of fulgides.

					
$\phi_{E \rightarrow C}$	0.23 ^a	0.57 ^a	0.12 ^b	0.51 ^b	0.79 ^c
$\phi_{C \rightarrow E}^{Vis}$	0.10 ^a	0.09 ^a	0.21 ^b	0.26 ^b	0.03 ^c
$\phi_{C \rightarrow E}^{UV}$	0.06 ^a	0.12 ^a	0.06 ^b	0.28 ^b	0.08 ^c
$\phi_{E \rightarrow Z}$	0.17 ^a	0.00 ^a	0.10 ^b	0.02 ^b	0.00 ^c
					
$\phi_{E \rightarrow C}$	0.05 ^d	0.23 ^d	0.04 ^d	0.07 ^d	0.15 ^e
$\phi_{C \rightarrow E}^{Vis}$	0.05 ^d	0.05 ^d	0.42 ^d	0.42 ^d	0.12 ^e
$\phi_{C \rightarrow E}^{UV}$	0.16 ^d	0.31 ^d	0.52 ^d	0.91 ^d	-
$\phi_{E \rightarrow Z}$	0.04 ^d	0.00 ^d	0.11 ^d	0.00 ^d	-

^a This work, $\lambda_{UV} = 335$ nm, $\lambda_{Vis} = 500$ nm, solvent n-hexane.

^b Yokoyama *et al.* [79], $\lambda_{UV} = 366$ nm, $\lambda_{Vis} = 492$ nm, solvent toluene.

^c Kiji *et al.* [80], $\lambda_{UV} = 366$ nm, $\lambda_{Vis} = 492$ nm, solvent toluene.

^d Uchida *et al.* [81], $\lambda_{UV} = 405$ nm, $\lambda_{Vis} = 608$ nm, solvent toluene.

^e Brust *et al.* [82], $\lambda_{UV} = 414$ nm, $\lambda_{Vis} = 594$ nm, solvent 1,4-dioxane.

The unwanted $E \rightarrow Z$ side reaction was successfully suppressed by the replacement of the methyl group at C⁴ by an isopropyl group in **4** (Fig. 1.12) by Yokoyama *et al.* in 1988. [78] The influence of bulky substituents on the isomerization quantum yields of furfurylfulgides was studied intensively in the following years. Yokoyama *et al.* showed that the $E \rightarrow C$ reaction quantum yield ($\phi_{E \rightarrow C}$) increases with the steric bulkiness of the alkyl substituent at C⁴, while the $C \rightarrow E$ ring opening reaction quantum yield after excitation in the visible ($\phi_{C \rightarrow E}^{Vis}$) was not affected. [78] The structures and quantum yields of differently substituted furfurylfulgides **3-7** are given in Table 1.1. The highest value of $\phi_{E \rightarrow C} = 0.79$ could be reached by the replacement of the methyl group at C⁴ by a *tert*-butyl group in FF **7**. [80] The increase in $\phi_{E \rightarrow C}$ for FF **7** compared to FF **4** suggests that the effect in $\phi_{E \rightarrow C}$ caused by sterically demanding groups at C⁴ is not only due to the inhibition of the $E \rightarrow Z$ reaction, since FF **7** and FF **4** both do not show $E \rightarrow Z$ isomerization. On the other hand, $\phi_{C \rightarrow E}^{Vis}$ could be increased via the replacement of the isopropylidene group by a bulky adamantylidene group as in **5**. Interestingly, $\phi_{C \rightarrow E}^{UV}$ was not affected by these structural changes, which is in violation of Kasha's rule and suggests different isomerization mechanisms for excitation to the S_1 state versus excitation to higher (S_n) states. A combination of steric modification at C⁴ (*iso*-propyl) and C⁷ (adamantylidene)

in FF **6** could successfully increase $\phi_{E \rightarrow C}$ and $\phi_{C \rightarrow E}^{Vis}$, but also led to an increased value of $\phi_{C \rightarrow E}^{UV}$. This undesirably decreases the selectivity of the wanted $E \rightarrow C$ reaction on excitation with UV light.

Besides the photoisomerization quantum yields, an important aspect regarding the use of fulgides as photochromic switches is their photochemical stability. Kaneko *et al.* demonstrated that the indolyfulgide (IF) **8** (see Table 1.1) shows a lower photochemical fatigue than furylfulgides by a factor of ≈ 30 .^[83] However, the isomerization quantum yields of IF **8** are much lower compared to those of the furylfulgides, apart from the undesirably high value of $\phi_{C \rightarrow E}^{UV}$. Therefore, Uchida *et al.* applied structural modifications at C⁴ (isopropyl instead of methyl) and C⁷ (adamantylidene instead of isopropylidene) in analogy to the modifications of FF **3-6**. Interestingly, modifications either at C⁴ or at C⁷ did lead to the desired higher isomerization quantum yields, but a combined effect due to modifications at C⁴ and C⁷ did not lead to an increase of $\phi_{E \rightarrow C}$ and $\phi_{C \rightarrow E}^{Vis}$. This was found for FF **6**. Therefore, it was not possible to increase the photoisomerization quantum yields of both desired reactions of indolyfulgides by steric modifications in analogy to furylfulgides.

A promising approach to overcome this problem was taken by Yokoyama *et al.*, who used an electron withdrawing CF₃-group at C⁴.^[84] Besides a remarkable improvement in photochemical and thermal fatigue, an increase of $\phi_{E \rightarrow C}$ was achieved. Finally, Islamova *et al.* combined the introduction of the CF₃-group at C⁴ with the replacement of the methyl groups of the isopropylidene group by cyclopropyl groups in IF **12**. This resulted in an improvement in thermal and photochemical fatigue and an increase of $\phi_{E \rightarrow C}$ and $\phi_{C \rightarrow E}^{Vis}$. Nevertheless, the isomerization quantum yields of the indolyfulgides are still far below those found for furylfulgides. The different influences of steric effects on the reactions of furylfulgides and indolyfulgides need further investigation. The summarized isomerization quantum yields of furylfulgides and indolyfulgides show that steric and electronic modifications by an enlargement of the π -electron system influence the photochemistry of fulgides.

In addition to their influence on the quantum yields, structural modifications affect the static absorption spectra of furylfulgides and indolyfulgides. This is exemplarily shown for FF **3**, IF **8** and IF **12** in Fig. 1.13. In particular, the electron rich indolyl substituent causes a remarkable bathochromic shift of the absorption maxima of both the open and the closed forms compared with the furylfulgide **3**. The open *E*-form of the furylfulgide exhibits an absorption maximum at about 340 nm, whereas the indolyfulgides show an absorption maximum at about 400 nm and the first absorption band of the *C*-form is shifted from 470 nm to 600 nm, respectively.^[83,85] The furylfulgide **3** exhibits well separated absorption bands of the open *E*-form and the closed *C*-form, which allows for selective excitation

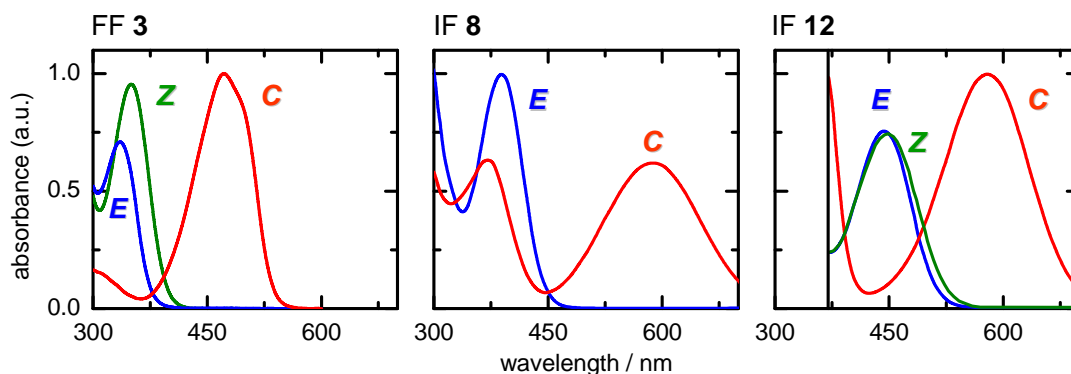


Figure 1.13: Absorption spectra of the *E*-, *C*- and *Z*-isomers of FF **3** in *n*-hexane, IF **8** in acetonitrile and IF **12** in toluene. The spectra of fulgide IF **8** were redrawn according to Brust *et al.*^[86] (no *Z*-spectrum available) and the spectra of fulgide IF **12** were redrawn according to Islamova *et al.*^[87]. For IF **12** the cyclizable isomer has been denoted “*E*-form” for compatibility reasons, disregarding the nomenclature of fluorinated fulgides.

of both isomers. The indolyfulgide **8** features high molar absorption of the *C*-form in the spectral region of the absorption band of the *E*-isomer, making it inappropriate for photochromic applications. In this case, the advantage of low photochemical fatigue was achieved at the expense of applicability and isomerization quantum yields. The electron withdrawing CF_3 -group of the indolyfulgide IF **12** led to a bathochromic shift of the first absorption band of the open cyclizable *E*-isomer².^[84] Consequently, IF **12**, a photochromic switch with well separated absorption bands, high photochemical fatigue, and acceptable photoisomerization quantum yields could be synthesized.^[87]

Interestingly, a pyrrolyl-substituted fulgide (not shown) showed similar bathochromic shifts of the the *E*- and the *C*-spectrum as indolyfulgides, but a much higher *E* \rightarrow *C* isomerization quantum yield of $\phi_{E \rightarrow C} = 0.52$.^[88] Therefore, for pyrrolyl- and indolyfulgides the benzannulation seems to influence the isomerization quantum yields. This raises the question, whether benzannulation of furylfulgides and pyrrolylfulgides itself influences their photochemistry. The comparison of the photochemical properties of different fulgides shows that fulgides without benzannulation exhibit highest values of $\phi_{E \rightarrow C}$ and $\phi_{C \rightarrow E}^{Vis}$. The origin of the increase in $\phi_{E \rightarrow C}$ and the inhibition of the *E* \rightarrow *Z* isomerization due to structural modifications at C^4 and the influence of the enlargement of the conjugated π -system has to be investigated in order to apply these effects more systematically to other fulgides.

Although much synthetic work since the early 20th century could improve the properties of fulgides significantly, detailed knowledge about the underlying processes and the influence of structural modification at the molecular level on their reaction dynamics is still missing.

²Disregarding the nomenclature of trifluorinated indolyfulgides, all open, cyclizable isomers will be denoted as *E*-isomers.

This Thesis will provide first explanations for the increase of isomerization quantum yields due to steric modifications of FF **4** compared with **3**, the mechanistic reasons of the inhibition of the unwanted $E \rightarrow Z$ photochemical side reaction, and the influence of electronic effects caused by an enlargement of the π -electron system due to benzannulation of **3**.

1.2.3 Conformational Forms of E -Fulgides and their Thermal Equilibration

Besides the photochemical reactions of fulgides, thermally activated reversible ground state diastereotopomerization leads to a non-cyclizable so-called E_β conformer, where the geometry of the hexatriene unit does not allow for electrocyclic ring closure (see Fig. 1.14). The cyclizable E_α conformer and the non-cyclizable E_β conformer are in thermal equilibrium.^[89,90] The conformational change between E_α and E_β with the lowest potential energy barrier in the electronic ground state is caused by a rotation around the $C^{3a} - C^4$ bond accompanied by a change in helical conformation between left-helical (M) and right-helical (P) (horizontal reactions in Fig. 1.14). Diastereotopomerization without change in helicity (diagonal structures) and (M)- $E_\beta \rightleftharpoons$ (P)- E_β enantiotopomerizations (vertical reaction) include higher potential energy barriers. The latter process could be observed by NMR spectroscopy.^[89,90] In contrast, the (M)- $E_\alpha \rightleftharpoons$ (P)- E_α enantiotopomerization does not occur, since the methyl group at C^{7a} cannot pass the isopropylidene group. The existence of a non-cyclizable E_β -isomer decreases the overall $E \rightarrow C$ isomerization

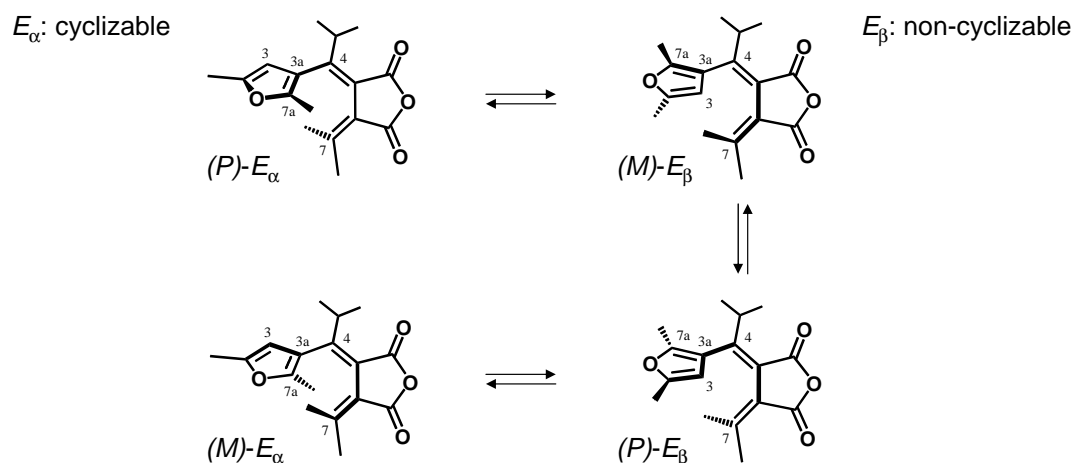


Figure 1.14: Thermal diastereotopomerization and enantiotopomerization processes of fulgides. Only the E_α -conformer can undergo photochemical cyclization, the E_β does not. The top row shows the simultaneous diastereotopomerization and helical change between (P)- E_α and (M)- E_β , the bottom row the change between (M)- E_α and (P)- E_β . The vertical arrow describes the enantiotopomerization between (P)- E_β and (M)- E_β conformers. Other possible thermal interconversions not labeled with arrows are energetically unfavorable.^[90]

quantum yield for fulgides. To the best of the author's knowledge, it was not possible to block this unwanted $(M)-E_\alpha \rightleftharpoons (P)-E_\beta$ diastereotopomerization process before the present work. It might be possible that bulky groups like the isopropyl group at C⁴ influence the conformer equilibrium and therefore provide an explanation for the increased values of $\phi_{E \rightarrow C}$ mentioned above. A detailed investigation of these processes was one of the tasks of the present Thesis.

1.2.4 Reaction Mechanism and Photo-Induced Dynamics of Fulgides

First investigations on the photochemical reaction mechanisms of fulgides were performed by NMR spectroscopy. Heller *et al.* showed that fulgides undergo photochemical conrotatory and thermal disrotatory ring closure and ring opening reactions according to the Woodward-Hoffmann rule for pericyclic reactions.^[75,91] For a detailed insight into the reaction mechanism and molecular dynamics, micro- and nanosecond laser flash techniques^[92] and picosecond time-dependent measurements on the ring closure reaction of fulgides were performed.^[49,93–96] However, those measurements lacked the required temporal resolution and could only give an upper limit for the isomerization times. First femtosecond time-resolved transient absorption measurements were performed by Handschuh *et al.* in 1997.^[97] Port *et al.* presented femtosecond time-resolved transient absorption measurements of the ring opening reaction of a furylfulgide in 2005.^[98] During the last five years the ring closure reaction^[82,99–102] and the ring opening reaction^[82,86,99–101,103–110] of fulgides and fulgimides were studied intensively by femtosecond time-resolved absorption spectroscopy in the UV/VIS and infrared (IR) spectral ranges as well as by fs time-resolved fluorescence spectroscopy.

For the $E \rightarrow C$ ring closure reaction, different isomerization mechanisms are under discussion: (i) Handschuh *et al.* proposed a complex reaction mechanism, which includes a direct sub-picosecond pathway from the photo-excited E -isomer to the electronic ground state of the C -isomer and a parallel slower (> 10 ps) indirect route, involving an intermediate for the formation of the C -form.^[97] The indirect pathway could be observed for photoisomerization in different solvents (toluene, acetonitrile), but was absent in a poly-methylmethacrylate (PMMA) matrix.^[98] (ii) Heinz *et al.* suggested a sequential cyclization of an indolylfulgimide involving two excited electronic states based on two picosecond excited-state depopulation times in transient absorption and fluorescence.^[99] Their model was comparable to the prototypical hexatriene/cyclohexadiene (HT/CHD) reaction system.^[111,112] The photo-excited state is assumed to be the S_2 state ($1B_2$ in HT), leading to the S_1 state ($2A_1$ in HT) via a CI and finally to the S_0 state ($1A_1$ in HT) of the product or the reactant. (iii) A direct ring closure reaction for E -fulgides after photo-excitation into an optically bright excited S_1 state was proposed by quantum chemical

calculations^[113] in agreement with recent fs time-resolved investigations of indolylfulgides. The ring closure reaction was found to be a non-activated process on a sub-picosecond time scale with time constants in the range between 200 and 400 fs.^[82,100–102] The bright S_1 state was assumed to be reached by a $\pi\pi^*$ transition with charge translocation upon excitation from the heteroaromatic ring to the anhydride moiety.^[113]

For the $C \rightarrow E$ ring opening reaction, two different isomerization mechanisms were discussed: (i) Heinz *et al.* interpreted two excited-state decay times of an indolylfulgimide observed by fs transient absorption and fluorescence spectroscopy^[99] as excitation to the S_2 state and ultrafast dynamics via two CIs to the S_1 and the S_0 state, in analogy to the prototypical HT/CHD system^[114,115]. The $C \rightarrow E$ isomerization time was found to be $\tau = 2.4$ ps, which is longer than the isomerization times found for the ring closure reaction. (ii) More recent studies interpret the two decay times observed in transient absorption spectroscopy as wave packet motion from the Franck–Condon (FC) region and initial solvent dynamics within several hundred femtoseconds to a vibrationally relaxed S_1 state. Isomerization then occurs from the relaxed S_1 state via a CI to the ground state. The reaction pathway involves an excited-state energy barrier and the isomerization is therefore an “activated” process.^[82,108–110] Ring opening reaction times between 2 and 20 ps were reported. The isomerization times were strongly dependent on the polarity of the solvent and on structural modifications of the indolylfulgides and -fulgimides. Interestingly, the indolylfulgides with the highest isomerization quantum yields ($\phi_{C \rightarrow E}^{Vis}$) and the lowest photochemical fatigue (see, e.g., fulgide **12** in Table 1.1) show the lowest excited-state energy barriers and consequently faster isomerization times.

The latter isomerization mechanism is in good agreement with recent quantum chemical calculations from Tomasello *et al.*^[113] Geometry optimizations of the first excited state of a furylfulgide suggest an excited-state minimum along the ring opening reaction coordinate and a potential energy barrier towards a CI that connects the S_1 state with the electronic ground state. The S_1 state was found to be a zwitterionic state that might be sensitive to structural and solvent effects.

The ring opening efficiency of fulgides could be increased by photo-excitation to higher excited states.^[105–107] Cordes *et al.* showed that photo-excitation of a fluorinated indolylfulgide into a S_n state at $\lambda = 340$ nm led to increased $C \rightarrow E$ quantum yields. In contradiction to Kasha’s rule, only ≈ 40 % of the excited molecules showed relaxation via the S_1 state. A direct reaction path leading from the S_n state directly to the product and the reactant ground states was observed. An even more effective increase of isomerization quantum yields was observed by Ishibashi *et al.* by a successive two-photon absorption from a 15 ps laser pulse.^[105,107] These results may be very interesting regarding multi-dimensional high density data storage, where two-photon absorption processes are

required (see Section 1.2.1 above). Furthermore, fs time-resolved pump-repump-probe spectroscopy in the UV/VIS spectral range^[116] revealed that promoting active modes of the photo-induced ring opening reaction are efficiently excited by a directly preceding ring closure reaction. With this preceding ring closure reaction, a ring opening reaction with increased quantum yield could be observed.^[108,110,116]

The $Z \rightarrow E$ isomerization of a furylfulgide (FF **3**) was investigated in our laboratory with femtosecond time-resolved transient absorption spectroscopy by Renth *et al.*^[117] They observed a barrierless excited-state pathway after excitation at $\lambda_{pump} = 387$ nm with a time constant of 220 fs.

One of the tasks of this Thesis was to study the effects of structural modifications of FF **4** compared with FF **3** that led to inhibition of the undesired $E \rightarrow Z$ isomerization and to an increase of $E \rightarrow C$ isomerization quantum yields by means of fs time-resolved transient absorption spectroscopy. To the best of the author's knowledge, the $E \rightarrow Z$ isomerization was mostly neglected in fs time-resolved measurements before the present work. As transient absorption spectroscopy allows for monitoring the vibronic transformations from the initial photo-excited molecules all the way to the equilibrated final products, a comparative study of FF **3** and **4** can provide information of the excited-state pathway for both reaction channels. Furthermore, the effect of structural modifications on the dynamics of the $C \rightarrow E$ and the $Z \rightarrow E$ isomerization was investigated.

1.2.5 Investigated Furylfulgides and Aims of this Thesis

One of the main tasks of this Thesis was a comparative study of four different structurally modified furylfulgides performed by determination of isomerization quantum yields, femtosecond time-resolved transient absorption spectroscopy, and quantum chemical calculations. The parent furylfulgide 2-[1-(2,5-dimethyl-3-furyl)-ethylidene]-3-isopropylidene succinic anhydride (MeF), introduced in Table 1.1 as reference molecule **1**, was modified structurally and electronically. The methyl substituent at the central hexatriene (HT) unit was replaced by an isopropyl substituent (iPrF) or by intramolecular bridging (7rF) as steric constraints. In 7rF, the alkyl bridge should inhibit the undesired conformer equilibrium between E_α and E_β . Furthermore, in MeBF the conjugated system of MeF was enlarged by benzannulation as an additional electronic effect.

This extensive investigation should answer the open questions of (*i*) the origin of the increase of isomerization quantum yields due to steric modifications, (*ii*) the role of the non-cyclizable E_β conformer, (*iii*) the mechanistic reasons for the inhibition of the unwanted $E \rightarrow Z$ photochemical side reaction due to steric modifications, and (*iv*) the influence of electronic effects caused by an enlargement of the π -electron system due to benzannulation. As mentioned above, MeF can undergo the desired $C \rightarrow E$ ring opening

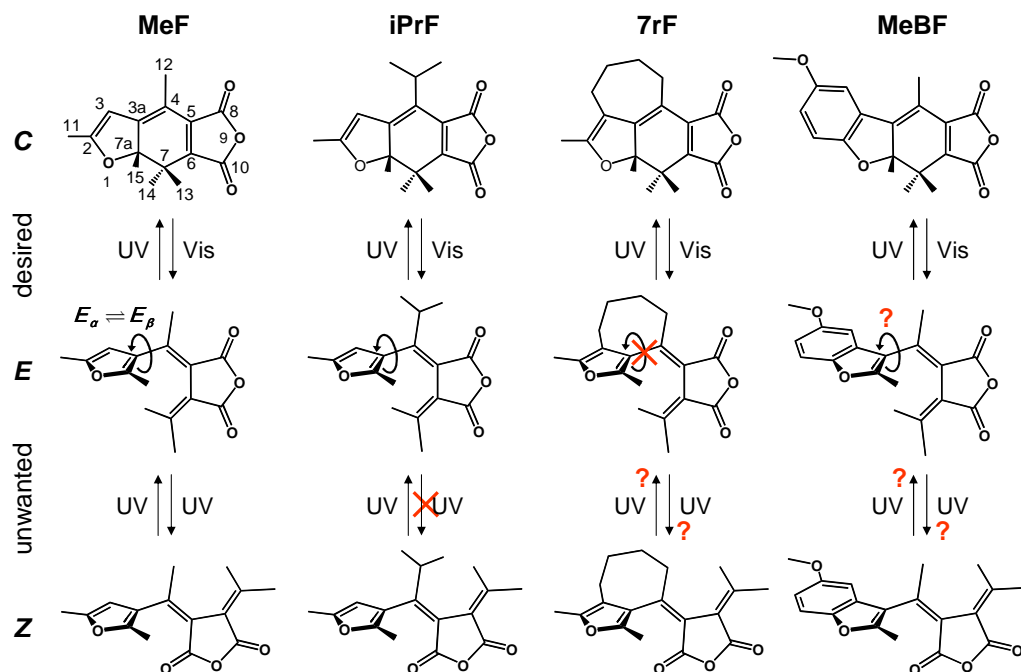


Figure 1.15: Structures and investigated photochemical reactions of the four fulgides MeF, iPrF, 7rF and MeBF.

and $E \rightarrow C$ ring closure reactions as well as the unwanted $E \rightarrow Z$ side reaction, and additionally shows the $E_\alpha \rightleftharpoons E_\beta$ diastereotopomerization. The investigated fulgides in their C -, E -, and Z -forms are shown in Fig. 1.15. For iPrF, the methyl group at C^4 is replaced by an isopropyl group. As will be shown, this leads to inhibition of the unwanted $E \rightarrow Z$ side reaction and an increase of the $E \rightarrow C$ isomerization quantum yield of a factor of ≈ 3 , which cannot be explained only by the suppression of the $E \rightarrow Z$ reaction. On the other hand, the thermal $E_\alpha \rightleftharpoons E_\beta$ conversion is not suppressed for iPrF.^[89,90] In the course of this Thesis, fulgide 7rF was therefore designed, where the furyl and the hexatriene subunits are linked via a butyl chain, thus forming a 7-membered ring. To the author's knowledge, this is the first fulgide with a completely blocked $E_\alpha \rightleftharpoons E_\beta$ conversion and $(M)-E_\beta \rightleftharpoons (P)-E_\beta$ racemization that allows for the first investigation of a pure E_α -fulgide. Consequently, the influence of the conformer equilibrium on the photochemistry can be investigated directly by comparison with MeF, iPrF, and 7rF. The methoxy group attached to the benzofuran in MeBF allows for further attachments of additional chromophores, e.g., for fluorescence modulation and far-field fluorescence nanoscopy^[32–36] as discussed in Section 1.2.1. Therefore, the influence of the methoxy-benzannulation on the dynamics and photochemical properties is of enormous importance. Besides, the large benzofuryl group might reduce the $E_\alpha \rightleftharpoons E_\beta$ conversion and racemization processes.

1.3 Azobenzenes as Photochromic Switches

Azobenzene (AB) and its derivatives are a very important and well investigated class of photochromic switches. The photochemical E (*trans*) \rightleftharpoons Z (*cis*) isomerization goes along with large-amplitude structural and dipole moment changes between the elongated E - and the more compact Z -form. The E -form is the thermodynamically stable isomer, whereas the Z -isomer undergoes thermal $Z \rightarrow E$ back-isomerization. The photoisomerization between the E - and the Z -form is fully reversible and high photostability guarantees a large number of switching cycles. Figure 1.16 shows the structural changes of AB induced by photoisomerization. The $E \rightarrow Z$ isomerization of AB produces a change in the end-to-end distance $d(C^4 - C^{4'})$ of about 3 Å. The elongated E -form has a planar structure and a dipole moment of zero. In the Z -isomer the phenyl rings are twisted because of steric hindrance which results in a non-planar structure. The energy difference between both isomers is $\Delta E_{Z-E} \approx 0.6$ eV.^[118] The Z -isomer has a dipole moment of $\mu \approx 3$ D perpendicular to the NN axis.^[119]

The spectral absorption changes induced by photoisomerization of AB are shown in Fig. 1.17.^[120] The E - and Z -isomer display a low-intensity $S_1(n\pi^*)$ absorption band at VIS wavelength ($\lambda_{max} = 450$ nm and 440 nm, respectively) and a high-intensity $S_2(\pi\pi^*)$ band in the UV ($\lambda_{max} = 315$ nm and 275 nm, respectively). The $n\pi^*$ transition occurs from the highest occupied molecular orbital (HOMO), i.e., the non-bonding lone pair of the central nitrogens, to the lowest unoccupied molecular orbital (LUMO) which is the lowest antibonding π^* orbital. For the planar E -AB, the $n\pi^*$ transition is symmetry forbidden and therefore shows a very low oscillator strength. For the Z -isomer the twisted structure leads to a loss of symmetry, which results in higher molar absorption coefficients of the now partially allowed $n\pi^*$ transition (see Fig. 1.17). The $\pi\pi^*$ transition of AB occurs from the LUMO \leftarrow HOMO-1 transition, where HOMO-1 is dominated by the π orbital of the central nitrogens^[119] with higher molar absorption coefficients for E -AB.

The two isomers can be switched by irradiation with light corresponding to the energy gap of the $n\pi^*$ or the $\pi\pi^*$ transition. As the $n\pi^*$ absorption bands of E - and Z -AB lie in

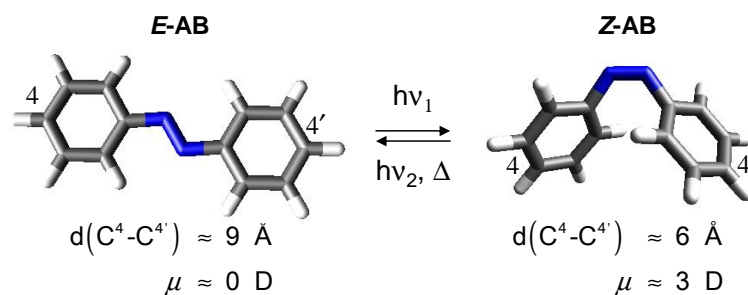


Figure 1.16: Photoisomerization reaction of azobenzene. The isomerization goes along with a change in molecular length and dipole moment.

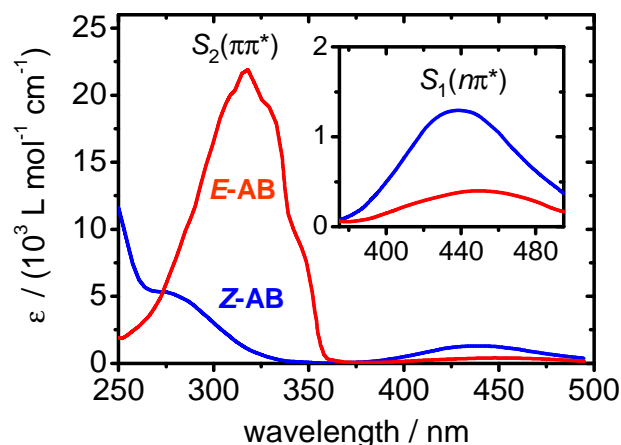


Figure 1.17: UV/VIS absorption spectra of the *E*- and the *Z*-AB in *n*-hexane.^[120]

the same spectral range and differ only in their respective oscillator strength, an effective *E* → *Z* isomerization requires UV excitation in the $\pi\pi^*$ band. The higher $n\pi^*$ oscillator strength of *Z*-AB allows for effective *Z* → *E* isomerization with VIS excitation.

The energetic ordering of the $n\pi^*$ and $\pi\pi^*$ electronic states can be changed by electron-donating or withdrawing groups on the phenyl rings. A classification scheme of three spectral types of ABs based on this effect was introduced by Rau *et al.*:^[121] (i) AB-type molecules (see, e.g., Fig. 1.16) show a low-intensity $n\pi^*$ absorption band in the VIS spectral range and an intense $\pi\pi^*$ band in the UV, as described above. (ii) Substitution of AB with an electron-donating group, e.g., an NH_2 group, leads to the amino-AB type, where the $n\pi^*$ and $\pi\pi^*$ bands lie in the near-visible UV at comparable wavelength or even spectrally overlapped due to an increase in the π orbital energy and a decrease in the energy of the π^* orbital.^[121,122] (iii) This effect is even enhanced^[121] for so-called push-pull ABs having an electron donor and electron acceptor group at the 4 and 4' positions. This leads to a reverse order of the respective states compared with AB-type molecules and a shift of the $\pi\pi^*$ band towards VIS wavelength. Push-pull ABs are allocated to the pseudo-stilbene spectral type.

Besides the spectral differences of these three types of ABs, they exhibit different thermal *Z* → *E* isomerization times. While AB type molecules show thermal isomerization only within hours or days, push-pull ABs re-form their *E*-isomer within minutes or even milliseconds depending on the solvent polarity.^[123]

Although the large change in geometry and dipole moment of AB is required for several applications of photochemical switches, the photoswitching properties of AB are far from ideal, in particular for applications which require other molecular moieties attached to the AB unit. As an effective *E* → *Z* isomerization requires UV excitation below 375 nm, the photoswitching efficiency in the required wavelength range may suffer from photodamage of the attached moieties.

1.3.1 Applications of Azobenzenes

Azobenzenes are widely used molecular switches,^[8,25,27] which were successfully employed in, e.g., light-driven machines or manipulators,^[9,10,124–126] non-linear optical devices,^[127,128] photoregulation of biomolecules,^[11–14,16,129–140] dendrimers,^[141,142] polymers^[143–146] or emulsions,^[147] for innovative photoresponsive surfaces,^[17,18,27,30,148–158] in liquid crystalline systems,^[2,159–162] and high-density optical data storage.^[1–3,163] For several applications, in which a large change in geometry or dipole moment is required, azobenzenes are usually the first choice. It would exceed the scope of this introduction to give a complete overview, so only a few recent examples from the literature have to suffice to illustrate the importance of ABs.

The photoregulation of biomolecules (such as model peptides and proteins) has been investigated intensively within the last decades. One of the pioneers in this field was Goodman who brought azobenzene into polypeptides already in the 1960s.^[164,165] The review articles by Willner *et al.*, Renner *et al.*, and Woolley summarize the advances in the development of photobiological switches.^[11,12,137,166] In recent work taken as an example, Schierling *et al.*^[16] constructed photoswitchable restriction enzymes (variants of the natural restriction endonuclease PvuII) by cross-linking suitable cysteine amino acids of the protein with AB derivatives as shown in Fig. 1.18. The switchable efficiency of the enzyme is based on the dependence of protein activity on its three-dimensional structure. The DNA cleavage activity of the restriction enzyme could be increased by a factor of 16 by switching the configuration of the incorporated AB moieties from the *E*- to the *Z*-form.^[16] Highest switching efficiency of the enzyme was achieved by ABs attached close to the

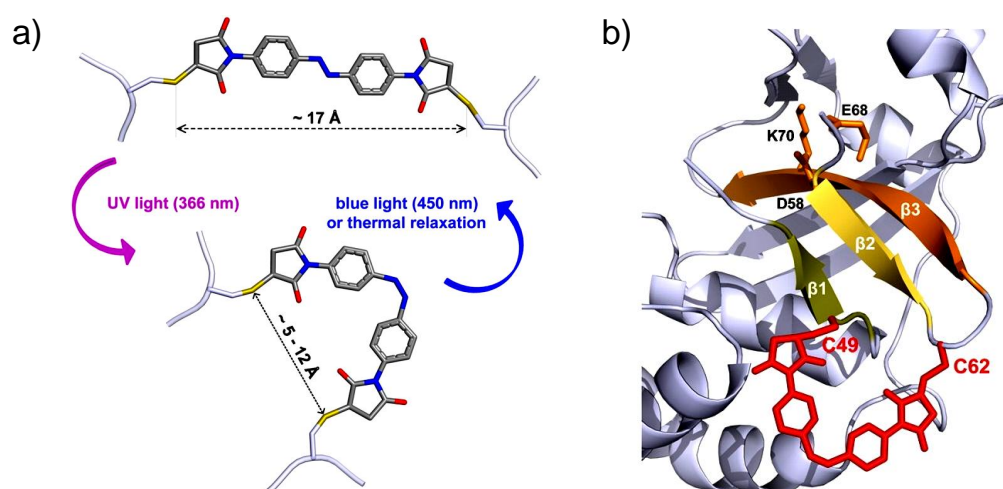


Figure 1.18: a) Scheme of the $E \rightleftharpoons Z$ isomerization of an AB derivative attached to cysteine amino acids of an enzyme. Photoisomerization of the switching unit changes the sulfur-sulfur distance remarkably. b) Detail of the crystal structure of a restriction enzyme (see text), which shows the azobenzene moiety attached to the active center of the protein. Figure adapted by permission from National Academy of Sciences: PNAS, Schierling *et al.*^[16], copyright 2010.

active site of the protein as illustrated in Fig. 1.18b. A general problem of this approach is the destructive UV wavelength needed for photochemical switching of AB under ambient conditions, e.g., in living cells. On the other hand, the desired large amplitude structural changes induced by AB cannot be realized easily with other photoswitchable molecules.

Another important approach for the application of ABs is the functionalization of surfaces. Such “smart surfaces” can respond to an external trigger in a specific manner depending on the functionalization. They have considerable potential for controlling surface properties, such as wetting and dewetting, (bio)adhesion, transport processes, and catalysis.^[17,18,27,30,148–158] Vertically oriented ABs chemisorbed on a surface form densely packed self-assembled monolayers (SAMs) of the planar and extended *E*-isomer (see Fig. 1.19a). Commonly, alkylthiols exposing AB headgroups adsorbed on a gold surface are used because of the strong binding between sulfur and gold.

An almost quantitative switching process upon light irradiation at the surface could be realized by a rigid biphenyl-based AB derivative.^[154] This SAM could be used to convert light into mechanical work in the so-called “cargo lifter” due to photoinduced thickness changes of the SAM by approximately 7 Å.^[17] Despite this promising example, most of the SAMs of pure AB-substituted alkanethiols suffer from sterical restrictions of the photoinduced *E* → *Z* isomerization. Switching to the bent non-planar *Z*-isomer is often possible only to a small degree due to lack of free switching volume as indicated in Fig. 1.19a or due to electronic coupling to the gold surface.^[152,167] Different approaches to overcome the problem of steric restrictions have been attempted. For example, mixed SAMs of AB-substituted alkanethiols and short alkanethiols on gold should provide enough free volume to allow for the *E* → *Z* isomerization of AB.^[157,167,168] However, this approach often leads to phase separation and aggregation of the AB-substituted alkanethiols.

A promising approach to overcome the problem of lack of free switching volume is to place the functional device on a rigid molecular mount, such as a tripod.^[158,169,170] The

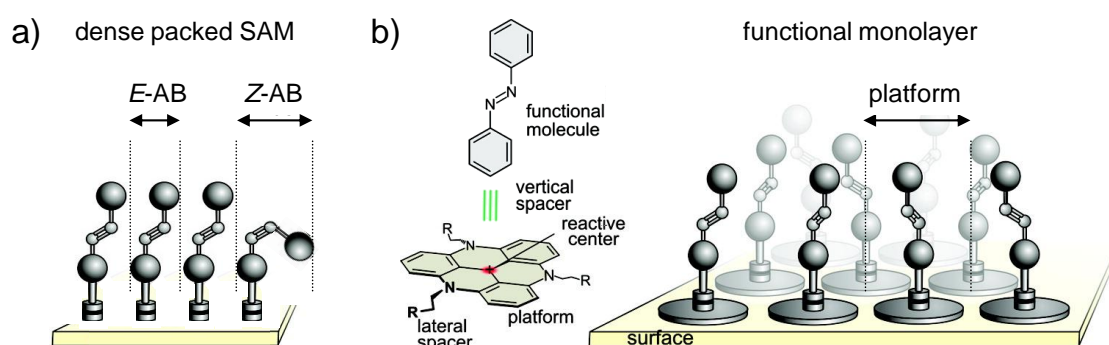


Figure 1.19: a) Densely packed SAM illustrating lack of free volume for the photo-induced *E* → *Z* isomerization of azobenzenes. b) Platform approach from the Herges group. Figure adapted by permission from American Chemical Society: J. Am. Chem. Soc., Baisch *et al.*^[18], copyright 2009.

resulting systems showed reversible switching behavior of the AB-functionalized SAM similar to free molecules in solution. The alternative platform approach of Herges and co-workers *et al.*^[18] is shown in Fig. 1.19b. The free volume is determined approximately by the diameter of the platform and more than large enough to provide enough space for the *Z*-AB. The thermodynamically stable *Z*-brAB molecule investigated in this Thesis might be used in this field in order to build photoswitchable SAMs, as in this case the sterically demanding form could be assembled on the solid layer, thus providing enough free volume for itself.

The geometric changes induced by isomerization of AB can be used for the photo-controlled alignment and organization of liquid crystalline (LC) phases.^[2,159–162,171–174] Incorporation of azobenzenes in bulk materials already allow for the realization of a light-driven motor based on liquid crystalline elastomers (LCEs).^[175] LCEs exist in a nematic and an isotropic phase. The phase change from nematic to isotropic is accompanied by a reversible contraction along the alignment direction with a contraction/elongation ratio of up to 400%.^[176] Yamada *et al.* could transfer the stretching and contraction of a main-chain AB-LCE to a polyethylene film by laminating it with the AB-LCE. The coated polyethylene belt was placed over a pulley system. A schematic picture taken from Yamada *et al.*^[175] of this light-driven plastic motor is shown in Fig. 1.20a. The used liquid crystalline monomers containing AB as the photochromic switch are shown in Fig. 1.20b. By irradiating the belt with UV light and VIS light at a different area simultaneously, the whole system starts a continuous rotation. Altogether, this setup realizes a direct conversion of light energy into mechanical work.

In summary, ABs are very robust photochemical switches with the unique photochemical property of large-amplitude structural changes usable in several different environments, such as AB attached to biomolecules, on surfaces, and in liquid crystals. However, their application potential for many biological applications is limited by the similar S_1 absorption bands of *E*- and *Z*-AB and the requirement of UV-excitation wavelengths shorter than 375 nm.

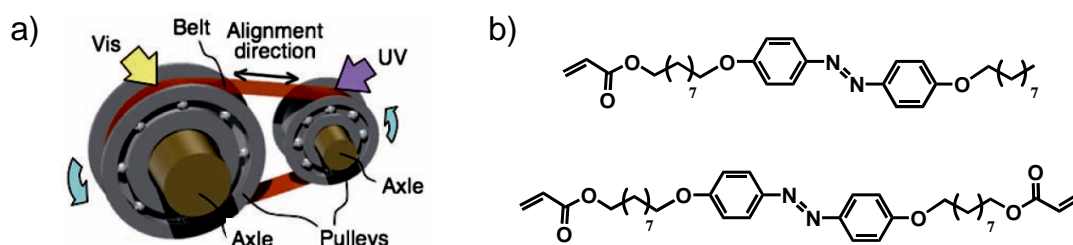


Figure 1.20: a) Schematic illustration of a light-driven motor system containing an AB-LCE coated polyethylene belt (details see text). b) Chemical structures of the monofunctional LC monomer and the difunctional LC diacrylate used for polymerization of the AB-LCE. Figure adapted by permission from Wiley-VCH Verlag GmbH & Co. KGaA: *Angew. Chem., Int. Ed.*, Yamada *et al.*^[175], copyright 2008.

1.3.2 Reaction Mechanism and Photo-Induced Dynamics of Azobenzenes

The isomerization mechanism of azobenzene has been extensively studied in the last two decades. Bortolus *et al.* first determined the isomerization quantum yields of *E*- and *Z*-AB after S_1 ($n\pi^*$) and S_2 ($\pi\pi^*$) excitation.^[177] The results are an example of the violation of Kasha’s rule, because the quantum yields (ϕ) after S_1 excitation are twice the values found for S_2 excitation of AB. On the other hand, Kasha’s rule is obeyed in a sterically hindered azobenzene bridged by a crown ether (AB-crown), which shows the same quantum yields for S_1 and S_2 excitation.^[178] A comparison of the quantum yields of AB and AB-crown determined by Rau *et al.* is given in Table 1.2.

First interpretations of these results suggested a rotational isomerization mechanism including a free rotation of the phenyl rings for AB after S_2 excitation in contrast to an inversion mechanism via a planar transition structure with higher efficiency for S_1 excitation. In AB-crown, the free large-scale motion rotation of the phenyl rings is hindered and consequently the rotation mechanism after S_2 excitation was assumed to be blocked.

The results of Rau *et al.* inspired numerous experimental^[179–187] and theoretical^[188–194] studies of AB, which revealed a more complex reaction mechanism. In principle, the four different mechanisms shown in Fig. 1.21 were discussed. These are (*i*) the inversion of one phenyl group via a planar transition structure, (*ii*) a large-scale rotation of one phenyl ring around the N=N axis, (*iii*) a concerted inversion of both phenyl groups via a planar and linear transition structure, and (*iv*) a combined change of the CNNC torsion angle and rotation around the CN-bond; this so-called “hula-twist” leads to $E \rightleftharpoons Z$ isomerization without a large-scale rotation of the phenyl groups via a transition structure with a 90° CNNC torsion angle.

Environmental effects, e.g., in solutions, on surfaces or in bulk materials might strongly influence or even inhibit the different $E \rightleftharpoons Z$ isomerization mechanisms. For the case of mechanism-dependent isomerization quantum yields as suggested by Rau *et al.*, a detailed knowledge about the isomerization pathways is extremely important. Understanding the reaction mechanism may lead to improvement of photochemical properties by blocking less efficient pathways by chemical modifications.

Femtosecond time-resolved transient absorption and fluorescence measurements of the

Table 1.2: Isomerization quantum yields of AB and an AB bridged by a crown ether (AB-crown) from Rau *et al.*^[178] for S_1 and S_2 excitation in ethanol as solvent.

	$\phi_{E \rightarrow Z}$		$\phi_{Z \rightarrow E}$	
	$S_1 \leftarrow S_0$	$S_2 \leftarrow S_0$	$S_1 \leftarrow S_0$	$S_2 \leftarrow S_0$
AB	0.24	0.12	0.53	0.31
AB-crown	0.29	0.29	0.56	0.53

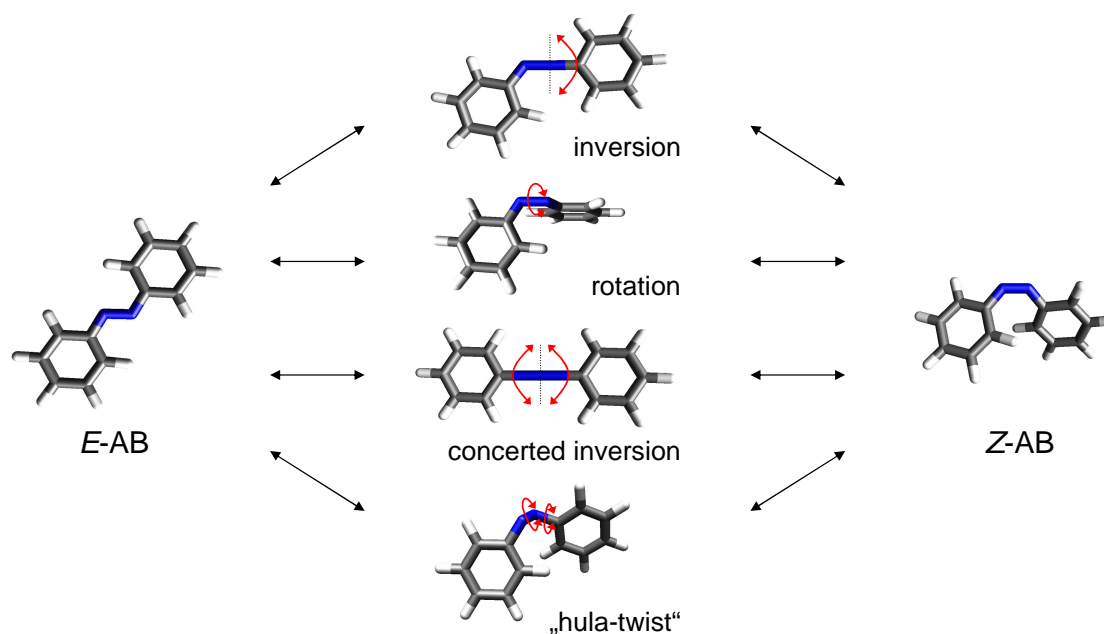


Figure 1.21: Schematic isomerization mechanisms and possible transition structures in the $E \rightleftharpoons Z$ isomerization of AB.

$E \rightarrow Z$ isomerization after S_1 excitation^[179,184,186,187,195] yielded two excited-state decay times, $\tau_1 \approx 0.30$ ps, which was attributed to the initial departure of the wave packet from the FC region, and $\tau_2 \approx 2 - 3$ ps assigned to the isomerization via a CI to the electronic ground state of the product or the reactant. For the photochemical $Z \rightarrow E$ isomerization, a similar behavior was found with even faster decay times of $\tau_1 \approx 0.17$ ps and $\tau_2 \approx 1$ ps.^[179,186,196] Fluorescence anisotropy measurements in solvents with different viscosity revealed discrepancies to Rau's hypothesis of the assignment of the isomerization mechanisms after S_1 and S_2 excitation. They observed a decaying anisotropy in *n*-hexane due to depolarization of the initial in-plane transition moment caused by the rotational mechanism.^[187] However, in the viscous solvent ethylene glycol, no noticeable decay of anisotropy was observed.^[187] This result was explained by assuming a planar inversion mechanism in viscous solvents, which is in good agreement with quantum chemical calculations.^[197–200] These propose an energy barrier along the inversion pathway on the S_1 surface and a direct barrierless pathway for the rotation mechanism via a CI to the electronic ground state. It seems reasonable to suggest that in non-restricting environments the rotational mechanism is favored. Therefore, environmental effects might determine the isomerization mechanism of ABs.

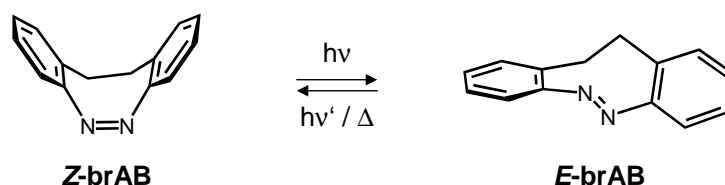
Femtosecond time-resolved results for the $E \rightarrow Z$ photoisomerization after S_2 excitation^[180–183,196,201,202] were interpreted in favor of a fast internal conversion from the S_2 to the S_1 state and a subsequent deactivation via a CI to the electronic ground state. Satzger

et al. performed time-resolved UV/VIS absorption spectroscopy and determined three excited-state decay times for *E*-AB.^[196] The shortest excited-state decay time $\tau_1 = 0.13$ ps was attributed to the decay time of the S_2 state. Two slower decay times were interpreted as vibrational relaxation and isomerization in the S_1 state with $\tau_2 = 0.42$ ps and $\tau_3 = 2.9$ ps, respectively. For *Z*-AB, the observed two decay times of $\tau_1 = 0.2$ ps and $\tau_2 = 1.1$ ps after excitation to S_2 were attributed to the decay of the S_2 and S_1 states, respectively. Time-resolved absorption and Raman spectroscopy showed that the transient UV/VIS spectra attributed to the S_1 state were practically identical after S_1 and S_2 excitation and that the NN bond retains a double bond nature in the S_1 state.^[183,201] Reduced isomerization quantum yields after S_2 excitation were explained by assuming a smaller isomerization yield for the hot S_1 state molecules.

Experimental and theoretical investigations of rotationally hindered ABs provided important information regarding the isomerization mechanisms.^[195,202] The rotational hindering reduced the number of possible isomerization mechanism, which simplifies the interpretation of the data. For example, from femtosecond time-resolved fluorescence measurements of an *E*-AB derivative bridged by a crown ether (AB-crown) ten times longer isomerization times after S_1 excitation were observed compared with *E*-AB.^[195] On the other hand, Lu *et al.* presented comparable ultrafast dynamics for the $S_2 \rightarrow S_1$ relaxation for restricted azobenzophanes and the parent compound AB.^[202] These data also indicate that a different isomerization mechanism for AB in the S_2 state is unlikely. Quantum chemical calculations on the above mentioned rotational restricted ABs indicate that the rotational constraints in these molecules only impede the large-amplitude rotation of the phenyl rings,^[188,203] but the “hula-twist” mechanism introduced in Fig. 1.21 is possible. Diao *et al.* found an additional CI along a concerted inversion pathway for the *E* \rightarrow *Z* isomerization of AB, which could become energetically accessible from hot S_1 states and might lead to a higher amount of S_0 reactant formation.^[199] This could explain the lower isomerization quantum yields after S_2 excitation, because a symmetric vibration of both CNN angles will lead predominantly back to the respective reactant. Furthermore, Nonnenberg *et al.* could show that the symmetric increase of both CNN angles is disfavored in the case of the capped azobenzene.^[188] Their results are in good agreement with recent quantum chemical calculations^[191,192,203] and support the importance of the CNN-coordinate in AB-photochemistry. It was suggested, that a restriction of the opening of the NNC angle might lead to AB molecular switches with higher quantum yields.^[188,191,192]

1.3.3 Investigated Azobenzene Derivative and Aims of this Thesis

The second main task of this Thesis was the investigation of the $E \rightarrow Z$ and $Z \rightarrow E$ isomerization of the highly constrained bridged AB-derivative 5,6-dihydrodibenzo- $[c,g][1,2]$ diazocine (brAB) shown in Scheme 1.1 by determination of isomerization quantum yields, femtosecond time-resolved transient absorption spectroscopy, and quantum chemical calculations.



Scheme 1.1

The short alkyl bridge between the two phenyl rings of brAB should completely block a large-amplitude rotation of the phenyl rings and constrain the CNN angle opening, altogether leading to fast and direct photoisomerization, perhaps via a hula-twist like motion. As mentioned above, the symmetric or non-symmetric CNN angle opening turned out to be an important parameter in the photo-induced reactions of ABs. Therefore, the restriction of the CNN angle opening might even increase the isomerization quantum yields, as the inhibition of the reaction pathway via concerted inversion might reduce deactivation processes.

Furthermore, a multitude of applications of ABs (see, e.g., Fig. 1.19) requires a directed and defined motion during the switching process and therefore a restriction of the number of possible isomerization mechanisms, possibly realized in brAB. Additionally, the reaction mechanism with steric constraints is of interest, as AB derivatives will be incorporated in complex environments for most applications. If the isomerization mechanism is dependent on the environment as shown by Chang *et al.*^[187] for AB, this may lead to either blocking or opening up of undesired isomerization pathways.

The bridged compound brAB has been synthesized the first time 100 years ago^[204–206] and was rediscovered by us because of its strong steric restrictions due to the ethylenic bridge.^[26] The results obtained in this Thesis reveal the huge potential of brAB as a molecular photoswitch. It could unambiguously be shown that brAB possesses strongly improved photochemical properties compared with unsubstituted AB, such as increased photoisomerization quantum yields and superior photochromic properties. Therefore, the diazocine brAB can be regarded as the parent molecule of a new class of photochromic azobenzenes.

References

- [1] Z. F. Liu, K. Hashimoto, A. Fujishima, *Nature* **1990**, *347*, 658–660.
- [2] T. Ikeda, O. Tsutsumi, *Science* **1995**, *268*, 1873–1875.
- [3] S. Kawata, Y. Kawata, *Chem. Rev.* **2000**, *100*, 1777–1788.
- [4] Y. C. Liang, A. S. Dvornikov, P. M. Rentzepis, *Proc. Natl. Acad. Sci. U. S. A.* **2003**, *100*, 8109–8112.
- [5] E. Walker, P. M. Rentzepis, *Nature Photonics* **2008**, *2*, 406–408.
- [6] A. S. Dvornikov, E. P. Walker, P. M. Rentzepis, *J. Phys. Chem. A* **2009**, *113*, 13633–13644.
- [7] M. Gu, X. Li, *Opt. Photonics News* **2010**, *21*, 28–33.
- [8] B. L. Feringa, *Molecular Switches*, Wiley-VCH, Weinheim **2001**.
- [9] V. Balzani, A. Credi, B. Ferrer, S. Silvi, M. Venturi, *Top. Curr. Chem.* **2005**, *262*, 1–27.
- [10] V. Balzani, A. Credi, M. Venturi, *Molecular Devices and Machines: Concepts and Perspectives for the Nanoworld*, Wiley-VCH, Weinheim **2008**.
- [11] I. Willner, S. Rubin, *Angew. Chem. Int. Ed.* **1996**, *35*, 367–385.
- [12] I. Willner, *Acc. Chem. Res.* **1997**, *30*, 347–356.
- [13] L. Ulysse, J. Cubillos, J. Chmielewski, *J. Am. Chem. Soc.* **1995**, *117*, 8466–8467.
- [14] S. Spörlein, H. Carstens, H. Satzger, C. Renner, R. Behrendt, L. Moroder, P. Tavan, W. Zinth, J. Wachtveitl, *Proc. Natl. Acad. Sci. U. S. A.* **2002**, *99*, 7998–8002.
- [15] Y. Liang, A. S. Dvornikov, P. M. Rentzepis, *Macromolecules* **2002**, *35*, 9377–9382.
- [16] B. Schierling, A.-J. Noël, W. Wende, L. T. Hien, E. Volkov, E. Kubareva, T. Oretskaya, M. Kokkinidis, A. Römpf, B. Spengler, A. Pingoud, *Proc. Natl. Acad. Sci. U. S. A.* **2010**, *107*, 1361–1366.
- [17] V. Ferri, M. Elbing, G. Pace, M. D. Dickey, M. Zharnikov, P. Samori, M. Mayor, M. A. Rampi, *Angew. Chem., Int. Ed.* **2008**, *47*, 3407–3409.
- [18] B. Baisch, D. Raffa, U. Jung, O. M. Magnussen, C. Nicolas, J. Lacour, J. Kubitschke, R. Herges, *J. Am. Chem. Soc.* **2009**, *131*, 442–443.
- [19] D. Liu, Y. Xie, H. Shao, X. Jiang, *Angew. Chem., Int. Ed.* **2009**, *48*, 4406–4408.
- [20] Y. Yokoyama, *Chem. Rev.* **2000**, *100*, 1717–1739.
- [21] A. S. Dvornikov, Y. Liang, C. S. Cruse, P. M. Rentzepis, *J. Phys. Chem. B* **2004**, *108*, 8652–8658.
- [22] M. Irie, *Chem. Rev.* **2000**, *100*, 1685–1716.
- [23] G. Berkovic, V. Krongauz, V. Weiss, *Chem. Rev.* **2000**, *100*, 1741–1753.
- [24] V. I. Minkin, *Chem. Rev.* **2004**, *104*, 2751–2776.

-
- [25] K. G. Yager, C. J. Barrett, *J. Photochem. Photobiol., A* **2006**, *182*, 250–261.
- [26] R. Siewertsen, H. Neumann, B. Buchheim-Stehn, R. Herges, C. Näther, F. Renth, F. Temps, *J. Am. Chem. Soc.* **2009**, *131*, 15594–15595.
- [27] M.-M. Russew, S. Hecht, *Adv. Mater.* **2010**, *22*, 3348–3360.
- [28] R. Siewertsen, J. B. Schönborn, B. Hartke, F. Renth, F. Temps, *Phys. Chem. Chem. Phys.* **2011**, *13*, 1054–1063.
- [29] A. H. Zewail, *Angew. Chem., Int. Ed.* **2000**, *39*, 2586–2631.
- [30] W. R. Browne, B. L. Feringa, *Annu. Rev. Phys. Chem.* **2009**, *60*, 407–428.
- [31] W. R. Browne, B. L. Feringa, *Nat. Nanotechnol.* **2006**, *1*, 25–35.
- [32] S. W. Hell, J. Wichmann, *Opt. Lett.* **1994**, *19*, 780–782.
- [33] T. A. Klar, S. W. Hell, *Opt. Lett.* **1999**, *24*, 954–956.
- [34] S. W. Hell, *Science* **2007**, *316*, 1153–1158.
- [35] M. Heilemann, S. van de Linde, M. Schuttpelz, R. Kasper, B. Seefeldt, A. Mukherjee, P. Tinnefeld, M. Sauer, *Angew. Chem., Int. Ed.* **2008**, *47*, 6172–6176.
- [36] S. W. Hell, In A. Gräslund, R. Rigler, J. Widengren, eds., *Single Molecule Spectroscopy in Chemistry, Physics and Biology*, vol. 96 of *Springer Series in Chemical Physics*. Springer, Berlin **2010**, 365–398.
- [37] S. E. Braslavsky, A. U. Acuña, W. Adam, F. Amat, D. Armesto, T. D. Z. Atvars, A. Bard, E. Bill, L. O. Björn, C. Bohne, J. Bolton, R. Bonneau, H. Bouas-Laurent, A. M. Braun, R. Dale, K. Dill, D. Döpp, H. Dürr, M.-A. Fox, T. Gandolfi, Z. R. Grabowski, A. Griesbeck, A. Kutateladze, M. Litter, J. Lorimer, J. Mattay, J. Michl, R. J. D. Miller, L. Moggi, S. Monti, S. Nonell, P. Ogilby, G. Olbrich, E. Oliveros, M. Olivucci, G. Orellana, V. Prokorenko, K. R. Naqvi, W. Rettig, A. Rizzi, R. A. Rossi, E. San, Román, F. Scandola, S. Schneider, E. W. Thulstrup, B. Valeur, J. Verhoeven, J. Warman, R. Weiss, J. Wirz, K. Zachariasse, *Pure Appl. Chem.* **2007**, *79*, 293–465.
- [38] P. Klàn, J. Wirz, *Photochemistry of Organic Compounds. From Concepts to Practice*, John Wiley & Sons Inc., Chichester **2009**.
- [39] A. Jablonski, *Z. Phys.* **1935**, *94*, 38–46.
- [40] M. Kasha, *Discuss. Faraday Soc.* **1950**, *9*, 14–19.
- [41] T. Förster, *Pure Appl. Chem.* **1970**, *24*, 443–449.
- [42] J. I. Steinfeld, J. S. Francisco, W. L. Hase, *Chemical Kinetics and Dynamics*, Englewood Cliffs, NJ : Prentice Hall **1989**.
- [43] K. A. Holbrook, M. J. Pilling, S. H. Robertson, *Unimolecular reactions*, Wiley-VCH, New York **1996**.
- [44] S. H. Pullen, N. A. Anderson, I. Walker, Larry A., R. J. Sension, *J. Chem. Phys.* **1997**, *107*, 4985–4993.

- [45] M. Barbatti, A. J. A. Aquino, H. Lischka, C. Schrieffer, S. Lochbrunner, E. Riedle, *Phys. Chem. Chem. Phys.* **2009**, *11*, 1406–1415.
- [46] E. Uhlmann, G. Gauglitz, *J. Photochem. Photobiol., A* **1996**, *98*, 45–49.
- [47] S. Rath, M. Heilig, H. Port, J. Wrachtrup, *Nano Lett.* **2007**, *7*, 3845–3848.
- [48] T. Kardinahl, H. Franke, *Appl. Phys. A: Mater. Sci. Process.* **1995**, *61*, 23–27.
- [49] S. C. Martin, N. Singh, S. C. Wallace, *J. Phys. Chem.* **1996**, *100*, 8066–8069.
- [50] N. Menke, B. Yao, Y. Wang, W. Dong, M. Lei, Y. Chen, M. Fan, T. Li, *J. Mod. Opt.* **2008**, *55*, 1003–1011.
- [51] S. Z. Janicki, G. B. Schuster, *J. Am. Chem. Soc.* **1995**, *117*, 8524–8527.
- [52] M. L. Bossi, J. B. Rodríguez, P. F. Aramendía, *J. Photochem. Photobiol., A* **2006**, *179*, 35–41.
- [53] I. B. Ramsteiner, A. Hartschuh, H. Port, *Chem. Phys. Lett.* **2001**, *343*, 83–90.
- [54] F. M. Raymo, M. Tomasulo, *J. Phys. Chem. A* **2005**, *109*, 7343–7352.
- [55] J. Cusido, E. Deniz, F. M. Raymo, *Eur. J. Org. Chem.* **2009**, 2031–2045.
- [56] M. Heilemann, P. Dedecker, J. Hofkens, M. Sauer, *Laser Photon Rev.* **2009**, *3*, 180–202.
- [57] B. Seefeldt, R. Kasper, M. Beining, J. Mattay, J. Arden-Jacob, N. Kemnitzer, K. H. Drexhage, M. Heilemann, M. Sauer, *Photochem. Photobiol. Sci.* **2010**, *9*, 213–220.
- [58] M. Irie, T. Fukaminato, T. Sasaki, N. Tamai, T. Kawai, *Nature* **2002**, *420*, 759–760.
- [59] T. Fukaminato, T. Sasaki, T. Kawai, N. Tamai, M. Irie, *J. Am. Chem. Soc.* **2004**, *126*, 14843–14849.
- [60] E. Abbe, *Arch. Mikrosk. Anat.* **1873**, *9*, 413–420.
- [61] E. Betzig, G. H. Patterson, R. Sougrat, O. W. Lindwasser, S. Olenych, J. S. Bonifacino, M. W. Davidson, J. Lippincott-Schwartz, H. F. Hess, *Science* **2006**, *313*, 1642–1645.
- [62] H. Shroff, C. G. Galbraith, J. A. Galbraith, E. Betzig, *Nat. Methods* **2008**, *5*, 417–423.
- [63] M. J. Rust, M. Bates, X. Zhuang, *Nat. Methods* **2006**, *3*, 793–796.
- [64] M. Bates, B. Huang, G. T. Dempsey, X. Zhuang, *Science* **2007**, *317*, 1749–1753.
- [65] B. Huang, W. Wang, M. Bates, X. Zhuang, *Science* **2008**, *319*, 810–813.
- [66] S. van de Linde, M. Sauer, M. Heilemann, *J. Struct. Biol.* **2008**, *164*, 250–254.
- [67] M. K. Cheezum, W. F. Walker, W. H. Guilford, *Biophys. J.* **2001**, *81*, 2378–2388.
- [68] R. E. Thompson, D. R. Larson, W. W. Webb, *Biophys. J.* **2002**, *82*, 2775–2783.
- [69] A. Yildiz, J. N. Forkey, S. A. McKinney, T. Ha, Y. E. Goldman, P. R. Selvin, *Science* **2003**, *300*, 2061–2065.
- [70] X. Qu, D. Wu, L. Mets, N. F. Scherer, *Proc. Natl. Acad. Sci. U. S. A.* **2004**, *101*,

- 11298–11303.
- [71] L. S. Churchman, Z. Öekten, R. S. Rock, J. F. Dawson, J. A. Spudich, *Proc. Natl. Acad. Sci. U. S. A.* **2005**, *102*, 1419–1423.
- [72] H. Stobbe, *Ber. Dtsch. Chem. Ges.* **1905**, *38*, 3673–3682.
- [73] H. Stobbe, *Ber. Dtsch. Chem. Ges.* **1907**, *40*, 3372–3382.
- [74] H. Stobbe, *Ann. Chem.* **1911**, *380*, 1–129.
- [75] H. G. Heller, S. Oliver, *J. Chem. Soc., Perkin Trans. 1* **1981**, 197–201.
- [76] H. G. Heller, R. M. Megit, *J. Chem. Soc., Perkin Trans. 1* **1974**, 923–927.
- [77] P. J. Darcy, H. G. Heller, P. J. Strydom, J. Whittall, *J. Chem. Soc., Perkin Trans. 1* **1981**, 202–205.
- [78] Y. Yokoyama, T. Goto, T. Inoue, M. Yokoyama, Y. Kurita, *Chem. Lett.* **1988**, *17*, 1049–1052.
- [79] Y. Yokoyama, T. Inoue, M. Yokoyama, T. Goto, T. Iwai, N. Kera, I. Hitomi, Y. Kurita, *Bull. Chem. Soc. Jpn.* **1994**, *67*, 3297–3303.
- [80] J. Kiji, T. Okano, H. Kitamura, Y. Yakoyama, S. Kubota, Y. Kurita, *Bull. Chem. Soc. Jpn.* **1995**, *68*, 616–619.
- [81] S. Uchida, S. Yamada, Y. Yokoyama, Y. Kurita, *Bull. Chem. Soc. Jpn.* **1995**, *68*, 1677–1682.
- [82] T. Brust, S. Draxler, A. Popp, X. Chen, W. J. Lees, W. Zinth, M. Braun, *Chem. Phys. Lett.* **2009**, *477*, 298–303.
- [83] A. Kaneko, A. Tomoda, M. Ishizuka, H. Suzuki, R. Matsushima, *Bull. Chem. Soc. Jpn.* **1988**, *61*, 3569–3573.
- [84] Y. Yokoyama, K. Takahashi, *Chem. Lett.* **1996**, *25*, 1037–1038.
- [85] Y. Yokoyama, T. Tanaka, T. Yamane, Y. Kurita, *Chem. Lett.* **1991**, *20*, 1125–1128.
- [86] T. Brust, S. Draxler, S. Malkmus, C. Schulz, M. Zastrow, K. Rück-Braun, W. Zinth, M. Braun, *J. Mol. Liq.* **2008**, *141*, 137–139.
- [87] N. I. Islamova, X. Chen, S. P. Garcia, G. Guez, Y. Silva, W. J. Lees, *J. Photochem. Photobiol., A* **2008**, *195*, 228–234.
- [88] W. Zhao, Y. Ming, Z. Zhu, M. Fan, *J. Photochem. Photobiol., A* **1992**, *63*, 235–240.
- [89] Y. Yokoyama, T. Iwai, Y. Yokoyama, Y. Kurita, *Chem. Lett.* **1994**, *23*, 225–226.
- [90] Y. Yokoyama, K. Ogawa, T. Iwai, K. Shimazaki, Y. Kajihara, T. Goto, Y. Yokoyama, Y. Kurita, *Bull. Chem. Soc. Jpn.* **1996**, *69*, 1605–1612.
- [91] R. Hoffmann, R. B. Woodward, *Acc. Chem. Res.* **1968**, *1*, 17–22.
- [92] C. Lenoble, R. S. Becker, *J. Phys. Chem.* **1986**, *90*, 2651–2654.
- [93] H. D. Ilge, M. Kaschke, D. Khechinashvili, *J. Photochem.* **1986**, *33*, 349–58.
- [94] H. D. Ilge, J. Suhnel, D. Khechinashvili, M. Kaschke, *J. Photochem.* **1987**, *38*,

- 189–203.
- [95] S. Kurita, A. Kashiwagi, Y. Kurita, H. Miyasaka, N. Mataga, *Chem. Phys. Lett.* **1990**, *171*, 553–557.
- [96] D. A. Parthenopoulos, P. M. Rentzepis, *J. Mol. Struct.* **1990**, *224*, 297–302.
- [97] M. Handschuh, M. Seibold, H. Port, H. C. Wolf, *J. Phys. Chem. A* **1997**, *101*, 502–506.
- [98] H. Port, P. Gärtner, M. Hennrich, I. Ramsteiner, T. Schöck, *Mol. Cryst. Liq. Cryst.* **2005**, *430*, 15–21.
- [99] B. Heinz, S. Malkmus, S. Laimgruber, S. Dietrich, C. Schulz, K. Rück-Braun, M. Braun, W. Zinth, P. Gilch, *J. Am. Chem. Soc.* **2007**, *129*, 8577–8584.
- [100] F. O. Koller, W. J. Schreier, T. E. Schrader, S. Malkmus, C. Schulz, S. Dietrich, K. Rück-Braun, M. Braun, *J. Phys. Chem. A* **2008**, *112*, 210–214.
- [101] S. Draxler, T. Brust, S. Malkmus, F. O. Koller, B. Heinz, S. Laimgruber, C. Schulz, S. Dietrich, K. Rück-Braun, W. Zinth, M. Braun, *J. Mol. Liq.* **2008**, *141*, 130–136.
- [102] T. Cordes, T. T. Herzog, S. Malkmus, S. Draxler, T. Brust, J. A. DiGirolamo, W. J. Lees, M. Braun, *Photochem. Photobiol. Sci.* **2009**, *8*, 528–534.
- [103] S. Malkmus, F. O. Koller, B. Heinz, W. J. Schreier, T. E. Schrader, W. Zinth, C. Schulz, S. Dietrich, K. Rück-Braun, M. Braun, *Chem. Phys. Lett.* **2006**, *417*, 266–271.
- [104] F. O. Koller, W. J. Schreier, T. E. Schrader, A. Sieg, S. Malkmus, C. Schulz, S. Dietrich, K. Rück-Braun, W. Zinth, M. Braun, *J. Phys. Chem. A* **2006**, *110*, 12769–12776.
- [105] Y. Ishibashi, M. Murakami, H. Miyasaka, S. Kobatake, M. Irie, Y. Yokoyama, *J. Phys. Chem. C* **2007**, *111*, 2730–2737.
- [106] T. Cordes, S. Malkmus, J. A. DiGirolamo, W. J. Lees, A. Nenov, R. de Vivie-Riedle, M. Braun, W. Zinth, *J. Phys. Chem. A* **2008**, *112*, 13364–13371.
- [107] Y. Ishibashi, T. Katayama, C. Ota, S. Kobatake, M. Irie, Y. Yokoyama, H. Miyasaka, *New J. Chem.* **2009**, *33*, 1409–1419.
- [108] S. Draxler, T. Brust, S. Malkmus, J. A. DiGirolamo, W. J. Lees, W. Zinth, M. Braun, *Phys. Chem. Chem. Phys.* **2009**, *11*, 5019–5027.
- [109] T. Brust, S. Malkmus, S. Draxler, S. A. Ahmed, K. Rück-Braun, W. Zinth, M. Braun, *J. Photochem. Photobiol., A* **2009**, *207*, 209–216.
- [110] T. Brust, S. Draxler, J. Eicher, W. J. Lees, K. Rück-Braun, W. Zinth, M. Braun, *Chem. Phys. Lett.* **2010**, *489*, 175–180.
- [111] P. Celani, F. Bernardi, M. A. Robb, M. Olivucci, *J. Phys. Chem.* **1996**, *100*, 19364–19366.
- [112] A. Hofmann, L. Kurtz, R. De Vivie-Riedle, *Appl. Phys. B: Lasers Opt.* **2000**, *71*, 391–396.

- [113] G. Tomasello, M. J. Bearpark, M. A. Robb, G. Orlandi, M. Garavelli, *Angew. Chem.* **2010**, *122*, 2975–2978.
- [114] W. Fuß, W. E. Schmid, S. A. Trushin, *J. Chem. Phys.* **2000**, *112*, 8347–8362.
- [115] K. Kosma, S. A. Trushin, W. Fuß, W. E. Schmid, *Phys. Chem. Chem. Phys.* **2009**, *11*, 172–181.
- [116] S. Draxler, T. Brust, J. Eicher, W. Zinth, M. Braun, *Opt. Commun.* **2010**, *283*, 1050–1054.
- [117] F. Renth, M. Foca, A. Petter, F. Temps, *Chem. Phys. Lett.* **2006**, *428*, 62–67.
- [118] F. W. Schulze, H. J. Petrick, H. K. Cammenga, H. Klinge, *Z. Phys. Chem. Neue Fol.* **1977**, *107*, 1–19.
- [119] G. Füchsel, T. Klamroth, J. Dokic, P. Saalfrank, *J. Phys. Chem. B* **2006**, *110*, 16337–16345.
- [120] H. H. Perkampus, *UV-VIS Atlas of Organic Compounds*, Wiley-VCH, Weinheim **1992**.
- [121] H. Rau, *Photochemistry and Photophysics*, CRC Press, Boca Ratan **1990**.
- [122] R. H. El Halabieh, O. Mermut, C. J. Barrett, *Pure Appl. Chem.* **2004**, *76*, 1445–1465.
- [123] K. Gille, H. Knoll, K. Quitzsch, *Int. J. Chem. Kinet.* **1999**, *31*, 337–350.
- [124] B. L. Feringa, *Acc. Chem. Res.* **2001**, *34*, 504–513.
- [125] V. Balzani, A. Credi, M. Venturi, *Chem. Soc. Rev.* **2009**, *38*, 1542–1550.
- [126] X. Liang, H. Nishioka, N. Takenaka, H. Asanuma, *ChemBioChem* **2008**, *9*, 702–705.
- [127] J. A. Delaire, K. Nakatani, *Chem. Rev.* **2000**, *100*, 1817–1845.
- [128] P. Krawczyk, *J. Mol. Model.* **2010**, *16*, 659–668.
- [129] R. Behrendt, C. Renner, M. Schenk, F. Q. Wang, J. Wachtveitl, D. Oesterhelt, L. Moroder, *Angew. Chem. Int. Ed.* **1999**, *38*, 2771–2774.
- [130] J. R. Kumita, O. S. Smart, G. A. Woolley, *Proc. Natl. Acad. Sci. U. S. A.* **2000**, *97*, 3803–3808.
- [131] C. Renner, R. Behrendt, S. Spörlein, J. Wachtveitl, L. Moroder, *Biopolymers* **2000**, *54*, 489–500.
- [132] C. Renner, J. Cramer, R. Behrendt, L. Moroder, *Biopolymers* **2000**, *54*, 501–514.
- [133] D. G. Flint, J. R. Kumita, O. S. Smart, G. A. Woolley, *Chem. Biol.* **2002**, *9*, 391–397.
- [134] X. Liang, H. Asanuma, M. Komiyama, *J. Am. Chem. Soc.* **2002**, *124*, 1877–1883.
- [135] V. Borisenko, G. A. Woolley, *J. Photochem. Photobiol., A* **2005**, *173*, 21–28.
- [136] A. Aemissegger, V. Kräutler, W. F. van Gunsteren, D. Hilvert, *J. Am. Chem. Soc.* **2005**, *127*, 2929–2936.
- [137] C. Renner, L. Moroder, *ChemBioChem* **2006**, *7*, 868–878.

- [138] S. Jurt, A. Aemissegger, P. Güntert, O. Zerbe, D. Hilvert, *Angew. Chem.* **2006**, *118*, 6445–6448.
- [139] U. Kusebauch, S. A. Cadamuro, H. J. Musiol, M. O. Lenz, J. Wachtveitl, L. Moroder, C. Renner, *Angew. Chem. Int. Ed.* **2006**, *45*, 7015–7018.
- [140] T. E. Schrader, W. J. Schreier, T. Cordes, F. O. Koller, G. Babitzki, R. Denschlag, C. Renner, M. Löweneck, S.-L. Dong, L. Moroder, P. Tavan, W. Zinth, *Proc. Natl. Acad. Sci. U. S. A.* **2007**, *104*, 15729–15734.
- [141] A. Archut, F. Vögtle, L. De, Cola, G. C. Azzellini, V. Balzani, P. S. Ramanujam, R. H. Berg, *Chem. Eur. J.* **1998**, *4*, 699–706.
- [142] F. Vögtle, M. Gorka, R. Hesse, P. Ceroni, M. Maestri, V. Balzani, *Photochem. Photobiol. Sci.* **2002**, *1*, 45–51.
- [143] G. S. Kumar, D. C. Neckers, *Chem. Rev.* **1989**, *89*, 1915–1925.
- [144] A. Natansohn, P. Rochon, *Chem. Rev.* **2002**, *102*, 4139–4175.
- [145] T. Hugel, N. B. Holland, A. Cattani, L. Moroder, M. Seitz, H. E. Gaub, *Science* **2002**, *296*, 1103–1106.
- [146] N. B. Holland, T. Hugel, G. Neuert, A. Cattani-Scholz, C. Renner, D. Oesterhelt, L. Moroder, M. Seitz, H. E. Gaub, *Macromolecules* **2003**, *36*, 2015–2023.
- [147] I. Porcar, P. Perrin, C. Tribet, *Langmuir* **2001**, *17*, 6905–6909.
- [148] K. Ichimura, S. K. Oh, M. Nakagawa, *Science* **2000**, *288*, 1624–1626.
- [149] S. Yasuda, T. Nakamura, M. Matsumoto, H. Shigekawa, *J. Am. Chem. Soc.* **2003**, *125*, 16430–16433.
- [150] M. Ito, T. X. Wei, P. L. Chen, H. Akiyama, M. Matsumoto, K. Tamada, Y. Yamamoto, *J. Mater. Chem.* **2005**, *15*, 478–483.
- [151] S. Hagen, F. Leyssner, D. Nandi, M. Wolf, P. Tegeder, *Chem. Phys. Lett.* **2007**, *444*, 85–90.
- [152] M. J. Comstock, N. Levy, A. Kirakosian, J. Cho, F. Lauterwasser, J. H. Harvey, D. A. Strubbe, J. M. J. Frechet, D. Trauner, S. G. Louie, M. F. Crommie, *Phys. Rev. Lett.* **2007**, *99*, 038301/1–038301/4.
- [153] L. Óvári, M. Wolf, P. Tegeder, *J. Phys. Chem. C* **2007**, *111*, 15370–15374.
- [154] G. Pace, V. Ferri, C. Grave, M. Elbing, C. von Haenisch, M. Zharnikov, M. Mayor, M. A. Rampi, P. Samori, *Proc. Natl. Acad. Sci. U. S. A.* **2007**, *104*, 9937–9942.
- [155] S. Hagen, P. Kate, F. Leyssner, D. Nandi, M. Wolf, P. Tegeder, *J. Chem. Phys.* **2008**, *129*, 164102/1–164102/8.
- [156] S. Hagen, P. Kate, M. V. Peters, S. Hecht, M. Wolf, P. Tegeder, *Appl. Phys. A: Mater. Sci. Process.* **2008**, *93*, 253–260.
- [157] A. S. Kumar, T. Ye, T. Takami, B. C. Yu, A. K. Flatt, J. M. Tour, P. S. Weiss, *Nano Lett.* **2008**, *8*, 1644–1648.

- [158] S. Wagner, F. Leyssner, C. Kördel, S. Zarwell, R. Schmidt, M. Weinelt, K. Rück-Braun, M. Wolf, P. Tegeder, *Phys. Chem. Chem. Phys.* **2009**, *11*, 6242–6248.
- [159] T. Ikeda, S. Horiuchi, D. B. Karanjit, S. Kurihara, S. Tazuke, *Macromolecules* **1990**, *23*, 42–48.
- [160] T. Hayashi, H. Kawakami, Y. Doke, A. Tsuchida, Y. Onogi, M. Yamamoto, *Eur. Polym. J.* **1995**, *31*, 23–28.
- [161] O. Tsutsumi, T. Shiono, T. Ikeda, G. Galli, *J. Phys. Chem. B* **1997**, *101*, 1332–1337.
- [162] A. Shishido, O. Tsutsumi, A. Kanazawa, T. Shiono, T. Ikeda, N. Tamai, *J. Phys. Chem. B* **1997**, *101*, 2806–2810.
- [163] D. Gindre, A. Boeglin, A. Fort, L. Mager, K. D. Dorkenoo, *Opt. Express* **2006**, *14*, 9896–9901.
- [164] M. Goodman, A. Kossoy, *J. Am. Chem. Soc.* **1966**, *88*, 5010–5015.
- [165] M. Goodman, M. L. Falxa, *Journal of the American Chemical Society* **1967**, *89*, 3863–3867.
- [166] G. A. Woolley, *Acc. Chem. Res.* **2005**, *38*, 486–493.
- [167] S. D. Evans, S. R. Johnson, H. Ringsdorf, L. M. Williams, H. Wolf, *Langmuir* **1998**, *14*, 6436–6440.
- [168] K. Tamada, H. Akiyama, T. X. Wei, S. A. Kim, *Langmuir* **2003**, *19*, 2306–2312.
- [169] E. Galoppini, *Coord. Chem. Rev.* **2004**, *248*, 1283–1297.
- [170] S. Zarwell, K. Rück-Braun, *Tetrahedron Lett.* **2008**, *49*, 4020–4025.
- [171] K. Anderle, R. Birkenheide, M. J. A. Werner, J. H. Wendorff, *Liq. Cryst.* **1991**, *9*, 691–699.
- [172] K. Ichimura, *Chem. Rev.* **2000**, *100*, 1847–1873.
- [173] V. Shibaev, A. Bobrovsky, N. Boiko, *Prog. Polym. Sci.* **2003**, *28*, 729–836.
- [174] Y. L. Yu, T. Ikeda, *J. Photochem. Photobiol., C* **2004**, *5*, 247–265.
- [175] M. Yamada, M. Kondo, J.-i. Mamiya, Y. Yu, M. Kinoshita, C. J. Barrett, T. Ikeda, *Angew. Chem., Int. Ed.* **2008**, *47*, 4986–4988.
- [176] H. Finkelmann, E. Nishikawa, G. G. Pereira, M. Warner, *Phys. Rev. Lett.* **2001**, *87*, 015501/1–015501/4.
- [177] P. Bortolus, S. Monti, *J. Phys. Chem.* **1979**, *83*, 648–652.
- [178] H. Rau, *J. Photochem.* **1984**, *26*, 221–225.
- [179] T. Nägele, R. Hoche, W. Zinth, J. Wachtveitl, *Chem. Phys. Lett.* **1997**, *272*, 489–495.
- [180] I. K. Lednev, T.-Q. Ye, R. E. Hester, J. N. Moore, *J. Phys. Chem.* **1996**, *100*, 13338–13341.
- [181] I. K. Lednev, T. Q. Ye, P. Matousek, M. Towrie, P. Foggi, F. V. R. Neuwahl, S. Umaphathy, R. E. Hester, J. N. Moore, *Chem. Phys. Lett.* **1998**, *290*, 68–74.

- [182] T. Fujino, S. Y. Arzhantsev, T. Tahara, *J. Phys. Chem. A* **2001**, *105*, 8123–8129.
- [183] T. Fujino, S. Y. Arzhantsev, T. Tahara, *Bull. Chem. Soc. Jpn.* **2002**, *75*, 1031–1040.
- [184] Y.-C. Lu, C.-W. Chang, E. W.-G. Diau, *J. Chin. Chem. Soc.* **2002**, *49*, 693–701.
- [185] H. Rau, In H. Dürr, H. Bouas-Laurent, eds., *Photochromism: Molecules and Systems*. Elsevier, Amsterdam **2003**.
- [186] H. Satzger, S. Spörlein, C. Root, J. Wachtveitl, W. Zinth, P. Gilch, *Chem. Phys. Lett.* **2003**, *372*, 216–223.
- [187] C.-W. Chang, Y.-C. Lu, T.-T. Wang, E. W.-G. Diau, *J. Am. Chem. Soc.* **2004**, *126*, 10109–10118.
- [188] C. Nonnenberg, H. Gaub, I. Frank, *ChemPhysChem* **2006**, *7*, 1455–1461.
- [189] G. Granucci, M. Persico, *Theor. Chem. Acc.* **2007**, *117*, 1131–1143.
- [190] S. Yuan, Y. Dou, W. Wu, Y. Hu, J. Zhao, *J. Phys. Chem. A* **2008**, *112*, 13326–13334.
- [191] I. Conti, M. Garavelli, G. Orlandi, *J. Am. Chem. Soc.* **2008**, *130*, 5216–5230.
- [192] L. Wang, W. Xu, C. Yi, X. Wang, *J. Mol. Graph. Model.* **2009**, *27*, 792–796.
- [193] Y. Ootani, K. Satoh, A. Nakayama, T. Noro, T. Taketsugu, *J. Chem. Phys.* **2009**, *131*, 194306/1–194306/10.
- [194] G. Tiberio, L. Muccioli, R. Berardi, C. Zannoni, *ChemPhysChem* **2010**, *11*, 1018–1028.
- [195] T. Pancur, F. Renth, F. Temps, B. Harbaum, A. Krüger, R. Herges, C. Näther, *Phys. Chem. Chem. Phys.* **2005**, *7*, 1985–1989.
- [196] H. Satzger, C. Root, M. Braun, *J. Phys. Chem. A* **2004**, *108*, 6265–6271.
- [197] P. Cattaneo, M. Persico, *Phys. Chem. Chem. Phys.* **1999**, *1*, 4739–4743.
- [198] A. Cembran, F. Bernardi, M. Garavelli, L. Gagliardi, G. Orlandi, *J. Am. Chem. Soc.* **2004**, *126*, 3234–3243.
- [199] E. W.-G. Diau, *J. Phys. Chem. A* **2004**, *108*, 950–956.
- [200] M. L. Tiago, S. Ismail-Beigi, S. G. Louie, *J. Chem. Phys.* **2005**, *122*, 094311/1–094311/7.
- [201] T. Fujino, T. Tahara, *J. Phys. Chem. A* **2000**, *104*, 4203–4210.
- [202] Y.-C. Lu, E. W.-G. Diau, H. Rau, *J. Phys. Chem. A* **2005**, *109*, 2090–2099.
- [203] C. Ciminelli, G. Granucci, M. Persico, *J. Chem. Phys.* **2005**, *123*, 174317/1–174317/10.
- [204] H. Duval, *Bull. Soc. Chim. Fr.* **1910**, *7*, 727–732.
- [205] W. W. Paudler, A. G. Zeiler, *J. Org. Chem.* **1969**, *34*, 3237–3239.
- [206] E. Tauer, R. Machinek, *Liebigs Ann.* **1996**, 1213–1216.

2 Experimental Methods

Femtosecond time-resolved spectroscopy is based on the generation of ultrashort laser pulses, which are conveniently supplied by a regeneratively amplified titanium-sapphire (Ti:Sa) laser. The laser system used to run the experiments carried out in this Thesis (Clark-MXR CPA 2001) is based on the principle of chirped pulse amplification (CPA). The femtosecond laser pulses are generated by passive Kerr lens mode locking using a glass fiber oscillator doped with Er^{3+} ions. The fiber emits pulses at a wavelength of 1550 nm and a repetition rate of 34.5 MHz. These are compressed to ≈ 100 fs duration in a prism compressor. The compressed oscillator output pulses are frequency doubled to give a wavelength of 775 nm and stretched to a temporal length of 200 ps, before they act as seed pulses for the regenerative amplifier. This regenerative amplifier consists of a Ti:Sa crystal pumped by a frequency-doubled Nd:YAG laser at 532 nm. The seed pulses are amplified and thereafter re-compressed by a grating pair. The entire laser system provides femtosecond pulses with 150 – 200 fs full width at half maximum (FWHM) duration at a center wavelength of 775 nm with 800 – 900 mW output power at a repetition rate of 1 kHz. Half of this laser output was used to run the transient absorption setup.

In this Chapter, the experimental setup for femtosecond time-resolved transient absorption spectroscopy is presented in some detail, including optimization procedures for the setup. Subsequently, methodic artifacts are described, which can be used for further optimization of the experimental conditions, but need to be eliminated from the data. The last Section of this Chapter explains the data analysis.

2.1 The Principle of Femtosecond Time-Resolved Transient Absorption Spectroscopy

Femtosecond transient absorption spectroscopy (fsTAS) relies on the pump-probe principle which is depicted schematically in Fig. 2.1. The laser output from the Ti:Sa laser system is divided into a pump and a probe beam. The pump pulse can be set to the suitable excitation wavelength via non-linear frequency conversion processes, and the probe beam is converted into a supercontinuum (SC) with a broad spectral bandwidth. A variation of the temporal delay between the pump and probe pulses is achieved via an optical delay stage. Using a back-reflector, a temporal delay of 6.6713 fs can be achieved by moving the delay stage by 1 μm . The probe beam is divided into a probe and a reference beam and only the probe beam is spatially overlapped with the pump beam in the sample cell. After passing through a polychromator, the transmitted light of the probe and reference pulses is detected with a multi-channel detector. Using this setup, the change in optical density (ΔOD) induced by the pump pulse in the sample can be monitored at different

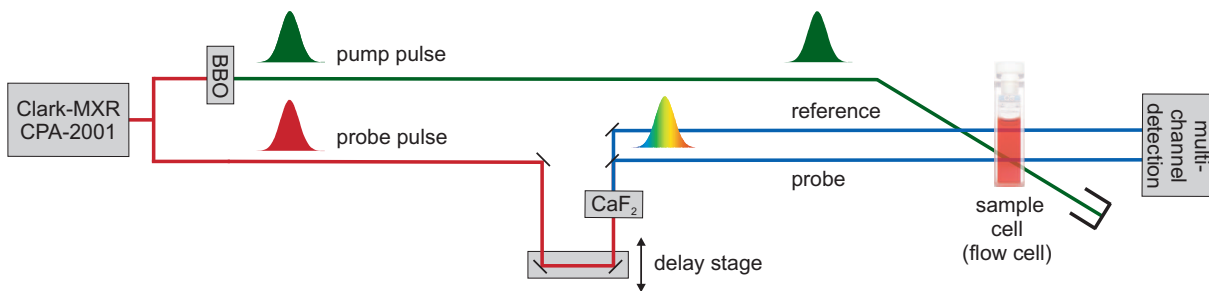


Figure 2.1: Schematic femtosecond transient absorption pump-probe setup. BBO: Non-linear frequency conversion processes in β -barium borate (BBO). CaF_2 is used for supercontinuum (SC) generation.

delay times between pump and probe over a broad spectral range.

The non-linear frequency conversion processes used to convert the laser fundamental into the desired pump and probe wavelength are based on non-linear optical effects which are described in some detail in former Ph.D. Theses^[1-4] in the work group and in several textbooks.^[5-7] For the pump pulse generation, a home-built non-collinear optical parametric amplifier (NOPA) setup was used.^[8,9] The NOPA as a tunable light source for visible wavelengths. Optional subsequent second harmonic generation of the NOPA output allows one to generate pump pulses over the whole UV/VIS spectral range from 210 nm to 775 nm with a small gap from $375 \leq \lambda_{pump} \leq 450$ nm. The second harmonic of the laser fundamental at 387 nm lies within this gap, which can also be closed by sum-frequency generation of the NOPA and Ti:Sa fundamental. For the probe, a SC from $315 \leq \lambda_{probe} \leq 700$ nm generated in CaF_2 was used. The next Section gives a detailed description of the transient absorption setup.

2.2 Femtosecond Transient Absorption Setup

A detailed sketch of the femtosecond time-resolved transient absorption setup is shown in Fig. 2.2. The arrangement of all optical components is depicted as they were present on the optical table. The probe pulses could be delayed with respect to the pump pulses by the computer controlled main delay stage (Physik Instrumente, M-531.DG). After white light generation in CaF_2 , the pulses were divided into probe and reference beams, which both were focused into the sample cell before being focused onto the entrance slit of an imaging spectrograph (L.O.T. Oriel, MS260i). The spectra were simultaneously imaged onto a 1024×127 pixel array of a CCD camera (L.O.T. Oriel, DB401-UV).

The pump pulses were generated by a NOPA and subsequently compressed with a prism pair (P). Depending on the required excitation wavelength, the NOPA output could be frequency doubled before it was focused into the sample cell. The sample cell was a flow cell with a path length of 0.5 mm or 1 mm between two suprasil quartz (SQ) windows

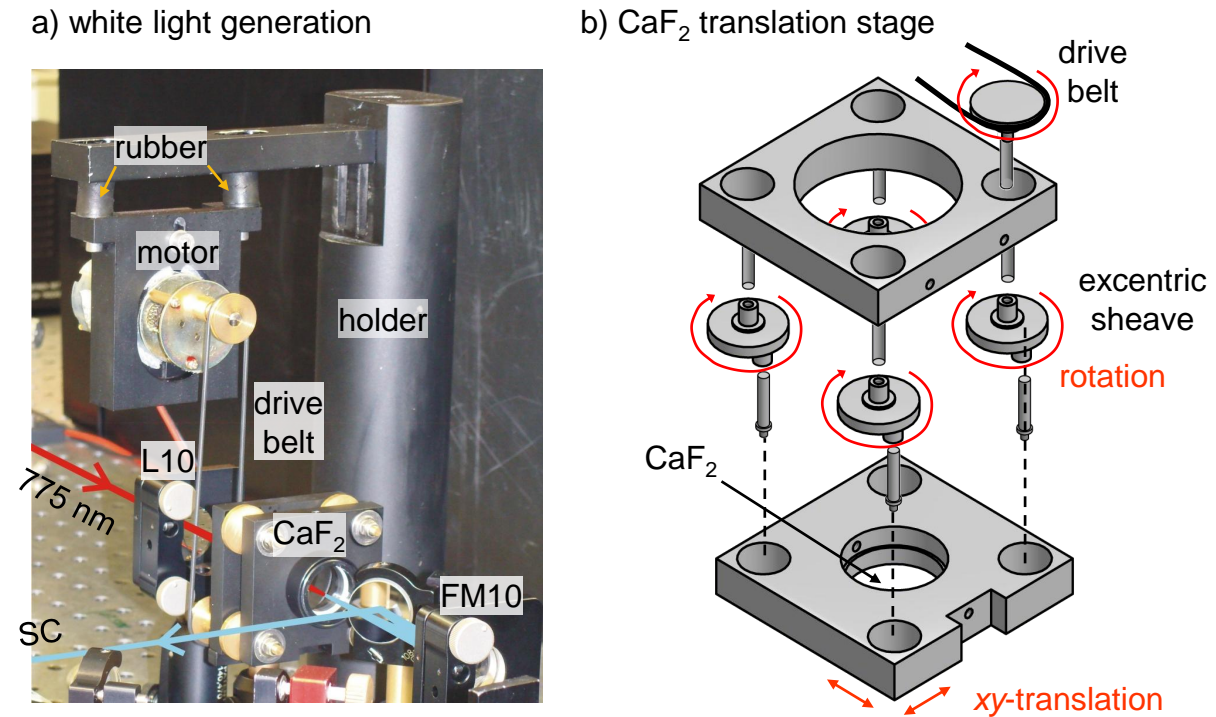


Figure 2.3: a) Photo of the white light generation setup including abbreviations from Fig. 2.2. b) Schematic picture of the CaF₂ translator. A rotational motion of a motor is transferred to periodic translational motion of the CaF₂ plate.

CaF₂ plate with respect to the plane of polarization of the pump light,^[11] a translation of the plate between two laser pulses without rotation had to be performed. For this purpose, a workshop-built xy -translator (with x and y as the directions perpendicular to the laser beam propagation direction) was used (see Fig. 2.3). A motor mounted on a solid steel holder drives a belt. Two rubbers between the holder and the motor prevent transfer of the motor vibrations to the optical table. The belt drives the CaF₂ translator, which consists of two metal plates with central apertures connected with rotating eccentric sheaves. The first metal plate (the upper one in Fig. 2.3b) is fixed on the optical table. The aperture of the second plate carries the CaF₂ plate. The rotation of the sheaves by the motor with the driving belt is transferred to a movement of the CaF₂ plate in x - and y -direction.

The spectrum of the SC, its chirp, and its pulse-to-pulse stability strongly depend on the focus position inside the CaF₂ plate and the intensity of the laser fundamental. To optimize these parameters, the pulse intensity could be tuned with a pair of gradient neutral density filters (GF). A translation stage allowed for a precise positioning of the focal point inside the CaF₂ plate. In order to reduce the chirp of the white light pulse, the focal position should be close to the back surface of the plate with regard to the laser propagation. In order to achieve an optimal SC, one should start with ≈ 2 mW of the laser fundamental and a focal position behind the CaF₂ plate (without SC generation) and

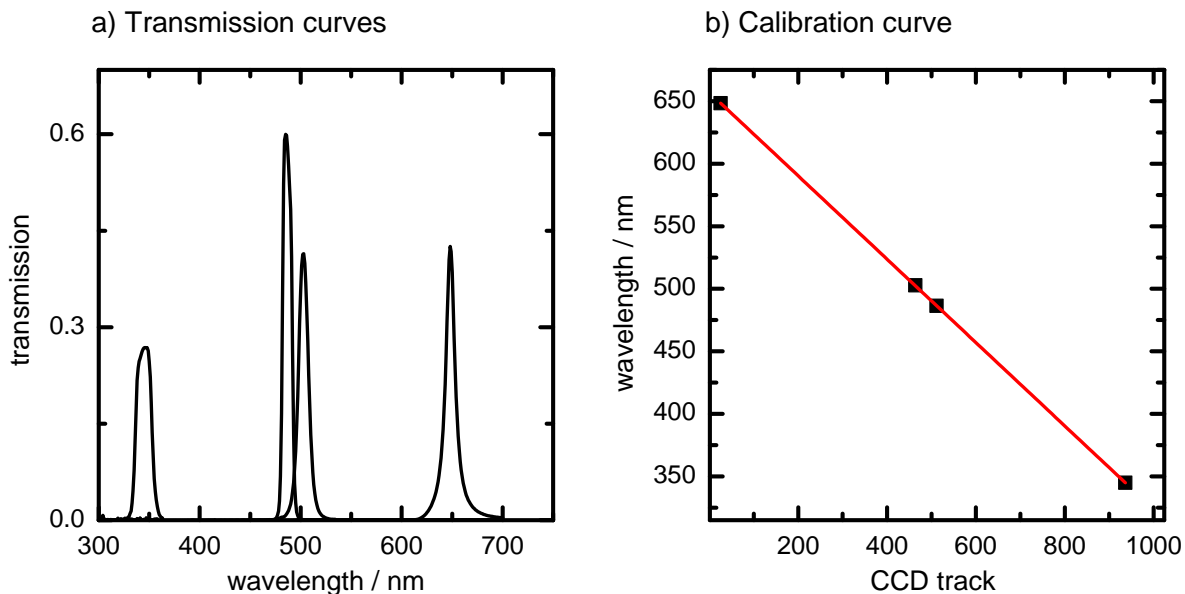


Figure 2.4: a) Transmission curves of the interference filters used for wavelength calibration. b) Wavelength of the transmission maximum vs. maximum light intensity measured with the CCD camera.

iteratively adjust the intensity and the focal position. An intense red ring surrounding the SC core has to be avoided during this process because it indicates too high pulse intensities which could lead to material damage. A further decrease in pulse energy leads first to a disappearance and then to a reappearance of the white light. The SC at lower pump energies was used to ensure a long-term durability of the CaF_2 plate for many months. In combination with proper settings of the focus, a white light spectrum as shown in Fig. 2.5 and good long-term stability was observed.

The supercontinuum was collected with a focusing mirror (FM10, $f = 100$ mm) mounted on a translation stage, and sent through an iris to cut out the central SC core. The probe and the reference pulses were generated via the front and back reflections from a quartz plate (Et, Laseroptik, SQ, $d = 5$ mm). The translation stage for the FM10 mirror allowed for adjusting the focal point of the probe and reference beams with respect to the sample cell. Typical beam diameters at the position of the sample cell were $\approx 150 \mu\text{m}$ ($1/e^2$ beam radius) determined by knife edge measurements.^[12] After passing the sample cell, the horizontal alignments of the probe and reference beams were changed to a vertical orientation with a periscope. This procedure was necessary because of the spectrograph geometry. The SC passed a BG38 filter (Schott) to cut out any remains of the laser fundamental and to reduce the NIR part of the SC which would be too intense for the CCD. A gradient neutral density filter (GF, Thorlabs, SQ) was used to attenuate the intensity of the SC to avoid saturation of the CCD camera within the accumulation time. Finally, the SC was focused with a lens (L10, SQ, $f = 100$ mm) on the entrance slit of the

spectrograph. An additional variable slit (S) was placed before the entrance slit to exclude scattered light caused by focusing the pump beam into the sample cell (see below). The focusing lens L10 in front of the spectrograph could be moved by a translation stage, which allowed one to adjust the focus position and the spot size of the two beams on the CCD camera. To obtain the probe and reference spectra, vertical binning for the respective tracks of the CCD camera was performed, controlled by a LabView program on a PC.^[2,13]

The calibration of the grating spectrograph was performed by successively placing four interference filters (Schott) in the SC beam and measuring the track position of the CCD camera at the transmission maximum. The transmission curves of the filters measured with a Shimadzu UV-2401 desktop spectrometer and an example of a calibration curve are given in Fig. 2.4. The calibration has to be performed after any change of the SC beam path, because slight geometrical modifications may result in a displacement of the spectrum on the CCD camera.

The SC stability can be expressed by the standard deviation σ of the noise of the change in optical density (ΔOD) in the absence of the pump pulse. Figure 2.5b shows the wavelength dependent stability of the SC calculated for typical integration times (150 ms) of the CCD camera and typical average numbers (90) for each temporal delay (150 \times 90 laser pulses, for details see below) at four different wavelength indicated as colored vertical lines in Fig. 2.5a (5 nm corresponding to 15 pixel of the CDD camera were averaged). The noise standard deviation was $\Delta OD \approx 9 \cdot 10^{-5}$ for probe wavelengths ≤ 350 nm and better than $\Delta OD \leq 5 \cdot 10^{-5}$ for wavelengths ≥ 350 nm.

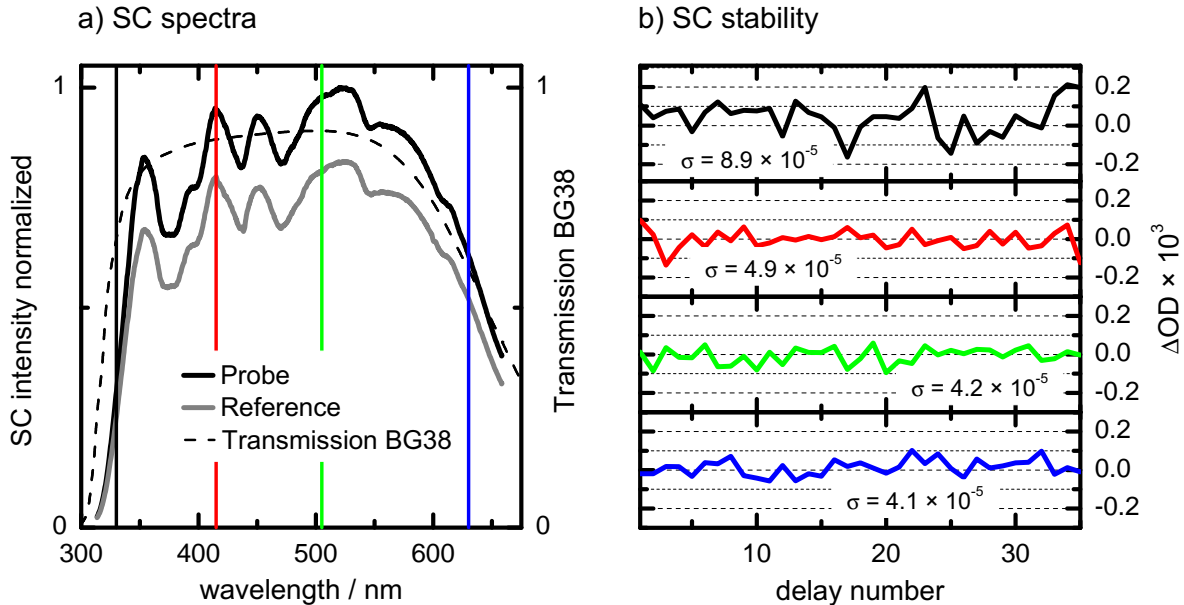


Figure 2.5: a) Spectrum of the SC generated in CaF₂ after passing a BG38 filter, detected with a CCD camera attached to a spectrograph. b) Stability of the SC expressed by the ΔOD values at different delay stage positions and at different probe wavelength (black: 330 nm, red: 415 nm, green: 505 nm, blue: 630 nm).

2.2.2 Optical Pathway for the NOPA Pump Pulses

Tunable pump pulses were generated by a home-built NOPA. In principle, the NOPA process is based on the temporal and spatial overlap of an intense UV pump pulse and a weak broadband seed pulse in a suitable non-linear crystal, thus amplifying the desired wavelength contained in the chirped broadband seed pulse. For visible wavelengths best results are obtained by overlapping both pulses under an angle of $\approx 6^\circ$ in a β -barium borate crystal (β -BaB₂O₄, or BBO for short) for simultaneous phase and group velocity matching.^[8,9] In the present setup, a small fraction (≈ 5 mW) of the pump laser fundamental was split off by a wedge (W, Laseroptik, 5° , $d = 3$ mm). The intensity of the front side reflection of the wedge was attenuated by a pair of gradient neutral density filters (GF) to ≈ 1 mW and sent through an iris to separate it from the back reflection of the wedge. The attenuated beam was focused with a lens (L05, $f = 50$ mm) into a sapphire plate (SP, $d = 2.3$ mm, Newport) to generate a SC (450 – 800 nm). SC generation in sapphire does not require the plate to be translated because of its high damage threshold. The focus position could be adjusted by moving the sapphire plate with a translation stage. The SC was collected with a focusing lens (L03, $f = 30$ mm) placed on a translation stage and refocused into the NOPA-BBO (BBO2, cut angle $\vartheta = 32^\circ$, $d = 2$ mm). The translation of L03 allowed for control of the focus position of the SC with respect to the crystal.

The main part of the pump laser fundamental (≈ 300 mW) passed the wedge (W) and could be delayed with respect to the SC with a delay stage. The beam was then frequency-doubled by second harmonic generation (SHG) in a BBO crystal (BBO1, cut angle $\vartheta = 30.2^\circ$, $d = 0.5$ mm) to provide UV pump pulses (387 nm, 90 mW) for the NOPA. These pump pulses were focused with a lens (L30, SQ, $f = 300$ mm) towards the NOPA-BBO under an angle of $\approx 6^\circ$ with respect to the SC in order to compensate for group velocity mismatch (GVM). The angle resulted from steering the beam first lower and again up to the NOPA crystal with two dielectric mirrors (HR387). The non-collinear angle could be tuned by changing the height of the UV pump beam induced by the two HR387 mirrors to optimize it for the desired NOPA output wavelength. The focus position of the UV pump beam should lie ≈ 5 cm in front of the BBO-crystal to avoid damage. Inside the non-linear crystal, the UV pump photons are converted into an IR photon (idler) and a VIS photon (signal) under conservation of energy and momentum.^[9] Idler and signal propagate on defined cones as depicted in Fig. 2.6. The SC seeds this parametric process, therefore spatial and temporal overlap of both pulses is required. The wavelengths of the resulting NOPA pulses could be varied within the range of the chirped white light supercontinuum pulse by changing the pump delay relative to the seed. The delay stage placed before the lens L30 allowed for a comfortable wavelength change without changing the spatial overlap and focus conditions inside the NOPA-BBO.

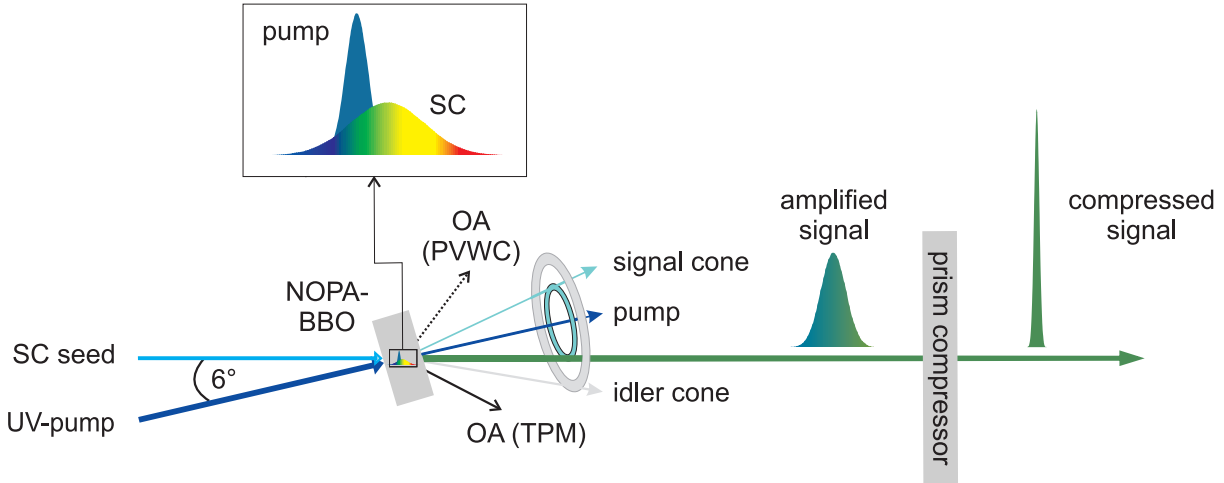


Figure 2.6: NOPA process for UV pump and SC seed in a BBO crystal. For details see text. Two orientations of the optical axis (OA, black arrows) of the BBO are possible: The seed beam propagation direction relative to the OA can lie between the OA and the pump beam (TPM-OA, solid OA) or the pump beam can be between the OA and the seed-beam (PVWC-OA, dotted line).

The alignment of the NOPA is an iterative process which includes the optimization of the following parameters: (i) The spatial overlap of the SC and the UV pump beam has to be optimized. It is easier to start with large SC diameters. (ii) Rotation of the NOPA-BBO changes the seed beam propagation direction relative to the optical axis of the crystal. There are two possible rotation angles for the relative orientation of the optical axis with respect to the seed beam and the amplified signal. The direction of the amplified signal beam can lie between the pump beam and the optical axis (tangential phase matching, TPM) or the pump beam can propagate between the optical axis and the amplified signal (Poynting vector walk-off compensation, PVWC).^[14,15] Both configurations are depicted in Fig. 2.6. The TPM configuration results in a higher gain and a more efficient NOPA operation.^[14] (iii) The non-collinear angle between the SC seed and the UV-pump can be used to minimize GVM. For longer wavelengths, the angle has to be enlarged. The horizontal angle between SC and pump has to be zero, i.e., both beams propagate “on top of each other”. (iv) The temporal overlap between SC and pump has to be adjusted in order to amplify the SC wavelength of interest (see Fig. 2.6). (v) The vertical tilt angle between the surface normal of the BBO and the UV-pump has to be changed to fulfill the phase matching condition. A good starting position is a value of \approx zero which can be found by overlapping the back reflection and the incoming beam. (vi) The focus size of the SC inside the BBO has to be optimized. (vii) The focus position of the UV-pump with respect to the BBO can be changed by moving the BBO crystal.

The iterative optimization of these parameters was performed by maximizing the intensity and simultaneously optimizing the spectral shape of the NOPA output, which

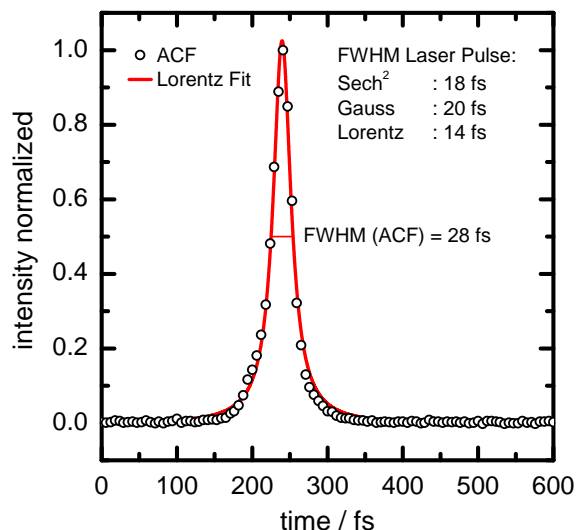


Figure 2.7: Typical autocorrelation function (ACF) of the compressed NOPA output centered at 500 nm (spectral FWHM = 50 nm). The replacement of transmissive focusing and collimating optics with reflective focusing mirrors (FM10) allowed for compression of the pulse duration down to ≤ 20 fs (FWHM) of the pulse (28 fs FWHM of the autocorrelation).

was controlled with a CCD spectrometer (APE-Berlin, PulseScope) after collimating the beam with a reflective focusing mirror (FM10). Due to the high intensity of the NOPA output, the reflection from a white card was used for the CCD detection. The NOPA pulses could be tuned within the white light range of 450 – 700 nm and had intensities between 6 – 20 mW depending on the amplified wavelength.

A prism compressor of two prisms (P) and a folding mirror was used to compress the temporal duration of the NOPA pulses. In Fig. 2.7, the autocorrelation function (ACF) for pulses around 500 nm (spectral width of 50 nm FWHM) is shown. They could be compressed down to 18 fs FWHM (sech^2) of the pulse (28 fs FWHM of the autocorrelation), which is quite close to the Fourier limit. For wavelengths < 600 nm, a BK7 glass prism pair (P , Linos, 60° , 30×30 mm) was used, but for wavelengths > 600 nm the distance between BK7 prisms needed for optimal compression becomes quite large. For this reason, a pair of F2 glass prisms (P , Linos, 60° , 30×30 mm) was used for the longer wavelength range. This typically yielded pulse lengths of 30 – 40 fs FWHM (sech^2), probably due to the third-order dispersion of F2 glass that is not compensated in a prism compressor.

A wavelength change of the NOPA output requires the adjustment of the distance between the two prisms (P) and the optical pathway inside the prisms. In order to allow for a fast and convenient wavelength change, the second prism and the folding mirror were placed on an optical rail and both prisms were mounted on translation stages.

For femtosecond time-resolved transient absorption spectroscopy, it may be useful to reduce the spectral width of the pump pulse. For this purpose, an iris was placed after the second prism of the prism compressor to block undesired wavelengths of the dispersed

laser beam. For further narrowing of the spectral width, a glass plate (SQ, 5 mm) can be placed in the SC seed beam pathway for the NOPA. This increases the chirp of the SC and lowers the spectral range, for which the temporal overlap of SC and UV pump in the NOPA-BBO is possible.

In order to generate pump pulses at UV wavelengths, the compressed NOPA output was frequency doubled in a suitable BBO crystal (BBO3). The program SNLO written by Smith can be used to calculate the appropriate cutting angle of the BBO for each desired wavelength.^[16] The NOPA output was focused to a point slightly before the BBO crystal and the generated second harmonic was re-collimated. Because transmissive optics introduce a large chirp, focusing and collimating were performed with a pair of focusing mirrors (FM10). This is most important for UV pump pulses because a pre-chirping with the prism compressor to compensate this chirp would directly lower the SHG efficiency. An iris was used to attenuate the pump beam to $\approx 0.2 - 0.3$ mW, which was the typical excitation energy for all experiments. Finally, a Berek's variable wave plate was used to set the polarization of the pump beam to parallel, perpendicular, or magic angle polarization with respect to the SC probe beam. The pump beam was focused with a reflective focusing mirror optic (FM20) into the sample cell and spatially and temporally overlapped with the SC probe beam under an angle of $\approx 5^\circ$. Typical beam diameters at the position of the sample cell were $\approx 200 \mu\text{m}$ ($1/e^2$ beam radius) determined by knife edge measurements.^[12]

2.2.3 Data Acquisition

As mentioned, the probe and reference spectra were obtained by vertical binning of the respective tracks of the CCD camera. The change in optical density ($\Delta\text{OD}(\lambda, t)$) induced by the pump pulse in the probed volume of the sample cell with respect to the reference volume was calculated from these spectra. The transient absorption as the negative logarithmic value of the transient transmission is proportional to the probe (Pr) and the reference (Ref) SC intensities $I^{Pr,Ref}(\lambda, t)$ for the wavelength λ at the delay time t :

$$\Delta\text{OD}(\lambda, t) = -\log T(\lambda, t) \sim -\log \left(\frac{I^{Pr}(\lambda, t)}{I^{Ref}(\lambda, t)} \right). \quad (3)$$

In order to calculate the transient transmission $T(\lambda, t)$, the intensities $I^{Pr,Ref}(\lambda, t)$ were normalized by $I_0^{Pr,Ref}(\lambda, t)$ obtained without the presence of the pump pulse. This procedure is required because of intensity differences between probe and reference beam, resulting from either the front or back reflection at the etalon, unequal reflectivity of the optics and different sensitivity of the pixels of the CCD camera. Furthermore, the ambient background signals $I_B^{Pr,Ref}(\lambda, t)$ were subtracted from the intensities $I_0^{Pr,Ref}(\lambda, t)$ and the amount of scattered light from the pump beam $I_S^{Pr,Ref}(\lambda, t)$ (which also includes

the ambient background) was subtracted from the intensities $I^{Pr,Ref}(\lambda, t)$. Finally, the change in optical density ($\Delta OD(\lambda, t)$) could be calculated from

$$\Delta OD(\lambda, t) = -\log \left(\frac{(I^{Pr}(\lambda, t) - I_S^{Pr}(\lambda, t))}{(I^{Ref}(\lambda, t) - I_S^{Ref}(\lambda, t))} \times \frac{(I_0^{Ref}(\lambda, t) - I_B^{Ref}(\lambda, t))}{(I_0^{Pr}(\lambda, t) - I_B^{Pr}(\lambda, t))} \right) \quad (4)$$

In order to measure the required spectra in Eq. (4), mechanical shutters (Electro-Optical Products Corp.) were placed in the laser fundamental beam path before the splitting into pump and probe (Sh1 in Fig. 2.2) and into the beam path of the probe and pump (Sh2 and Sh3, respectively). Each of the recorded spectra was accumulated on the CCD for typically 150 laser shots (i.e., 0.15 s) before readout. Shutter Sh1 was used to block all beams during the readout time period of the CCD. $I^{Pr,Ref}(\lambda, t)$ were detected with Sh3 and Sh2 open, $I_0^{Pr,Ref}(\lambda, t)$ with Sh3 closed, $I_S^{Pr,Ref}(\lambda, t)$ with Sh2 closed and $I_B^{Pr,Ref}(\lambda, t)$ with Sh2 and Sh3 closed. The synchronization of the shutters with the CCD camera and the delay stage was performed by a LabView program on a PC.^[13] Typically, 30 – 90 measurements were averaged for one delay time. The transient spectra were saved as a matrix of the $\Delta OD(\lambda, t)$ values and delay times. The wavelength for each track of the CCD camera could be obtained from the calibration curve obtained from the separately saved spectra of the interference filters (see Fig. 2.4b).

2.3 Experimental Artifacts in fs Time-Resolved Transient Absorption Spectroscopy

Femtosecond time-resolved spectroscopy uses excitation pulses with very high energy densities of $\approx 10 \text{ GW cm}^{-2}$. These energy densities easily induce (i) stimulated Raman scattering (SRS), (ii) two-photon absorption and (iii) non-linear modification of the refractive index of the solvent and the sample cell windows.^[17–19] In combination with broadband SC probe pulses, the modification of the refractive index leads to spectral redistribution of the spectrally broad probe pulse, but the reference pulse is not affected. This so-called cross-phase modulation (XPM) can be observed as a change in optical density during the interaction time of pump and probe. The temporal evolution of this change in optical density depends on the chirp of the SC, the temporal and spectral distribution of the pump pulse, the length of the sample cell (solvent and windows), and the diameters and the angle of intersection of the probe and the pump beam.^[17–19]

The coherent artifacts are produced by the simultaneous action of one pump photon and one probe photon. Therefore, their appearance is limited to the interaction time of pump and probe in the sample cell. Especially for the investigation of short-lived transient species in solution, a careful distinction between molecular signals and coherent

artifacts is necessary. On the other hand, SRS and XPM are very useful for optimizing the experimental conditions, temporal resolution and the determination of the wavelength dependent time-zero of the experiment.

In the following, the most important coherent artifacts XPM and SRS will be described for the example of the fsTAS measurement of pure *n*-hexane in a flow cell with a path length of $d = 1$ mm with two 0.2 mm quartz windows (SQ), pump pulses centered at $\lambda_{\text{pump}} = 500$ nm with a pulse length of 25 fs FWHM (sech^2) and power of 0.35 mW, and SC probe pulses. The recorded two-dimensional plot of $\Delta\text{OD}(\lambda, t)$ is shown in Fig. 2.8a. The absorption map features XPM with different temporal behavior ($315 \leq \lambda \leq 655$ nm), wavelength dependent time-zero positions due to the chirp of the SC (black line), a positive SRS signal on the blue side of the excitation wavelength ($\lambda \approx 430$ nm) and a negative SRS signal on its red side ($\lambda \approx 580$ nm).

The temporal shape of the XPM strongly depends on the chirp of the SC. For a linearly chirped SC and Fourier transform limited pump pulses, the XPM exhibits a W-shape with a positive maximum flanked by two negative minima.^[17–19] The positive maximum of the W-shaped XPM marks the time-zero of the experiment.^[17] For unchirped probe pulses, the shape of the XPM shows one maximum and one minimum, where the zero-crossing marks the time-zero.^[17] As can be seen in Fig. 2.8a from the temporal appearance of the XPM, the chirp of the SC is pronounced at wavelengths < 575 nm. Consequently, between 400 – 575 nm, a W-shaped XPM could be observed. At wavelengths > 575 nm the shape of the XPM changes from the W-form to an S-shape. In the spectral region below 400 nm, the wavelength of the pump pulse differs strongly from the probe wavelength. This results in different group velocities of the pulses and dispersion in the sample cell. Consequently, a walk-off between pump and probe is observed. The XPM signal splits into two separate features and the determination of the time-zero of the experiment becomes ambiguous.^[18,19] There also might be some walk-off effects in the spectral region from 550 – 655 nm. The error in the determined time-zero is of the order of $\approx 10 - 20$ fs because of these uncertainties.

The determined time-zero for all wavelengths was used for the time-zero correction of the 2D-absorption map by a self-written MATHEMATICA program.^[20] Briefly, the delay vector for each track was corrected by the difference between the experimentally determined time-zero of the respective track of the CCD camera and the track of the longest probe wavelength. Interpolation of this data set was performed for each track and values of ΔOD were calculated for a common delay file for all tracks.³ The time-zero corrected absorption map of the discussed solvent measurement is shown in Fig. 2.8b.

Time profiles taken from the time-zero corrected data featuring the three distinctive

³For the data analysis the raw data was taken.

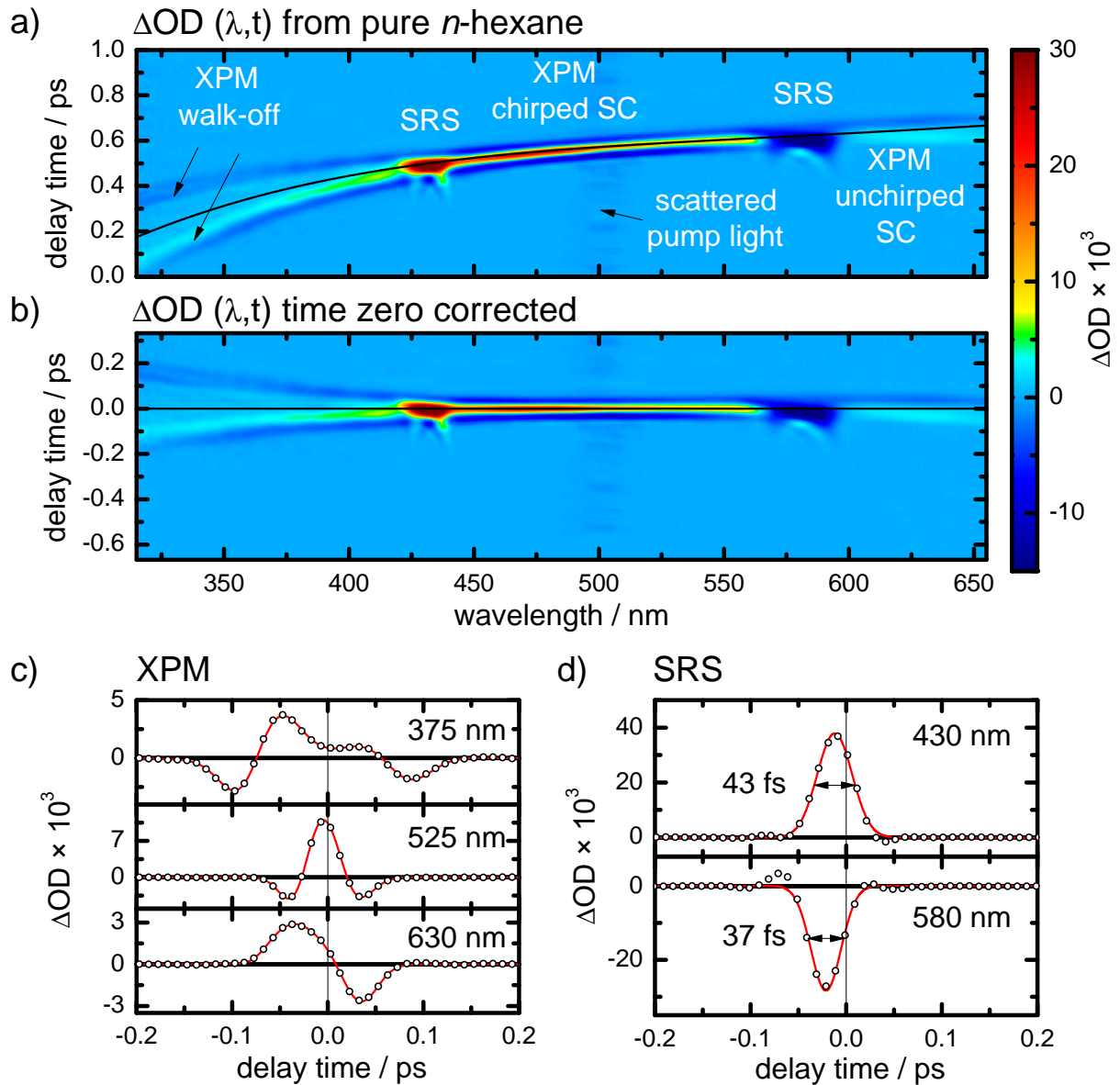


Figure 2.8: Coherent artifacts in transient absorption spectroscopy obtained from a flow cell filled with pure *n*-hexane ($\lambda_{\text{pump}} = 500$ nm). a) Raw data ($\Delta OD(\lambda, t)$) obtained from a chirped probe pulse and a compressed pump pulse (see text). b) Time-zero corrected $\Delta OD(\lambda, t)$ based on the cross phase modulation (XPM) signal. c) XPM time profiles at three different wavelengths (see text) of the time-zero corrected picture and Gaussian fits of the data (red lines). d) Time profiles of the stimulated Raman scattering (SRS) and Gaussian fits of the data (red lines). The FWHM of the SRS can be taken as the FWHM of the cross correlation between pump and probe and gives the temporal resolution of the experiment.

XPM shapes mentioned above are shown in Fig. 2.8c. The splitting into two separate XPM features due to the walk-off can be observed at 375 nm. The W-shape for a chirped SC pulse can nicely be seen at 525 nm, whereas at 630 nm the time profile is S-shaped. The signal at 630 nm is not symmetric, which might be due to walk-off effects at longer wavelengths. The splitting of the XPM at wavelengths far from the excitation wavelength complicates the characterization of the supercontinuum according to the theory of Kovalenko *et al.*,^[17] who neglected propagation effects. For this reason, the XPM was fitted with a sum of Gaussians in Fig. 2.8c and to quantify it for the fitting procedure (see below).

Time profiles of the two SRS signals are shown in Fig. 2.8d. The stimulated Raman effect occurs because of a coherent interaction of the pump and probe pulses in a medium with a vibrational resonance at the pump-probe difference frequency. On the red side of the excitation wavelength, $\omega_{vib} = \omega_{pump} - \omega_{probe}$ must be fulfilled, where ω_{vib} is the frequency of the Raman mode of the solvent. In the case of *n*-hexane and an excitation at 500 nm, the probe stimulates the Stokes scattering around 580 nm, which results in a negative SRA. On the blue side of the excitation wavelength, $\omega_{vib} = \omega_{probe} - \omega_{pump}$ must be fulfilled, and the pump photons stimulate the Stokes scattering resulting in a positive ΔOD around 430 nm. The SRS can be taken as the pump-probe cross-correlation function and it thus allows for a determination of the temporal resolution of the experiment at the respective probe wavelength. Time profiles of both SRS contributions are shown in Fig. 2.8d. The curves were subtracted by the XPM obtained at shorter wavelengths in order to obtain the pure SRS signals. The temporal resolution of the experiment can be taken from the FWHM of the SRS signal and was determined to be ≈ 40 fs in this case.

As the pump pulse has a certain spectral width, the SRS in broadband transient absorption spectroscopy provides phase information about the excitation pulse and can be used to optimize its phase inside the sample cell. This is most important in the case of UV pump pulses, because their temporal width could not be measured with the autocorrelator. Furthermore, dispersion, e.g., in transmissive optics like focusing lenses is most pronounced at shorter wavelength. Figure 2.9 shows the SRS signal for an excitation pulse centered at 335 nm obtained from a frequency doubled NOPA, which was compressed with a pair of F2-prisms to a pulse length of 30 fs FWHM (sech^2). Frequency doubling was performed first with a pair of lenses ($f = 100$ mm, SQ) and focusing into the sample cell with a third lens ($f = 200$ mm, SQ). The shape of the SRS signal (Fig. 2.9a) reflects a strongly chirped pump pulse. Sufficient pre-chirping of the NOPA pulse with the prism compressor was not possible, because this directly lowers the SHG efficiency. Therefore, all lenses were replaced by focusing mirrors as depicted in Fig. 2.2. The SRS signal obtained with the use of the reflective optics is shown in Fig. 2.9b. It can be clearly seen that the experimental setup with reflective optics allows for excitation with almost unchirped UV pump pulses.

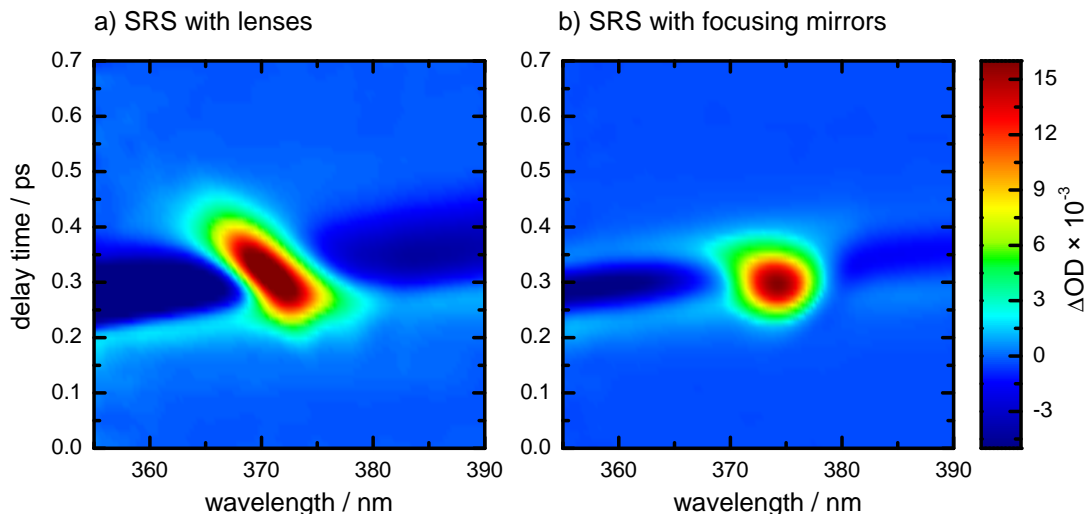


Figure 2.9: SRS signals in *n*-hexane ($\omega_{vib} = \omega_{pump} - \omega_{probe}$) for UV excitation at ≈ 335 nm from a frequency doubled NOPA output. a) Lenses were used for focusing the NOPA in the SHG-BBO, collimating of the UV pulse and focusing into the sample cell. b) Focusing and collimating were performed using concave mirrors (FM10, FM20, see Fig. 2.2).

Furthermore, an improvement of the temporal resolution of the experiment for visible excitation pulses by a factor of ≈ 2 compared with the setup using transmitting optics^[2] could be achieved.

Each measurement of a molecular system has to go along with a previous solvent measurement without changing any measurement condition. The XPM and SRS signals were then approximated using a sum of Gaussians, which could be included in the fitting procedure of the data.

2.4 Data Analysis

Femtosecond time-resolved broadband transient absorption spectroscopy as described in Section 2.2 produces large data sets consisting of two $1024 \times$ (number of delays steps) large matrices of ΔOD values (from the solvent and from the sample), two delay files and the calibration curves of the interference filters. From these data, the spectro-temporal behavior of the investigated molecule has to be extracted. In the course of this Thesis, a MATHEMATICA^[20] program was written which allows for a convenient data handling including wavelength calibration, time-zero correction, extraction of transient spectra and time profiles, functionalization of the coherent artifacts, fitting of single time profiles with several fitting models including the functionalized coherent solvent contributions and a global fitting procedure, which takes the results from the single fits as input parameters. The global fitting procedure allows one to apply a kinetic model to the entire matrix of ΔOD values. Typically 5 – 15 time traces were fitted simultaneously. Because of the size

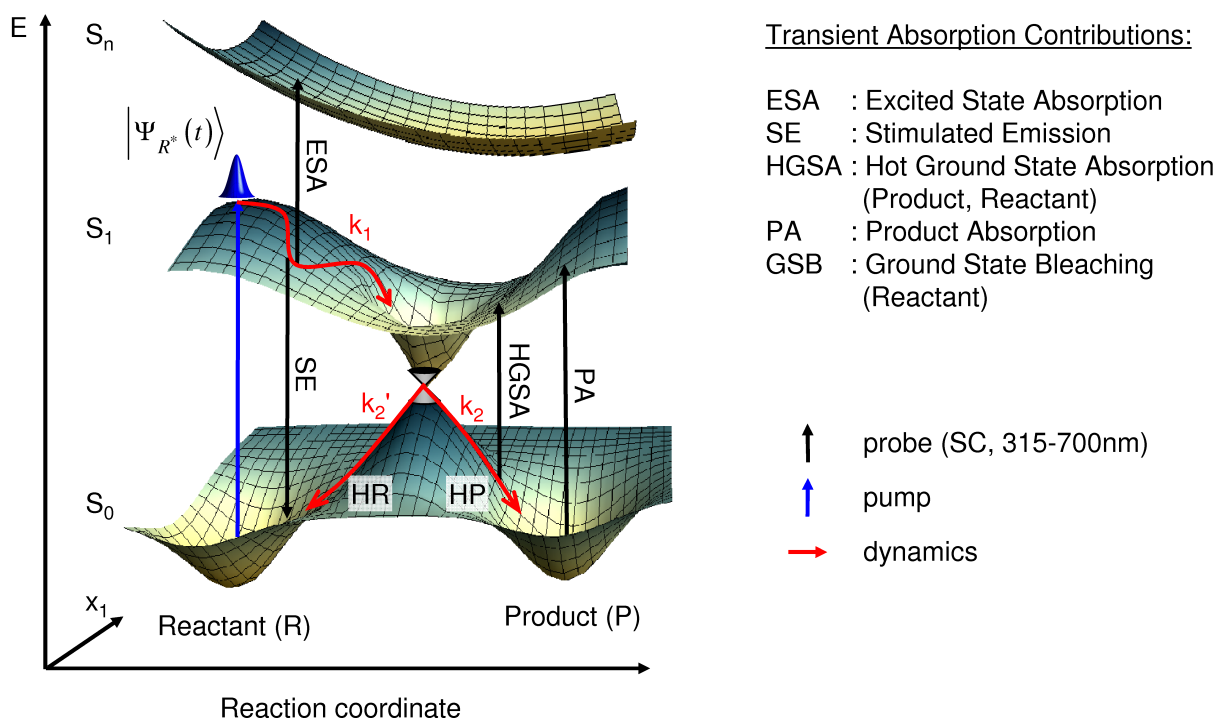


Figure 2.10: Molecular contributions to the femtosecond time-resolved transient absorption measurements for ultrafast non-adiabatic reactions with the involvement of a conical intersection (CI). The reactant is excited with an ultrashort pump pulse to the first excited state, which can be described with an excited state wavepacket $|\Psi_{R^*}(t)\rangle$. The wavepacket follows the energy gradient towards the CI and forms either vibrationally hot product (HP) or hot reactant (HR).

of the program source it is not printed in this Thesis, but is available on request from the author on CD. In the following, the most important fitting functions used for describing the extracted time profiles are presented.

Ultrafast photochemical reactions can be described by a consecutive kinetic reaction scheme for a diabatic reaction involving a Conical Intersection (CI) depicted in Fig. 2.10. A wavepacket $|\Psi_{R^*}(t)\rangle$ on the S_1 PES is created with an ultrashort pump pulse. The wavepacket then follows the energy gradient on the excited PES and excited-state absorption (ESA) of the SC probe pulse to higher states can be observed. The lifetime of the ESA reflects the excited-state life time of $|\Psi_{R^*}(t)\rangle$. Other coordinates besides the reaction coordinate (RC) might be involved in the excited-state dynamics leading to oscillating changes of the optical density. Molecules which return to the electronic ground state via the CI are vibrationally hot (hot product (HP) or hot reactant (HR)) and absorb at longer wavelengths than the respective ground state molecules, giving rise to hot ground state absorption (HGSA). The HP and HR undergo VR, until finally the reactant or the product in their electronic and vibrational ground states are formed. This reaction can be

described by the following consecutive reaction schemes:



or



The concentrations of the involved species R^* , HP and P for $k_1 \gg k_2$ are given by

$$\frac{\text{OD}(\text{R}^*)}{\epsilon(\text{R}^*) \cdot d} = [\text{R}^*]_0 \cdot \exp[-k_1 t] \quad (7)$$

$$\frac{\text{OD}(\text{HP})}{\epsilon(\text{HP}) \cdot d} = [\text{R}^*]_0 \cdot \frac{k_1}{k_2 - k_1} \cdot (\exp[-k_1 t] - \exp[-k_2 t]) \quad (8)$$

$$\frac{\text{OD}(\text{P})}{\epsilon(\text{P}) \cdot d} = [\text{R}^*]_0 \cdot (1 - \exp[-k_2 t]). \quad (9)$$

An analogous set of equations can be written for the deactivation of R^* to the reactant ground state. As the molar absorption coefficients of the excited species and the vibrationally hot species in the electronic ground state are unknown, the amplitude factors a , b and c were used to account for $\epsilon \cdot d \cdot [\text{R}^*]_0$. Furthermore, the fraction term in Eq. (8) is negative and its positive part is also included into the factor b :

$$\text{OD}(\text{R}^*) = a \cdot \exp[-k_1 t] \quad (10)$$

$$\text{OD}(\text{HP}) = b \cdot (\exp[-k_2 t] - \exp[-k_1 t]) \quad (11)$$

$$\text{OD}(\text{P}) = c \cdot (1 - \exp[-k_2 t]) \quad (12)$$

The changes in optical density for infinite short excitation pulses for the product formation can be described by the function $F^P(t)$ with $a' = a - b$ and $b' = b - c$:

$$F^P(t) = a \cdot \exp[-k_1 t] + b \cdot (\exp[-k_2 t] - \exp[-k_1 t]) + c \cdot (1 - \exp[-k_2 t]) \quad (13)$$

$$= a' \cdot \exp[-k_1 t] + b \cdot \exp[-k_2 t] + c \cdot (1 - \exp[-k_2 t]) \quad (14)$$

$$= a' \cdot \exp[-k_1 t] + b' \cdot \exp[-k_2 t] + c \quad (15)$$

In analogy, the function $F^R(t)$ with k_1 and k'_2 can be written to describe the deactivation (Eq. (6)). According to Eqs. (13-15), the dynamics depicted in Fig. 2.10 can be described with (i) one decaying exponential, a rising and subsequently decaying function and one exponential rise, (ii) two decaying exponential functions and one exponential rise, (iii) two decaying exponentials and one step function. For a global fitting procedure with a large number of time traces, Eq. (15) should be used in order to reduce computation

time. Furthermore, the ground state bleach (GSB) has to be taken into account and was described by adding a step function.

Oscillating components associated with the ESA or HPA signal were modeled with additional oscillation functions given in Eq. (16), which are characterized by their amplitudes $a_{i,osc}$, frequencies ν_i , phases ϕ_i , and damping times $\tau_{i,osc}$. Their temporal appearance with respect to time-zero is modeled by a time shift x , when they are associated with oscillations in the hot ground state.

$$F_{osc}(t) = \sum_i \sin(2\pi\nu_i t + \phi_i) \cdot a_{i,osc} \cdot e^{-\frac{t-x}{\tau_{i,osc}}} \quad (16)$$

The total transient signal ($\Delta OD(t)$) is given by the model functions $F^P(t) + F_{osc}(t) + GSB$ or $F^R(t) + F_{osc}(t) + GSB$ convoluted with a Gaussian. This Gaussian accounts for the limited temporal resolution of the experiment and will be referred to as the instrument response function (IRF).

The photoisomerization quantum yields (ϕ) can be taken into account in order to determine the initial GSB after photoexcitation. This initial GSB differs from the final GSB by the factor of ϕ . For more complex reaction systems with multi-exponential ESA (or stimulated emission) decay behavior, $F(t)$ was expanded by additional exponential functions:

$$F(t) = \sum_i a_i \cdot \exp[-k_i t] + b' \cdot \exp[-k_2 t] + c \quad (17)$$

Furthermore, the fitting program allows for an inclusion of the coherent signals XPM and SRS from the solvent measurement functionalized with a sum of Gaussians and weighted by an amplitude factor f in the fitting procedure of the data. Assuming that the coherent signals depend linearly on the pump pulse energy,^[19] the weighting factor f describes the decrease of intensity due to absorption within the sample:^[19]

$$f \approx \frac{1 - 10^{-OD}}{2.3 \cdot OD} \quad (18)$$

The calculated factor f from Eq. (18) can be taken as a good starting value for the fitting procedure.

The fitting program allows for a versatile combination of all fitting functions for individual reaction systems. A large number of probe wavelengths with selectable global fitting parameters can be described simultaneously, which allows the user to fit the two-dimensional transient absorption map $\Delta OD(\lambda, t)$ with a kinetic model.

References

- [1] T. Pancur, *Ph.D. Thesis*, Christian-Albrechts-Universität zu Kiel **2005**.
- [2] M. Foca, *Ph.D. Thesis*, Christian-Albrechts-Universität zu Kiel **2005**.
- [3] H. Studzinski, *Ph.D. Thesis*, Christian-Albrechts-Universität zu Kiel **2007**.
- [4] N. K. Schwalb, *Ph.D. Thesis*, Christian-Albrechts-Universität zu Kiel **2009**.
- [5] R. W. Boyd, *Nonlinear Optics*, Elsevier Inc., Amsterdam **2008**.
- [6] D. Meschede, *Optik, Licht und Laser*, Teubner, Wiesbaden **2005**.
- [7] W. Demtröder, *Laserspektroskopie: Grundlagen und Techniken*, Springer, Berlin **2000**.
- [8] T. Wilhelm, J. Piel, E. Riedle, *Opt. Lett.* **1997**, *22*, 1494–1496.
- [9] H. Studzinski, *Diploma Thesis*, Christian-Albrechts-Universität zu Kiel **2002**.
- [10] J. M. Klopff, P. Norris, *Appl. Surf. Sci.* **2007**, *253*, 6305–6309.
- [11] V. Kartazaev, R. R. Alfano, *Opt. Commun.* **2008**, *281*, 463–468.
- [12] J. Eichler, L. Dünkel, B. Eppich, *Laser Technik Journal* **2004**, *2*, 63–64.
- [13] F. Renth, Unpublished Results.
- [14] A. L. Oien, I. T. Mckinnie, P. Jain, N. A. Russell, D. M. Warrington, L. A. Gloster, *Opt. Lett.* **1997**, *22*, 859–861.
- [15] N. Ishii, *Ph.D. Thesis*, Ludwig-Maximilians-Universität München **2006**.
- [16] SNLO nonlinear optics code available from A. V. Smith, AS-Photonics, Albuquerque, NM, URL <http://www.as-photonics.com/SNLO>.
- [17] S. A. Kovalenko, A. L. Dobryakov, J. Ruthmann, N. P. Ernsting, *Phys. Rev. A: At., Mol., Opt. Phys.* **1999**, *59*, 2369–2384.
- [18] K. Ekvall, P. van der Meulen, C. Dhollande, L.-E. Berg, S. Pommeret, R. Naskrecki, J.-C. Mialocq, *J. Appl. Phys.* **2000**, *87*, 2340–2352.
- [19] M. Lorenc, M. Ziolk, R. Naskrecki, J. Karolczak, J. Kubicki, A. Maciejewski, *Appl. Phys. B: Lasers Opt.* **2002**, *74*, 19–27.
- [20] Wolfram Research, *Mathematica Version 7.0*, (Wolfram Research, 2008).

3 Parallel Ultrafast *E-C* Ring Closure and *E-Z* Isomerisation in a Photochromic Furylfulgide Studied by Femtosecond Time-Resolved Spectroscopy

Ron Siewertsen,^a Falk Renth,^{*a} Friedrich Temps,^{*a} Frank Sönnichsen^b

^a Institut für Physikalische Chemie, Christian-Albrechts-Universität zu Kiel,
Olshausenstr. 40, D-24098 Kiel, Germany

^b Otto-Diels-Institut für Organische Chemie, Christian-Albrechts-Universität zu Kiel,
Otto-Hahn-Platz 4, D-24098 Kiel, Germany

Reproduced with permission of the PCCP Owner Societies

Phys. Chem. Chem. Phys. **2009**, *11*, 5952-5961

Copyright 2009

- **Own contributions presented in the paper:**
 - Femtosecond time-resolved transient absorption spectroscopy
 - Femtosecond time-resolved fluorescence up-conversion spectroscopy
 - Data analysis and writing of the data analysis software
 - Quantum chemical calculations
 - Static UV/VIS spectroscopic investigations

- **NMR spectroscopy:** Prof. F. D. Sönnichsen

*To whom correspondence should be addressed. E-mail: temps@phc.uni-kiel.de, renth@phc.uni-kiel.de

Abstract

The photo-induced parallel $E \rightarrow C$ ring closure and $E \rightarrow Z$ isomerisation reactions of the (E) isomer of the photochromic furylfulgide 1-[1-(2,5-dimethyl-3-furyl)-ethylidene]-3-isopropylidene succinic anhydride (**1**) in n -hexane have been studied using femtosecond time-resolved spectroscopy. Broadband transient absorption data after femtosecond laser excitation at $\lambda_{pump} = 335$ nm provide time constants of 100 fs and 250 fs that belong to the formation of the (C) and the (Z) isomers, respectively, to yield a (C) : (Z) product ratio of about 2 : 1. The results are consistent with a conformer-specific photoreaction of the (E)-isomer of **1**, where one conformer (α) undergoes predominantly $E \rightarrow C$ ring closure and the other (β) $E \rightarrow Z$ isomerisation, or alternatively with an ultrafast branching of the excited wavepacket of the α -conformer within $\Delta t < 250$ fs after the pump pulse. The observed isomerisation times suggest that the ensuing transformations proceed *via* distinctive conical intersections between the respective potential energy hypersurfaces. Oscillations of the transient absorption with frequencies of ≈ 64 and 114 cm^{-1} are found and interpreted as excited-state vibrations induced during the $E \rightarrow Z$ isomerisation reaction. Slower spectral dynamics at delay times up to ≈ 10 ps reflect the cooling of the vibrationally hot reactant and product molecules after their return to their electronic ground states. Time-dependent DFT calculations were performed to shed light on the involved reaction coordinates. The emerging picture for the dynamics of **1** obtained in this work is of interest in the broader context for our understanding of conformer-specific photochemistry and competing ultrafast reactions in polyatomic molecules.

3.1 Introduction

Photochromic molecules, which show reversible changes of their absorption spectra as a result of photo-induced chemical transformations, for example E/Z isomerisation, electrocyclic reactions, or proton transfer, are of great interest as optical switches and memory devices or light-driven molecular machines.^[1–6] Fulgides and their derivatives are particularly important in this context because their photoreactions are thermally irreversible and they can be switched back and forth purely photochemically between cyclic and open forms by light of two different colours. Applications of fulgides have been reported for, *e.g.*, molecular memories,^[5,7] photo-control of enzyme activity,^[3] photo-modulation of optical materials,^[8] photo-induced liquid crystal phase changes,^[9] photo-switching of electron and energy transfer processes,^[10,11] or fluorescence modulation.^[12]

Figure 3.1 illustrates the photochemical reactions interconverting the three thermally stable isomers of the furylfulgide **1** (Aberchrome ACR540) that is the subject in this paper. The photochromic properties of this compound rest on the UV light-induced

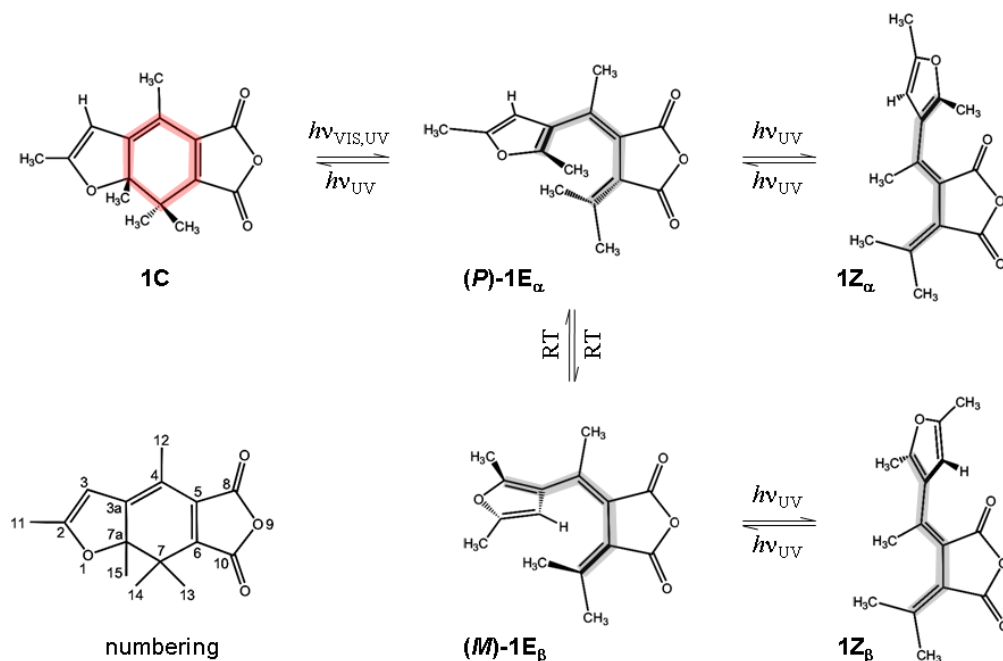


Figure 3.1: Photo-induced isomerisation reactions of the furylfulgide **1**. The atom numbering scheme has been sketched for **1C** at the bottom left.

electrocyclic $E \rightarrow C$ ring closure from the open **1E** (1-[1-(2,5-dimethyl-3-furyl)-ethylidene]-3-isopropylidene succinic anhydride) to the cyclic **1C** isomer (7,7a-dihydro-2,4,7,7a-penta-methylbenzo[b]furan-5,6-dicarboxylic anhydride) and the reverse $C \rightarrow E$ ring opening that can be initiated with visible light. A competing second photoisomerisation, which connects the (E) and (Z) isomers, is a side reaction that may hamper applications, but at the same time creates considerable fundamental interest in the ensuing detailed reaction dynamics in the electronically excited states. In its open (E) and (Z) forms, compound **1** exists in two conformers, **1E $_{\alpha}$** and **1E $_{\beta}$** resp. **1Z $_{\alpha}$** and **1Z $_{\beta}$** ,^[5,13] but as shown, only the **1E $_{\alpha}$** conformer (s -*cis* considering the involved $C^{3a}=C^{7a}$ with respect to the $C^4=C^5$ double bond) can easily undergo ring closure to **1C**, while both **1E $_{\alpha}$** and **1E $_{\beta}$** can in principle isomerise to the respective (Z) isomers **1Z $_{\alpha}$** and **1Z $_{\beta}$** . The **1E $_{\beta}$** conformer (s -*trans*) is not able to isomerise to **1C**. In addition, both conformers are helically chiral and exist as enantiomer pairs. This is indicated in Fig. 3.1 by taking the (P)-**1E $_{\alpha}$** and (M)-**1E $_{\beta}$** enantiomers as examples. The thermal enantiotopomerisation between (P)-**1E $_{\alpha}$** and (M)-**1E $_{\beta}$** is indicated as well, because it is responsible for the equilibration between both conformers in solution at room temperature.^[13] The chirality of the (C)-isomer has been left out for clarity.

As can be seen from the stationary UV/VIS absorption spectra in Fig. 3.2, the open isomers **1E** and **1Z** absorb only in the UV, with maxima of their first bands at $\lambda = 335$ and 350 nm, respectively, whereas the closed isomer **1C** shows a strong absorption in the visible between $\lambda = 400$ and 550 nm, peaking at $\lambda = 470$ nm. Since the open isomers do not absorb in that region, the (C) isomer can be switched quantitatively to the (E) form

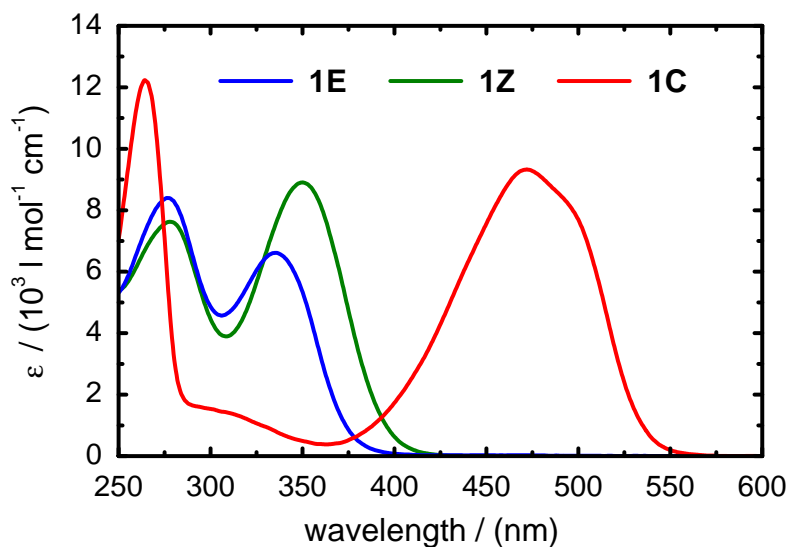


Figure 3.2: Stationary UV/VIS absorption spectra of **1C** (red), **1E** (blue) and **1Z** (green).

by irradiation around $\lambda \approx 470$ nm. The $E \rightarrow C$ conversion is accomplished using UV light, typically at $\lambda = 365$ nm, and proceeds with a quantum yield between $\phi_{EC,365} = 0.18$ and 0.20 in different solvents.^[14] However, the $E \rightarrow Z$ isomerisation of **1E** has a quantum yield that is not much lower ($\phi_{EZ,365} = 0.12 - 0.13$). This is unlike the situation encountered in, *e.g.*, the related indolyl-fulgimides, where ring closure dominates.^[15] But even in systems, where $E \rightarrow Z$ isomerisation plays only a minor role, the competition between the two reaction channels is important, since for any real application one has to consider multiple switching cycles. Thus, even low $E \rightarrow Z / E \rightarrow C$ branching ratios have strong impact on the functionality of the photoswitch. Precisely because of its comparatively high branching ratio, the furylfulgide **1** used here offers a unique opportunity to address the $E \rightarrow Z / E \rightarrow C$ branching issue and study the related molecular dynamics in some detail.

The presence of **1E_α** and **1E_β** in solution^[13] raises an interesting question, whether the branching could be due to conformer-specific photoreactions or whether the observed two product channels originate from a common **1E_α** excited state. In the latter case, the branching might either occur early, in the vicinity of the Franck-Condon (FC) region of the excited-state potential energy hypersurface, and result in two distinct excited-state reaction pathways, or could take place after an initial evolution of the excited-state wavepacket, possibly *via* a common intersection space with the lowest excited-state potential surface.^[16] Great interest arises pertaining to the possible ability to influence the branching of the excited wavepacket by coherent control techniques,^[17,18] where compound **1E** may offer substantial potential.

Time-resolved studies of the ring closure reactions of fulgides^[19,20] and the related

fulgimides^[7,21-23] reported to date have not taken the $E \rightarrow Z / E \rightarrow C$ branching into account. For the ring closure of **1E** in acetonitrile and toluene, a mechanism involving a direct pathway on a sub-ps time scale and an indirect pathway with a time constant of ≈ 16 ps have been reported.^[19] However, no evidence for the indirect pathway was found for the isomerisation in a solid PMMA matrix,^[20] and it was also absent in recent studies of the ring closure of an indolyl-fulgimide.^[22,23] In a preceding study of the $Z \rightarrow E$ isomerisation of **1Z** in our laboratory, we observed an excited-state decay after excitation at $\lambda = 387$ nm with a time constant of 220 fs, followed by cooling of vibrationally hot molecules in the electronic ground state on a time scale of 4.1 ps.^[24] In addition, oscillations of the excited state absorption corresponding to a vibrational frequency of ≈ 57 cm^{-1} were found and interpreted as vibrational coherence involving excitation of a low-frequency torsional mode during the isomerisation.

In this Article, we report on the photo-induced branching into the $E \rightarrow C$ and $E \rightarrow Z$ reaction channels of the (E) isomer of the furylfulgide **1** in n -hexane solution following absorption of UV light at $\lambda_{pump} = 335$ nm. The dynamics of the excited molecules were probed using broadband femtosecond time-resolved transient absorption spectroscopy. Additionally, a fluorescence up-conversion measurement was carried out to determine the lifetime of the optically excited state. The experimental results provide clear evidence for reaction pathways that lead to $E \rightarrow C$ ring closure and $E \rightarrow Z$ isomerisation with time constants of 0.1 and 0.25 ps with a (C) : (Z) product ratio of 2 : 1. The involved initial reaction steps were elucidated by time-dependent density functional (TDDFT) calculations to shed some light on the respective reaction pathways.

3.2 Methods

Materials

Pure **1E** was prepared from a mixture of the (E) and (Z) isomers of **1** kindly provided by Prof. E. Bartsch of the University of Freiburg. The isomeric mixture was dissolved in toluene and irradiated at $\lambda = 365$ nm, until the photostationary state with a maximal concentration of **1C** ($\approx 95\%$) was reached. The product was isolated as pure solid by recrystallisation in the dark from n -hexane/chloroform (3:1). The (C) isomer was then quantitatively converted to the (E) isomer by irradiation in n -hexane at $\lambda = 500$ nm using a small c.w. photodiode. The purity of the product was checked by thin layer chromatography and by UV/VIS spectroscopy and was found to be $> 98\%$.

The conformational properties of **1E** were studied by ^1H and ^{13}C NMR spectroscopy in CDCl_3 as solvent within a range of temperatures from 298 to 338 K. The data allowed a complete and unambiguous assignment of the NMR signals and were consistent with a fast

thermal equilibration between the $1\mathbf{E}_\alpha$ and $1\mathbf{E}_\beta$ conformers in solution even at the lowest temperature, in agreement with the literature.^[13] 2D- ^1H , ^1H -NOESY experiments provided intensity-derived distances that were also consistent with a fast enantiotopomerisation leading to a both conformers in solution. Corresponding details are given in the supporting information.

The time-resolved measurements were performed in a flow cell with 1 mm optical path length and 0.2 mm quartz windows. Solutions of $1\mathbf{E}$ at a concentration of 0.6 mM corresponding to an optical density of 0.4 were prepared using *n*-hexane (Uvasol, Merck) as solvent and pumped through the sample cell with a peristaltic pump (Ismatec). To minimize accumulation of the $1\mathbf{C}$ product, the sample reservoir was continuously irradiated at $\lambda = 500$ nm. All time-resolved measurements were done at room temperature.

Broadband femtosecond absorption spectroscopy

Our experimental setup for broadband femtosecond absorption spectroscopy based on a regeneratively amplified Ti:Sa laser system (Clark CPA2001) has been described previously.^[24] Excitation pulses of 0.3 μJ at $\lambda_{\text{pump}} = 335$ nm were obtained by frequency doubling the output of a home-built noncollinear optical parametric amplifier (NOPA). Broadband supercontinuum probe and reference pulses between $\lambda_{\text{probe}} = 350$ and 700 nm were generated in CaF_2 . The pulses were focused into the sample cell to a spot size of ≈ 150 μm with an intersection angle between pump and probe of 5° . The probe and reference beams were spectrally dispersed through an imaging spectrograph (L.O.T.-Oriel, MS260i) and detected with a 1024×127 pixel CCD camera (L.O.T.-Oriel, DB401-UV). A BG18 filter (Schott) was inserted before the spectrograph to attenuate the intense near-IR part of the supercontinuum. Time resolution was achieved by means of a computer-controlled linear translation stage in the probe path.

Independent measurements of the pump-induced cross-phase modulation (XPM) and stimulated Raman scattering (SRS) contributions were made with pure solvent. The SRS signal was used to optimise the prism compressor of the NOPA for temporal resolution and minimal residual pump chirp. The time-zero correction for the supercontinuum chirp was obtained from the XPM. XPM and SRS were subtracted from the sample signals taking into account the pump pulse absorption and the time-zero correction for each probe wavelength to derive the two-dimensional spectro-temporal absorption map and the transient spectra of the sample. For non-linear least-squares fits of the temporal absorption profiles, the observed XPM was used as input. The width of the instrument response function (IRF) estimated from the SRS was about 110 fs (FWHM) assuming Gaussian pulse shapes.

Fluorescence up-conversion measurements

The setup for fluorescence up-conversion has been described by Pancur *et al.*^[25] Excitation pulses of $\approx 0.2 \mu\text{J}$ at $\lambda_{\text{pump}} = 387 \text{ nm}$ were generated by frequency doubling part of the Ti:Sa laser output and focused into the sample cell to a spot size of $\approx 400 \mu\text{m}$. The resulting fluorescence was collected and refocused into a BBO crystal for up-conversion by type II sum frequency generation with $\approx 120 \mu\text{J}$ gate pulses at $\lambda = 775 \text{ nm}$ from the Ti:Sa laser using a pair of off-axis parabolic mirrors (Melles-Griot, $f = 119 \text{ mm}$). The up-converted light was focused onto the entrance slit of a $f = 0.1 \text{ m}$ double monochromator (Jobin-Yvon HR 10) and detected with a photomultiplier (Hamamatsu R1527P) connected through a preamplifier (Stanford Research SR 445) to a gated photon counter (Stanford Research SR 400). Suitable glass filters were inserted into the optical path to remove scattered pump photons and light from unwanted nonlinear optical processes. Temporal fluorescence profiles were recorded using a delay line in the gate beam path. Cross correlation of the pump and gate pulses indicated an IRF with 220 fs FWHM.

Computational methods

Quantum chemical calculations were carried out using the TURBOMOLE package.^[26] Structures and vibrational frequencies in the electronic ground states and vertical excitation energies to the excited electronic states were calculated using density functional theory (DFT) resp. time-dependent density functional theory (TDDFT) at the B3LYP/def2-SVP and B3LYP/def2-TZVP levels of theory. The calculations also provided an estimate for the energy difference between the α and β conformers of **1E**. The reaction pathways in the excited states were explored by TDDFT calculations at the B3LYP/def2-SVP level and checked at selected points with the def2-TZVP basis set. Excited-state vibrational frequencies were obtained where applicable with the B3LYP/def2-SVP method. The computed excited-state reaction pathways were additionally compared at several points to second-order approximate coupled-cluster (CC2/def2-SVP) calculations.^[27] Since the three excited-state calculations gave very similar results in all cases, the use of the B3LYP/def2-SVP method seems justified, and only the results obtained with this will be described in this paper in the following.

3.3 Results

Spectro-temporal absorption map and transient spectra

Figure 3.3 shows the observed spectro-temporal evolution of the transient absorption following excitation of **1E** at $\lambda_{\text{pump}} = 335 \text{ nm}$ for probe wavelengths in the range $350 \text{ nm} \leq \lambda_{\text{probe}} \leq 600 \text{ nm}$. The three panels display the two-dimensional map of the change in

optical density, $\Delta OD(\lambda, t)$, for delay times between $-0.2 \text{ ps} \leq \Delta t \leq 3 \text{ ps}$ (Fig. 3.3a), the transient spectra at selected delay times (Fig. 3.3b), and the spectrum in the stationary final state reached at long delay times ($\Delta t = 20 \text{ ps}$; Fig. 3.3c). The wide probe wavelength range allows us to directly follow the photochemical depletion of the (E) isomer of **1** and the formation of both the (C) and (Z) isomers. As can be seen, the strongest changes occur within the first 0.5 ps.

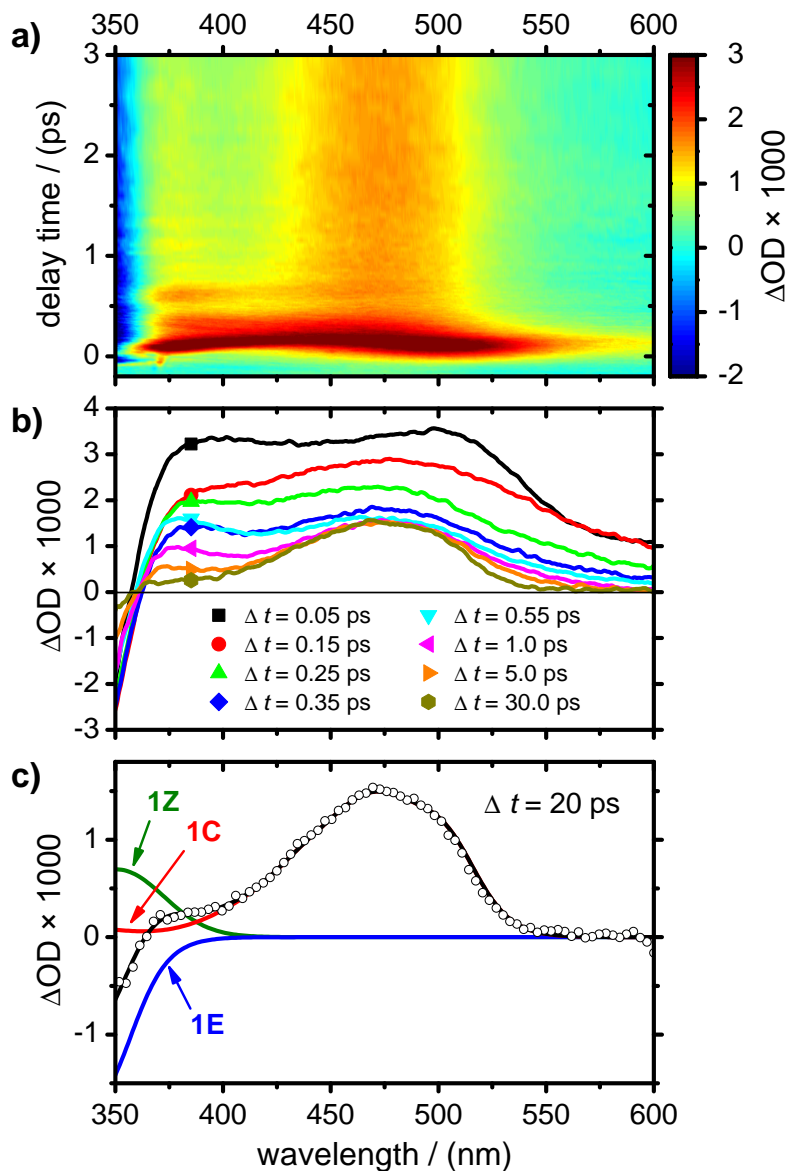


Figure 3.3: a) Two-dimensional plot of the change in optical density (ΔOD) following excitation of **1E** at $\lambda_{pump} = 335 \text{ nm}$ for probe wavelengths in the range $350 \text{ nm} \leq \lambda_{probe} \leq 600 \text{ nm}$ and delay times between $-0.2 \text{ ps} \leq \Delta t \leq 3.0 \text{ ps}$. b) Transient spectra at delay times from $\Delta t = 0.05 \text{ ps}$ up to $\Delta t = 30 \text{ ps}$. c) Spectrum at $\Delta t = 20 \text{ ps}$ (open circles) and its fit by a weighted sum of the static UV/VIS absorption spectra of the (E), (C) and (Z) isomers.

At probe wavelengths of $\lambda_{probe} \leq 365$ nm, a pronounced negative transient absorption occurs virtually instantaneously after excitation and decays rapidly on a sub-picosecond time scale to a practically constant final signal level at $\Delta t \gtrsim 10$ ps. The negative amplitude and immediate appearance suggest that it is mainly caused by the ground state bleach (GSB) of the (*E*) isomer and a contribution from stimulated emission (SE) from the excited state, with an overlapping positive spectral component from product absorptions (PA) due to formation of **1Z** and **1C**. The observed final negative amplitude at $\lambda_{probe} = 365$ nm at long times (Figs. 3.3b and 3.3c) is the net effect of the conversion of **1E** into **1Z** and **1C**. At $\lambda_{probe} = 365$ nm, PA arises mostly from the (*Z*) isomer, the contribution from the (*C*) isomer is minimal (Fig. 3.2).

In contrast, the transient signal at wavelengths of $\lambda_{probe} > 365$ nm is always positive. A fast rise of two very broad and overlapping absorption bands with maxima at $\lambda_{probe} \approx 390$ and ≈ 500 nm is visible. Taking into account their immediate rise, positive amplitudes, and subsequent decays, both bands are assigned to excited-state absorptions (ESA). The 500 nm band appears to decay faster than the 390 nm band. In addition, there is an apparent blue-shift of its maximum from $\lambda \approx 500$ to ≈ 470 nm during the first ≈ 300 fs. The broad absorption with a maximum at $\lambda_{probe} \approx 470$ nm remaining at long times belongs to the (*C*) product, which clearly appears in $\Delta t < 250$ fs. Furthermore, the ESA at $\lambda_{probe} \geq 450$ nm decays within only ≈ 250 fs (see the spectra at $\Delta t = 50$ and 250 fs in Fig. 3.3b). This observation underlines the extraordinarily fast deactivation of the excited electronic state(s) especially for the 500 nm ESA band.

Distinct additional features in the transient absorption at $\lambda_{probe} < 450$ nm and $\Delta t < 1$ ps are superimposed damped oscillations that have their largest amplitudes at short probe wavelengths. The oscillations are rapidly damped on a time scale similar to that of the decay of the ESA. This suggests that they reflect molecular dynamics in the excited state.

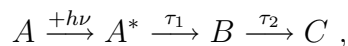
At delay times of $\Delta t > 0.5$ ps, the transient spectra are already fairly similar to the final spectrum reached at $\Delta t \gtrsim 10$ ps. The still observable comparatively slow spectrotemporal changes reflect the vibrational deactivation of the reactant and different product molecules that have returned from the excited to their ground electronic states. Hot ground state absorption (HGSA) from vibrationally excited (*E*) molecules contributes at shorter probe wavelengths ($\lambda_{probe} < 450$ nm). Taking the $E \rightarrow C$ and $E \rightarrow Z$ isomerisation quantum yields of Uhlmann *et al.*^[14], $\approx 69\%$ of the initially excited (*E*) molecules return to their ground state. Likewise, hot product absorptions (HPA) stem from vibrationally excited (*Z*) product molecules ($\approx 12\%$) at short ($\lambda_{probe} < 450$ nm) and mostly from vibrationally excited (*C*) product molecules ($\approx 19\%$) at longer wavelengths ($\lambda_{probe} > 450$ nm). The pronounced absorption band of the ring closure product **1C** with maximum at $\lambda_{probe} \approx 470$ nm becomes slightly narrower on a time scale of several picoseconds due

to the vibrational cooling (at earlier times this band spectrally overlaps with ESA). The negative band due to GSB at $\lambda_{probe} < 365$ nm is filled in by HGSA from (E) molecules and by HPA of (Z) molecules. The evident presence of HGSA/HPA already at $\Delta t \lesssim 0.5$ ps at $\lambda_{probe} < 450$ nm and of HPA at $\Delta t \lesssim 0.25$ ps at $\lambda_{probe} > 450$ nm confirms the ultrafast electronic deactivation time scale deduced from the ESA decay. The decay of the HGSA and HPA and corresponding rise of the PA bands on the time scale of several picoseconds can be attributed entirely to vibrational cooling.

At delay times of $\Delta t > 10$ ps, vibrational cooling is essentially over, and spectral changes thereafter are almost negligible. Thus, taking the steady-state UV/VIS absorption spectra of the three isomers, the final spectrum ($\Delta t = 20$ ps, Fig. 3.3c) can be described by a weighted sum of the bleach of **1E** (negative signal near $\lambda_{probe} = 350$ nm) and the absorptions of the products **1Z** (positive contribution also around 350 nm) and **1C** (broad positive band around 470 nm). The weighting factors determined by a least-squares fit give a **1C**:**1Z** product ratio of $\approx 2 : 1$, in excellent agreement with the isomerisation quantum yields of Uhlmann *et al.*^[14] This, and the overall spectral evolution prove unambiguously that the $E \rightarrow C$ and the $E \rightarrow Z$ isomerisation reactions occur in parallel and on a sub-picosecond time scale.

Time profiles at selected probe wavelengths

Figure 3.4 shows the absorption *vs.* time profiles together with the results of nonlinear least-squares fits at four selected probe wavelengths, $\lambda_{probe} = 355, 390, 500,$ and 560 nm, that are representative for the respective spectral regions. As can be seen, the observed absorptions are complex temporal functions with fast and slow rise and decay components, constant offsets at long times, and additional damped oscillations at $\lambda_{probe} = 355$ and 390 nm. The different shapes arise from the superimposed changing contributions of GSB (at $\lambda_{probe} = 355$ nm only, grey dotted line), and ESA/SE, HGSA/HPA, and PA (red, green and blue dotted lines, respectively), which depend on λ_{probe} and vary with time Δt . The data were interpreted assuming a scheme of consecutive reactions of the type



where A^* denotes the excited-state molecules responsible for the transient ESA/SE signals, B the vibrationally hot electronic ground state molecules giving rise to transient HGSA/HPA signals, and C the reaction products leading to final PA signals (**1C**, **1Z**, and **1E** returned to the ground state). The time constant τ_1 belongs to the decay of ESA/SE and the rise of HGSA/HPA by the photoisomerisation and electronic deactivation steps, τ_2 describes the decay of HGSA/HPA and the rise of PA by the subsequent vibrational

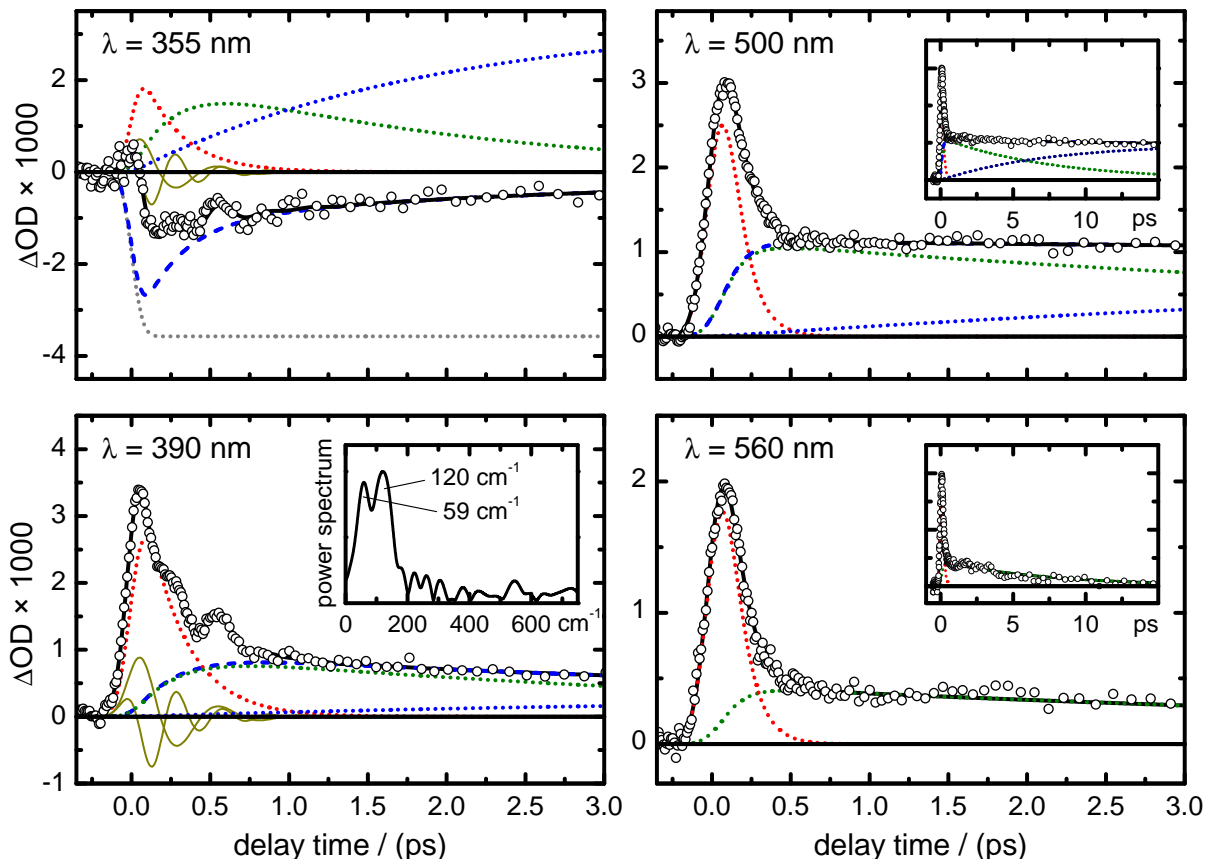


Figure 3.4: Time profiles of the transient absorption signals after excitation of **1E** at $\lambda_{pump} = 335$ nm for probe wavelengths of $\lambda_{probe} = 355, 390, 500,$ and 560 nm. The open circles are the data points, the solid black lines are the non-linear least-squares fits. The different contributions to the transient absorption signals are indicated by dotted lines (see text), the oscillating components by thin solid lines. The inset at $\lambda_{probe} = 390$ nm shows the Fourier power spectrum of the oscillating parts obtained after subtraction of a fitted simple biexponential decay curve from the data points. The insets at $\lambda_{probe} = 500$ and 560 nm show the transient absorptions on a longer time scale.

cooling of hot ground state molecules. As mentioned above, the contributions to the transient absorptions from the different processes depend on λ_{probe} .

The absorption time profile at $\lambda_{probe} = 390$ nm in Fig. 3.4 consists of two main components, a fast rise due to ESA, which decays in < 500 fs, and a longer-lived signal mainly due to HGSA of **1E** molecules returning to their ground state. The final PA signal at long times remains small, since none of the three different molecules absorbs strongly at $\lambda_{probe} = 390$ nm (see Fig. 3.2). A least-squares fit using the above scheme with two superimposed oscillations (thin solid lines) of the ESA with damping time τ_1 yielded time constants of $\tau_1 = 0.25(6)$ ps and $\tau_2 = 4.0(8)$ ps (2σ error limits in parentheses). The oscillating components were fitted with frequencies of $\nu_1 = 64(7)$ and $\nu_2 = 114(6)$ cm^{-1} , in good agreement with the values obtained by a direct Fourier transform of the oscillating part of the transient absorption (see Fourier power spectrum in the inset of Fig. 3.4).

The transient absorption signal at $\lambda_{probe} = 355$ nm was fitted with the same τ_1 time constant and same oscillation frequencies as for $\lambda_{probe} = 390$ nm, although the time profile appears quite different at first glance. However, the negative amplitude found at $\lambda_{probe} = 355$ nm is mostly just the consequence of the photochemical consumption of **1E**. The corresponding GSB leads to the sizable negative signal, but ESA/SE and HGSA/HPA and PA (mostly by **1Z**, as shown in Figs. 3.3b and 3.3c) play roles as well. The overlapping spectrally broad ESA and the spectrally narrower GSB and SE signals at $\lambda_{probe} = 355$ nm all reflect excited state population, but could be untangled at least partially. As already stated, the initial ($\Delta t = 0$) GSB amplitude was derived from the final PA signals and the known quantum yields. The slowly rising contributions from the final products were inferred by comparison of the PA spectrum at $\Delta t \geq 20$ ps with the steady-state UV/VIS spectra of the three isomers (the net signal from GSB, HGSA/HPA, and PA is shown as dashed blue line). The ESA appears to be reduced in amplitude at this probe wavelength by spectrally and temporally coincident SE. The time constant describing the vibrational cooling could not be well determined at this probe wavelength because of the small change of the net signal at $\Delta t \geq 1$ ps.

At the selected two long probe wavelengths, $\lambda_{probe} = 500$ and 560 nm, a fit to the temporal profiles yielded an ESA decay time constant of $\tau'_1 = 0.10(1)$ ps. This value is, surprisingly, significantly shorter than the time constant of $\tau_1 = 0.25(6)$ ps found at the probe wavelengths in the UV ($\lambda_{probe} = 390$ and 355 nm). Being close to our experimental time resolution, τ'_1 has a larger uncertainty, but the difference compared to τ_1 is significant. Additionally, a time-resolved up-conversion measurement performed at $\lambda_{probe} = 525$ nm following excitation at $\lambda_{pump} = 387$ nm showed an ultrafast fluorescence decay with a time constant of $\tau_{fl} \approx 0.08(2)$ ps, almost identical with τ'_1 within the error limits. For this reason, the value of τ'_1 can be assigned to the lifetime of the optically bright excited state of **1E** that is reached by the pump pulse. Furthermore, however, the very fast rise of the HPA from the ring closure product **1C** indicates that the $E \rightarrow C$ isomerisation occurs on the same time scale. By inference, the second, slightly longer ($\tau_1 \approx 0.25$ ps) sub-picosecond time constant is related to the $E \rightarrow Z$ isomerisation. The slightly larger value of τ_1 compared to τ_{fl} suggests that a non-emissive intermediate state might be involved in the photoinduced dynamics. In the red wing of the absorption band ($\lambda_{probe} = 560$ nm), vibrational cooling leads to a slow decay ($\tau_2 \approx 7.5$ ps) accompanied by a spectral shift towards the band center. No slow decay component can be discerned closer to the maximum of the **1C** absorption band ($\lambda_{probe} = 500$ nm), where the stable final product is detected.

3.4 Discussion

The transient spectro-temporal absorption maps of the furylfulgide **1** recorded in the present work demonstrate that, while a large fraction of the investigated photo-excited (E) isomer returns to its ground state by efficient electronic relaxation, the ensuing reactions of the excited molecules lead to the (C) and to the (Z) isomer with a 2 : 1 product ratio in parallel. The immediate conclusions regarding the dynamics of these two reactions that we can draw from the experimental data are the following: (*i*) The ultrafast decays of the ESA signals and rise times of the HPA signals show that the $E \rightarrow C$ ring closure and $E \rightarrow Z$ isomerisation reactions take place within only 0.10 – 0.25 ps. (*ii*) The refilling of the GSB signal reflects the radiationless electronic deactivation of the photo-excited (E) molecules. (*iii*) The known $E \rightarrow C$ ring closure and $E \rightarrow Z$ isomerisation quantum yields^[14] can be verified and rationalised by the observed femto- and picosecond dynamics. (*iv*) The ultrafast time scales suggest that the excited-state transformation pathways are barrierless or have only negligible energy barriers. Considering evidence from other E/Z isomerisations and pericyclic reactions,^[28–30] it is reasonable to assume that one or more conical intersections (CIs) are involved.

The observed photochemical dynamics of **1E** can be compared with the excited-state lifetimes of 0.06 – 0.4 ps of a related (E)-fulgimide, for which only the ring closure reaction has been supposed.^[22] Interestingly, however, our data show two ESA decay times, $\tau_1 \approx 0.25$ ps at UV probe wavelengths ($\lambda_{probe} < 400$ nm) and $\tau'_1 \approx 0.10$ ps at visible probe wavelengths ($\lambda_{probe} \geq 500$ nm). The latter value is virtually identical within the error limits with the observed fluorescence lifetime ($\tau_{fl} \approx 0.085$ ps), which gives the lifetime of the optically bright FC excited state. Our experimental data evidently show different rise times of the HPA signals of the (C) and (Z) isomers (≈ 0.1 and ≈ 0.25 ps, see Fig. 3.4), indicating that the $E \rightarrow C$ isomerisation seems to be faster than the $E \rightarrow Z$ isomerisation. Feasible explanations for this striking experimental observation could be given either by (1) the aforementioned conformer-specific photoreactivities of **1E $_{\alpha}$** and **1E $_{\beta}$** or (2) a reaction pathway originating in the FC region of **1E $_{\alpha}$** that subsequently branches into the two product channels.

Considering first the conformer-specific mechanism, our ^1H and ^{13}C NMR data for **1E** are consistent with a fast thermal equilibration in the electronic ground state between the α and β conformers.^[13] Accordingly, the two observed sub-picosecond time constants τ_1 and τ'_1 might therefore be interpreted in favour of two entirely separate excited-state reaction pathways, one leading from photoexcited **1E $_{\alpha}$** to the (C)-isomer, the other leading from **1E $_{\beta}$** to the (Z)-isomer. A similar case of conformer-specific photoisomerisation has been observed for, e.g., *cis*-1-(2-naphthyl)-2-phenylethene as well as in the photochemistry of previtamin D.^[31,32] It requires a non-equilibration of the rotamers in the excited states (the

so-called NEER-principle),^[33] which is fully reasonable given the short isomerisation time scales. Experimental confirmation for such a possible conformer-specific photoreactivity of **1E** might be achieved by a systematic variation of the excitation energies to selectively excite one of the conformers, provided that their absorption spectra differ. Such experiments were, however, not attempted in this work in view of the broad spectral widths of our fs excitation pulses, which would wash out distinctive features within a 10 nm wavelength range. At present, it can only be speculated whether the absorption spectra of both conformers of **1E** differ enough for a successful selective excitation. A more promising alternative strategy that might prove successful in future work would involve studies of chemically modified furylfulgides with sterically demanding substituents, which could block the thermal equilibration between the conformers. In addition, a temperature dependent investigation could help as well.

Regarding the second explanation (branching from the photoexcited state), only the **1E***_α conformer appears to be a sensible common starting structure for the photoisomerisation of **1E** to **1C** and **1Z** (leaving aside the very remote possibility of a reaction of photoexcited **1E**_β to **1C**, *cf.* Fig. 3.1). Assuming this mechanism to be valid, the parallel formation of both products should therefore be discussed in context with, *e.g.*, the ring closure of the related (*E*)-fulgimide,^[22] the prototypical hexatriene/cyclohexadiene (HT/CHD) reaction system,^[34–36] and the $E \rightarrow Z$ photoisomerisation of polyenes.^[37,38] These reaction scenarios each involve a single excited-state as starting point, so that the two reaction products would have to arise by a branching of the reaction pathway on the excited-state PES. In the HT/CHD case, and similarly for the $E \rightarrow Z$ photoisomerisation of polyenes, the photo-excited state is assumed to be the $1B_2$ state, from which the excited wavepacket first crosses to the $2A_1$ state *via* a conical intersection CI_1 , before it reaches a second intersection CI_2 with the ground state ($1A_1$).^[34–38] The $2A_1$ state would be optically dark in emission, but may appear in a transient absorption experiment at UV probe wavelengths. A similar scheme seems conceivable also for **1E**_α. Starting with the photoexcited **1E**_α conformer in its FC region in that case, the two time constants could be due to an internal conversion to an intermediate state within ≈ 0.1 ps and subsequent further transformations to the electronic ground state(s) from there. Assuming that the excited wavepacket crosses rapidly (in < 100 fs) to an intermediate state (such as $2A_1$ by analogy with HT/CHD), it could then transform to the (*C*) and (*Z*) products *via* two different CIs to the two ground states. This case of a “late” branching of the wavepacket prepared by the fs UV excitation pulses would imply that the CI for the $E \rightarrow C$ reaction is reached faster (almost instantaneously after population of the intermediate state from the optically excited state) than the CI for the $E \rightarrow Z$ reaction, which would be reached after ≈ 0.25 ps after the pump pulse to rationalize the experimental data. Alternatively, on the other hand, the

different isomerisation times could also be due to an “early” branching of the photo-excited wavepacket, which might then follow different reaction pathways than in the HT/CHD case. This case might show up experimentally as a biphasic behaviour of the fluorescence and/or ESA decays on time scales below 100 fs. Unfortunately, such fast processes are beyond our current experimental time resolution.

We note furthermore in this context that the electrocyclic ring opening of CHD to HT is known to take place on a sub-100 fs time scale in the gas phase,^[36] and it strikes us that, as our data show, the ring closure of the much larger furylfulgide **1E** in solution occurs in almost the same time, despite the friction owing to the viscosity of the solvent. Moreover, it should be noted that a case of a competing ultrafast *cis-trans* isomerisation and ring closure has been reported for cyclohepta-1,3-diene and cycloocta-1,3-diene^[16] (CHD cannot undergo $E \rightarrow Z$ isomerisation due to ring strain). Finally, our data do not provide evidence for an additional slow (16 ps) indirect $E \rightarrow C$ isomerisation pathway, as has been proposed in a previous study of photoexcited **1E** in acetonitrile and toluene.^[19]

A second striking feature in the measured temporal absorption profiles in the UV region ($\lambda_{probe} < 450$ nm) are the apparent oscillations, which correspond to vibrational frequencies of ≈ 64 and 114 cm^{-1} and decay on the same time scale as the observed ESA with $\tau \approx 0.25$ ps. A similar oscillatory behaviour has not been seen in the case of the (*E*)-fulgimide,^[22] but there are a few other examples in the literature, such as the $E \rightarrow Z$ photoisomerisations of stilbene^[39] or retinal^[40] and the excited-state dynamics of azulene,^[41] where the oscillations have been interpreted as vibrational coherences. B3LYP/def2-TZVP calculations on the electronic ground state of **1E_α** indeed gave low-frequency modes of 68 and 130 cm^{-1} , corresponding to torsional motions of the furyl ring and the isopropylidene group, respectively, and similar vibrations are probable in the excited state as well. The same reasoning applies of course also to **1E_β**, which is not discussed explicitly here. Thus, it is likely that the modulation of the transient absorption in our case is caused by oscillations of the vibrational wavepacket following its projection at time $\Delta t = 0$ to the FC region of the excited-state potential surface(s) (PES) by the ultrashort pump pulse. An excitation of low-frequency modes can be caused, in principle, by a shallow potential energy minimum in the vicinity of the FC region, by a gradient in the FC region of the excited-state PES along a coordinate perpendicular to the reaction coordinate, or by a sudden change of the direction of the reaction coordinate, probably after the crossing of the wavepacket from the $1B_2$ to the $2A_1$ state.

In order to gain further insight into the ensuing dynamics, we attempted to follow the evolution of the prepared wavepacket after its projection by the pump pulse from the ground to the excited state by B3LYP/def2-SVP TDDFT calculations for both conformers. Figure 3.5a summarizes the most interesting results for **1E_α** (the chirality is dropped

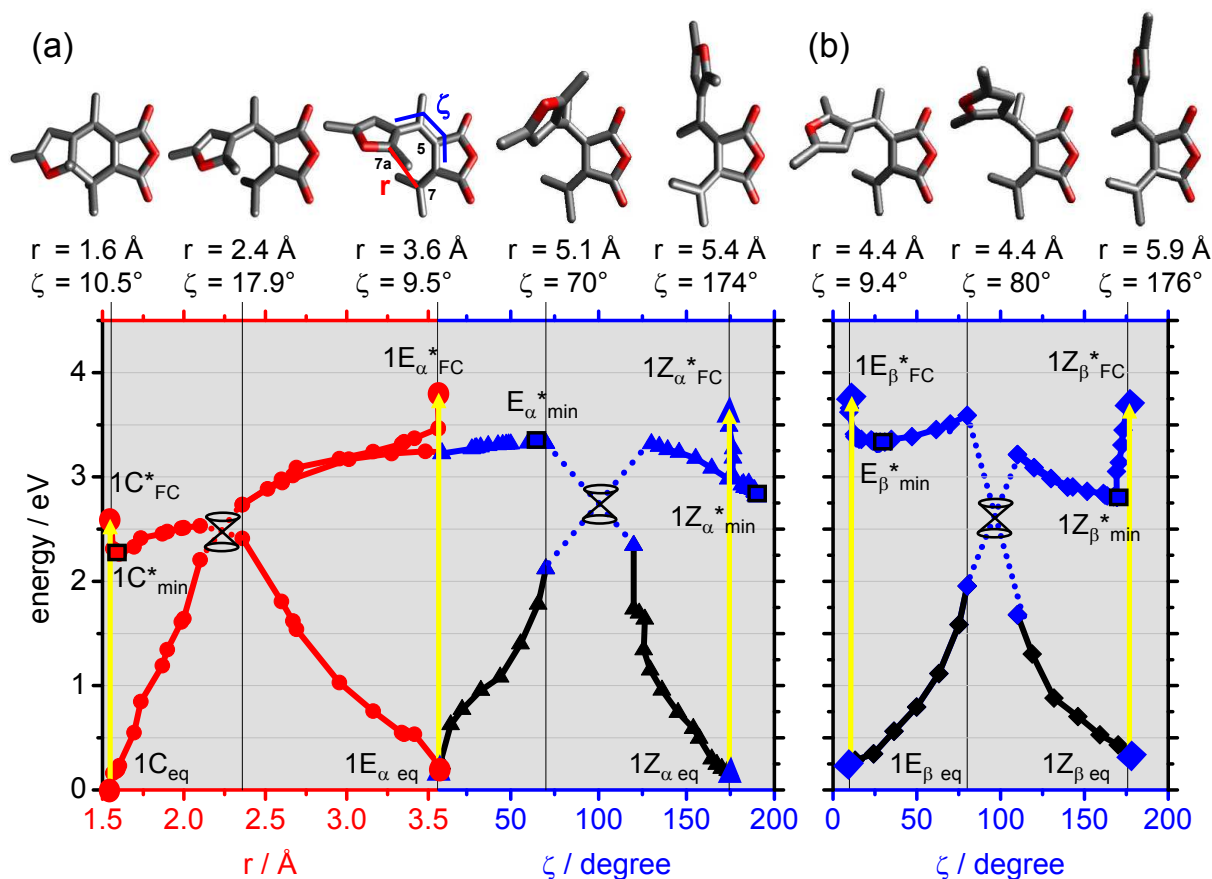


Figure 3.5: a) Summary of the results of the B3LYP/def2-SVP TDDFT calculations for the $1E_\alpha$ conformer. Center: Calculated ground equilibrium structure $1E_{\alpha,\text{eq}}$ and energy of the excited FC state $1E_{\alpha,\text{FC}}^*$. Left half: Evolution of the calculated ground and excited states in the $E \rightarrow C$ isomerisation as function of the distance r between the two C atoms connected by the ring closure (red circles). Right half: Calculated energies and structures relating to the $E \rightarrow Z$ isomerisation as function of the dihedral angle ζ describing the torsion around the double bond (blue and black triangles). b) Results for the $E \rightarrow Z$ isomerisation of the $1E_\beta$ conformer as a function of ζ (blue and black diamonds). The calculated ground state equilibrium structure $1E_{\beta,\text{eq}}$ and the energy of the excited FC state $1E_{\beta,\text{FC}}^*$ are shown on the left axis. Here, the calculated excited-state reaction pathway does not seem to lead straightforward to a simple two-state CI for interconversion of the (E) and (Z) isomers (see text). All converged energy minima in the excited state are indicated by black squares, all energies are relative to $1C_{\text{eq}}$. The black symbols indicate energies and structures from ground state optimisations.

for the remainder of this discussion when it is not relevant; Tables with the calculated structures are given in the supporting information. Starting with the ground state in its calculated equilibrium structure $1E_{\alpha,\text{eq}}$ and the resulting vertically excited FC state $1E_{\alpha,\text{FC}}^*$ at the center, the calculated evolution of the two states from the (E) towards the (C) isomer is displayed on the left, and from the (E) towards the (Z) isomer on the right. The respective abscissas are the distance r between the atoms C_7 and C_{7a} , which form the single bond in the $E \rightarrow C$ ring closure reaction, and the $C_{3a}-C_6$ dihedral angle ζ , which measures the torsion around the C_4-C_5 double bond during the $E \rightarrow Z$ isomerisation (see

illustration of $\mathbf{1E}_{\alpha,\text{eq}}$ at the top of Fig. 3.5). The red circles and blue triangles represent the energies and structures obtained in the course of geometry optimisations of the excited states starting at different points as described below, the black triangles represent energies and structures obtained from ground state optimisations. Structures corresponding to converged energy minima (zero imaginary vibrational frequencies) in the excited state are indicated by squares. The computed (B3LYP/def2-SVP) vertical excitation energies shown by the yellow arrows of 3.6 eV ($\mathbf{1E}_{\alpha}$), 2.6 eV ($\mathbf{1C}$), and 3.4 eV ($\mathbf{1Z}_{\alpha}$) are in good agreement with the observed longest-wavelength UV/VIS absorption bands. As noted, checks by B3LYP/def2-TZVP and CC2/def2-SVP calculations gave essentially identical results. Considering first the $E \rightarrow C$ ring closure, starting at $\mathbf{1E}_{\alpha,\text{FC}}^*$, the computed optimised pathway follows a steep decrease in energy with a simultaneous decrease of r to about 2.4 Å, which is roughly halfway to the $\mathbf{1C}_{\text{eq}}$ structure. At the same time, the ground state energy increases rapidly. At $r = 2.4$ Å, the TDDFT geometry optimisation stopped to converge, as is typical with this method near a CI. We therefore extrapolated beyond the anticipated CI to a structure with $r = 2.1$ Å, which we first optimised along all other coordinates keeping r fixed, and then allowed it to optimise freely. The resulting structure converged rapidly from $r = 2.1$ Å to an excited-state minimum $\mathbf{1C}_{\text{min}}^*$ with $r = 1.6$ Å. Conversely, the optimised pathway originating at the excited-state structure $\mathbf{1C}_{\text{FC}}^*$, corresponding to a vertical excitation of the $\mathbf{1C}_{\text{eq}}$ isomer, also leads to $\mathbf{1C}_{\text{min}}^*$, which differs only very slightly from $\mathbf{1C}_{\text{eq}}$. These findings provide strong evidence for a direct, barrierless reaction pathway for the $E \rightarrow C$ ring closure through a CI located at $r \approx 2.3$ Å starting from $\mathbf{1E}_{\alpha}$, explaining the observed ultrafast reaction rate. Since the CI is lower in energy than $\mathbf{1C}_{\text{FC}}^*$, it may also be involved in the ultrafast photo-induced $C \rightarrow E$ ring opening reaction.

The elucidation of a possible $E \rightarrow Z$ isomerisation pathway of $\mathbf{1E}_{\alpha,\text{FC}}^*$ proved more difficult. For a first picture, we performed constrained excited-state geometry optimisations at specific fixed torsional angles ζ . The resulting structures were then taken as new starting points for subsequent free geometry optimisations. In these calculations, all structures with values of ζ up to 50° rapidly approached the $E \rightarrow C$ reaction pathway just described above. Increasing ζ to 60° resulted in convergence to a shallow excited-state minimum at $\zeta = 65^\circ$, denoted $\mathbf{1E}_{\alpha,\text{min}}^*$ in Fig. 3.5. The same minimum was also reached starting from the other side at $\zeta \leq 80^\circ$. The existence of this shallow potential energy well has to be treated with caution, but it would provide a rationalization for the slower $E \rightarrow Z$ reaction rate compared to the $E \rightarrow C$ reaction and it could be easily responsible for the observed low-frequency oscillations in the transient absorption profiles. A frequency calculation for $\mathbf{1E}_{\alpha,\text{min}}^*$ did indeed show a low-frequency mode with $\tilde{\nu} = 50 \text{ cm}^{-1}$ involving a torsion around ζ as well as other low-frequency torsional modes involving, *e.g.*, the isopropyl group.

As expected, restricted TDDFT geometry optimisations started with values of ζ fixed in the vicinity of the anticipated CI at $\approx 90^\circ$ ($80^\circ < \zeta < 120^\circ$) failed to converge. Continuing further with $\zeta > 120^\circ$, however, all excited-state optimisations proceeded straight into the excited-state energy minimum $\mathbf{1Z}_{\alpha,\text{min}}^*$. An optimisation of the respective ground state structure with the same initial structure ($\zeta = 120^\circ$) converged to the ground state equilibrium structure and energy of $\mathbf{1Z}_{\alpha,\text{eq}}$ (black symbols). Thus, the localisation of a CI between the ground and excited-state PES along the $E \rightarrow Z$ isomerisation coordinate at the torsional angle $\zeta \approx 90^\circ$ appears highly likely, but it is not as clearly visible in Fig. 3.5a as it is in the case of the $E \rightarrow C$ ring closure. Because the pathway on the (E) side of the CI is energetically below $\mathbf{1E}_{\alpha,\text{FC}}^*$, it seems that the CI can be reached from $\mathbf{1E}_{\alpha,\text{FC}}^*$ via only a small energy barrier. This could provide a photochemical funnel for the ultrafast $E \rightarrow Z$ isomerisation of $\mathbf{1E}_\alpha$. The torsional pathway seems plausible considering the discussions of other photo-induced isomerisations around CC double bonds found in the literature.^[29,42,43]

An excited-state optimisation starting at the vertically excited FC state $\mathbf{1Z}_{\alpha,\text{FC}}^*$ converged into the excited-state minimum $\mathbf{1Z}_{\alpha,\text{min}}^*$ located ≈ 0.8 eV below $\mathbf{1Z}_{\alpha,\text{FC}}^*$. The photoisomerisation in the $Z \rightarrow E$ direction, which we have earlier shown to take place with a time constant of 220 fs,^[24] therefore either seems to have to run over a small potential energy barrier or proceeds along some entirely different route.

Figure 3.5b shows the results for the $\mathbf{1E}_\beta$ conformer with the calculated ground state equilibrium structure $\mathbf{1E}_{\beta,\text{eq}}$ and the resulting vertically excited FC state $\mathbf{1E}_{\beta,\text{FC}}^*$ on the left, using the dihedral angle ζ as abscissa. The calculated energy of $\mathbf{1E}_{\beta,\text{eq}}$ is slightly higher ($\Delta E = 0.03$ eV) compared to $\mathbf{1E}_{\alpha,\text{eq}}$. Assuming equal entropies, the latter would therefore be expected to be the dominant conformer ($\approx 70\%$) in thermal equilibrium at room temperature. The computed vertical excitation energies of 3.5 eV ($\mathbf{1E}_\beta$) and 3.4 eV ($\mathbf{1Z}_\beta$) are virtually identical with those of the respective α -conformers, suggesting fairly similar properties of the corresponding UV/VIS absorption bands which would make a selective experimental excitation of just one conformer under room temperature conditions difficult if not impossible.

The $E \rightarrow Z$ geometry optimisation pathway starting at $\mathbf{1E}_{\beta,\text{FC}}^*$ leads to a local excited-state energy minimum $\mathbf{1E}_{\beta,\text{min}}^*$ at $\zeta = 26^\circ$ that is 0.4 eV lower in energy than $\mathbf{1E}_{\beta,\text{FC}}^*$. The constrained TDDFT geometry optimisations at fixed larger angles of ζ failed to converge between $80^\circ < \zeta < 110^\circ$. All TDDFT optimisations with $\zeta \geq 110^\circ$ led to the excited-state minimum $\mathbf{1Z}_{\beta,\text{min}}^*$ which was also the final point of the optimisation pathway starting at the vertically excited $\mathbf{1Z}_{\beta,\text{FC}}^*$ conformer (right side in Fig. 3.5b). The ground state pathways starting with the structures obtained at $\zeta = 80^\circ$ and $\zeta = 110^\circ$ led to the respective ground state equilibrium structures and energies (black symbols).

The excited and ground state pathways suggest that for both isomerisation directions, conical intersections lower in energy than the initially excited FC states are involved in the electronic deactivation, but the pathways might not be barrierless. This would explain the observed ultrafast, but compared to the $E \rightarrow C$ reaction slightly slower time scales of the $E \rightarrow Z$ isomerisation and our previous experimental results on the $Z \rightarrow E$ isomerisation.^[24] However, barrierless reaction pathways *via* an indirect route involving, *e.g.*, an optically dark intermediate state cannot be ruled out. Indeed, the look of the calculated pathways in Fig. 3.5b, which do not seem to lead straightforwardly to a CI that connects the two PES, qualitatively speaks for a more complex dynamics involving perhaps a third electronic state. Otherwise, the calculations for the β -conformers resemble those for the α -conformers except for low ζ angles, where the pathways for the $\mathbf{1E}_\alpha^*$ starting structures lead to the CI located on the $E \rightarrow C$ reaction coordinate. Whether this can be interpreted in favour of a conformer-specific photochemistry is debatable. As already stated above, the excited-state minima could be responsible for the observed low-frequency oscillations in the transient absorption profiles, and a torsional pathway is plausible in light of the discussion of photo-induced $E \rightarrow Z$ isomerisations in the literature.^[29,42,43]

While higher level *ab initio* calculations at, *e.g.*, the CASSCF and CASPT2 levels are awaited, the results of the presented TDDFT calculations for α - and β -conformers appear to rationalize the sub-picosecond $E \rightarrow C$ and $E \rightarrow Z$ isomerisations by the existence of CIs along the r and ζ coordinates, respectively, and by conformer-specific reaction channels. The apparently steeper energy gradient on the $E \rightarrow C$ pathway of $\mathbf{1E}_\alpha$ compared to the $E \rightarrow Z$ channels suggests that the (*C*) isomer should be formed faster. This is in accordance with the observed shorter HPA rise time for the (*C*) compared to the (*Z*) isomer. The excited-state potential energy minima $\mathbf{1E}_{\alpha,\min}^*$ and $\mathbf{1E}_{\beta,\min}^*$ may be responsible for the excitation of low-frequency vibrational modes during the $E \rightarrow Z$ isomerisation and thereby for the observed oscillations of the transient absorption.

3.5 Conclusions

In conclusion, we have investigated the photo-induced isomerisation of the (*E*) isomer of the furylfulgide **1** in *n*-hexane following excitation at $\lambda_{pump} = 335$ nm using broadband femtosecond transient absorption spectroscopy. Two time constants, $\tau_1' = 0.1$ and $\tau_1 = 0.25$ ps, were found for the ensuing chemical and radiationless electronic transformations *via* distinct conical intersections. A time-resolved fluorescence up-conversion measurement suggests that the 100 fs time constant is virtually identical with the lifetime of the optically excited state. The rise times of the absorption signals of the product molecules indicate that the 100 fs and 250 fs time constants belong to the formation of the (*C*) and the (*Z*) isomers, respectively. The data are consistent with two alternative scenarios that are both

of fundamental interest in their own right. A conformer-specific photochemistry could result from two entirely separate excited-state reaction pathways, one leading from photoexcited $1E_\alpha$ to the (C)-isomer, the other leading from $1E_\beta$ to the (Z)-isomer. Alternatively, the data are also consistent with excited-state isomerisation pathways originating from the photoexcited $1E_\alpha$ conformer only and involve a subsequent branching of the excited-state wavepacket into the $E \rightarrow C$ and $E \rightarrow Z$ channels within $\Delta t < 0.25$ ps, especially because $1E_\alpha$ is the predominant conformer at room temperature. The ensuing spectral dynamics for pump-probe delays up to $\Delta t \approx 10$ ps could be entirely attributed to the cooling of vibrationally hot reactant and product molecules. The spectrum thereafter matches the weighted sum of the steady-state spectra of the three isomers with a (C) : (Z) ratio of approximately 2 : 1. Distinct oscillations of the transient absorption with frequencies of ≈ 64 and 114 cm^{-1} were observed and interpreted as excited-state vibrational coherences. The results were substantiated by TDDFT calculations which supported a barrierless $E \rightarrow C$ ring closure reaction *via* a CI, but probably a low potential energy barrier along the $E \rightarrow Z$ reaction coordinate, although a barrierless $E \rightarrow Z$ reaction *via* an indirect route (*e.g.*, *via* an intermediate state) cannot be ruled out. The calculations also confirmed the existence of low-frequency torsional vibrational modes explaining the observed coherent oscillations. Higher level *ab initio* excited-state calculations appear desirable to localise the CIs that mediate the fast electronic deactivation and isomerisation. The picture of the dynamics of the investigated furylfulgide emerging from this work is of interest in the broader context regarding the role of conformer-specific photochemistry and understanding competing ultrafast reactions in polyatomic molecules, and considering possible applications, for steering chemical reactivity by coherent control schemes. Work on sterically more demanding furylfulgides is currently underway in our laboratory in order to distinguish between the discussed mechanisms.

Acknowledgment

This work has been carried out within sub-project A1 of the Sonderforschungsbereich 677 “Function by Switching” supported by the Deutsche Forschungsgemeinschaft. The authors thank Professor E. Bartsch for a sample of the furylfulgide, N. K. Schwalb for help with the fluorescence up-conversion measurements, and one of the referees for valuable comments.

References

- [1] B. L. Feringa, Ed., *Molecular Switches*, Wiley-VCH, Weinheim **2001**.
- [2] V. Balzani, A. Credi, B. Ferrer, S. Silvi, M. Venturi, *Top. Curr. Chem.* **2005**, *262*, 1–27.
- [3] I. Willner, S. Rubin, *Angew. Chem. Int. Ed.* **1996**, *35*, 367–385.
- [4] I. Willner, *Acc. Chem. Res.* **1997**, *30*, 347–356.
- [5] Y. Yokoyama, *Chem. Rev.* **2000**, *100*, 1717–1739.
- [6] V. Balzani, A. Credi, M. Venturi, *Molecular Devices and Machines: Concepts and Perspectives for the Nanoworld*, Wiley-VCH, Weinheim **2008**.
- [7] Y. C. Liang, A. S. Dvornikov, P. M. Rentzepis, *Proc. Natl. Acad. Sci. U. S. A.* **2003**, *100*, 8109–8112.
- [8] T. Kardinahl, H. Franke, *Appl. Phys. A* **1995**, *61*, 23–27.
- [9] S. Z. Janicki, G. B. Schuster, *J. Am. Chem. Soc.* **1995**, *117*, 8524–8527.
- [10] F. M. Raymo, M. Tomasulo, *Chem. Soc. Rev.* **2005**, *34*, 327–336.
- [11] I. B. Ramsteiner, A. Hartschuh, H. Port, *Chem. Phys. Lett.* **2001**, *343*, 83–90.
- [12] F. M. Raymo, M. Tomasulo, *J. Phys. Chem. A* **2005**, *109*, 7343–7352.
- [13] Y. Yokoyama, K. Ogawa, T. Iwai, K. Shimazaki, Y. Kajihira, T. Goto, Y. Yokoyama, Y. Kurita, *Bull. Chem. Soc. Jpn.* **1996**, *69*, 1605–1612.
- [14] E. Uhlmann, G. Gauglitz, *J. Photochem. Photobiol. A* **1996**, *98*, 45–49.
- [15] M. A. Wolak, C. J. Thomas, N. B. Gillespie, R. R. Birge, W. J. Lees, *J. Org. Chem.* **2003**, *68*, 319–326.
- [16] W. Fuß, S. Panja, W. E. Schmidt, S. A. Trushin, *Mol. Phys.* **2006**, *105*, 1133–1143.
- [17] O. Kühn, L. Wöste, Eds., *Analysis and Control of Ultrafast Photoinduced Reactions*, Springer, New York **2007**.
- [18] H. Tamura, S. Nanbu, T. Ishida, H. Nakamura, *J. Chem. Phys.* **2006**, *125*, 034307/1–10.
- [19] M. Handschuh, M. Seibold, H. Port, H. C. Wolf, *J. Phys. Chem. A* **1997**, *101*, 502–506.
- [20] H. Port, P. Gärtner, M. Hennrich, I. Ramsteiner, T. Schöck, *Mol. Cryst. Liq. Cryst.* **2005**, *430*, 15–21.
- [21] A. S. Dvornikov, Y. Liang, C. S. Cruse, P. M. Rentzepis, *J. Phys. Chem. B* **2004**, *108*, 8652–8658.
- [22] B. Heinz, S. Malkmus, S. Laimgruber, S. Dietrich, C. Schulz, K. Rück-Braun, M. Braun, W. Zinth, P. Gilch, *J. Am. Chem. Soc.* **2007**, *129*, 8577–8584.

- [23] F. O. Koller, W. J. Schreier, T. E. Schrader, S. Malkmus, C. Schulz, S. Dietrich, K. Rück-Braun, M. Braun, *J. Phys. Chem. A* **2008**, *112*, 210–214.
- [24] F. Renth, M. Foca, A. Petter, F. Temps, *Chem. Phys. Lett.* **2006**, *428*, 62–67.
- [25] T. Pancur, F. Renth, F. Temps, B. Harbaum, A. Krüger, R. Herges, C. Näther, *Phys. Chem. Chem. Phys.* **2005**, *7*, 1985–1989.
- [26] R. Ahlrichs, M. Bär, M. Häser, H. Horn, C. Kölmel, *Chem. Phys. Lett.* **1989**, *162*, 165–169.
- [27] O. Christiansen, H. Koch, P. Jorgensen, *Chemical Physics Letters* **1995**, *243*, 409–18.
- [28] W. Fuß, S. Lochbrunner, A. M. Müller, T. Schikarski, W. E. Schmid, S. A. Trushin, *Chem. Phys.* **1998**, *232*, 161–174.
- [29] W. Domcke, D. R. Yarkony, H. Köppel, Eds., *Conical Intersections*, World Scientific, Singapore **2004**.
- [30] R. A. Mathies, C. H. B. Cruz, W. T. Pollard, C. V. Shank, *Science* **1988**, *240*, 777–779.
- [31] J. Saltiel, N. Tarkalanov, D. F. Sears Jr., *J. Am. Chem. Soc.* **1995**, *117*, 5586–5587.
- [32] J. Saltiel, L. Cires, A. M. Turek, *Conformer-specific photochemistry in the vitamin D field.*, chap. 27, Second edn. CRC Press LLC, Boca Raton **2004**, 1 – 22.
- [33] H. J. C. Jacobs, E. Havinga, *Adv. Photochem.* **1979**, *11*, 305–73.
- [34] P. Celani, F. Bernardi, M. A. Robb, M. Olivucci, *J. Phys. Chem.* **1996**, *100*, 19364–19366.
- [35] A. Hofmann, R. de Vivie-Riedle, *J. Chem. Phys.* **2000**, *112*, 5054–5059.
- [36] M. Garavelli, C. S. Page, P. Celani, M. Olivucci, W. E. Schmid, S. A. Trushin, W. Fuß, *J. Phys. Chem. A* **2001**, *105*, 4458–4469.
- [37] F. Bernardi, M. Olivucci, *Chem. Soc. Rev.* **1996**, *25*, 321–328.
- [38] W. Fuß, Y. Haas, S. Zilberg, *Chem. Phys.* **2000**, *256*, 273–295.
- [39] S. Takeuchi, T. Tahara, *Chem. Phys. Lett.* **2000**, *326*, 430–438.
- [40] S. Ruhmann, B. Hou, N. Friedmann, M. Ottolenghi, M. Sheves, *J. Am. Chem. Soc.* **2002**, *124*, 8854–8858.
- [41] A. J. Wurzer, S. Lochbrunner, E. Riedle, *Appl. Phys. B* **2000**, *71*, 405–409.
- [42] C. Dugave, L. Demange, *Chem. Rev.* **2003**, *103*, 2475–2532.
- [43] B. G. Levine, T. J. Martinez, *Annu. Rev. Phys. Chem.* **2007**, *58*, 613–634.

Supporting Information

^1H and ^{13}C NMR data

The molecule of interest 1-[1-(2,5-dimethyl-3-furyl)-ethylidene]-2-isopropylidene succinic anhydride (**1E**) has been obtained quantitatively by irradiating the closed 7,7a-dihydro-2,4,7,7a-pentamethylbenzo[b]furan-5,6-dicarboxylic anhydride (**1C**) at $\lambda = 500$ nm in CDCl_3 . NMR data were acquired on Bruker Avance 600 MHz and DRX-500 spectrometers. For comparison, samples of 1-[1-(2,5-dimethyl-3-furyl)-2-methylpropylidene]-2-isopropylidene succinic anhydride (**2E**) were measured under the same conditions. The numbering of **1E** and **2E** has been taken from **1C** and is given in Figure S1.

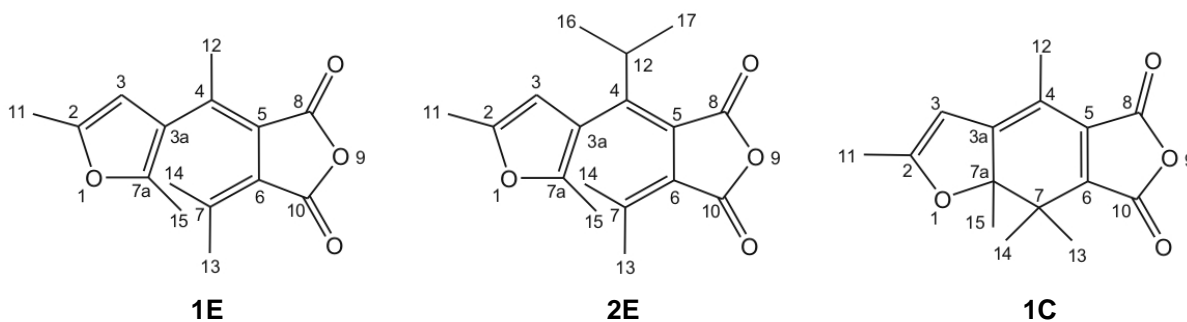
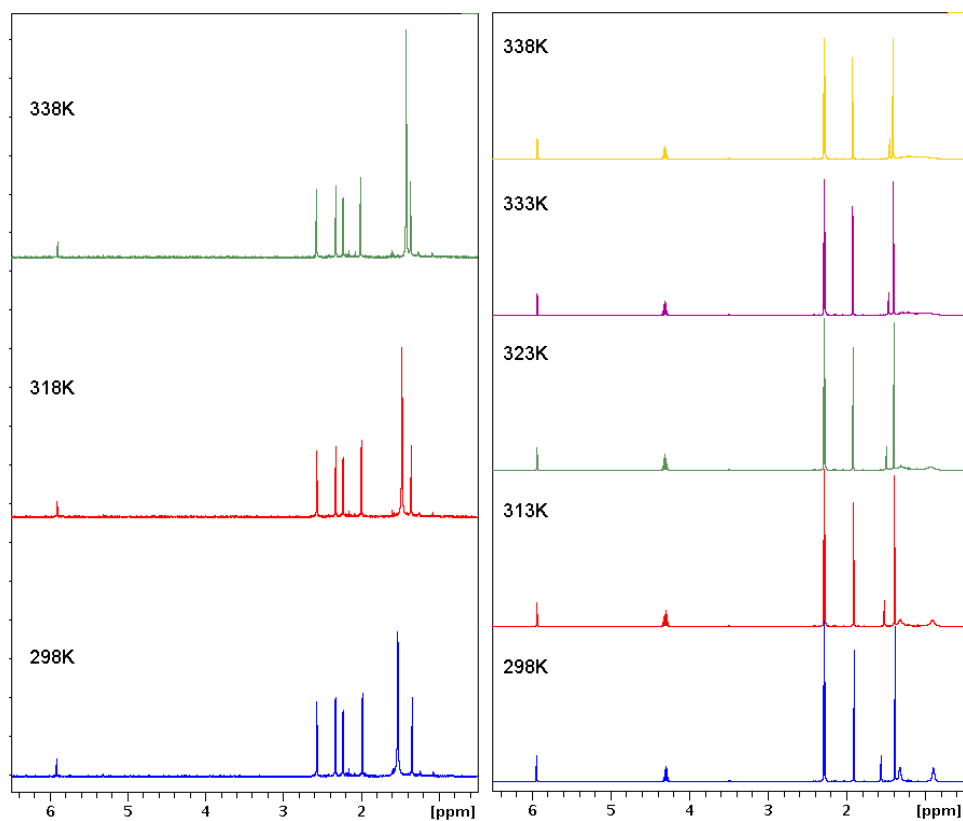


Figure S1: Structures and numbering of **1E**, **2E** and **1C**.

The assignment of the ^1H and ^{13}C -chemical shifts were made by analysis of ^1H -1D-NMR, natural abundance ^1H , ^{13}C -HSQC and ^1H , ^{13}C -HMBC experiments. The assignments are complete and unambiguous, and are based largely on $^3\text{-}^5\text{J}$ -correlations in the HMBC experiment with the exception of the isopropylidene-methyl groups, which were distinguished based on the NOE intensities in a 2D-NOESY experiment owing to the conformation-independent closer proximity of 14-H to all other protons in the compound. The assignments are collected in Table S1. Figure S2 shows the 1D- ^1H -NMR data measured at temperatures from 298 to 338 K. As seen in Fig. S2, a single set of uniformly sharp resonances persists at temperatures up to 338 K. This suggests a fast interconversion between the two **1E** conformers. Published results show that the thermal enantiotopomerisation of the chemically very similar furylfulgide 1-[1-(2,5-dimethyl-3-furyl)-2-methylpropylidene]-2-isopropylidene succinic anhydride (**2E**) occurs with a barrier of 52.9 kJ/mol.^[1,2] Since the isopropyl-group in **2E** is not expected to have a significant effect on either the furyl-group rotation or the inversion of the helical chirality, a similarly fast process is very likely for **1E**, which is consistent with our NMR data. The 2D-NOESY data are shown in Fig. S3, the NOE cross peak intensities derived from the data are given in Table S2.

Table S1: Chemical Shifts of **1E**.

Atom number	^{13}C -shift (ppm)	^1H -shift (ppm)
7a	148.14	
3a	124.01	
3	105.7	5.927
2	151.05	
4	146.62	
5	119.12	
6	120.84	
7	153.49	
8	163.70	
10	163.14	
15	13.82	2.000
11	13.22	2.247
12	22.08	2.582
14	26.71	1.358
13	22.54	2.344

**Figure S2:** 500 MHz 1D- ^1H -NMR Spectra for **1E** (left) and **2E** (right) at temperatures from 298 to 338 K.

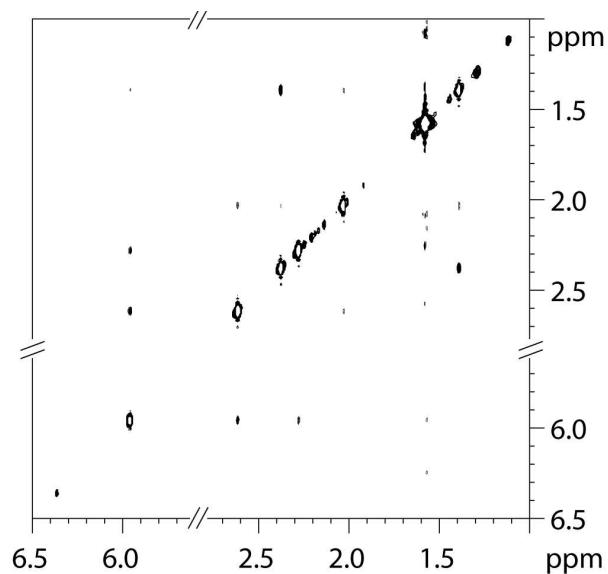


Figure S3: 2D- $^1\text{H},^1\text{H}$ -NOESY experiment of **1E** acquired at 600 MHz, mixing time $d_8 = 1.5$ s.

In the isopropyl-furylfulgide, the presence of a prochiral-group allows to directly assess the chirality of the molecule. Notably, as previously published, the prochiral methyl groups of the isopropyl groups are chemically inequivalent at room temperature confirming the chirality. They are broadened due to slow interconversion, which is substantiated by exchange cross peaks in a 2D-NOESY spectrum (data not shown). The resonance broadening increases with elevating temperature, and the estimated coalescence temperature was 65C/500 MHz, which is consistent with the published rotational barrier for the furyl group of 52.9 kJ/mol.^[1,2] This conformational barrier is too high to originate in hindered rotation of the isopropyl group itself, which is also confirmed by the observation that the methine-proton of this group is not broadened at any temperature. Thus, the underlying isomerisation is remote, and can be assigned to the furyl-ring rota-

Table S2: NOE intensities and estimated (averaged) distances based on a two-spin approximation and calibration of distances using the fixed proton distances between furyl-H and methyl, and the isopropylidene methyl groups.

Protons	Protons	relative NOE intensity	distance (Å)	measured E distance in E_α (Å)	measured distance in E_β (Å)	
12-H	3-H	35.2	2.92	3.06	3.79	
12-H	15-H	20.3	3.20	4.52	3.39	
3-H	11-H	26.0	3.08	2.56	2.56	Fixed distance
3-H	14-H	12.8	3.46	3.67	3.36	
15-H	13-H	12.3	3.48	4.41	6.86	
15-H	14-H	19.7	3.22	4.02	4.46	
13-H	14-H	78.2	2.56	2.56	2.56	Calibration distance

tion/diastereotopomerization based on the calculated energetic barrier for this process. Further, as the isopropyl group does not exert a significant effect on either the furyl-group rotation or the inversion of the helical chirality, the determined rotational barrier is also reflective of the barrier in the methyl-furylfugide.

The NOE intensity-derived distances were shorter than expected for the conformers $1\mathbf{E}_\alpha$ or $1\mathbf{E}_\beta$ alone and indicate a fast rotation and averaging over the conformers. This confirms the above statement of a fast thermal enantiotopomerisation that leads to a thermal equilibrium of both conformers in solution.

Quantum Chemical Calculations

Quantum chemical calculations were carried out using the Turbomole package. The ground state equilibrium structures of $1\mathbf{E}_\alpha$ and $1\mathbf{E}_\beta$ were calculated by DFT calculations at the B3LYP/def2-SVP level; the excited state structures are the results of a TDDFT geometry optimization with the same functional and basis set. The structural parameters are given in Table S3-S13.

Table S3: Atomic cartesian coordinates (\AA) of the calculated ground state equilibrium structures of $1\mathbf{E}_\alpha$ ($1\mathbf{E}_{\alpha,eq}$, $1\mathbf{E}_{\alpha,FC}^*$).

	x	y	z		x	y	z
C	2.257664	1.565058	-0.066287	H	0.494693	3.389943	-0.506535
C	1.001996	0.785992	-0.258485	H	-1.020098	3.014708	-1.331062
C	1.425853	-0.627503	-0.236525	H	-1.028442	3.247152	0.403451
C	2.769183	-0.624164	0.403210	H	1.902351	-3.358588	-1.829561
O	3.228380	0.686590	0.403838	H	2.368971	-3.142583	-0.130900
C	-0.232561	1.361911	-0.239603	H	0.779676	-3.798139	-0.563616
C	-0.436834	2.844498	-0.421217	H	-5.456076	0.368023	-1.097451
C	0.931662	-1.701714	-0.897650	H	-5.262665	-1.292533	-0.521927
C	1.549519	-3.068870	-0.835054	H	-5.673073	-0.011666	0.615953
O	3.454019	-1.497224	0.848038	C	-0.258976	-1.612251	-1.802573
O	2.523917	2.722378	-0.203739	H	-1.169434	-1.923672	-1.282004
C	-1.471872	0.622109	0.010453	H	-0.427734	-0.604871	-2.174941
C	-2.737584	0.832294	-0.653990	H	-0.128487	-2.288631	-2.649142
C	-3.644704	0.027447	-0.055995	H	-0.559710	-1.880126	1.849916
O	-3.036174	-0.655096	0.964883	C	-0.914212	-0.875809	2.098108
C	-1.721955	-0.288338	1.002825	H	-1.510875	-0.948467	3.008032
C	-5.086238	-0.242909	-0.275822	H	-0.040426	-0.260433	2.301633
H	-2.928595	1.486203	-1.487851				

Table S4: Atomic cartesian coordinates (\AA) of the calculated ground state equilibrium structures of $\mathbf{1E}_\beta$ ($\mathbf{1E}_{\beta,eq}$, $\mathbf{1E}_{\beta,FC}^*$).

	x	y	z		x	y	z
C	2.297049	1.507361	0.228512	H	0.265195	3.255962	0.897896
C	1.054148	0.751937	-0.086148	H	0.110678	3.337309	-0.842161
C	1.476595	-0.655250	-0.214247	H	-1.358897	3.155420	0.172441
C	2.825685	-0.716821	0.430195	H	1.962077	-3.263240	-2.030854
O	3.272435	0.586172	0.584485	H	2.367225	-3.192415	-0.287286
C	-0.182909	1.343347	-0.013339	H	0.769404	-3.787326	-0.840923
C	-0.312171	2.851869	0.051038	H	-4.183723	-2.678291	0.849782
C	0.975476	-1.663294	-0.987328	H	-3.090169	-2.610691	2.259734
C	1.568900	-3.046101	-1.021147	H	-4.538288	-1.568791	2.191076
O	3.519515	-1.637726	0.756206	C	-0.185444	-1.461032	-1.919586
O	2.523731	2.684128	0.265847	H	-0.013446	-2.023522	-2.852304
C	-1.418160	0.560032	0.145726	H	-1.118645	-1.851307	-1.476797
C	-1.590644	-0.595260	1.002375	H	-0.352045	-0.404727	-2.164418
C	-2.904719	-0.949563	0.937105	H	-3.906541	2.496421	-0.907283
O	-3.556234	-0.105194	0.079624	C	-3.203487	1.787021	-1.378148
C	-2.667403	0.809847	-0.389935	H	-3.757261	1.262540	-2.174478
C	-3.721025	-2.006633	1.593064	H	-2.394557	2.363411	-1.844321
H	-0.824738	-1.068467	1.612023				

Table S5: Atomic cartesian coordinates (\AA) of the calculated ground state equilibrium structures of $\mathbf{1Z}_\alpha$ ($\mathbf{1Z}_{\alpha,eq}$, $\mathbf{1Z}_{\alpha,FC}^*$).

	x	y	z		x	y	z
C	0.600140	1.560918	0.060126	H	1.050404	-2.378063	0.956932
C	0.780826	0.081635	-0.033245	H	-0.672936	-2.532212	1.393144
C	2.238452	-0.135804	-0.039115	H	-0.157830	-2.927694	-0.239112
C	2.826814	1.143764	0.468342	H	4.906354	-0.433790	0.140204
O	1.830018	2.101415	0.430108	H	4.807737	-2.178887	-0.263089
C	-0.244009	-0.803203	0.191129	H	4.913849	-0.987501	-1.560593
C	0.023762	-2.231265	0.597329	H	-4.385779	1.315109	-2.563957
C	2.982056	-1.118185	-0.626866	H	-5.489161	0.109148	-1.843697
C	4.485303	-1.164254	-0.557106	H	-5.248976	1.680276	-1.046318
O	3.935402	1.431995	0.820490	C	2.366003	-2.200668	-1.470290
O	-0.357954	2.265425	-0.059564	H	2.332838	-3.165553	-0.933799
C	-1.659838	-0.420844	0.050708	H	1.347101	-1.955531	-1.796574
C	-2.252096	0.246518	-1.087226	H	2.990415	-2.367052	-2.364059
C	-3.589836	0.328132	-0.852998	H	-1.857013	-1.303287	2.785175
O	-3.866540	-0.230160	0.367302	C	-2.830149	-1.269933	2.277835
C	-2.710349	-0.687146	0.910288	H	-3.247711	-2.292418	2.257955
C	-4.738573	0.885287	-1.616102	H	-3.509839	-0.653231	2.887203
H	-1.724782	0.615371	-1.963201				

Table S6: Atomic cartesian coordinates (\AA) of the calculated ground state equilibrium structures of $\mathbf{1Z}_\beta$ ($\mathbf{1Z}_{\beta,eq}$, $\mathbf{1Z}_{\beta,FC}^*$).

	x	y	z		x	y	z
C	0.733724	0.539999	-1.432762	H	0.768135	-1.536488	2.062881
C	0.772917	0.165311	0.011928	H	-0.437168	-0.480794	2.853236
C	2.201842	0.003439	0.335328	H	-5.414430	2.262152	0.008481
C	2.887180	-0.140505	-0.987754	H	-4.175768	3.251025	-0.814687
O	1.991721	0.260236	-1.962550	H	-5.035466	1.965271	-1.703233
C	-0.339897	-0.249777	0.699405	H	-2.073904	-2.773779	0.244451
C	-0.224904	-1.082116	1.952656	C	-3.021626	-2.222860	0.304898
C	2.871243	0.215209	1.506086	H	-3.674177	-2.577963	-0.508480
O	3.999047	-0.475804	-1.282934	H	-3.516086	-2.485868	1.257259
O	-0.143249	0.941588	-2.138503	C	2.189147	0.740186	2.740467
C	-1.707240	0.083963	0.263939	C	4.356249	0.016432	1.652017
C	-2.197703	1.401439	-0.075292	H	2.049647	-0.051881	3.497459
C	-3.528201	1.280117	-0.332980	H	2.826892	1.507094	3.211249
O	-3.894351	-0.032593	-0.192806	H	1.208846	1.184995	2.526872
C	-2.804645	-0.753195	0.171965	H	4.825590	-0.392127	0.751829
C	-4.594277	2.238569	-0.729541	H	4.550545	-0.664366	2.500582
H	-1.610382	2.314707	-0.119933	H	4.842839	0.973712	1.912594
H	-0.978014	-1.883306	1.943435				

Table S7: Atomic cartesian coordinates (\AA) of the calculated ground state equilibrium structures of $\mathbf{1C}$ ($\mathbf{1C}_{eq}$, $\mathbf{1C}_{FC}^*$).

	x	y	z		x	y	z
C	2.646454	1.108158	0.066034	H	0.835454	3.597008	0.497856
C	1.197067	0.752856	0.029421	H	0.783102	3.308191	-1.226110
C	1.111274	-0.600180	-0.036081	H	-0.717368	3.625172	-0.345600
C	2.469073	-1.143789	-0.110964	H	0.515950	-3.390246	-0.124694
O	3.369187	-0.064431	-0.009432	H	0.175638	-2.742194	1.468875
C	0.073676	1.653087	-0.031953	H	-1.163258	-3.197642	0.402341
C	0.248137	3.123688	-0.291011	H	-5.163238	1.150493	-0.702882
C	-0.200095	-1.347048	-0.186021	H	-4.883397	-0.517188	-1.248382
C	-0.166608	-2.753350	0.434776	H	-5.226218	-0.201387	0.448099
O	2.871449	-2.261538	-0.247509	C	-0.498304	-1.480609	-1.700644
O	3.172686	2.176777	0.149887	H	-1.429726	-2.023885	-1.859010
C	-1.133180	1.029875	0.062873	H	-0.578382	-0.506162	-2.184612
C	-2.475137	1.447007	-0.196684	H	0.307319	-2.036145	-2.181154
C	-3.267257	0.344594	-0.169715	H	-1.464557	-1.472705	2.399118
O	-2.606012	-0.794874	0.133063	C	-1.192274	-0.480649	2.042987
C	-1.239416	-0.425782	0.508325	H	-1.898958	0.240980	2.453315
C	-4.717912	0.194096	-0.435277	H	-0.197409	-0.231198	2.410681
H	-2.811486	2.437706	-0.454649				

Table S8: Atomic cartesian coordinates (\AA) of the calculated first excited state equilibrium structures of $1\mathbf{C}_{min}^*$.

	x	y	z		x	y	z
C	2.647903	1.111775	0.080121	H	1.073101	3.543964	0.224188
C	1.243889	0.787934	-0.023180	H	0.564262	3.232036	-1.419510
C	1.098627	-0.593025	-0.136151	H	-0.672869	3.703441	-0.209322
C	2.459859	-1.172439	-0.105876	H	0.481805	-3.357814	-0.483142
O	3.337361	-0.120833	0.007122	H	0.257823	-2.866594	1.192759
C	0.079776	1.675657	-0.033662	H	-1.175849	-3.199619	0.174201
C	0.244194	3.118989	-0.365992	H	-5.187733	1.132743	-0.656253
C	-0.207348	-1.306653	-0.295943	H	-4.856315	-0.531321	-1.231842
C	-0.162162	-2.768253	0.182913	H	-5.250751	-0.258070	0.474435
O	2.824129	-2.325115	-0.173970	C	-0.661265	-1.285201	-1.778726
O	3.241079	2.165959	0.200664	H	-1.641141	-1.780525	-1.875451
C	-1.138527	1.045906	0.163720	H	-0.739022	-0.260721	-2.171811
C	-2.472834	1.463280	-0.138994	H	0.068297	-1.831836	-2.393782
C	-3.279612	0.349330	-0.090284	H	-1.349587	-1.650558	2.353195
O	-2.604161	-0.755568	0.280292	C	-1.041394	-0.633699	2.075426
C	-1.224782	-0.414071	0.564893	H	-1.660202	0.084629	2.633830
C	-4.722452	0.173707	-0.392799	H	0.011931	-0.487724	2.354113
H	-2.798788	2.456615	-0.441696				

Table S9: Atomic cartesian coordinates (\AA) of the calculated excited state structures of $1\mathbf{E}$ at the final point of a TDDFT geometry optimization $1\mathbf{E}_{CI}^*$.

	x	y	z		x	y	z
C	2.599585	1.179833	0.092458	H	1.070052	3.489179	-0.522907
C	1.171029	0.810700	-0.196422	H	-0.434630	3.285180	-1.457703
C	1.164809	-0.596653	-0.430939	H	-0.521896	3.702541	0.267081
C	2.484273	-1.102663	-0.068142	H	0.397102	-3.530419	-0.965282
O	3.319552	0.025335	0.179861	H	0.696370	-3.035516	0.699237
C	0.033780	1.644752	-0.109811	H	-0.993583	-3.222464	0.092984
C	0.040181	3.111450	-0.473898	H	-5.237129	0.797590	-0.804226
C	-0.003436	-1.450012	-0.623099	H	-4.886146	-0.960203	-0.760381
C	0.025880	-2.873931	-0.153806	H	-5.336495	-0.106416	0.729953
O	2.943328	-2.211779	0.002370	C	-0.779946	-1.221134	-1.901911
O	3.079437	2.267175	0.275667	H	-1.855699	-1.438968	-1.783469
C	-1.196476	0.976846	0.116889	H	-0.659241	-0.204136	-2.295543
C	-2.529482	1.317229	-0.322411	H	-0.411957	-1.923100	-2.677819
C	-3.344949	0.298808	0.038704	H	-0.061524	-1.710675	1.863040
O	-2.636386	-0.650292	0.757184	C	-0.604835	-0.777264	2.047606
C	-1.346436	-0.243193	0.854926	H	-1.337814	-0.974368	2.845972
C	-4.775747	-0.007582	-0.215606	H	0.109130	-0.029588	2.421689
H	-2.829764	2.185181	-0.906728				

Table S10: Atomic cartesian coordinates (\AA) of the calculated first excited state equilibrium structures of $1\mathbf{E}_{\alpha, min}^*$.

	x	y	z		x	y	z
C	1.371801	1.797476	0.097555	H	0.119963	1.898310	-3.014277
C	0.867127	0.608783	-0.565438	H	-1.622813	1.671848	-2.766357
C	1.666410	-0.512390	-0.101361	H	-0.682646	2.796980	-1.732979
C	2.613030	0.066897	0.916544	H	3.428102	-3.161688	-0.727839
O	2.440932	1.427014	0.935055	H	3.202062	-2.490957	0.913612
C	-0.358609	0.648658	-1.333502	H	2.099174	-3.751002	0.270968
C	-0.662338	1.812621	-2.241051	H	-3.532404	-3.311964	0.673947
C	1.765713	-1.800436	-0.574064	H	-3.770543	-2.337432	2.160415
C	2.677283	-2.841429	0.019515	H	-4.884401	-2.137160	0.796937
O	3.436108	-0.454289	1.622703	C	1.035189	-2.259713	-1.807320
O	0.981517	2.948264	0.104788	H	0.400008	-3.143394	-1.604307
C	-1.468750	0.059030	-0.556122	H	0.423294	-1.464637	-2.257679
C	-1.886475	-1.273814	-0.370230	H	1.770835	-2.599458	-2.560294
C	-2.960113	-1.268766	0.510179	H	-2.882967	2.439025	1.566275
O	-3.230961	0.014838	0.905170	C	-2.357823	2.257439	0.618502
C	-2.330615	0.821325	0.303565	H	-2.883926	2.812208	-0.181557
C	-3.828866	-2.327876	1.057790	H	-1.329944	2.658005	0.644306
H	-1.473112	-2.158363	-0.843331				

Table S11: Atomic cartesian coordinates (\AA) of the calculated first excited state equilibrium structures of $1\mathbf{E}_{\beta, min}^*$.

	x	y	z		x	y	z
C	2.260729	1.625619	-0.025875	H	0.253356	3.378122	-0.802690
C	1.113756	0.770592	-0.313618	H	-1.488404	3.046233	-0.628176
C	1.610016	-0.595735	-0.314093	H	-3.250155	-1.319188	3.218057
C	2.999022	-0.512035	0.253775	H	-4.741514	-0.887326	2.311863
O	3.358722	0.804404	0.319019	H	-3.881218	-2.383314	1.917176
C	-0.203287	1.293434	-0.428561	H	-1.980347	0.812279	-2.701804
C	-0.483987	2.778789	-0.254868	C	-2.868480	0.453495	-2.166784
C	1.104954	-1.766866	-0.843583	H	-3.634014	1.252444	-2.185997
O	3.768082	-1.375469	0.591889	H	-3.308536	-0.424038	-2.667653
O	2.399215	2.826666	0.002719	C	-0.062014	-1.788589	-1.795942
C	-1.364158	0.469608	-0.000047	C	1.736974	-3.119426	-0.643156
C	-1.678598	0.018808	1.287277	H	-0.342881	-0.779997	-2.125596
C	-2.930200	-0.608640	1.238953	H	0.214995	-2.364642	-2.699223
O	-3.436353	-0.512220	-0.021948	H	-0.949638	-2.304513	-1.381425
C	-2.513215	0.136299	-0.779007	H	2.133812	-3.512784	-1.599889
C	-3.735336	-1.335374	2.234455	H	0.971984	-3.850193	-0.315502
H	-1.050498	0.103149	2.171350	H	2.555068	-3.104995	0.083429
H	-0.429911	3.122950	0.800476				

Table S12: Atomic cartesian coordinates (Å) of the calculated first excited state equilibrium structures of $\mathbf{1Z}_{\alpha, min}^*$.

	x	y	z		x	y	z
C	0.395616	1.317565	-0.251827	H	1.008270	-2.171599	1.766058
C	0.769425	-0.046834	0.039991	H	-0.724737	-2.279048	2.107345
C	2.221001	-0.099742	-0.042166	H	-0.039629	-3.183806	0.752834
C	2.657521	1.322761	-0.207137	H	4.923106	0.013474	0.138569
O	1.527047	2.103624	-0.404767	H	5.037295	-1.717824	0.591275
C	-0.212313	-0.996392	0.429974	H	5.042889	-1.251507	-1.110920
C	0.018845	-2.214275	1.289143	H	-4.859157	-1.124436	-2.381913
C	3.103825	-1.156027	-0.159115	H	-5.790968	-0.661209	-0.917699
C	4.600923	-0.997738	-0.127541	H	-5.106985	0.600233	-1.957747
O	3.743364	1.835574	-0.236747	C	2.648082	-2.568162	-0.411938
O	-0.713153	1.844445	-0.327464	H	2.758964	-3.215306	0.479014
C	-1.629762	-0.644972	0.160121	H	1.605521	-2.622808	-0.747813
C	-2.466586	-1.084420	-0.874821	H	3.283278	-3.021546	-1.194367
C	-3.681709	-0.418197	-0.756343	H	-2.037816	2.105079	1.860178
O	-3.646957	0.402970	0.339406	C	-2.167117	1.043612	2.131325
C	-2.433217	0.277483	0.906344	H	-1.239259	0.693694	2.598740
C	-4.923052	-0.409969	-1.551625	H	-3.014360	0.964262	2.831182
H	-2.205399	-1.782965	-1.666092				

Table S13: Atomic cartesian coordinates (Å) of the calculated first excited state equilibrium structures of $\mathbf{1Z}_{\beta, min}^*$.

	x	y	z		x	y	z
C	0.425998	-0.210215	-1.243513	H	0.511738	-1.108423	2.731669
C	0.661080	-0.112177	0.178294	H	-0.477068	0.259913	3.281081
C	2.102684	-0.186662	0.360637	H	-5.699510	1.789998	-0.257705
C	2.653135	-0.519042	-0.991322	H	-4.592315	3.198070	-0.126818
O	1.618376	-0.436567	-1.913332	H	-4.770130	2.310175	-1.674521
C	-0.427707	-0.071611	1.089629	H	-1.616328	-2.493895	-0.042980
C	-0.408474	-0.545563	2.521036	C	-2.474160	-2.058555	-0.568182
C	2.919257	0.145616	1.424116	H	-2.304518	-2.154254	-1.653480
O	3.763458	-0.777436	-1.369703	H	-3.401554	-2.598020	-0.314531
O	-0.622227	-0.171678	-1.886401	C	2.410655	0.872599	2.640060
C	-1.761547	0.250831	0.522017	C	4.403327	-0.107438	1.444892
C	-2.460663	1.465320	0.544956	H	2.360777	0.220837	3.533290
C	-3.627655	1.302675	-0.193983	H	3.114359	1.684435	2.899034
O	-3.700434	0.014790	-0.654650	H	1.420747	1.318617	2.484655
C	-2.599512	-0.633443	-0.232236	H	4.751438	-0.704755	0.596901
C	-4.728208	2.206349	-0.575977	H	4.681892	-0.618344	2.386736
H	-2.133417	2.392429	1.009449	H	4.963712	0.847571	1.445839
H	-1.253132	-1.230125	2.732601				

References

- [1] Y. Yokoyama, K. Ogawa, T. Iwai, K. Shimazaki, Y. Kajihara, T. Goto, Y. Yokoyama, Y. Kurita, *Bull. Chem. Soc. Jpn.* **1996**, *69*, 1605–1612.
- [2] Y. Yokoyama, *Chem. Rev.* **2000**, *100*, 1717–1739.

4 Tuning of Switching Properties and Excited-State Dynamics of Fulgides by Structural Modifications

Ron Siewertsen,^a Frank Strübe,^b Falk Renth,^{*a} Jochen Mattay,^b Friedrich Temps^{*a}

^a Institut für Physikalische Chemie, Christian-Albrechts-Universität zu Kiel,
Olshausenstr. 40, D-24098 Kiel, Germany

^b Organische Chemie I, Fakultät für Chemie, Universität Bielefeld, Postfach 100131,
D-33501 Bielefeld, Germany

Reproduced with permission of the PCCP Owner Societies

Phys. Chem. Chem. Phys. **2011**, *13*, 3800-3808

Copyright 2011

- **Own contributions presented in the paper:**
 - Femtosecond time-resolved transient absorption spectroscopy
 - Data analysis and writing of the data analysis software
 - Determination of isomerisation quantum yields
 - Static UV/VIS spectroscopic investigations
 - Quantum chemical calculations

- **Synthesis:** Frank Strübe in the group of Prof. J. Mattay

*To whom correspondence should be addressed. E-mail: temps@phc.uni-kiel.de, renth@phc.uni-kiel.de

Abstract

The ultrafast photo-induced dynamics of the E -isomers of four selected photochromic fulgides with distinct structural motifs have been elucidated by femtosecond broadband transient absorption spectroscopy in n -hexane as solvent. $E \rightarrow C$ and $E \rightarrow Z$ isomerisations, respectively, with time constants of $\approx 0.12 \pm 0.02$ ps and $\approx 0.34 \pm 0.03$ ps taking place in parallel were found for derivatives with a methyl substituent at the central hexatriene (HT) unit. In contrast, fulgides with increased steric constraints by an *iso*-propyl substituent or by intramolecular bridging displayed virtually zero $E \rightarrow Z$ isomerisation, but instead a desired accelerated and more efficient ring closure in a reaction time of only $\approx 50 \pm 10$ fs. Both photoisomerisations appear to follow excited-state pathways with distinctive conical intersections. For the ring closure, direct barrierless pathways with steep downhill gradients are likely. Furthermore, the results indicate conformer-specific reactions, with ring closure exclusively by the E_α conformer and $E \rightarrow Z$ isomerisation predominantly by the E_β conformer, because the $E_\alpha \rightarrow Z$ channel is unfavoured by the faster and kinetically more competitive $E_\alpha \rightarrow C$ reaction. DFT calculations of the equilibrium structures showed that the sterically demanding groups at the HT unit shift the conformer equilibria towards the E_α conformers. At the same time, they appear to cause a favourable pre-orientation of the furyl unit that accelerates the conrotatory ring closure in the $E_\alpha \rightarrow C$ reaction. Benzo-annulation of the furyl unit has little effect on the observed dynamics. Overall, the results demonstrate how the excited-state dynamics and thereby the photoswitching properties of fulgides can be successfully tuned and improved by structural modifications at the chromophores.

4.1 Introduction

Fulgides are important thermally irreversible photochromic optical switches with excellent photostability^[1–3] and great potential for, *e.g.*, optical data storage, modulation of fluorescence and electron/energy transfer, photo-control of phase behaviour and enzyme activity, or as photoswitchable nonlinear optical materials.^[4–12] As illustrated in Fig. 4.1 for the prototypical furylfulgide 2-[1-(2,5-dimethyl-3-furyl)-ethylidene]-3-isopropylidene succinic anhydride (MeF), the photochromism is based on the electrocyclic ring opening from the closed C -isomer to the open E -isomer by visible light and the reverse $E \rightarrow C$ ring closure on irradiation with UV light. The isomerisation of the E -isomer to the thermally stable Z -isomer is also UV-initiated. Competing $E \rightarrow Z$ isomerisation may therefore strongly impair the functionality of fulgide devices even if the $E \rightarrow Z$ quantum yield is low.

Moreover, the photoswitching efficiency of fulgides is affected by the equilibrium between two helically chiral conformations of the E -isomer, of which only the E_α conformer can

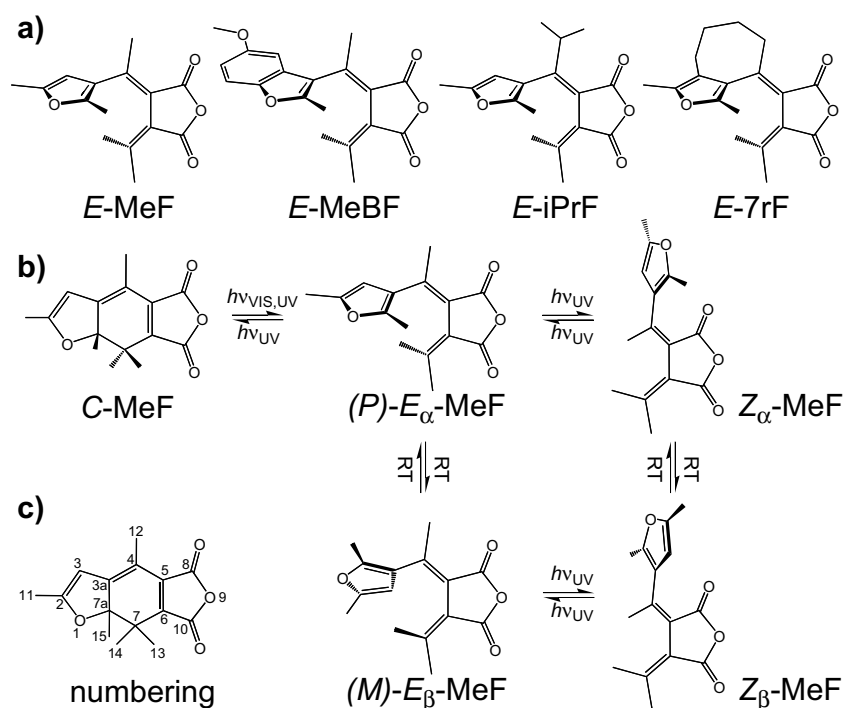


Figure 4.1: a) Structures of the selected four fulgides, b) photoisomerisation reactions for the example of MeF, and c) atom numbering scheme for *C*-MeF.

undergo ring closure, whereas both may isomerize to the *Z*-isomer (Fig. 4.1b). Thermal equilibrium between both conformers in solution at room temperature is established by interconversion between *(P)*-*E*_α-MeF and *(M)*-*E*_β-MeF or its enantiomeric version.^[3,13] Likewise, thermal interconversion has also been concluded to take place between the non-helical *Z*_α and *Z*_β conformers, which are sterically less congested than their *E*-isomer counterparts.^[14] Equilibration between the *Z* conformers is not expected on the time scale of our experiments. The possible rotamer equilibrium of the *Z* molecules produced in the reaction should thus not affect our data. Therefore, conformation of the *Z*-isomers is not indicated in the following for clarity.

As shown by the data in Table 4.1, the photoisomerisation quantum yield of MeF is far from ideal for applications, but several successful structural modifications turned out to yield much improved photoswitching properties.^[3,13,15–20] In particular, increased steric demands by large alkyl substituents at the C⁴ position as in iPrF and tBuF or by intramolecular bridging as in 7rF (see Fig. 4.1a for these molecules) lead to much higher *E* → *C* quantum yields and at the same time to efficient blocking of the competing *E* → *Z* reactions.^[15–18] Electronic effects, e.g., by benzo-annulation of the furyl moiety as in MeBF^[15] (Fig. 4.1a) or its replacement by other heteroaromatic systems^[3,21–23] shift the absorption bands and lower the photochemical fatigue.

Previous time-resolved studies and quantum chemical calculations elucidated various

Table 4.1: UV/VIS absorption maxima and quantum yields ϕ_{EC} and ϕ_{EZ} for the $E \rightarrow C$ ring closure and $E \rightarrow Z$ isomerisation reactions for the structurally modified fulgides of interest.

	MeF ^a	MeBF ^a	iPrF ^a	7rF ^a	tBuF ^b
λ_E / nm	335	330	335	344	350
λ_Z / nm	350	345	352	362	–
λ_C / nm	470	485	475	490	492
ϕ_{EC}	0.23	0.17	0.57	0.53	0.79
ϕ_{EZ}	0.14	0.15	0.00	0.00	0.00

^a Ref. [15], excitation at 335 nm, solvent *n*-hexane. ^b Ref. [16], compound with *tert*-butyl group at C⁴, highest reported $E \rightarrow C$ quantum yield. Excitation at 366 nm, solvent toluene.

aspects of the ultrafast photo-induced dynamics of fulgides.^[24–37] Our study of E -MeF showed parallel $E \rightarrow C$ and $E \rightarrow Z$ photoisomerisations with respective time constants of 0.1 ps and 0.25 ps. The observed dynamics were consistent with conformer-specific $E_\alpha \rightarrow C$ and $E_\beta \rightarrow Z$ reactions as in the similar case of previtamin D,^[38] but a branching of the excited-state pathways from the photoexcited E_α conformer could not be ruled out.^[34] TDDFT calculations rationalised the ultrafast isomerisation times by distinctive reaction pathways involving conical intersections.^[34] Recent CASPT2//CASSCF computations confirmed a direct and barrierless reaction pathway for the ring closure reaction and revealed the significance of the zwitterionic S_1 excited state and its conical intersection (CI) with the S_0 electronic ground state for the reactions.^[37]

Despite all efforts, however, the reasons behind the observed significant changes of the photoswitching properties of fulgides upon structural variation are still poorly understood. This motivated us to perform a comparative study of the ultrafast photo-induced $E \rightarrow C$ and $E \rightarrow Z$ isomerisation reactions of four fulgide derivatives with selected structural motifs (see Fig. 4.1a) by femtosecond broadband transient absorption spectroscopy. The UV/VIS absorption spectra of the compounds are shown in Fig. 4.2.

Judged from the similar band structures, excitation of the E -isomers at $\lambda_{\text{pump}} \approx 350$ nm should populate the same excited electronic states for all derivatives and comparisons of the ensuing dynamics should therefore be feasible. The different conversion yields in the photostationary states (PSS) upon UV irradiation evidenced by the PSS spectra can be explained by the photoisomerisation quantum yields (see Table 4.1) and the molar absorption coefficients of the isomers at the irradiation wavelength. In particular, the lower $E \rightarrow C$ conversion for MeBF compared to MeF despite similar $E \rightarrow C$ quantum yields evident in the PSS spectrum in Fig. 4.2 can be traced back to the higher UV absorption of C -MeBF that leads to a larger effect of the reverse ring opening reaction and thereby a lower C -MeBF concentration in the PSS. The measurements described in the present paper reveal that increased steric demands lead to accelerated and more efficient $E \rightarrow C$

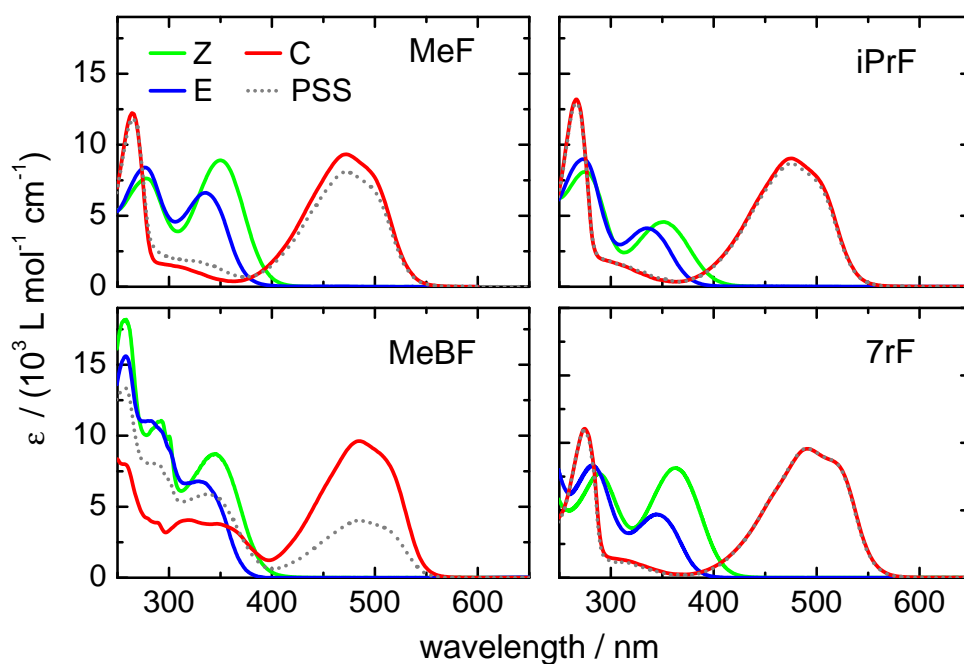


Figure 4.2: UV/VIS absorption spectra of the *C*-, *E*-, and *Z*-isomers for the fulgides MeF, iPrF, MeBF and 7rF in *n*-hexane (red, blue and green lines). The spectra in the photostationary state (PSS) by irradiation at 365 nm (335 nm for MeBF) are indicated by the dotted lines.

isomerisation reactions. Complementary experiments on the reverse $C \rightarrow E$ ring opening reactions will be reported in a follow-up paper.^[39]

4.2 Experimental

Details of the synthesis of the four fulgides will be published elsewhere.^[15] The *E*- and *Z*-isomers were isolated from the resulting mixtures of both isomers by column chromatography and recrystallization in adapted solvent mixtures of cyclohexane and ethyl acetate (9:1 and 7:3, respectively).^[15] The *C*-isomers of MeF (MeBF) were isolated from solutions in toluene (diethylether) that had been irradiated into the PSS at $\lambda = 365$ (350) nm and contained a mixture of *E*- and *C*-isomers. Pure *C*-isomers were finally obtained by recrystallization in the dark from *n*-hexane/chloroform (3:1) or cyclohexane/ethyl acetate (9:1).^[15] The purities of all isomers ($> 98\%$) were checked by thin layer chromatography and by $^1\text{H-NMR}$ spectroscopy. The UV/VIS spectra of all *E*- and *Z*-isomers, *C*-MeF and *C*-MeBF were thus taken from solutions of the pure respective isomers. The spectra of *C*-iPrF and *C*-7rF were obtained according to the method of Maafi^[40] by following the evolution of the absorption during irradiation of solutions of the *E*-isomers in *n*-hexane.^[41] All measurements were done at room temperature. Under these conditions, all isomers are thermally stable and thermal interconversion between them can be safely neglected.^[3,15] The time-resolved measurements were performed in flow cells of 0.5 or 1 mm optical path

length with 0.2 mm quartz windows. Solutions in *n*-hexane (Uvasol, Merck) as solvent were adjusted to an optical density of ≈ 0.3 at the excitation wavelength and pumped through the cuvettes with a peristaltic pump. To avoid accumulation of the *C*-isomer photoproducts, the sample reservoirs were continuously irradiated at 500 nm. The broadband femtosecond absorption setup^[25,34] employed a regeneratively amplified Ti:Sa laser system (Clark CPA2001). Tunable excitation pulses of 0.2 μJ at $\lambda_{\text{pump}} = 350$ nm with a bandwidth of $\Delta\lambda_{\text{pump}} = 6$ nm (FWHM) were supplied by a frequency-doubled noncollinear optical parametric amplifier (NOPA). Broadband light pulses between $\lambda_{\text{probe}} = 315$ and 650 nm were generated in CaF_2 , split into probe and reference beams, and focused into the sample cell to spot sizes of ≈ 150 μm . The pump polarisation with respect to the detection pulses was set to the magic angle. Probe and reference spectra were detected by an imaging spectrograph equipped with a 1024×127 pixel CCD camera. The pump-probe delay was varied by a computer-controlled linear translation stage in the probe path. The cross-phase modulation (XPM) and stimulated Raman scattering (SRS) contributions were taken into account as before.^[34] The instrument response function (IRF) had a Gaussian FWHM of ≈ 70 fs, resulting in a time resolution of the experiment after deconvolution of ≈ 30 fs.

Quantum chemical calculations of the electronic ground state structures and the mole fractions x_α of the E_α conformer in thermal equilibrium were performed with the GAUSSIAN09 software^[42] using density functional theory (DFT) at the B3LYP/6-31+G(d,p) level.

4.3 Results

Transient absorption maps and spectra

Figure 4.3a shows the measured spectro-temporal transient absorption maps following excitation of the *E*-isomers of MeF, MeBF, iPrF and 7rF at $\lambda_{\text{pump}} = 350$ nm. As can be seen, the obtained charts display superimposed distinctive ground-state bleach (GSB), excited-state absorption (ESA), stimulated emission (SE), hot ground state absorption (HGSA), and product absorption (PA) signals, which were assigned on the basis of their spectro-temporal evolutions with reference to the static UV/VIS spectra of the relevant isomers.^[34]

The absorption maps in Fig. 4.3a display at first glance that the MeF and MeBF pair (top) and the iPrF and 7rF pair (bottom) exhibit quite similar behaviours, respectively, whereas clear differences exist between the two sets. The distinctive behaviours can also be discerned clearly from the representative transient spectra of MeBF and 7rF at selected temporal delay times Δt in Fig. 4.3b. In addition, the main observations are as follows:

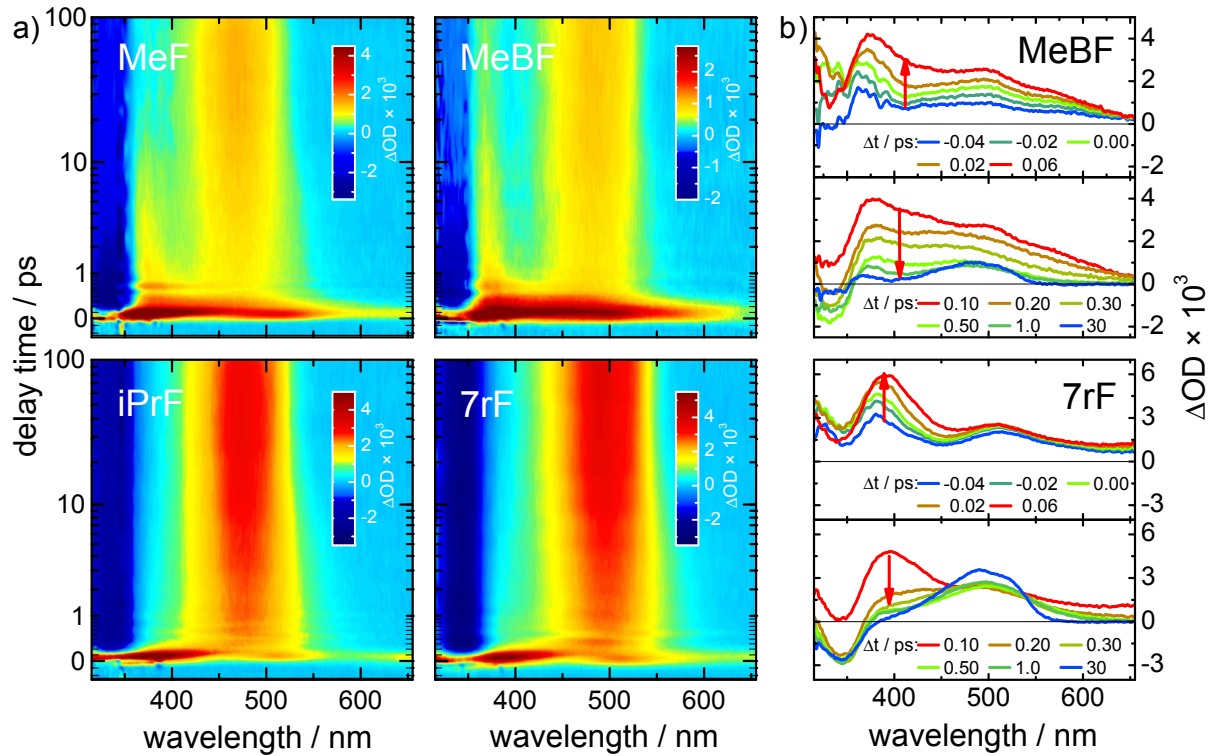


Figure 4.3: a) Two-dimensional transient absorption maps of the change in optical density ΔOD following excitation of the four *E*-fulgides at $\lambda_{\text{pump}} = 350$ nm for probe wavelengths between $315 \text{ nm} \leq \lambda_{\text{probe}} \leq 655$ nm and delay times of $-0.2 \leq \Delta t \leq 100$ ps (see Ref. [43] for an explanation of the time scale). b) Representative transient spectra of photo-excited MeBF and 7rF at the delay times indicated in the legends.

1. All charts show negative transient absorptions due to GSB (and possibly SE), which extend to $\lambda_{\text{probe}} \approx 360$ nm for MeF/MeBF and ≈ 370 nm for iPrF/7rF. GSB refilling happens mostly within the first few picoseconds and is more relevant for MeF/MeBF than for iPrF/7rF, as can also be seen by comparing the transient spectra of MeBF and 7rF for delays of $\Delta t = 1$ ps and $\Delta t = 30$ ps below $\lambda_{\text{probe}} \approx 370$ nm.
2. Large ESA amplitudes lead to positive initial transient absorptions with spectrally broad maxima at $\lambda_{\text{probe}} \approx 380$ and 525 nm, but the signals very rapidly turn negative in regions with large GSB during the subsequent decay of the ESA. Most importantly, the two fulgide pairs exhibit distinctly different ESA decays: Whereas the signals of iPrF and 7rF consist of only one component that decays extremely rapidly within only ≈ 100 fs at all probe wavelengths, MeF and MeBF show similar fast decays only at $\lambda_{\text{probe}} > 450$ nm. At shorter wavelengths, MeF and MeBF show an additional slower ESA decay component visible up to $\Delta t \approx 1$ ps, which is superimposed with weak damped oscillations. This component is seen as a distinctive band in the $\lambda_{\text{probe}} = 400 - 450$ nm region of the transient spectrum of MeBF in Fig. 4.3b at $\Delta t = 0.3$ ps.

3. The ESA decays leave broad positive HGSA bands from vibrationally excited molecules returned to their electronic ground states. The dominant band centered at $\lambda_{\text{probe}} \approx 480$ nm comes from the *C*-products and is established on the time scale of the faster ESA decay (see, e.g., spectrum at $\Delta t = 1$ ps). Its larger amplitude for iPrF and 7rF indicates high $E \rightarrow C$ isomerisation quantum yields. In the transient absorption maps for these molecules, damped oscillations can also be seen in the *C*-HGSA band, where they appear delayed with respect to the ESA, persist beyond its decay, and display alternating phases in the blue and red wings of the band.
4. A second HGSA band at shorter wavelengths ($\lambda_{\text{probe}} \approx 370$ nm) that rises slightly more slowly can be assigned to vibrationally hot *Z*-products. It is readily observed for MeF and MeBF, but is virtually absent in the cases of iPrF and 7rF. The following slower spectro-temporal changes, like the spectral narrowing and slight blue-shift of the *C* band, are due to vibrational cooling in the electronic ground state.
5. No further spectral changes are detectable beyond $\Delta t = 30$ ps. The final, permanent absorption changes seen in the spectra at $\Delta t = 30$ ps in Fig. 4.4b can be described well by the static $E - C$ difference spectra in the cases of iPrF and 7rF, and by a weighted sum of the steady-state UV/VIS absorption spectra of all three isomers for MeF and MeBF. These final absorption changes reproduce the known quantum yields.^[17,44]

Thus, the transient absorption maps and transient spectra show unambiguously that MeF and MeBF undergo $E \rightarrow C$ and $E \rightarrow Z$ photoisomerisations in parallel, whereas iPrF and 7rF perform practically only ring closure. All reactions proceed on sub-picosecond time scales, but the $E \rightarrow C$ isomerisations are clearly faster than the $E \rightarrow Z$ isomerisations.

Time profiles

Figure 4.4 shows time profiles of the transient absorptions after excitation of the *E*-isomers at $\lambda_{\text{pump}} = 350$ nm at selected probe wavelengths. The curves at $\lambda_{\text{probe}} = 600$ and 550 nm display bi-exponential decays towards small offsets with a very fast sub-picosecond ESA decay time and a much slower second component of several picoseconds related to the vibrational cooling of the *C*-product molecules. The amplitudes of the slower decays and final offsets show wavelength-dependencies related to the static absorption spectra of the *C*-isomers and are much larger for iPrF/7rF compared to MeF/MeBF because of the higher $E \rightarrow C$ quantum yields.

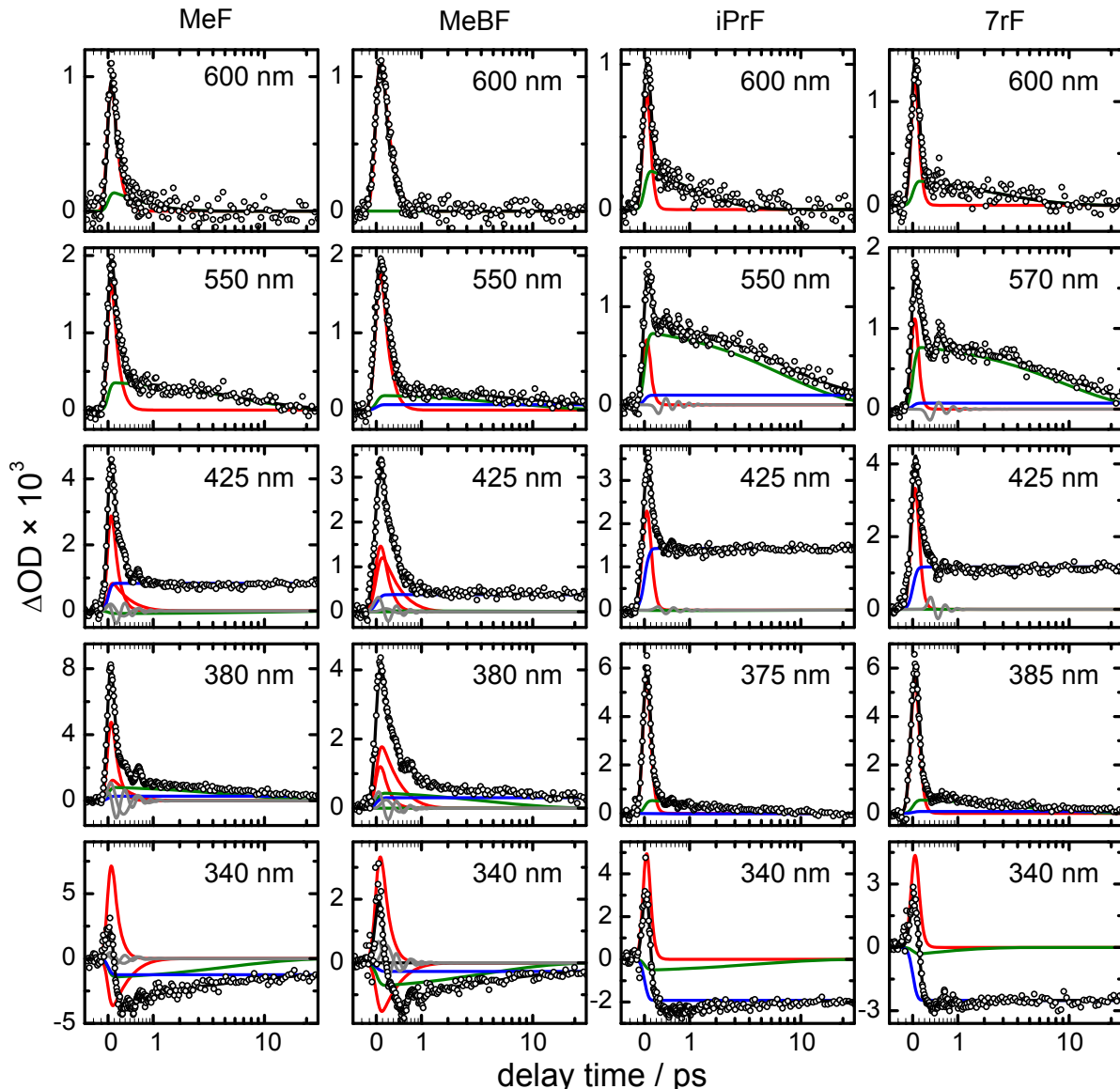


Figure 4.4: Transient absorption-time profiles at selected probe wavelengths after excitation of the *E*-isomers at $\lambda_{\text{pump}} = 350$ nm for delay times (Ref. [43]) from $\Delta t = -0.2$ to 25 ps. Data points are shown by open circles, the global non-linear least-squares fits by black lines. Final offsets are given by blue lines, exponential components by red and green lines, and oscillating components by grey lines.

The selected time profiles at the three shorter probe wavelengths demonstrate clearly that a second, longer sub-picosecond time constant is required to describe the ESA decays of MeF and MeBF. Such components are not required for iPrF and 7rF. The slowest component of several picoseconds is again related to vibrational cooling. The profiles at $\lambda_{\text{probe}} = 340$ nm reflect large permanent GSB. HGSA cannot be discerned at 425 nm, which is in the blue wing of the *C*-isomer absorption, where spectral changes due to vibrational cooling are expected to be small. The HGSA component at shorter probe wavelengths is related to the cooling of the *E*-isomer for iPrF and 7rF, and to the cooling of *E*- and

Z-isomers for MeF and MeBF, with hot *Z*-products dominating at 380 nm. For iPrF and 7rF, the large positive permanent offsets at $\lambda_{\text{probe}} = 425$ nm reflect the high $E \rightarrow C$ quantum yields, whereas the transient absorption decays to a level of practically zero at $\lambda_{\text{probe}} \approx 380$ nm suggest negligible $E \rightarrow Z$ conversion. The final offsets in the case of MeF and MeBF indicate lower $E \rightarrow C$ quantum yields and parallel $E \rightarrow Z$ photoreactions.

Very weak superimposed modulations with two frequency components that appear and decay with the ESA can be seen in the cases of MeF and MeBF. The minute modulations in the time profiles at $\lambda_{\text{probe}} = 425$ nm for iPrF and 7rF have different signatures, with only one frequency and a phase shift from the blue to the red wing of the *C*-HGSA band.

All time profiles were analysed in the way described previously for MeF^[34] by global non-linear least-squares fits using decaying exponentials with time constants τ_1 and τ_2 for the ESA decays and time constant τ_3 for vibrational cooling. The results are compiled in Table 4.2. To take into account different cooling times of the three isomers, τ_3 was allowed to vary with wavelength. Damped oscillatory components with appropriate phases and delays were included to accommodate the observed modulations. The damping times τ_d were equal to the ESA decay time τ_2 for MeF and MeBF. Values of $\tau_d = 0.4(2)$ ps significantly larger than the ESA decay time, an additional delay of 0.2 ps and phase shifts of zero ($\lambda_{\text{probe}} = 470 - 655$ nm) and π ($\lambda_{\text{probe}} = 425$ nm) were found in the case of iPrF and 7rF.

Table 4.2: Time constants and vibrational frequencies from global fits of the transient absorption time profiles (standard deviations of 2σ in the last digits in parentheses).

	τ_1/ps	τ_2/ps	τ_3/ps^a	τ_3/ps^b	ω_1/cm^{-1}	ω_2/cm^{-1}
MeF	0.11(2)	0.33(2)	6.4(21)	7.5(40)	55(03)	106(02)
MeBF	0.14(1)	0.35(4)	6.1(31)	8.6(37)	61(41)	104(26)
iPrF	0.05(1)	—	5.5(29)	8.4(17)	113(9)	—
7rF	0.05(1)	—	5.4(20)	10.0(20)	90(9)	—

^a Averaged from $\lambda_{\text{probe}} = 315-450$ nm. ^b Averaged from $\lambda_{\text{probe}} = 470 - 655$ nm.

4.4 Discussion

The present transient absorption results reveal, how the excited-state dynamics and the photoswitching properties of the selected fulgides tune with targeted structural modifications.

Time constants and ultrafast dynamics

The described spectro-temporal transient absorption maps and time profiles demonstrate that MeF and MeBF undergo $E \rightarrow C$ as well as $E \rightarrow Z$ isomerisation. Both show bi-exponential ESA decays with time constants of $\tau_1 = 0.11 - 0.14$ and $\tau_2 = 0.33 - 0.35$ ps. Conversely, iPrF and 7rF react virtually only to the C -isomers, their single-exponential ESA decay time constants of $\tau_1 = 0.05$ ps have to be associated with the $E \rightarrow C$ reaction times. Since the ultrafast ESA decays of iPrF/7rF and the faster decay components of MeF/MeBF share the same spectral characteristics and magnitudes, the latter can be assigned to the $E \rightarrow C$ reactions of MeF/MeBF. This assignment is corroborated further by the matching fast rise of the C -MeF and C -MeBF product HGSA bands. The time constants τ_2 that describe the slower ESA decay components of MeF/MeBF should therefore refer to the respective $E \rightarrow Z$ isomerisations. The observed ESA is thus comprised of two spectrally overlapping bands, an ESA₁ band that extends over the whole spectral range, decays with τ_1 and is related to the $E \rightarrow C$ isomerisation, and an ESA₂ band, which occurs only at $\lambda_{\text{probe}} < 450$ nm, decays with τ_2 and belongs to the $E \rightarrow Z$ reaction.

This behaviour is not compatible with the decay of a single photo-excited species on a single excited-state pathway, but can be explained by two distinctive excited-state reaction pathways leading towards the C - and Z -isomer products. In that case, different regions of the excited-state potential energy hypersurface are accessed via the respective routes, giving rise to the observed two different ESA bands. Furthermore, different isomerisation times for the two products are expected. Two scenarios are plausible: First, distinct pathways sharing a common origin in the Franck-Condon (FC) region of the photo-excited E_α conformer could be caused by an excited-state branching, similar as supposed for the competing ultrafast *cis-trans* isomerisations and ring closures of cyclohepta-1,3-diene and cyclo-octa-1,3-diene.^[45] As has been noted before,^[13,34] only the E_α conformer needs to be considered as starting structure in this case, since ring closure of the E_β conformer would lead to a severely strained E, Z -cyclohexa-1,3-diene and is not viable, cf. Fig. 4.5. Alternatively, two entirely separate pathways could be caused by conformer-specific $E_\alpha \rightarrow C$ and $E_\beta \rightarrow Z$ photoisomerisations. Besides thermal equilibrium between both conformers (cf. Table 4.3), this relies on the so-called NEER-principle,^[46] i.e., the non-equilibration of the α and β rotamers in the excited states on the short isomerisation times. Thus,

conformation is conserved during the $E \rightarrow C$ and $E \rightarrow Z$ photoreactions, and conformer-specific photochemistry is feasible. This picture confirms our previous interpretation for MeF.^[34] Furthermore, the observed $E \rightarrow C$ isomerisation times agree with reported excited-state lifetimes of related E -fulgides and fulgimides.^[32–34,47,48] The present data do not support an additional slow (16 ps) indirect pathway proposed in the early literature.^[24] The superimposed weak oscillatory components in the absorption maps at early times (≤ 1 ps) featuring frequencies of ≈ 60 and 105 cm^{-1} for MeF and MeBF and $\approx 113 \text{ cm}^{-1}$ (90 cm^{-1}) for iPrF (7rF) are interpreted as signatures of collective low-frequency (e.g., torsional) motions accompanying the major chemical transformations of the molecules along their minimum energy isomerisation routes. Similar behaviour has been observed in previous time-resolved studies of $E \rightarrow Z$ photoisomerisations and excited-state relaxation dynamics.^[49–52] The spectral range, rise and damping of the oscillatory features observed for MeF and MeBF relate them to the ESA₂ component and their $E \rightarrow Z$ reaction. The modulations in the transient absorptions of iPrF and 7rF occur in the C -spectra. The delayed appearances and phase jumps of $\approx \pi$ at the maxima of the C -absorption bands suggest their interpretation as (collective) low-frequency motions in the C -product ground states.^[53] Considering the multi-dimensional structural transformations, we do not attempt to assign them to any specific vibrational modes.

Slightly longer vibrational cooling times of $\tau_3 = 8 - 10$ ps at $\lambda_{\text{probe}} > 470$ nm versus 5–6 ps at shorter wavelengths reflect somewhat slower vibrational cooling of the C -isomers compared to the open isomers.

Photoisomerisation pathways

Most studies of the photo-induced dynamics of fulgides have focused only on the photo-reversible ring closure/ring opening reaction pathways.^[24,26–33,35–37] However, as Fig. 4.5 reveals, the central HT unit in principle offers three reactive sites that may contribute to electronic deactivation or lead to isomerisation of the E -isomers.

Whereas the HT moiety as a whole allows for the desired electrocyclic $E \rightarrow C$ ring closure, additional $E \rightarrow Z$ isomerisation pathways are provided by the C⁴=C⁵ ethylenic double bond (leading to the Z -isomer), and by the C⁶=C⁷ isopropenylic double bond, where isomerisation results exclusively in ultrafast^[54] electronic deactivation since product and reactant are the same. Conformation is conserved for all three reaction pathways indicated in Fig. 4.5. These characteristic features distinguish the photo-induced dynamics of E -fulgides from a simple ring closure.

In line with evidence from other pericyclic ring closure and $E \rightarrow Z$ isomerisation reactions,^[55–58] the observed time scales τ_1 and τ_2 indicate that the photo-excited molecules return to the E reactant and C resp. Z product minima in the electronic ground state via

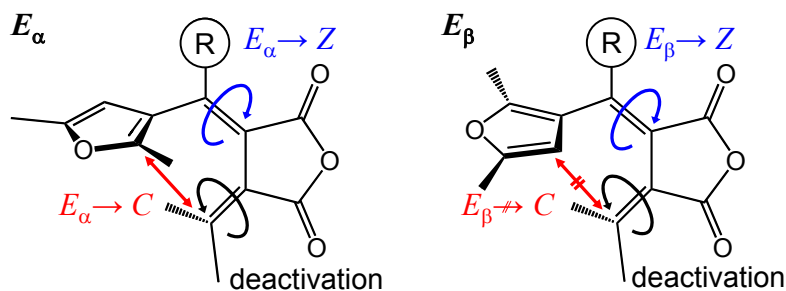


Figure 4.5: Fulgide photoreactions involving the central HT unit: $E \rightarrow C$ ring closure, $E \rightarrow Z$ isomerisation about the $C^4=C^5$ ethylenic double bond and electronic deactivation via degenerate $E \rightarrow Z$ isomerisation of the isopropylenic $C^6=C^7$ double bond. Reactions of the E_α and E_β conformers are shown on the left and right, respectively.

distinct pathways that involve conical intersections (CI). Furthermore, the extremely short ring closure reaction times of only 0.05 – 0.14 ps suggest direct and barrierless $E \rightarrow C$ isomerisation pathways with steep gradients of the excited-state potential energy hypersurfaces (PEHS) along the reaction coordinates. This scenario is in accordance with TDDFT calculations for E_α -MeF,^[34] which suggested a S_1/S_0 CI located at a significantly shortened $C^{7a}-C^7$ distance compared to the reactant molecules at equilibrium. These TDDFT results were confirmed by more recent CASPT2//CASSCF ab initio computations,^[37] which also showed that the photoexcitation of E_α -MeF occurs to an optically bright S_1 state that is zwitterionic in nature. This contrasts with the hexatriene/cyclohexadiene (HT/CHD) system,^[59–63] where a covalent S_1 state determines the photochemistry, and raises questions regarding the applicability of the HT/CHD system as model for fulgides.^[32–34,36,47,48,64]

TDDFT calculations have also supported the feasibility of ultrafast $E \rightarrow Z$ isomerisation reactions via CIs for the E_α and E_β conformers of MeF.^[34] Energetically accessible CIs along a torsional coordinate were indicated for both conformers in agreement with the accepted generic picture for $E \rightarrow Z$ isomerisations in the literature.^[54] The observed oscillatory ESA components suggest that low-frequency torsional degrees of freedom are involved in the excited-state dynamics.

As has been discussed above, the observed ultrafast dynamics may be explained either by conformer-specific $E_\alpha \rightarrow C$ and $E_\beta \rightarrow Z$ photoisomerisations or by a branching of reaction pathways originating from the FC region of the E_α conformer. For further discussion of the significance of these scenarios for the different fulgides, the mole fractions of the E_α conformers in thermal equilibrium, which were calculated via the $E_\beta - E_\alpha$ free energy differences using DFT,^[42] and the resulting $E_\alpha \rightarrow C$ quantum yields $\phi_{E_\alpha C}$ are listed in Table 4.3.

The E -isomer of fulgide 7rF is a pure α conformer, since the β -conformer suffers from severe ring strain. In contrast to a previously published lower value of $x_\alpha \approx 0.6$ for iPrF,^[13] the fulgides with a bulkier alkyl substituent (iPrF and tBuF) are also found to be almost

Table 4.3: Calculated $E_\beta - E_\alpha$ free energy differences ΔG , resulting mole fractions x_α and $E_\alpha \rightarrow C$ quantum yields $\phi_{E_\alpha C}$.

	MeF	MeBF	iPrF	7rF	tBuF
$\Delta G / \text{eV}$	0.017	0.039	0.093	0.379	0.062
x_α	0.66	0.82	0.97	1.00	0.92
$\phi_{E_\alpha C}$	0.34	0.21	0.59	0.53	0.86

pure E_α . The two other fulgides contain larger amounts of the β -conformer in equilibrium at room temperature. The resulting ring closure quantum yields of E_α -MeF and E_α -MeBF are lower than the corresponding values for iPrF, 7rF and tBuF.

Based on these calculations, the absence of detectable $E \rightarrow Z$ isomerisation for iPrF and 7rF could be explained by shifts in the conformer equilibria towards the E_α conformer provided that E_α can only undergo ring closure. This is a strong argument in favour of fully conformer-specific reactions for these two derivatives.

It is, however, doubtful whether MeF and MeBF, which both show $E \rightarrow Z$ isomerisation, also undergo purely conformer-specific reactions. In that case, formation of the Z -product exclusively via the $E_\beta \rightarrow Z$ reaction would require extraordinarily high $\phi_{E_\beta Z}$ quantum yields (≈ 0.83 for MeBF, taking $\phi_{EZ} = 0.15$ and an equilibrium mole fraction of $x_\beta = 1 - x_\alpha = 0.18$ from Table 4.3). This is quite unlikely. Contrary to iPrF and 7rF, at least part of the Z -photoproduct for MeF and MeBF should therefore originate from the E_α conformer. The underlying $E_\alpha \rightarrow Z$ reaction channel is most likely not very efficient and can be considered as minor pathway given its kinetic competition with the $E_\alpha \rightarrow C$ route. MeF and MeBF thus show a propensity towards conformer-specific reactions, where the Z -isomer is formed mostly via the $E_\beta \rightarrow Z$ reaction and E_α reacts preferentially to the C -isomer. The conformer-specific photoreactivity of the E -isomers might offer an interesting way to tune the ratio of the competing reactions, if the absorption spectra of both conformers were different. In that case, choosing appropriate wavelengths for preferential or even selective excitation of the conformers should be possible. However, transient absorption data with excitation of E -MeF at $\lambda_{\text{pump}} = 335$ ^[34] and 350 nm did not show significant differences. Furthermore, the quantum yields for excitation of MeF at 335 nm in Table 4.1 agree well with published quantum yields at 366 nm within experimental error.^[44] Thus, at present, there appears to be no experimental evidence for possible wavelength-selective excitation of the two conformers.

The presumed differences of the $E_\alpha \rightarrow Z$ reaction channels between MeF and MeBF on the one hand and iPrF and 7rF on the other suggest that the $E_\alpha \rightarrow Z$ isomerisation is influenced by chemical structure, either indirectly via kinetic competition with the $E_\alpha \rightarrow C$ reaction, or directly, e.g. by additional excited-state energy barriers. That scenario is also suggested by a computational study of the ring closure reaction of E_α -iPrF by Schönborn

et al., which confirmed the $E_\alpha \rightarrow C$ reaction as the preferred pathway, but identified the $E_\alpha \rightarrow Z$ isomerisation about the $C^4=C^5$ ethylenic double bond as well as the deactivation by the degenerate $E \rightarrow Z$ isomerisation of the isopropyleneic $C^6=C^7$ double bond as viable pathways.^[65] Since the latter pathway, which involves a third CI,^[54,65] leads exclusively to electronic deactivation, it would not show up in our experiments. However, it could be responsible for the fairly low photoreaction quantum yields of many fulgide compounds. From the data in Table 4.1, it is evident that electronic deactivation is much more likely for the sterically less hindered fulgides (63 – 68%) than for the constrained fulgides iPrF, 7rF and tBuF (21 – 43%). At least part of this trend could be caused by a decreasing importance of the isopropyleneic pathway with increasing sterical hindrance. However, it must be stressed that electronic deactivation is possible via any of the three pathways and depends on the details of the molecular dynamics leading to the respective conical intersection. Therefore, more detailed considerations regarding the importance of the deactivating isopropyleneic $E \rightarrow Z$ reaction channel are difficult, in particular in view of the lack of experimental information for this reaction.

Effects of chemical modification

Further insight into how chemical structure affects the switching process can be gained by comparing and relating the quantum yields, structural properties and observed ultrafast dynamics of the different fulgides.

The transient absorption data of MeF, iPrF and 7rF show clearly that increasing steric demands by an *iso*-propyl substituent at the C^4 atom or by intramolecular bridging accelerate the photo-induced $E \rightarrow C$ ring closure. The virtually indistinguishable results of iPrF and 7rF, which is fixed in the E_α conformation by the intramolecular bridge, confirm that the detected dynamics in both cases belong exclusively to the photo-excited E_α conformer. Moreover, iPrF and 7rF show a very efficient $E \rightarrow C$ reaction, but no detectable $E \rightarrow Z$ isomerisation. In line with previous arguments,^[13] it is evident from the clear trend of the effective E_α ring closure quantum yields in Table 4.3 that simple shifts of the conformer equilibria towards the E_α conformer cannot account for the observed increases of ϕ_{EC} upon structural modification. Rather, changes in the ultrafast excited-state molecular dynamics must be responsible.

For further discussion, Table 4.4 lists important properties of the E_α electronic ground state structures for the studied fulgides and derivative tBuF calculated by DFT.^[42] The relevant structures and parameters are illustrated in Fig. 4.6.

The structural parameter that should be most directly related to the $E \rightarrow C$ ring closure dynamics by chemical intuition and considering quantum chemical calculations^[34,37] is the distance r_{CC} between the atoms C^{7a} and C^7 that form the single bond during ring closure.

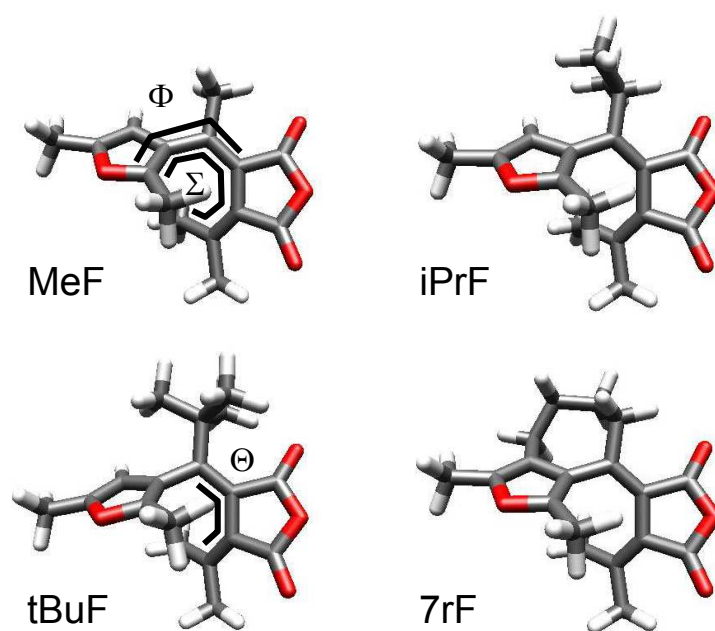
Table 4.4: Parameters of the calculated E_α conformer ground state structures.

	MeF	MeBF	iPrF	7rF	tBuF
$r_{CC} / \text{\AA}$	3.56	3.62	3.56	3.59	3.60
$\Phi / ^\circ$	46	51	53	53	60
$\Theta / ^\circ$	42	40	44	43	51
$\Sigma / ^\circ$	96	99	103	102	119

Quite notably, r_{CC} is hardly affected ($r_{CC} \approx 3.6 \text{ \AA}$) by the chemical modifications and thus cannot explain the observed changes.

In contrast, the torsional angles Φ and Θ change significantly. Larger steric demands lead to an increased torsion of the aryl moiety about the C^{3a} - C^4 bond, with angles Φ ranging from 46° in MeF to 60° in tBuF. Similar, but less pronounced effects are seen for the dihedral angle Θ , which is related to the torsion of the succinic anhydride part. In particular the bulky *tert*-butyl substituent causes a significant increase to $\Theta = 51^\circ$. The benzo-annulation of the furyl group has opposing effects on the torsional angles, with Φ increased to 51° , but Θ lowered to 40° . The structural parameter that correlates closest with the observed ultrafast dynamics and quantum yields is Σ , the sum of the dihedral angles of the HT unit including C^{14} (see Fig. 4.6), which increases from $\Sigma = 96^\circ$ in E_α -MeF to 119° in E_α -tBuF.

This suggests that the relevant effect of the increased steric hindrance is a larger twist of the furyl unit with respect to the isopropylidene group. Since this pre-orientation anticipates partially the structural changes associated with the conrotatory ring closure

**Figure 4.6:** Structures of the E_α conformers of relevant fulgides.

reaction according to the Woodward-Hoffman rules,^[2,66] it could be responsible for the accelerated $E \rightarrow C$ dynamics. The exceptionally fast dynamics leads to high momenta of the atoms that may be decisive for driving the molecules through the S_1/S_0 ring closure CI towards the C -isomer with increased efficiency compared to MeF and MeBF. Therefore, the accelerated ring closure dynamics very likely contributes to the increased $E \rightarrow C$ quantum yields of sterically constrained fulgides. An analogous case of improved photoswitching properties due to accelerated dynamics caused by favourable pre-orientation has been reported for the photo-induced isomerisation of a bridged azobenzene.^[67–70]

Moreover, the competing $E_\alpha \rightarrow Z$ isomerisation about the $C^4=C^5$ ethylenic double bond, as well as the electronic deactivation via the third (isopropylenic) pathway, are impeded more effectively for fulgides with accelerated ring closure by way of kinetic competition. As suggested by quantum dynamics calculations,^[65] larger and heavier alkyl substituents at the C^4 position could also slow down torsion about the $C^4=C^5$ double bond, which is the relevant reaction coordinate for the ethylenic $E \rightarrow Z$ isomerisation.^[54] This would decrease the significance of the $E_\alpha \rightarrow Z$ reaction channel even further.

The comparison of MeF and MeBF provides some insight into the steric and electronic effects of chemical modifications of the furyl unit on the ring closure reaction. The observed ultrafast dynamics for both derivatives show not much difference. The close similarity of the recorded transient absorption maps suggests that significant electronic effects of the benzo-annulation are unlikely. Moreover, the larger benzofuryl unit in MeBF leads to opposing changes of the torsional angles Φ and Θ that compensate each other and apparently do not cause relevant changes in the conformation of the central HT unit. Therefore the effect of benzo-annulation on the ring closure reaction is small.

4.5 Conclusions

In conclusion, we have studied the $E \rightarrow C$ and $E \rightarrow Z$ photoisomerisations of four structurally modified fulgides by femtosecond broadband transient absorption spectroscopy in n -hexane as solvent. Fulgides with increased sterical constraints by a large alkyl substituent at the central HT unit or by intramolecular bridging (iPrF and 7rF) showed a very fast and efficient ring closure of the E_α conformer within only ≈ 50 fs as the only photo-induced isomerisation reaction. In contrast, fulgides MeF and MeBF, which carry the smaller methyl substituent, undergo parallel $E \rightarrow C$ and $E \rightarrow Z$ isomerisations with respective time constants of ≈ 0.12 ps and ≈ 0.34 ps. The reaction times suggest that both photoisomerisations proceed via distinct conical intersections. Direct and barrierless pathways with steep downhill gradients are indicated for the ring closure in agreement with calculations.^[34,37] Our results suggest conformer-specific photoreactions, where ring closure is performed only by the E_α conformer and the Z -isomer is formed mostly via

the $E_\beta \rightarrow Z$ reaction. The $E_\alpha \rightarrow Z$ isomerisation is impeded in particular for iPrF and 7rF by the kinetic competition with the faster $E_\alpha \rightarrow C$ ring closure. DFT calculations of the equilibrium structures showed that increased sterical hindrance not only shifts the conformer equilibria towards the E_α conformer, but also causes a favourable pre-orientation of the furyl unit that accelerates the conrotatory ring closure and explains the more efficient $E_\alpha \rightarrow C$ reaction. Benzo-annulation of the furyl unit does not lead to significant changes in the observed dynamics. Therefore, chemical modifications of the furyl moiety have only small effects on the ring closure reaction and might be used to tune the reverse ring opening reaction without interference. Our results show that the photoswitching properties and the underlying excited-state dynamics of fulgides can be tuned successfully by structural modifications as an alternative to existing coherent control schemes.

Acknowledgments

This work has been supported by the Deutsche Forschungsgemeinschaft through subproject A1 of the SFB 677 “Function by Switching” (RS, FR, FT) and by the Biophotonics Initiative (Grant no. 13N9234) of the German Ministry of Research and Education (FS, JM). The authors thank Bernd Hartke and Jan Boyke Schönborn for stimulating discussions and providing access to their simulation data prior to publication.

References

- [1] H. G. Heller, S. Oliver, *J. Chem. Soc., Perkin Trans. 1* **1981**, 197–201.
- [2] P. J. Darcy, H. G. Heller, P. J. Strydom, J. Whittall, *J. Chem. Soc., Perkin Trans. 1* **1981**, 202–205.
- [3] Y. Yokoyama, *Chem. Rev.* **2000**, *100*, 1717–1739.
- [4] Y. C. Liang, A. S. Dvornikov, P. M. Rentzepis, *Proc. Natl. Acad. Sci. U. S. A.* **2003**, *100*, 8109–8112.
- [5] A. S. Dvornikov, E. P. Walker, P. M. Rentzepis, *J. Phys. Chem. A* **2009**, *113*, 13633–13644.
- [6] I. Willner, S. Rubin, *Angew. Chem. Int. Ed.* **1996**, *35*, 367–385.
- [7] I. Willner, *Acc. Chem. Res.* **1997**, *30*, 347–356.
- [8] S. Z. Janicki, G. B. Schuster, *J. Am. Chem. Soc.* **1995**, *117*, 8524–8527.
- [9] F. M. Raymo, M. Tomasulo, *Chem. Soc. Rev.* **2005**, *34*, 327–336.
- [10] J. Cusido, E. Deniz, F. M. Raymo, *Eur. J. Org. Chem.* **2009**, 2031–2045.
- [11] J. A. Delaire, K. Nakatani, *Chem. Rev.* **2000**, *100*, 1817–1845.
- [12] P. Seal, S. Chakrabarti, *J. Phys. Chem. A* **2010**, *114*, 673–679.
- [13] Y. Yokoyama, K. Ogawa, T. Iwai, K. Shimazaki, Y. Kajihira, T. Goto, Y. Yokoyama, Y. Kurita, *Bull. Chem. Soc. Jpn.* **1996**, *69*, 1605–1612.
- [14] Y. Yokoyama, Y. Shimizu, S. Uchida, Y. Yokoyama, *J. Chem. Soc., Chem. Commun.* **1995**, 785–786.
- [15] F. Strübe, R. Siewertsen, F. D. Sönnichsen, F. Renth, F. Temps, J. Mattay, *Eur. J. Org. Chem.* **2011**, 1947–1955.
- [16] J. Kiji, T. Okano, H. Kitamura, Y. Yokoyama, S. Kubota, Y. Kurita, *Bull. Chem. Soc. Jpn.* **1995**, *68*, 616–619.
- [17] Y. Yokoyama, T. Goto, T. Inoue, M. Yokoyama, Y. Kurita, *Chem. Lett.* **1988**, *17*, 1049–1052.
- [18] Y. Yokoyama, T. Iwami, Y. Yokoyama, Y. Kurita, *Chem. Lett.* **1994**, *23*, 225–226.
- [19] Y. Liang, A. S. Dvornikov, P. M. Rentzepis, *J. Mater. Chem.* **2000**, *10*, 2477–2482.
- [20] M. A. Wolak, C. J. Thomas, N. B. Gillespie, R. R. Birge, W. J. Lees, *J. Org. Chem.* **2003**, *68*, 319–326.
- [21] Y. Yokoyama, T. Tanaka, T. Yamane, Y. Kurita, *Chem. Lett.* **1991**, *20*, 1125–1128.
- [22] A. Tomoda, A. Kaneko, H. Tsuboi, R. Matsushima, *Bull. Chem. Soc. Jpn.* **1993**, *66*, 330–333.
- [23] Y. Yokoyama, T. Sagisaka, Y. Mizuno, Y. Yokoyama, *Chem. Lett.* **1996**, *25*, 587–588.
- [24] M. Handschuh, M. Seibold, H. Port, H. C. Wolf, *J. Phys. Chem. A* **1997**, *101*,

- 502–506.
- [25] F. Renth, M. Foca, A. Petter, F. Temps, *Chem. Phys. Lett.* **2006**, *428*, 62–67.
- [26] Y. Ishibashi, M. Murakami, H. Miyasaka, S. Kobatake, M. Irie, Y. Yokoyama, *J. Phys. Chem. C* **2007**, *111*, 2730–2737.
- [27] T. Cordes, S. Malkmus, J. A. DiGirolamo, W. J. Lees, A. Nenov, R. de Vivie-Riedle, M. Braun, W. Zinth, *J. Phys. Chem. A* **2008**, *112*, 13364–13371.
- [28] S. Draxler, T. Brust, S. Malkmus, J. A. DiGirolamo, W. J. Lees, W. Zinth, M. Braun, *Phys. Chem. Chem. Phys.* **2009**, *11*, 5019–5027.
- [29] Y. Ishibashi, T. Katayama, C. Ota, S. Kobatake, M. Irie, Y. Yokoyama, H. Miyasaka, *New J. Chem.* **2009**, *33*, 1409–1419.
- [30] T. Brust, S. Malkmus, S. Draxler, S. A. Ahmed, K. Rück-Braun, W. Zinth, M. Braun, *J. Photochem. Photobiol. A* **2009**, *207*, 209–216.
- [31] T. Brust, S. Draxler, J. Eicher, W. J. Lees, K. Rück-Braun, W. Zinth, M. Braun, *Chem. Phys. Lett.* **2010**, *489*, 175–180.
- [32] T. Brust, S. Draxler, A. Popp, X. Chen, W. J. Lees, W. Zinth, M. Braun, *Chem. Phys. Lett.* **2009**, *477*, 298–303.
- [33] T. Cordes, T. T. Herzog, S. Malkmus, S. Draxler, T. Brust, J. DiGirolamo, W. J. Lees, M. Braun, *Photochem. Photobiol. Sci.* **2009**, *8*, 528–534.
- [34] R. Siewertsen, F. Renth, F. Temps, F. Sönnichsen, *Phys. Chem. Chem. Phys.* **2009**, *11*, 5952–5961.
- [35] H. Port, P. Gärtner, M. Hennrich, I. Ramsteiner, T. Schöck, *Mol. Cryst. Liq. Cryst.* **2005**, *430*, 15–21.
- [36] J. Voll, T. Kerscher, D. Geppert, R. De Vivie-Riedle, *J. Photochem. Photobiol. A* **2007**, *190*, 352–358.
- [37] G. Tomasello, M. J. Bearpark, R. M. A., G. Orlandi, M. Garavelli, *Angew. Chem., Int. Ed.* **2010**, *49*, 2913–2916.
- [38] J. Saltiel, L. Cires, A. M. Turek, In W. Horspool, F. Lenci, eds., *CRC Handbook Org. Photochem. Photobiol.*, second edn., chap. 27. CRC Press LLC, Boca Raton **2004**, 1–22.
- [39] R. Siewertsen, F. Strübe, J. Mattay, F. Renth, F. Temps, To be published.
- [40] M. Maafi, R. G. Brown, *Photochem. Photobiol. Sci.* **2008**, *7*, 1360–1372.
- [41] Absorption was monitored at 335 nm for *C*-iPrF and 350 nm for *C*-7rF. In each case, absorption traces for iosbestic irradiation (377 and 388 nm) and with irradiation at the respective observation wavelengths were acquired (cf. Ref. 15).
- [42] M. J. Frisch, G. W. Trucks, H. B. Schlegel, G. E. Scuseria, M. A. Robb, J. R. Cheeseman, G. Scalmani, V. Barone, B. Mennucci, G. A. Petersson, H. Nakatsuji, M. Caricato, X. Li, H. P. Hratchian, A. F. Izmaylov, J. Bloino, G. Zheng, J. L.

- Sonnenberg, M. Hada, M. Ehara, K. Toyota, R. Fukuda, J. Hasegawa, M. Ishida, T. Nakajima, Y. Honda, O. Kitao, H. Nakai, T. Vreven, J. A. Montgomery, Jr., J. E. Peralta, F. Ogliaro, M. Bearpark, J. J. Heyd, E. Brothers, K. N. Kudin, V. N. Staroverov, R. Kobayashi, J. Normand, K. Raghavachari, A. Rendell, J. C. Burant, S. S. Iyengar, J. Tomasi, M. Cossi, N. Rega, J. M. Millam, M. Klene, J. E. Knox, J. B. Cross, V. Bakken, C. Adamo, J. Jaramillo, R. Gomperts, R. E. Stratmann, O. Yazyev, A. J. Austin, R. Cammi, C. Pomelli, J. W. Ochterski, R. L. Martin, K. Morokuma, V. G. Zakrzewski, G. A. Voth, P. Salvador, J. J. Dannenberg, S. Dapprich, A. D. Daniels, Ö. Farkas, J. B. Foresman, J. V. Ortiz, J. Cioslowski, D. J. Fox, Gaussian09 Revision A.02, Gaussian Inc., Wallingford CT, 2009.
- [43] To display the transient absorption maps and time profiles with optimal dynamic ranges, they are plotted in this paper using a logarithmic scale by taking $\log(1+\Delta t/\text{ps})$. The scales in the plots were then appropriately relabelled by hand to correctly range from $\Delta t = -0.2$ to 100 ps.
- [44] E. Uhlmann, G. Gauglitz, *J. Photochem. Photobiol. A* **1996**, *98*, 45–49.
- [45] W. Fuß, S. Panja, W. E. Schmidt, S. A. Trushin, *Mol. Phys.* **2006**, *104*, 1133–1143.
- [46] H. J. C. Jacobs, E. Havinga, *Adv. Photochem.* **1979**, *11*, 305–373.
- [47] B. Heinz, S. Malkmus, S. Laimgruber, S. Dietrich, C. Schulz, K. Rück-Braun, M. Braun, W. Zinth, P. Gilch, *J. Am. Chem. Soc.* **2007**, *129*, 8577–8584.
- [48] S. Draxler, T. Brust, S. Malkmus, F. O. Koller, B. Heinz, S. Laimgruber, C. Schulz, S. Dietrich, K. Rück-Braun, W. Zinth, M. Braun, *J. Mol. Liq.* **2008**, *141*, 130–136.
- [49] S. Takeuchi, T. Tahara, *Chem. Phys. Lett.* **2000**, *326*, 430–438.
- [50] B. X. Hou, N. Friedman, M. Ottolenghi, M. Sheves, S. Ruhman, *Chem. Phys. Lett.* **2003**, *381*, 549–555.
- [51] J. Briand, O. Bräm, J. Rehault, J. Leonard, A. Cannizzo, M. Chergui, V. Zanirato, M. Olivucci, J. Helbing, S. Haacke, *Phys. Chem. Chem. Phys.* **2010**, *12*, 3178–87.
- [52] A. J. Wurzer, T. Wilhelm, J. Piel, E. Riedle, *Chem. Phys. Lett.* **1999**, *299*, 296–302.
- [53] A. T. N. Kumar, F. Rosca, A. Widom, P. M. Champion, *J. Chem. Phys.* **2001**, *114*, 701–724.
- [54] B. G. Levine, T. J. Martinez, *Annu. Rev. Phys. Chem.* **2007**, *58*, 613–634.
- [55] R. A. Mathies, C. H. B. Cruz, W. T. Pollard, C. V. Shank, *Science* **1988**, *240*, 777–779.
- [56] W. Fuß, S. Lochbrunner, A. M. Müller, T. Schikarski, W. E. Schmid, S. A. Trushin, *Chem. Phys.* **1998**, *232*, 161–174.
- [57] W. Domcke, D. R. Yarkony, H. Köppel, Eds., *Conical Intersections*, World Scientific, Singapore **2004**.
- [58] S. Aloise, M. Sliwa, Z. Pawlowska, J. Rehault, J. Dubois, O. Poizat, G. Buntinx, A. Perrier, F. Maurel, S. Yamaguchi, M. Takeshita, *J. Am. Chem. Soc.* **2010**, *132*,

- 7379–7390.
- [59] P. Celani, F. Bernardi, M. A. Robb, M. Olivucci, *J. Phys. Chem.* **1996**, *100*, 19364–19366.
- [60] M. Garavelli, P. Celani, M. Fato, M. J. Bearpark, B. R. Smith, M. Olivucci, M. A. Robb, *J. Phys. Chem. A* **1997**, *101*, 2023–2032.
- [61] A. Hofmann, R. de Vivie-Riedle, *J. Chem. Phys.* **2000**, *112*, 5054–5059.
- [62] K. Kosma, S. A. Trushin, W. Fuß, W. E. Schmid, *Phys. Chem. Chem. Phys.* **2009**, *11*, 172–181.
- [63] A. Nenov, P. Kölle, M. A. Robb, R. de Vivie-Riedle, *J. Org. Chem.* **2010**, *75*, 123–129.
- [64] F. O. Koller, W. J. Schreier, T. E. Schrader, S. Malkmus, C. Schulz, S. Dietrich, K. Rück-Braun, M. Braun, *J. Phys. Chem. A* **2008**, *112*, 210–214.
- [65] J. B. Schönborn, A. Koslowski, W. Thiel, B. Hartke, Unpublished work.
- [66] R. B. Woodward, R. Hoffmann, *Angew. Chem. Int. Ed.* **1969**, *8*, 781–853.
- [67] R. Siewertsen, H. Neumann, B. Buchheim-Stehn, R. Herges, C. Näther, F. Renth, F. Temps, *J. Am. Chem. Soc.* **2009**, *131*, 15594–15595.
- [68] M. Böckmann, N. L. Doltsinis, D. Marx, *Angew. Chem. Int. Ed.* **2010**, *49*, 3382–3384.
- [69] O. Carstensen, J. Sielk, J. B. Schönborn, G. Granucci, B. Hartke, *J. Chem. Phys.* **2010**, *133*, 124305/1–124305/12.
- [70] R. Siewertsen, J. B. Schönborn, B. Hartke, F. Renth, F. Temps, *Phys. Chem. Chem. Phys.* **2011**, *13*, 1054–1063.

5 Electronic and Steric Effects on the Photo-Induced $C \rightarrow E$ Ring-Opening of Structurally Modified Furylfulgides

Ron Siewertsen,^a Frank Strübe,^b Jochen Mattay,^b Falk Renth,^{*a} Friedrich Temps^{*a}

^a Institut für Physikalische Chemie, Christian-Albrechts-Universität zu Kiel,
Olshausenstr. 40, D-24098 Kiel, Germany

^b Organische Chemie I, Fakultät für Chemie, Universität Bielefeld, Postfach 100131,
D-33501 Bielefeld, Germany

Reproduced with permission of the PCCP Owner Societies
submitted to Phys. Chem. Chem. Phys. **2011**

- **Own contributions presented in the paper:**
 - Femtosecond time-resolved transient absorption spectroscopy
 - Femtosecond time-resolved fluorescence up-conversion spectroscopy
 - Data analysis and writing of the data analysis software
 - Determination of isomerisation quantum yields
 - Static UV/VIS spectroscopic investigations
 - Quantum chemical calculations

- **Synthesis:** Frank Strübe in the group of Prof. J. Mattay

*To whom correspondence should be addressed. E-mail: temps@phc.uni-kiel.de, renth@phc.uni-kiel.de

Abstract

The ultrafast $C \rightarrow E$ ring-opening dynamics of four selected, structurally or electronically modified furylfulgides have been studied by means of ultrafast broadband transient absorption spectroscopy after femtosecond laser excitation at $\lambda = 500$ nm. A large difference in the dynamics was found in the case of benzannulation at the furyl moiety as an example for an electronic effect compared to furylfulgides carrying sterically different alkyl substituents at the central cyclohexadiene (CHD) ring. The measured very similar spectro-temporal absorption maps for the furylfulgides with a methyl or isopropyl group at the CHD ring or an intramolecular alkyl bridge from the CHD to the furyl moiety showed two distinctive excited-state absorptions with slightly different decay times. The first time constant ($\tau_1 = 0.37 - 0.53$ ps) was assigned to the rapid departure of the excited wavepacket from the Franck-Condon region. The slightly longer second decay time of $\tau_2 = 0.65 - 0.94$ ps, depending on the compound, was attributed to the electronic deactivation and the ring-opening reaction via the conical intersection between the S_1 and S_0 states. In contrast, the benzannulation at the furyl moiety was found to lead to a bi-phasic excited-state decay with $\tau_2 = 4.6$ ps and a much slower additional contribution of $\tau_3 = 16.9$ ps, ≈ 25 times longer compared to the normal furylfulgides. The drastic change is attributed to a trapping of excited molecules in a local potential energy minimum en route to the S_1/S_0 intersection range.

5.1 Introduction

Fulgides are attractive optical molecular switches with excellent thermal stability, low photochemical fatigue and high application potential.^[1–13] Their well-established photochromism rests on the photo-induced ring-opening reaction of the cyclic C -isomer by visible (VIS) light and the reverse ring-closing reaction of the open E -isomer by ultraviolet (UV) light as shown in Fig. 5.1a. Applications of fulgides may suffer, however, from low photochemical quantum yields and from an unwanted isomerisation reaction of the E - to the Z -isomer. A targeted design of optimal fulgide switches thus requires detailed knowledge of the factors that influence the photo-induced molecular reactions. Structural or electronic modifications of the fulgide unit thereby can provide powerful tools to overcome those disadvantages.^[3,14–16]

We recently reported on the preparation and the femtosecond time-resolved photoswitching behaviour of a series of structurally and electronically modified E -furylfulgides.^[15,16] The investigated molecules, which are displayed in Fig. 5.1b, differ from the base compound (MeF) by the replacement of the methyl substituent at the central cyclohexadiene/hexatriene (CHD/HT) switching unit by an isopropyl substituent (iPrF), an in-

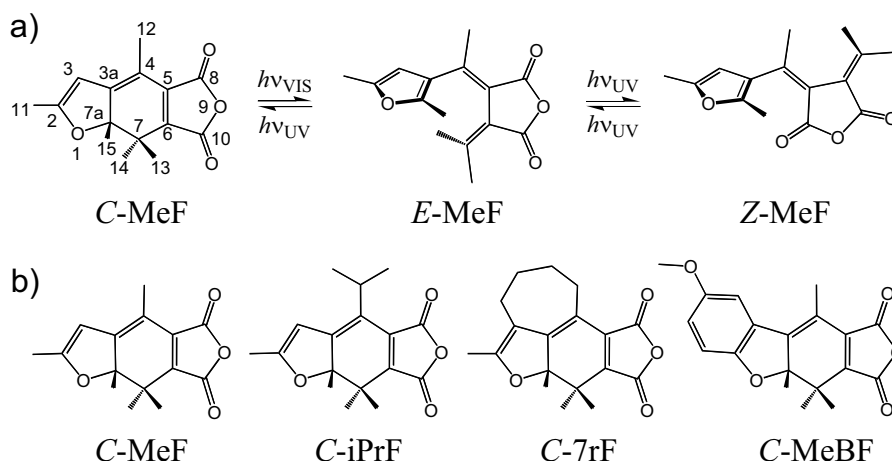


Figure 5.1: a) Photoisomerisation scheme for the furylfulgide MeF. b) *C*-isomers of the investigated furylfulgides MeF, iPrF, 7rF, and MeBF.

tramolecular alkyl bridge to the furyl ring (7rF), or by electronic modification through benzannulation of the furyl group (MeBF). Our results showed that the much higher $E \rightarrow C$ reaction quantum yields of iPrF and 7rF compared to MeF can be traced back to their substantially faster ring-closing reactions, but only a minor influence could be observed in the case of benzannulation (MeBF).^[15] Moreover, the unwanted $E \rightarrow Z$ reaction was efficiently blocked not only in iPrF, which was first studied by Yokoyama *et al.*,^[14] but also in the novel sterically constrained compound 7rF, which is forced by the intramolecular alkyl bridge into the correct configuration for the cyclization reaction.^[15,16]

In this paper, we present the complementary femtosecond time-resolved analysis of the reverse $C \rightarrow E$ ring-opening reactions of the same four furylfulgides initiated by visible light. The effects of the steric modifications on the ring-opening reactions of the *C*-isomers are of interest, because the improvements for the $E \rightarrow C$ channel should not impede the $C \rightarrow E$ reactions. Furthermore, the benzannulation in MeBF might result in a distinctive unidirectional modification of the $C \rightarrow E$ ring-opening reaction. As displayed in Fig. 5.2, the *C*-isomers absorb in the $S_1 \leftarrow S_0$ band in the visible spectrum at wavelengths from $\lambda \approx 400 - 560$ nm with maxima at $\approx 470 - 490$ nm. Since the open isomers do not absorb in that region, the *C*-isomers can be quantitatively switched to the *E*-form by light at ≈ 500 nm. Judged from the similar band structures, the same electronic states are populated at that wavelength in all four derivatives so that a direct comparison of the ensuing molecular switching dynamics appears feasible. The respective open isomers absorb only in the UV with the first maximum between $\lambda = 330 - 340$ nm in the case of the *E*-isomers and $345 - 360$ nm in the case of the *Z*-isomers (cf. Fig. 5.2).

The photo-induced ring-opening reactions of *C*-MeF and *C*-iPrF have been previously investigated by femtosecond spectroscopy,^[17,18] but the limited probe wavelength range ($\lambda_{\text{probe}} > 400$ nm) prevented a direct detection of the resulting *E*-products in those

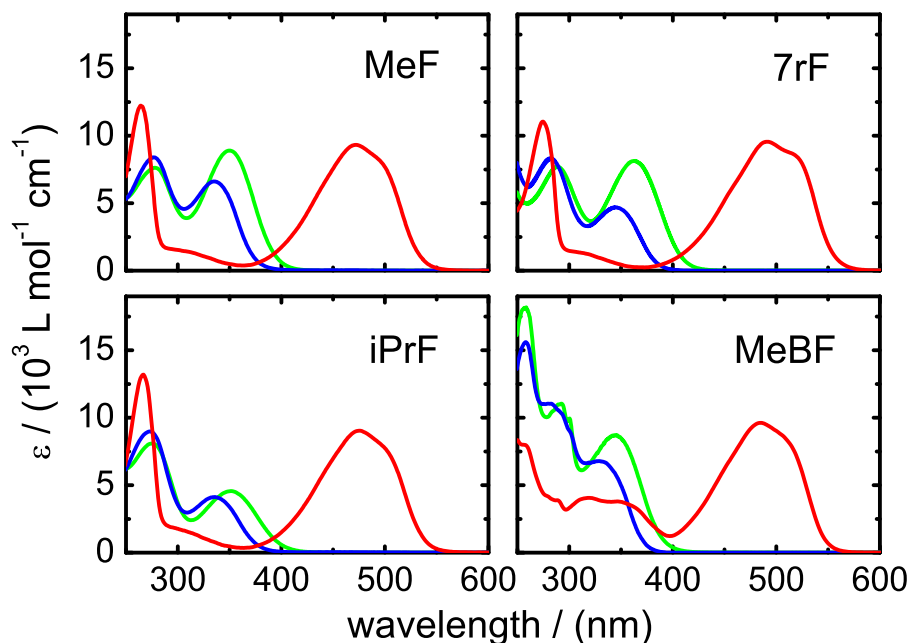


Figure 5.2: Steady-state UV/VIS absorption spectra of the C - (red), E - (blue), and Z - (green) isomers of MeF, iPrF, MeBF and 7rF in n -hexane.

studies. A successive two-photon absorption was proposed to explain observed increased reaction yields after excitation with picosecond laser pulses compared to femtosecond pump pulses.^[18] The ring-opening of related indolyl fulgimides and fulgides has been intensively investigated by the Zinth group,^[19–25] who found an “activated” excited-state reaction with isomerisation times of $\tau = 2 - 15$ ps attributed to a supposed shallow potential energy barrier and dependent on the solvent, excess energy, and chemical modification. No time-resolved experimental data have been available yet to our knowledge for compounds C -7rF and C -MeBF.

We measured the photo-induced $C \rightarrow E$ ring-opening dynamics of the four furylfulgides C -MeF, C -iPrF, C -7rF, and C -MeBF in n -hexane by femtosecond time-resolved broadband absorption spectroscopy with excitation laser pulses at $\lambda_{\text{pump}} = 500$ nm. The photophysical and photochemical transformations of the molecules were monitored all the way from the initially excited states to the thermally equilibrated final products. The experimental results which we present in this paper reveal a drastic difference in the excited-state dynamics between the furylfulgides with alkyl substituents at the CHD unit (C -MeF, iPrF and 7rF) and the benzannulated compound (C -MeBF) with considerable bearing for the design of optimal fulgide switches.

5.2 Experimental Details

The synthesis, isolation, and purification protocols for the different furylfulgide isomers and their UV/VIS absorption spectra have been published earlier.^[15,16] The purities of the products ($> 98\%$) were checked by thin layer chromatography and $^1\text{H-NMR}$ and UV/VIS spectroscopy.

The time-resolved experiments were performed on solutions of the compounds in *n*-hexane (Uvasol, Merck) at room temperature in the photostationary states (PSS) reached by irradiation of the respective *E*-isomers at $\lambda = 365$ nm. This simple and straightforward protocol was fully adequate in the present case because neither the *E*- nor the *Z*-isomers of the compounds absorb at visible excitation wavelengths. Under the conditions used, the *C*-isomer fractions in the PSS at 365 nm ranged from close to 100 % for *C*-iPrF and *C*-7rF, 85 % for *C*-MeF, to $\approx 26\%$ for *C*-MeBF. The sample solutions were pumped through a flow cell with 0.5 mm optical path length for MeF, iPrF, and 7rF and 1 mm path length for MeBF by a peristaltic pump. The concentrations were adjusted to optical densities of ≈ 0.3 at the excitation wavelength. The reservoirs were continuously irradiated at 365 nm to avoid accumulation of photoproducts.

The femtosecond broadband absorption spectrometer based on a regeneratively amplified Ti:Sa laser system (Clark CPA2001) at $\lambda = 775$ nm has been described previously.^[26,27] Briefly, a home-built noncollinear optical parametric amplifier (NOPA) supplied excitation pulses of $0.2\ \mu\text{J}$ at $\lambda_{\text{pump}} = 500$ nm. Broadband supercontinuum probe and reference pulses from $\lambda_{\text{probe}} = 315 - 655$ nm were generated in CaF_2 . The pump polarization with respect to the probe was set to the magic angle. The width of the instrument response function (IRF) determined from the stimulated Raman scattering (SRS) signal was between 60 and 70 fs (Gaussian FWHM) depending on the optical path length. The cross-phase modulation (XPM) was used for time-zero correction, and the SRS and XPM signals were subtracted from the data as described previously.^[27]

5.3 Results

Spectro-temporal absorption maps and transient spectra

The measured two-dimensional (2D) spectro-temporal transient absorption maps after excitation of the four *C*-fulgides at $\lambda_{\text{pump}} = 500$ nm are displayed in Fig. 5.3. The experimental data for MeF, iPrF and 7rF reveal similar photo-induced dynamics and are therefore considered together, the substantially different results for MeBF are described separately thereafter.

The transient absorption maps for the *C*-isomers of MeF, iPrF and 7rF exhibit several positive and negative contributions that light up at $\Delta t = 0$ (time-zero) and are therefore

attributed to ground-state bleaching (GSB, negative), stimulated emission (SE, negative), and excited-state absorption (ESA, positive). The GSB at probe wavelengths of $\lambda \approx 400 - 550$ nm mirrors the static absorption spectra of the molecules. SE appears at $\lambda \gtrsim 550$ nm and exhibits a very fast spectral red-shift of its maximum out of the detection window within the first few hundred fs. ESA is observed in two bands, centered at $\lambda \approx 400$ nm (ESA_1) and ≈ 550 nm (ESA_2). Both bands decay within the first ps, indicating that ultrafast electronic deactivation and chemical transformation of the excited molecules occurs on the sub-picosecond time scale. The stronger ESA_1 band disappears slightly faster than ESA_2 . The ESA_1 contribution spectrally overlaps with the GSB and shows a

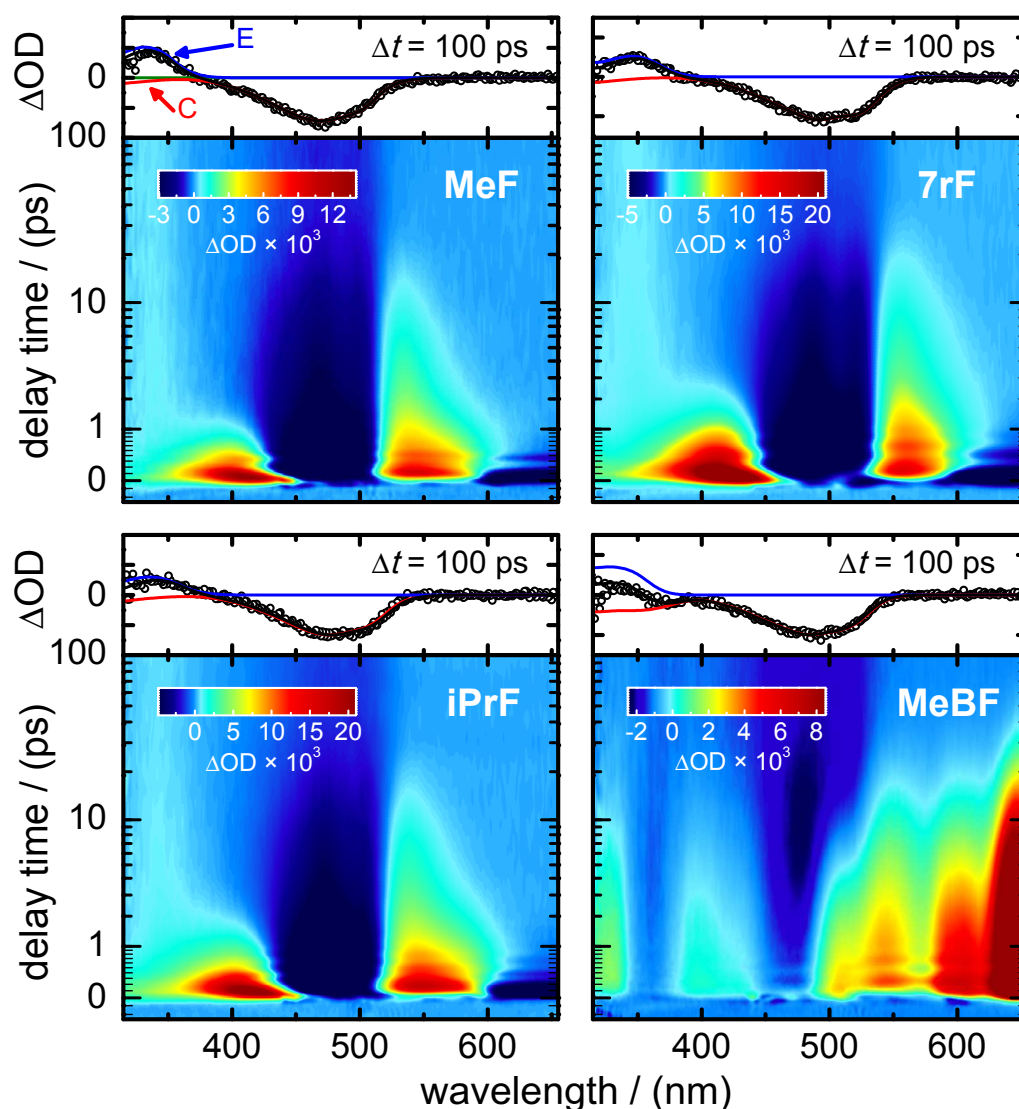


Figure 5.3: Measured spectro-temporal absorption maps after excitation of the C -fulgides at $\lambda_{\text{pump}} = 500$ nm for probe wavelengths between $315 \text{ nm} \leq \lambda_{\text{probe}} \leq 655$ nm and delay times (cf. Ref. [28]) between $-0.2 \text{ ps} \leq \Delta t \leq 100$ ps. The frames above the 2D maps show the spectra at $\Delta t = 100$ ps (150 ps for MeBF; open circles) and fits based on the static UV/VIS spectra of the respective E - and C -isomers (blue and red lines).

blue-shift within the first ≈ 200 fs, which can be seen best in the transient spectra that are given in Fig. 5.4.

The slightly delayed appearance of ESA_2 with respect to time-zero is explained by the simultaneous intense SE in the same wavelength range within the first $\approx 100 - 200$ fs. As can be seen, the SE and ESA_2 contributions show some weak damped oscillatory modulations. Furthermore, ESA_2 is superimposed by hot ground state absorption (HGSA) at $\lambda \approx 500 - 625$ nm from vibrationally excited C -molecules returned to their electronic ground state. The HGSA decay, which can be seen to take place within ≈ 10 ps, is accompanied by corresponding GSB refilling, but a negative amplitude that reflects the $C \rightarrow E$ ring-opening reaction of the molecules remains. The respective product absorption bands (PA) at $\lambda \approx 340$ nm by the resulting E -fulgides at long delay times (≥ 10 ps) are

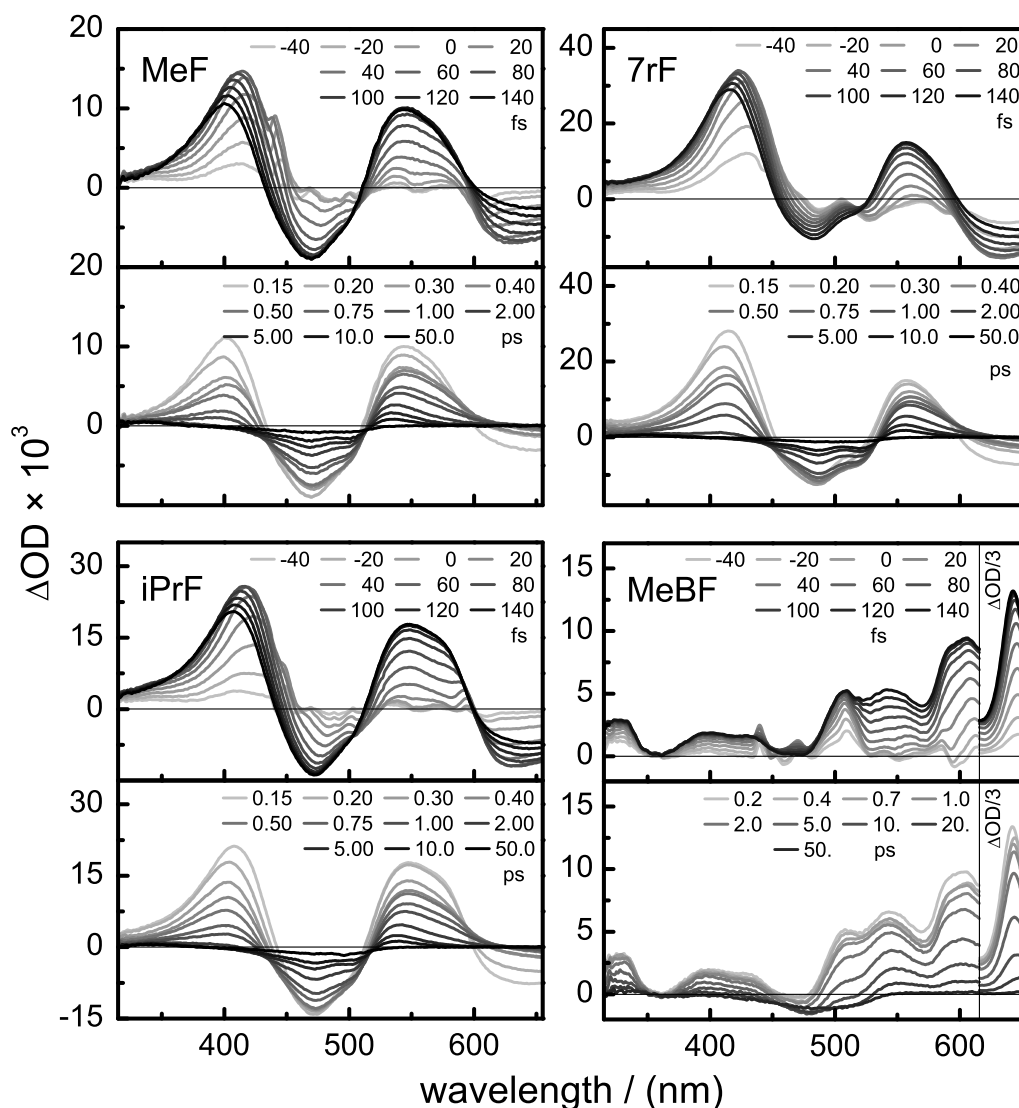


Figure 5.4: Transient spectra after $\lambda = 500$ nm excitation of the four C -fulgides at delay times from $\Delta t = -40$ fs to +50 ps.

matched by the corresponding observed permanent GSB signals. Eventually, the chemical transformations are reflected by the final spectra at $\Delta t = 100$ ps in Fig. 5.3 and their fits by the static UV/VIS difference spectra of the C - and E -fulgides. The early appearance of the PA bands in the transient spectra in Fig. 5.4 confirms the ultrafast nature of the ring-opening reactions for the three C -fulgides (MeF, iPrF, 7rF).

The transient absorption map for C -MeBF, on the other hand, reveals substantial differences in the ensuing dynamics. Compared to C -MeF, C -iPrF or C -7rF, C -MeBF exhibits a large number of ESA bands (cf. Fig. 5.3), which are identified by their immediate rise at $\Delta t = 0$. The additional number is easily explicable by the more extended π -electron system of C -MeBF due to the benzannulation at the furyl moiety. The most prominent ESA bands are now visible at $\lambda \approx 640$ nm and ≈ 600 nm, the former being a factor-of-four more intense than the latter. The striking difference is, however, that the excited-state lifetime of C -MeBF is more than an order of magnitude longer than found for the other three C -fulgides. This is most clearly shown by the strong 640 nm ESA band, which appears to have a decay time between $\approx 10 - 20$ ps.

The C -MeBF absorption map at shorter wavelengths is more complex. The coinciding negative SE band from $\lambda \approx 525 - 625$ nm results in a slightly delayed appearance of the positive ESA band in the same window. Likewise, the weaker contributions between 575 - 315 nm are superimposed by GSB and by C - and E -HGSA. ESA and HGSA contributions mask the expected GSB signal between $\lambda = 550$ and 315 nm for delay times of $\Delta t \lesssim 10$ ps. Based on their comparable time histories alone, it is therefore difficult to separate the ESA and HGSA contributions in the C -MeBF case. The permanent GSB at long delay times from $\lambda = 350 - 550$ nm and the weak PA band at $\lambda \approx 330$ nm eventually confirm the C -MeBF ring-opening and corresponding E -MeBF production, respectively. Thus, the transient spectrum at $\Delta t = 150$ ps in Fig. 5.3 is nicely fitted by the static UV/VIS difference spectrum of the two isomers.

The weak oscillatory modulations in the spectro-temporal transient absorption maps of the molecules have roughly similar low frequencies and damping times for all molecules. Such modulations are indicative of collective low-frequency motions of other molecular groups that accompany the main photochemical transformation of the molecules.^[15,27] As the frequencies, amplitudes and phases depend on the unknown topography of the electronic states involved in the probe transitions, they will not be further discussed in this paper.

Absorption-time profiles at selected wavelengths

Having identified the distinctive contributions to the spectro-temporal transient absorption maps, we turn to the specific time evolutions at a number of representative probe wavelengths. The respective experimental time profiles of the photo-excited *C*-fulgides at five selected wavelengths are displayed in Fig. 5.5. As described in our papers on the *E*-fulgides,^[15,27] the data were analyzed by non-linear least-squares fitting using a sum of exponentials with time constants τ_i and amplitudes a_i convoluted with the IRF. Offsets

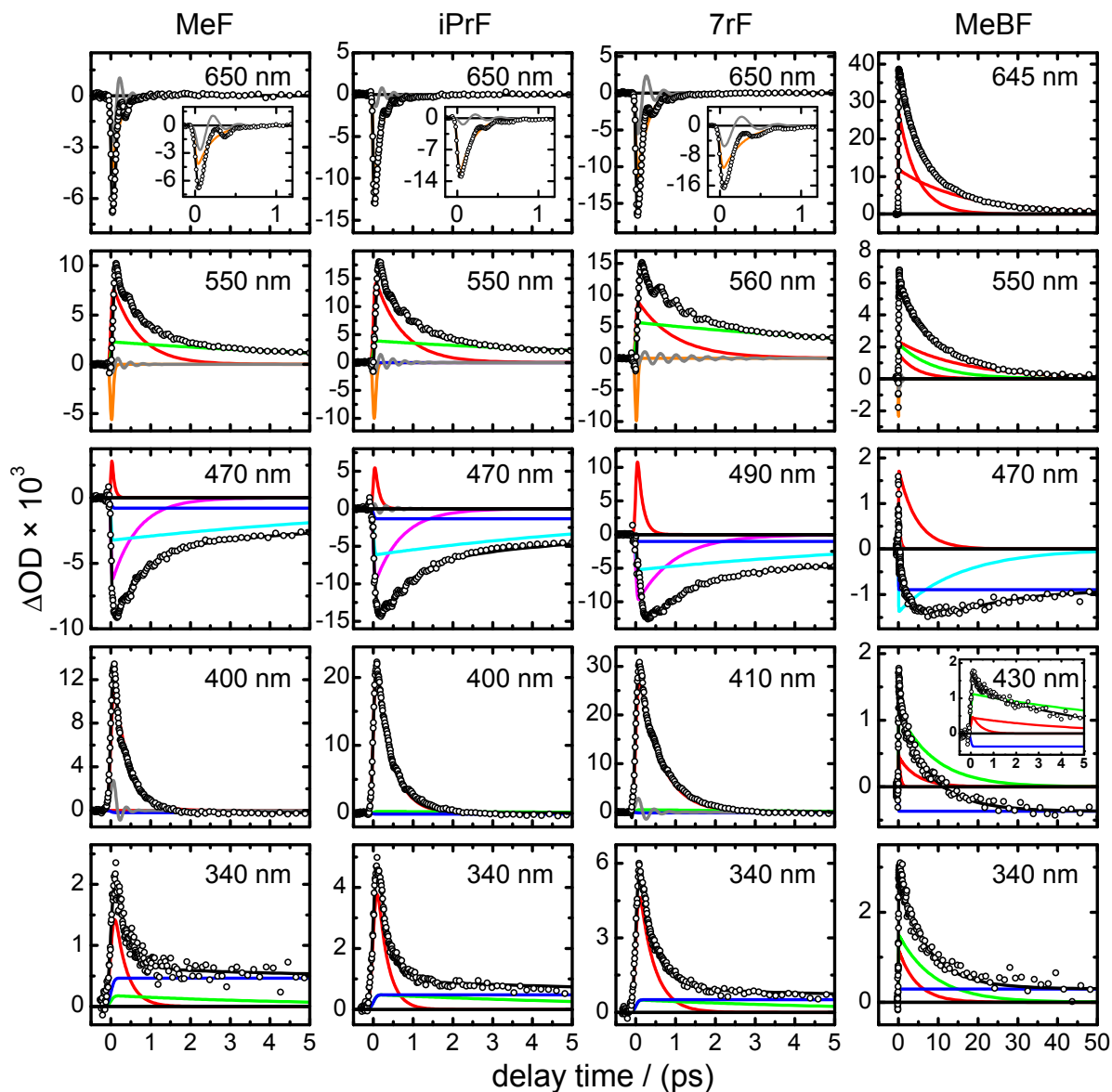


Figure 5.5: Transient absorption traces at representative probe wavelengths after excitation of the *C*-fulgides at $\lambda_{\text{pump}} = 500$ nm. Open circles are data points, black lines represent the overall fits, coloured lines the underlying contributions (SE: orange, ESA: red, HGSA: green, permanent GSB and PA: blue, GSB refilling: magenta and cyan, modulations: grey). The insets show fast decay contributions on an expanded time scale.

were added where appropriate to account for permanent GSB and PA contributions, weak oscillatory motions were described by a damped cosine function. The obtained molecular parameters are compiled in Table 5.1.

The time profiles for C -MeF, C -iPrF and C -7rF in the first three columns of Fig. 5.5 resemble each other closely. Adopting the assignments from the spectro-temporal absorption maps, they represent more or less directly the temporal evolutions of the SE ($\lambda = 650$ nm), ESA₂ (550 – 560 nm), GSB (470 – 490 nm), ESA₁ (400 – 410 nm), PA (340 nm), and the spectrally overlapping HGSA contributions (340 – 560 nm). The main observations are as follows:

(i) Since the SE band at $\lambda = 650$ nm shows a very fast red-shift that moves it out of the detection window (see Figs. 5.3 and 5.4), its temporal evolution cannot be described by a fixed time constant. Trial parameters increased from an IRF-limited $\tau \approx 0.03$ ps in the blue wing to values at $\lambda = 650$ nm of ≈ 0.18 , 0.16, and 0.24 ps for MeF, iPrF, and 7rF, respectively. These values are thus listed in Table 5.1 only for orientation. The very rapid spectral evolution clearly reflects an ultrafast departure of the excited wavepacket on the S_1 potential energy hypersurface (PEHS) from the $S_1 \leftarrow S_0$ Franck-Condon (FC) region.

(ii) At $\lambda \approx 550$ nm, the decay parameters for the ESA₂ band suggest excited-state lifetimes for the C -fulgides between 0.65 ps (MeF, iPrF) to 0.94 ps (7rF; see τ_2 values in Table 5.1). The slightly delayed ESA₂ appearance is caused by the spectral overlap with the SE in the window. As already mentioned, the weak and rapidly damped low frequency ($\approx 85 - 110$ cm⁻¹) modulations of the ESA and the SE are typical for collective low-frequency molecular motions involving other degrees of freedom. Beyond, the 550 nm time profiles show a much slower second decay component due to HGSA by the vibrationally hot C -fulgide molecules in the S_0 state after their electronic deactivation. The obtained 8.2 – 10.6 ps time constants (labeled τ_{HGSA} in Table 5.1) are common for vibrational relaxation of large organic molecules in apolar solvents like n -hexane.

Table 5.1: Time constants for the investigated C -fulgides.

parameter ^a	assignment	MeF	iPrF	7rF	MeBF
τ_1 /ps	ESA	0.37(1)	0.39(1)	0.53(1)	0.39(13)
τ_2 /ps	ESA	0.65(5)	0.68(7)	0.94(6)	4.60(10)
τ_3 /ps	ESA & GSB refill	–	–	–	16.9(4)
τ_{SE} /ps	SE	0.18(2) ^b	0.16(2) ^b	0.24(2) ^b	0.03 ^c
τ_{HGSA} /ps	HGSA & GSB refill	8.4(12)	8.2(14)	10.6(12)	8.6 ^d
ω /cm ⁻¹	osc.	106(20)	110(23)	85(1)	72(1)

^a2 σ error limits of last digits in parentheses, ^bat $\lambda_{\text{probe}} = 650$ nm, ^cfixed (IRF-limited), ^dfixed at HGSA decay time for C -MeBF given in Ref. [15].

(iii) Considering next the absorption-time profiles at $\lambda \approx 400$ nm, the decay times for the ESA₁ band were found to be of the order of $\tau_1 \approx 0.38$ ps for MeF and iPrF and ≈ 0.53 ps for 7rF, about two times shorter than the above τ_2 values. The observed fast spectral blue-shift (Figs. 5.3–5.4) results in an even shorter lifetime for the red wing of the band. The blue-shift and fast decay are compatible with a corresponding rapid detuning of the ESA₁ transition ($S_n \leftarrow S_1$) as the excited wavepacket leaves the initial $S_1 \leftarrow S_0$ FC region.

(iv) The clearly visible GSB refilling that predominates the time profiles in Fig. 5.5 in the $\lambda = 470 - 490$ nm region could be modeled using two exponentials with practically the same time constants as for the slower ESA contribution (τ_2) and the *C*-HGSA decay (τ_{HGSA}). The lifetime τ_2 is therefore assigned to the electronic deactivation of the excited state. The rapid initial decays at $\lambda = 470 - 490$ are attributed to contributions by ESA₁. The permanent negative offset with a relative amplitude of ≈ 10 % of the initial GSB, which remains at long delay times ($\Delta t \geq 30$ ps), reflects the *C*-isomer depletion by the photo-induced $C \rightarrow E$ transformation in good agreement with the observed isomerisation quantum yields ($\phi \approx 0.09$).^[16]

(v) In the time profiles at $\lambda = 340$ nm, the permanent GSB is nicely matched by the corresponding positive PA band from the resulting *E*-isomers. Unfortunately, the expected weak HGSA signal for the *E*-fulgide molecules (*E*-HGSA) cannot be disentangled from the data because of the superimposed ESA₁ and *C*-HGSA bands. Nevertheless, the *E*-PA band clearly indicates the completion of the $C \rightarrow E$ ring-opening reaction within less than a few picoseconds.

The corresponding transient absorption-time profiles for *C*-MeBF in the rightmost column of Fig. 5.5 show additional features compared to *C*-MeF, *C*-iPrF or *C*-7rF. With the much longer excited-state lifetime, which required an extended time scale to display the entire decay plots, the data showcase substantially altered molecular dynamics:

(i) The most striking difference can be immediately seen in the time profile at $\lambda = 645$ nm, where the photo-excited *C*-MeBF molecules exhibit an intense positive transient absorption. This feature is clearly related to an ESA contribution because of the immediate rise and the spectral position at $\lambda > 600$ nm. HGSA can be excluded in this wavelength window by reference to the static *C*-MeBF absorption spectrum in Fig. 5.2. The displayed ESA profile shows a bi-exponential decay with lifetimes $\tau_2 = 4.6$ ps and $\tau_3 = 16.9$ ps from fits at several probe wavelengths in the 600 – 655 nm window.

(ii) Because of the long-lived ESA, the HGSA band of electronically deactivated vibrationally hot *C*-MeBF molecules cannot be extracted from the transient absorption-time profile at $\lambda = 550$ nm, in contrast to the situation for the former three *C*-fulgides. The HGSA lifetime for *C*-MeBF was therefore fixed for the fitting at the value of $\tau = 8.6$ ps determined in our study of *E*-MeBF^[15] and practically equal to the average of the

respective data for MeF, iPrF, and 7rF ($\tau = 9.1$ ps) within experimental errors. The absorption-time profile for C -MeBF at $\lambda = 550$ nm in Fig. 5.5 then consists of three exponentials with already known decay times (4.6, 8.6 and 16.9 ps. As for the other fulgides, the delayed appearance of the ESA at this wavelength was attributed to a superimposed SE contribution with IRF-limited decay. The weak initial modulation of the transient absorption band within the first picosecond seen in the 2D absorption map in Fig. 5.3 could be modeled by a similar frequency as for the other fulgides.

(iii) The C -MeBF time profile at $\lambda = 470$ nm showcases the photo-induced ring-opening reaction of the molecules by the associated permanent GSB signal. The fit to the experimental curve also includes an initial ESA contribution ($\tau_2 = 4.6$ ps) and the subsequent slower GSB refilling that mirrors the excited-state lifetime $\tau_3 = 16.9$ ps of the molecules. As can be seen, ESA and GSB refilling almost compensate each other.

(iv) At $\lambda = 430$ nm, a very fast initial decay suggests a contribution by a short-lived ESA component ($\tau_1 = 0.39$ ps) as found for MeF, iPrF and 7rF, but superimposed other ESA, HGSA and GSB contributions determine the time history beyond the first ps.

(v) Last but not least, the time profile at the shortest probe wavelength, $\lambda = 340$ nm, again shows a mix of ESA and C - and E -HGSA, which cannot be disentangled, but in addition a permanent positive offset by PA from to the resulting E -fulgide, which remains at $\Delta t \geq 40$ ps.

5.4 Discussion

The preceding results demonstrate that the sterically modified fulgides C -MeF, C -iPrF and C -7rF exhibit fairly similar photo-induced dynamics, whereas the benzannulated derivative C -MeBF shows quite different behaviour.

Ring-opening dynamics of MeF, iPrF and 7rF

The results for the furylfulgides with different alkyl substituents demonstrate very fast electronic deactivation and ring-openings on the sub-picosecond time scale. The observed ESA bands decay with lifetimes of $\tau_1 = 0.37 - 0.53$ ps and $\tau_2 = 0.65 - 0.94$ ps. The ultrafast red-shift and decay of the SE and the matching blue-shift of the shorter-lived ESA component allow for the conclusion that τ_1 describes the initial motion of the excited-state wavepackets away from the FC region. This interpretation is further corroborated for C -MeF by the fluorescence lifetime of $\tau_{\text{fl}} = 0.37$ ps, virtually identical with τ_1 , which we measured in a separate experiment by time-resolved fluorescence up-conversion at $\lambda_{\text{fl}} = 675$ nm. Similar assignments have also been made in other cases of bi-exponential excited-state dynamics within < 1 ps.^[29,30] Judged from the short τ_1 values and the significant spectral

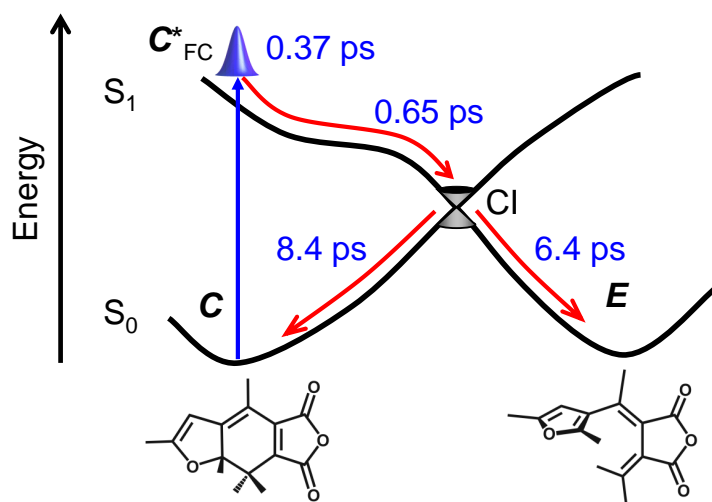


Figure 5.6: Sketch of the photo-induced ring-opening of sterically modified furylfulgides for *C*-MeF as example. The vibrational cooling time for *E*-MeF was taken from Ref. [15]).

shifts, fairly steep gradients of the excited-state PEHS in the vicinity of the FC region can be deduced. Likewise, the slower lifetimes τ_2 can be assigned to the excited-state decays of the molecules to their electronic ground states and the respective *C*-to-*E*-transformations via the conical intersection (CI) connecting the two states. Here, we emphasize that τ_2 is also important for the temporal GSB refilling. The similar sub-picosecond lifetimes suggest that the pathways for the three sterically modified furylfulgides are practically identical without significant potential energy barriers. The subsequent HGSA decays within $\tau \approx 9$ ps reflect the slower cooling of the vibrationally excited *C*-molecules after conversion to the electronic ground state. The data agree well with previous studies of the ring-opening reaction of *C*-MeF in toluene and *C*-iPrF in *n*-hexane,^[17,18] where the fast ESA component was not resolved due to the limited probe wavelength range, however. The quoted longer isomerisation time of *C*-MeF in toluene (1.2 ps) compared to the present value in *n*-hexane (0.65 ps) hints at a possible effect of solvation on the excited-state dynamics.

The proposed scenario, which is depicted schematically in Fig. 5.6, is supported by time-dependent density functional (TDDFT) geometry optimisations of *C*-MeF in the first excited state^[27] and, in particular, by more recent CASPT2//CASSCF results.^[31] The latter calculations^[31] suggested that the optically bright S_1 state of the *C*-furylfulgides is strongly dipolar and has an almost zwitterionic, charge-transfer character. Indications for an excited-state minimum at an elongated C^{7a} - C^7 distance (see Fig. 5.1 for numbering) from the TDDFT calculation were confirmed by the higher-level study, which suggested an energy barrier of ≈ 20 kJ mol⁻¹ on the excited-state PEHS that must be overcome on the way to the CI between the S_1 and S_0 states.^[31] Our time-resolved experimental data do, however, suggest that the impact of a potential energy barrier on the excited-state dynamics must be rather small. This could be due to the excess energy of the photo-excited

molecules in the S_1 state or to possible solvation effects on the shape of the PEHS. On the other hand, an extended rather flat region on the excited-state PEHS further away from the FC region (see Fig. 5.6) is supported by the observed bi-phasic ESA decay behaviour. Based on our present experimental data, a longer-lived intermediate excited-state species can be ruled out. The very different situation for the benzannulated MeBF is addressed below.

Last but not least, the agreement of the experimental and theoretical results on the photo-induced ring-closure reaction^[27] and the ring-opening reaction of MeF emphasizes the relevance of the optically bright zwitterionic S_1 state for the photochemistry of the sterically modified furylfulgides.^[31] The picture thus contrasts with the covalent S_1 state that determines the photochemistry of the CHD/HT system^[32–37] and questions the applicability of CHD/HT as a model system for furylfulgides.^[37]

Ring-opening dynamics of C -MeBF

As noted, the transient absorption map for the photo-excited benzanulated furylfulgide C -MeBF features strong additional ESA contributions at $\lambda_{\text{probe}} > 600$ nm compared to C -MeF, C -iPrF or C -7rF, which allow us to disentangle the excited-state time evolution from vibrational cooling processes in the electronic ground state. Modelling of the observed ESA decay for C -MeBF required two much slower components ($\tau_2 = 4.6$ ps and $\tau_3 = 16.9$ ps) than for the former fulgides. Although not easy to discern, the dynamics at very early times (< 0.5 ps) appear to resemble the above described behaviour. As above, the SE as well as the first ESA component ($\tau_1 = 0.39$ ps) and their ultrafast spectral shifts can be rationalised by assuming a fast departure of the excited-state wavepacket from the FC region due to a steep initial gradient of the S_1 PEHS. Conversely, the observed considerable increase of the excited-state lifetime revealed by the slower ESA contributions (τ_2, τ_3) reflect substantial changes in the excited-state dynamics thereafter. As argued in the results section, considering the lack of noticeable absorption at $\lambda > 550$ nm in the static UV/VIS spectrum, and considering the immediate rise of the transient absorption with the excitation laser pulse, the intense transient signals for C -MeBF in the spectral range beyond 600 nm cannot arise from HGSA. We therefore conclude that *both* slow ESA components, $\tau_2 = 4.6$ and $\tau_3 = 16.9$ ps, are related to the excited-state dynamics of C -MeBF. Moreover, the nicely matching GSB refilling behaviour, according to the measured spectro-temporal transient absorption maps, provides strong evidence for a bi-phasic excited-state decay. We note that our assigned excited-state lifetimes are considerably longer than the quoted 1.2 ps value in a previous study of the ring-opening of a related benzofurylfulgide, where a slow component of ≈ 13.3 ps was observed in the same spectral range, but ascribed exclusively to vibrational cooling.^[18] Considering the above arguments,

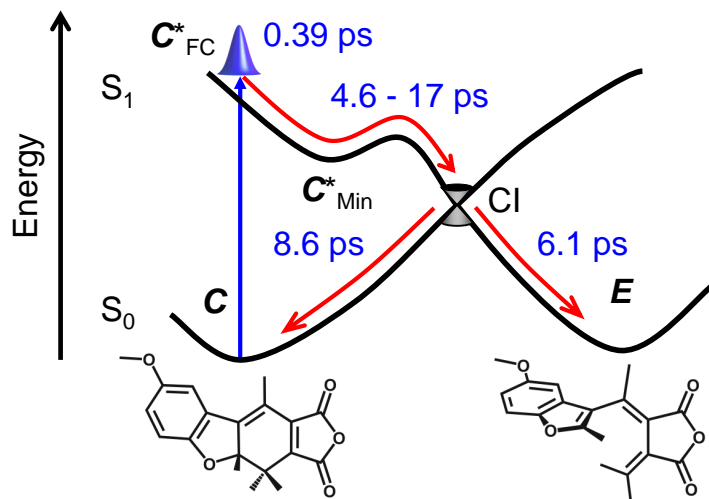


Figure 5.7: Sketch of the S_0 and S_1 potential energy surfaces for MeBF with a pronounced local minimum and an increased potential energy barrier on the S_1 PEHS. The vibrational cooling times for C - and E -MeBF were taken from Ref. [15]).

however, in particular the clearly evident GSB refilling, that interpretation does not seem to hold and the 13.3 ps time constant should be reassigned to the excited-state decay to obtain a consistent picture.

A plausible scenario to rationalize the experimental findings is shown in Fig. 5.7. Accordingly, the longer ESA lifetimes are explained by a fast initial motion of the photoexcited C -MeBF wavepacket away from the FC region to an excited-state intermediate associated with a local minimum C^*_{Min} of the S_1 PEHS. Isomerisation and electronic deactivation from there via the CI with the electronic ground state can evidently take place only after the resulting potential energy barrier before the CI is overcome. The energy barrier, which would explain the increased excited-state lifetime, appears to result from the electronic modification by the benzanullation at the furyl moiety. A similar picture has been put forward for C -indolylfulgides and -fulgimides.^[22–25] The two slower time constants (τ_2 , τ_3) needed to describe the ESA decay may then have several explanations. One possibility is that only a part of the wavepacket is trapped in the excited-state minimum, while another part bypasses the minimum by a slightly different trajectory. Alternatively, the deactivation to the electronic ground state from the excited-state minimum might occur via two different pathways with different energy barriers, a reactive channel leading to the open E -isomer and an unreactive one leading back to the C -isomer. The fact that τ_3 is longer than the vibrational cooling time in the electronic ground state implies that τ_3 also describes at least part of the GSB refilling. Further experimental evidence, for example rise time measurements for the E -product, would be needed to identify the ensuing mechanism. That the photo-induced ring-opening of C -MeBF is slower, while its $C \rightarrow E$ quantum yield ($\phi = 0.16$) is higher than for MeF, iPrF or 7rF ($\phi \approx 0.09$),^[16] contrasts with the

usually observed inverse correlation between quantum yields and isomerisation times.^[25] This effect may be explained by a higher excited-state potential energy barrier along the unreactive deactivation pathway leading back to the C -reactant compared to the reactive pathway to the E -product.

Structural effects and comparison of the ring-opening and ring-closure dynamics

Our previous femtosecond time-resolved transient absorption studies^[15,27] showed that the photo-induced ring-closure reactions of the E -isomers of MeF, iPrF, 7rF and MeBF occur on a barrierless pathway. The ring-closure reactions for all four compounds were found to be much faster ($\tau = 0.05 - 0.14$ ps)^[15] than the reverse ring-openings measured here. The correct pre-orientation of the molecular moieties in the E -fulgides is obviously a major point of importance, and strong attractive forces along the ring-closure coordinate appear to play very effective roles as well. The increased steric constraints by the isopropyl group in iPrF and the intramolecular bridging in 7rF were shown to lead to accelerated ultrafast $E \rightarrow C$ reactions and to much better $E \rightarrow C$ isomerisation quantum yields. At the same time, the competing $E \rightarrow Z$ reactions became negligible.^[15,27] Those steric modifications are clearly without much effect on the $C \rightarrow E$ ring-opening. Quite the contrary, the electronic effect by the benzanullation, which has little effect on the ring-closure of the E -fulgide (E -MeBF), appears to lead to the presence of an excited-state potential energy barrier along the ring-opening reaction and electronic deactivation pathway of the C -fulgide (C -MeBF) and a correspondingly increased excited-state lifetime. Despite the slower reaction, the ring-opening quantum yield for C -MeBF is fairly high compared to other fulgides and fulgimides.^[3,16,25] Unlike the ring-closure of the E -fulgides,^[15] the ring-opening efficiency thus does not benefit from accelerated excited-dynamics.

5.5 Conclusion

In conclusion, we have investigated the $C \rightarrow E$ ring-opening reactions of four structurally modified C -fulgides in solution in n -hexane using femtosecond broadband transient absorption spectroscopy after excitation at $\lambda = 500$ nm. The replacement of the methyl substituent at the central cyclohexadiene switching unit in MeF by isopropyl (iPrF) or by an intramolecular bridge (7rF) was found to affect the excited-state dynamics only little. Ultrafast departures of the excited wavepackets from the FC regions in times of $\tau_1 = 0.37 - 0.53$ ps followed by sub-picosecond electronic deactivation and ring-opening times of $\tau_2 = 0.65 - 0.94$ ps were observed. Thus, contrary to chemical intuition, the ring-opening reactions of the three furylfulgides are much slower than their ring-closure

reactions ($\tau = 0.11 - 0.05$ ps).^[15] Benzannulation at the furyl group (MeBF) was found to lead to strongly increased excited-state lifetimes ($\tau_2 = 4.6$ ps and $\tau_3 = 16.9$ ps). The latter value is ≈ 25 times longer than for the parent compound MeF. The long-lived excited-state absorption of the benzannulated fulgide was attributed to a trapping of the excited wavepacket in a local S_1 potential energy minimum and a sizable energy barrier en route to the conical intersection from the S_1 to the S_0 state. Surprisingly, the slower reaction of *C*-MeBF is accompanied by a higher ring-opening quantum yield than for the other fulgides. This effect may be explained by a selectively increased excited-state energy barrier along the unreactive deactivation pathway leading back to the *C*-reactant compared to the reactive pathway to the *E*-product. The effect of the structural and electronic modifications on the excited-state lifetimes may be used for selective improvements of the photoswitching dynamics of the fulgides.

Acknowledgment

This work has been supported by the Deutsche Forschungsgemeinschaft through project A1 of the Collaborative Research Centre 677 “Function by Switching” (RS, FR, FT) and by the Biophotonics Initiative (Grant No. 13N9234) of the Federal Ministry of Education and Research (FS, JM). The authors thank Bernd Hartke and Jan Boyke Schönborn for stimulating discussions and access to their results prior to publication.

References

- [1] H. G. Heller, S. Oliver, *J. Chem. Soc., Perkin Trans. 1* **1981**, 197–201.
- [2] P. J. Darcy, H. G. Heller, P. J. Strydom, J. Whittall, *J. Chem. Soc., Perkin Trans. 1* **1981**, 202–205.
- [3] Y. Yokoyama, *Chem. Rev.* **2000**, *100*, 1717–1739.
- [4] I. Willner, S. Rubin, *Angew. Chem. Int. Ed.* **1996**, *35*, 367–385.
- [5] I. Willner, *Acc. Chem. Res.* **1997**, *30*, 347–356.
- [6] A. S. Dvornikov, Y. Liang, C. S. Cruse, P. M. Rentzepis, *J. Phys. Chem. B* **2004**, *108*, 8652–8658.
- [7] A. S. Dvornikov, E. P. Walker, P. M. Rentzepis, *J. Phys. Chem. A* **2009**, *113*, 13633–13644.
- [8] Y. C. Liang, A. S. Dvornikov, P. M. Rentzepis, *Proc. Natl. Acad. Sci. U. S. A.* **2003**, *100*, 8109–8112.
- [9] S. Z. Janicki, G. B. Schuster, *J. Am. Chem. Soc.* **1995**, *117*, 8524–8527.
- [10] F. M. Raymo, M. Tomasulo, *Chem. Soc. Rev.* **2005**, *34*, 327–336.
- [11] J. Cusido, E. Deniz, F. M. Raymo, *Eur. J. Org. Chem.* **2009**, 2031–2045.
- [12] J. A. Delaire, K. Nakatani, *Chem. Rev.* **2000**, *100*, 1817–1845.
- [13] P. Seal, S. Chakrabarti, *J. Phys. Chem. A* **2010**, *114*, 673–679.
- [14] Y. Yokoyama, T. Goto, T. Inoue, M. Yokoyama, Y. Kurita, *Chem. Lett.* **1988**, *17*, 1049–1052.
- [15] R. Siewertsen, F. Renth, F. Strübe, J. Mattay, F. Temps, *Phys. Chem. Chem. Phys.* **2011**, *13*, 3800–3808.
- [16] F. Strübe, R. Siewertsen, F. D. Sönnichsen, F. Renth, F. Temps, J. Mattay, *Eur. J. Org. Chem.* **2011**, 1947–1955.
- [17] Y. Ishibashi, M. Murakami, H. Miyasaka, S. Kobatake, M. Irie, Y. Yokoyama, *J. Phys. Chem. C* **2007**, *111*, 2730–2737.
- [18] Y. Ishibashi, T. Katayama, C. Ota, S. Kobatake, M. Irie, Y. Yokoyama, H. Miyasaka, *New J. Chem.* **2009**, *33*, 1409–1419.
- [19] S. Malkmus, F. O. Koller, B. Heinz, W. J. Schreier, T. E. Schrader, W. Zinth, C. Schulz, S. Dietrich, K. Rück-Braun, M. Braun, *Chem. Phys. Lett.* **2006**, *417*, 266–271.
- [20] F. O. Koller, W. J. Schreier, T. E. Schrader, A. Sieg, S. Malkmus, C. Schulz, S. Dietrich, K. Rück-Braun, W. Zinth, M. Braun, *J. Phys. Chem. A* **2006**, *110*, 12769–12776.
- [21] B. Heinz, S. Malkmus, S. Laimgruber, S. Dietrich, C. Schulz, K. Rück-Braun, M. Braun, W. Zinth, P. Gilch, *J. Am. Chem. Soc.* **2007**, *129*, 8577–8584.

- [22] T. Brust, S. Draxler, S. Malkmus, C. Schulz, M. Zastrow, K. Rück-Braun, W. Zinth, M. Braun, *J. Mol. Liq.* **2008**, *141*, 137–139.
- [23] T. Brust, S. Malkmus, S. Draxler, S. A. Ahmed, K. Rück-Braun, W. Zinth, M. Braun, *J. Photochem. Photobiol., A* **2009**, *207*, 209–216.
- [24] S. Draxler, T. Brust, S. Malkmus, J. A. DiGirolamo, W. J. Lees, W. Zinth, M. Braun, *Phys. Chem. Chem. Phys.* **2009**, *11*, 5019–5027.
- [25] T. Brust, S. Draxler, J. Eicher, W. J. Lees, K. Rück-Braun, W. Zinth, M. Braun, *Chem. Phys. Lett.* **2010**, *489*, 175–180.
- [26] F. Renth, M. Foca, A. Petter, F. Temps, *Chem. Phys. Lett.* **2006**, *428*, 62–67.
- [27] R. Siewertsen, F. Renth, F. Temps, F. Sönnichsen, *Phys. Chem. Chem. Phys.* **2009**, *11*, 5952–5961.
- [28] To display the transient absorption maps with optimal dynamic ranges, they are plotted using a logarithmic scale by taking $\log(1 + \Delta t/\text{ps})$. The plot scale was then relabelled to correctly range from $\Delta t = -0.2$ to 100 ps.
- [29] H. Satzger, S. Spörlein, C. Root, J. Wachtveitl, W. Zinth, P. Gilch, *Chem. Phys. Lett.* **2003**, *372*, 216–223.
- [30] R. Siewertsen, J. B. Schönborn, B. Hartke, F. Renth, F. Temps, *Phys. Chem. Chem. Phys.* **2011**, *13*, 1054–1063.
- [31] G. Tomasello, M. J. Bearpark, M. A. Robb, G. Orlandi, M. Garavelli, *Angew. Chem.* **2010**, *122*, 2975–2978.
- [32] P. Celani, F. Bernardi, M. A. Robb, M. Olivucci, *J. Phys. Chem.* **1996**, *100*, 19364–19366.
- [33] M. Garavelli, P. Celani, M. Fato, M. J. Bearpark, B. R. Smith, M. Olivucci, M. A. Robb, *J. Phys. Chem. A* **1997**, *101*, 2023–2032.
- [34] A. Hofmann, R. de Vivie-Riedle, *J. Chem. Phys.* **2000**, *112*, 5054–5059.
- [35] K. Kosma, S. A. Trushin, W. Fuß, W. E. Schmid, *Phys. Chem. Chem. Phys.* **2009**, *11*, 172–181.
- [36] A. Nenov, P. Kölle, M. A. Robb, R. de Vivie-Riedle, *J. Org. Chem.* **2010**, *75*, 123–129.
- [37] J. B. Schönborn, J. Sielk, B. Hartke, *J. Phys. Chem. A* **2010**, *114*, 4036–4044.

6 Ultrafast $Z \rightarrow E$ Photoisomerisation of Structurally Modified Furylfulgides

Ron Siewertsen,^a Frank Strübe,^b Falk Renth,^{*a} Jochen Mattay,^b Friedrich Temps^{*a}

^a Institut für Physikalische Chemie, Christian-Albrechts-Universität zu Kiel,
Olshausenstr. 40, D-24098 Kiel, Germany

^b Organische Chemie I, Fakultät für Chemie, Universität Bielefeld, Postfach 100131,
D-33501 Bielefeld, Germany

Manuscript in preparation

- **Own contributions presented in the paper:**
 - Femtosecond time-resolved transient absorption spectroscopy
 - Data analysis and writing of the data analysis software
- **Synthesis:** Frank Strübe in the group of Prof. J. Mattay

*To whom correspondence should be addressed. E-mail: temps@phc.uni-kiel.de, renth@phc.uni-kiel.de

Abstract

Femtosecond broadband transient absorption spectroscopy was used in a comparative study of the ultrafast photo-induced dynamics of the $Z \rightarrow E$ photo-induced isomerisation reactions of four selected photochromic furylfulgides with distinctive structural motifs in *n*-hexane as solvent. The parent compound MeF carrying a methyl group at the cyclohexadiene (cHD) ring was systematically modified by sterically different alkyl substituents, i.e., with an isopropyl group (iPrF) or an intramolecular alkyl bridge from the cHD to the furyl moiety (7rF), or by benzannulation of the furyl moiety as an electronic effect (MeBF). In contrast to the photoexcited *E*-isomers [R. Siewertsen *et al.*, *Phys. Chem. Chem. Phys.* **2011**, *13*, 3800], the ensuing dynamics of the *Z*-isomers turned out to be almost unaffected by either increased steric constraints or electronic effects, except for slightly increased overall excited-state lifetimes of $\tau_{av} = 0.33$ ps for MeF to $\tau_{av} = 0.73$ ps for MeBF due to increased moments of inertia and solvent friction. The transient absorption comprised two distinctive sequential excited-state absorption contributions attributed to the lifetimes of the initial Franck-Condon state from $\tau_1 = 0.12$ ps for MeF to $\tau_1 = 0.24$ ps in the case of MeBF and an intermediate excited state with almost identical lifetimes, suggesting that internal conversion to the intermediate state and to the electronic ground state of the *E*- and *Z*-isomers proceeds via distinctive conical intersections. The results demonstrate that the desired photochromic $E \rightleftharpoons C$ reactions can be tuned selectively by steric and electronic structural modifications without influencing the restoring $Z \rightarrow E$ isomerisation.

6.1 Introduction

Fulgides are an important class of thermally irreversible photochromic switches^[1–3] with high application potential, e.g., as photoswitchable nonlinear optical materials,^[4,5] for optical data storage,^[3,6–8] liquid crystal phase changes,^[9,10] photo-modulation of fluorescence and electron/energy transfer,^[11–13] and photo-control of biomolecules activity.^[14] The desired photochromic behaviour is based on the $E \rightarrow C$ ring closing and reverse $C \rightarrow E$ ring opening electrocyclic reactions between the colorless, open *E*-isomer and the colored, closed *C*-isomer. This is shown in Fig. 6.1 for the prototypical furylfulgide 2-[1-(2,5-dimethyl-3-furyl)-ethylidene]-3-isopropylidene succinic anhydride (MeF). The $E \rightarrow Z$ isomerisation is an undesired non-photochromic side reaction that competes with the $E \rightarrow C$ ring closing and may compromise the performance of fulgide-based functional devices, where photochemical fatigue and the capability for multiple switching cycles are crucial. Therefore, the $E \rightarrow Z$ isomerisation has to be considered relevant, even if its quantum yield $\phi_{E \rightarrow Z}$ is low. Furthermore, the reverse $Z \rightarrow E$ reaction, which has

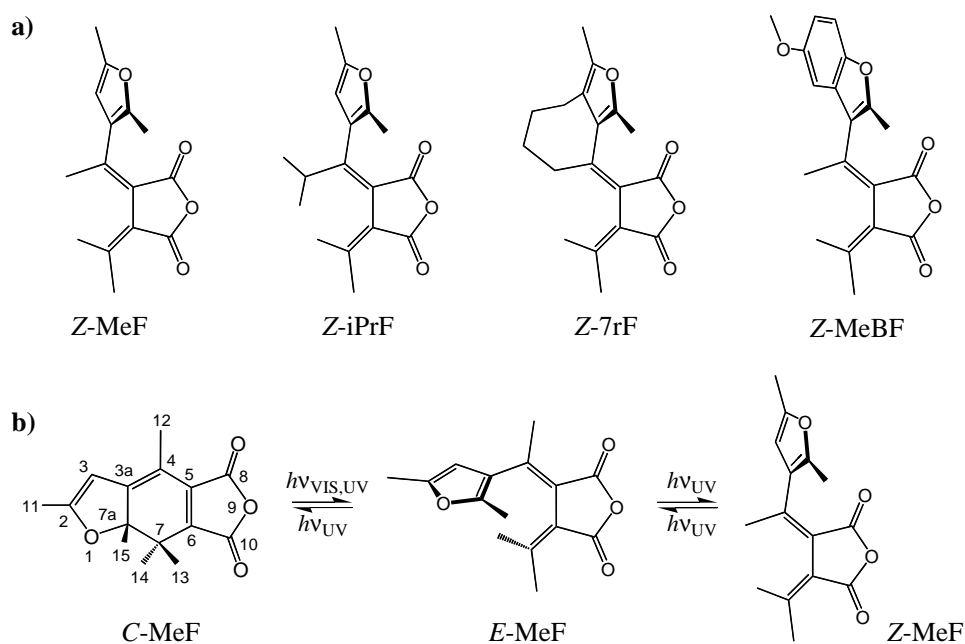


Figure 6.1: a) Structures of the selected four fulgides, b) photoisomerisation reactions for the example of MeF, and atom numbering scheme for *C*-MeF.

been shown to proceed with similar quantum yields as the $E \rightarrow Z$ reaction,^[15–17] gains considerable importance, since it avoids photochemical accumulation of the *Z*-isomer and ensures optical bistability of fulgide switches for practical purposes. The time scales of all reactions of MeF are on the femtosecond to picosecond range,^[16,18–22] which enables efficient photoreactions with low photochemical fatigue.

The effects of steric and electronic modifications on the dynamics of the competing $E \rightarrow C$ and $E \rightarrow Z$ reactions^[16,21] following excitation of the *E*-isomer and the $C \rightarrow E$ ring opening^[22] of MeF and its derivatives (structures shown in Fig. 6.1a) have been elucidated in two previous studies. It has turned out that the photoisomerisation properties of MeF could be improved much in structurally modified fulgides with increased steric constraints by replacing the methyl substituent at C^4 by an isopropyl substituent (iPrF) or by intramolecular bridging in 7rF.^[17,21,23] Electronic effects, e.g., by benzannulation of the furyl ring in the modified fulgide MeBF, or by exchange of the furyl unit by other heteroaromatic systems were shown to lower the photochemical fatigue.^[3,24–26]

Our results revealed strong steric effect on the photo-induced dynamics of the *E*-isomer, whereas the electronic effect of benzannulation did not lead to remarkable changes in the ultrafast ring closure dynamics.^[21,22] Derivatives with small substituents at C^4 (MeF and MeBF) showed parallel $E \rightarrow C$ and $E \rightarrow Z$ photoreactions involving distinctive conical intersections (CI) with respective time constants of $\tau \approx 0.12$ ps and $\tau \approx 0.34$ ps. In contrast, the derivatives with increased sterical hindrance by larger substituents (iPrF) or intramolecular bridging (7rF) lead to an even faster ring closure ($\tau = 0.05$ ps) with

much higher $E \rightarrow C$ quantum yields, but no noticeable $E \rightarrow Z$ isomerisation. The results could be explained by conformer-specific photochemical reactions, where the exclusive ring closure of the E_α -conformer is accelerated by favorable pre-orientation of the furyl unit due to sterically demanding groups. The $E \rightarrow Z$ isomerisation of MeF and MeBF occurs predominantly by the non-cyclizable E_β -conformer, and is inhibited for iPrF and 7rF due to kinetic competition with the accelerated $E \rightarrow C$ channel and a decreased population of the E_β -conformer.^[21]

Conversely, the excited-state $C \rightarrow E$ ring opening reaction of MeF was hardly affected by steric effects, but strongly influenced by the benzannulation.^[22] For MeF, iPrF and 7rF barrierless ultrafast excited state dynamics could be observed with $C \rightarrow E$ isomerisation times of $\tau < 1$ ps. Benzannulation in MeBF led to a strongly increased, longer-lived excited-state absorption with $\tau = 16.9$ ps. This was explained by the involvement of a minimum on the excited potential energy surface (PES) in the dynamics of benzannulated fulgides.

Whereas these studies provide detailed insight into the effects of structural modifications on the $E \rightarrow C$ ring closure and the $C \rightarrow E$ ring opening reactions, much less is known about the $Z \rightarrow E$ reaction. In order to obtain a complete picture of the effects of steric restrictions and benzannulation on the photoisomerisation of fulgides, a comparative study of the $Z \rightarrow E$ isomerisation of MeF, iPrF, 7rF, and MeBF is needed. Our previous study of Z -MeF showed an excited-state lifetime of $\tau = 220$ fs after photo-excitation at $\lambda_{\text{pump}} = 387$ nm, followed by cooling of vibrationally hot Z - and E -molecules in their electronic ground states on a time scale of 4.1 ps.^[20] An oscillating behaviour of the excited-state absorption with a vibrational frequency of $\nu = 57$ cm⁻¹ was tentatively interpreted as an indication of low-frequency torsional motions during the isomerisation. A reaction pathway including one or more conical intersections was inferred from the observed isomerisation time and could be rationalized in later TDDFT calculations.^[16]

In view of the successful tuning of the photoswitching properties of fulgides by structural modifications, the relevance of the $Z \rightarrow E$ reaction for ensuring optical bistability in photochromic fulgide systems has prompted us to perform a consecutive study of the photo-induced dynamics of the Z -isomers of MeF, iPrF, 7rF, and MeBF using femtosecond time-resolved transient absorption spectroscopy. Since the absorption bands of all investigated Z -isomers (see Fig. 6.2) are similar, the same excited electronic states for all derivatives should be populated upon excitation at $\lambda_{\text{pump}} \approx 350$ nm, which allows for a comparison of the resulting dynamics.

The results presented in this paper show that the dynamics of photo-excited Z -isomers are affected only slightly by the steric constraints (iPrF, 7rF) and electronic effects from benzannulation (MeBF). Both might therefore be used to tune the $E \rightarrow C$ and $C \rightarrow E$

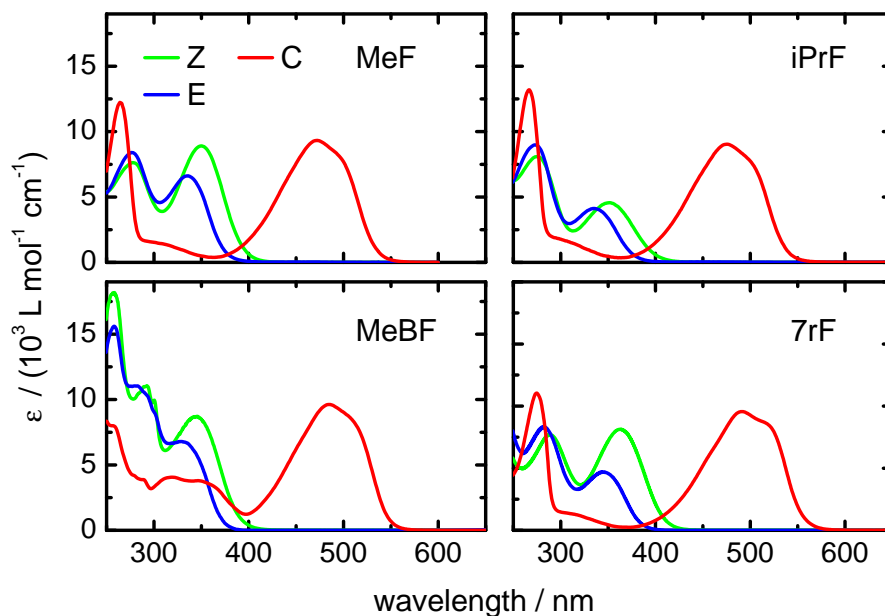


Figure 6.2: UV/VIS absorption spectra of the *C*-, *E*-, and *Z*-isomers for the fulgides MeF, iPrF, MeBF and 7rF in *n*-hexane (red, blue and green lines).^[21]

reactions without impairing the restoring $Z \rightarrow E$ channel. The observed dynamics indicate excited-state pathways that are consistent with isomerisations via conical intersections and could proceed via an intermediate optical dark state. In the absence of detailed theoretical calculations, this paper focuses on a quantitative description of the important features in the data and their implications based on the femtosecond time-resolved experimental data.

6.2 Experimental

Details of the synthesis of the four fulgides were published by Strübe *et al.*^[17] The *Z*- and *E*-isomers were isolated from the resulting mixtures of both isomers by column chromatography and recrystallization in solvent mixtures of cyclohexane and ethyl acetate (9:1 and 7:3, respectively).^[17] The purities (> 98%) were checked by thin layer chromatography and by ¹H-NMR spectroscopy.

The time-resolved measurements were performed in a flow cell with 0.2 mm quartz windows and an optical path of $d = 0.5$ mm for MeF, iPrF, and 7rF and $d = 1$ mm for MeBF. Solutions of an optical density of ≈ 0.3 were prepared in *n*-hexane (Uvasol, Merck) and pumped through the sample cell with a peristaltic pump (Ismatec). All time-resolved measurements were done at room temperature.

The experimental setup for broadband femtosecond absorption spectroscopy was based on a regeneratively amplified Ti:Sa laser system (Clark CPA2001) and has been described previously.^[16,20] A frequency doubled home-built noncollinear optical parametric amplifier

(NOPA) was used to generate excitation pulses of $0.2 \mu\text{J}$ at $\lambda_{\text{pump}} = 350 \text{ nm}$ with a bandwidth of $\Delta\lambda_{\text{pump}} = 6 \text{ nm}$ (FWHM). Broadband supercontinuum pulses between $\lambda_{\text{probe}} = 315$ and 650 nm were generated in CaF_2 and split into probe and reference beams. The pulses were focused into the sample cell to a spot size of $\approx 150 \mu\text{m}$ with an intersection angle of 5° between pump and probe. The polarization of the pump pulses with respect to the detection pulses was set to the magic angle by a Berek variable wave plate. The probe and reference beams were spectrally dispersed through an imaging spectrograph (L.O.T.-Oriel, MS260i) and detected with a 1024×127 pixel CCD camera (L.O.T.-Oriel, DB401-UV). A BG38 filter (Schott) was inserted before the spectrograph to attenuate the intense near-IR part of the supercontinuum. Time resolution was achieved by means of a computer-controlled linear translation stage in the probe path. The width of the instrument response function (IRF) was about 70 fs (FWHM), resulting in a time resolution of the experiment after deconvolution of $\approx 30 \text{ fs}$. The cross-phase modulation (XPM) and stimulated Raman scattering (SRS) contributions were taken into account as before.^[16]

6.3 Results

Two-dimensional transient absorption maps

The two-dimensional spectro-temporal transient absorption maps following excitation of the Z -fulgides at $\lambda_{\text{pump}} = 350 \text{ nm}$ for probe wavelengths between $315 \text{ nm} \leq \lambda_{\text{probe}} \leq 655 \text{ nm}$ are shown in Fig. 6.3. It is immediately obvious from inspection of Fig. 6.3 that all four fulgides show essentially the same behaviour. The transient absorption changes result from several superimposed contributions that can be assigned by their spectral and temporal characteristics as well as the known static UV/VIS spectra of the E - and the Z -isomers (cf. Fig. 6.2). The absorption maps feature a negative signal from ground state bleach (GSB) of the Z -isomers at probe wavelengths between $315 - 400 \text{ nm}$. This GSB reflects the absorption spectra of the photo-excited Z -isomers and is partially refilled within several picoseconds. At early delay times ($\Delta t \leq 1 \text{ ps}$), the GSB and also any possible negative contributions from stimulated emission (SE) are overlaid by large positive contributions due to excited-state absorption (ESA) which extends over almost the entire spectral range and leads to a positive transient absorption except where GSB dominates. The decay of the ESA happens within the first picosecond, and clearly does not correspond to a simple mono-exponential decay of a single component. A dip after $\approx 200 - 250 \text{ femtoseconds}$ can be discerned best at probe wavelengths of $\lambda_{\text{probe}} = 375 - 450 \text{ nm}$. The overall appearance of the ESA suggests the existence of two distinctive components, one of which (ESA_1) occurring immediately following the excitation and the other (ESA_2) rising only after a

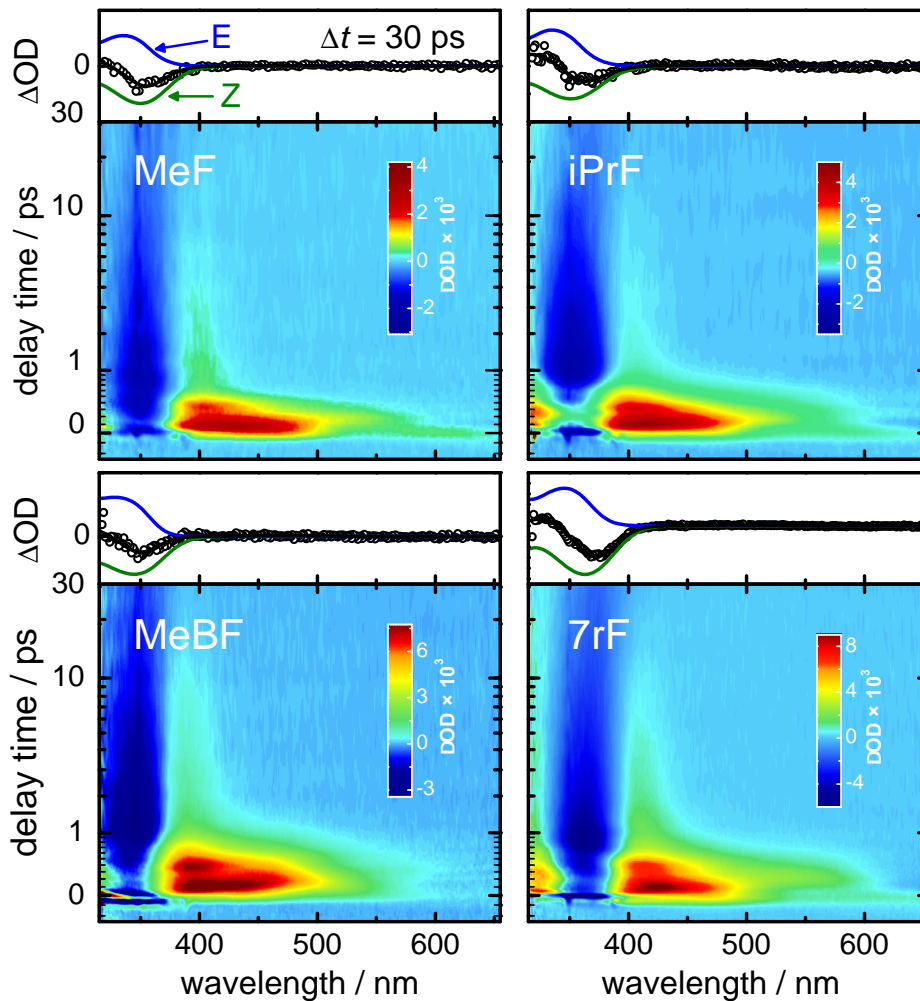


Figure 6.3: Two-dimensional absorption maps of the change in optical density ΔOD following excitation of the Z -isomers of the four investigated fulgides at $\lambda_{\text{pump}} = 350$ nm for probe wavelengths in the range of $315 \leq \lambda_{\text{probe}} \leq 655$ nm and delay times between $-0.2 \leq \Delta t \leq 30$ ps (see Ref. [27] for an explanation of the time scale). Transient spectra at delay times $\Delta t = 30$ ps and their fits by a weighted sum of the static UV/VIS absorption spectra of the E - and Z -isomers are shown above of the respective absorption maps.

short delay of a few hundred femtoseconds. The delayed ESA_2 components apparently shifts to shorter wavelengths with increasing delay times. The ESA decay leaves a positive band between $375 \text{ nm} \leq \lambda_{\text{probe}} \leq 425$ nm that can be assigned to hot ground-state absorption (HGSA) from vibrationally excited E - and Z -molecules returned to their electronic ground states. The subsequent slower spectral blue-shift of the HGSA reflects the vibrational cooling of the E - and Z -isomers. No further spectral changes are discernible beyond delays of $\Delta t > 20$ ps. These permanent absorption changes, clearly visible in the transient spectra at the final delay $\Delta t = 30$ ps, are described by the difference of the static E - and Z -isomer absorption spectra. No formation of C -isomers which would give a positive product absorption band peaked at $\lambda_{\text{probe}} \approx 500$ nm could be detected.

Time Profiles

Figure 6.4 displays the transient absorption-time profiles after excitation of the Z -isomers at four selected probe wavelengths. The time profiles at the two largest probe wavelengths ($\lambda_{\text{probe}} = 450 - 550$ nm) feature purely positive absorption changes ΔOD that decay completely on a sub-picosecond time scale and are caused by ESA. Although the temporal evolution of the ESA varies in detail between the different fulgides and also shows minor differences between the two wavelengths, it is obvious from the profiles that a fast rising ESA (ESA₁, red line) with larger amplitude and a second, delayed ESA component

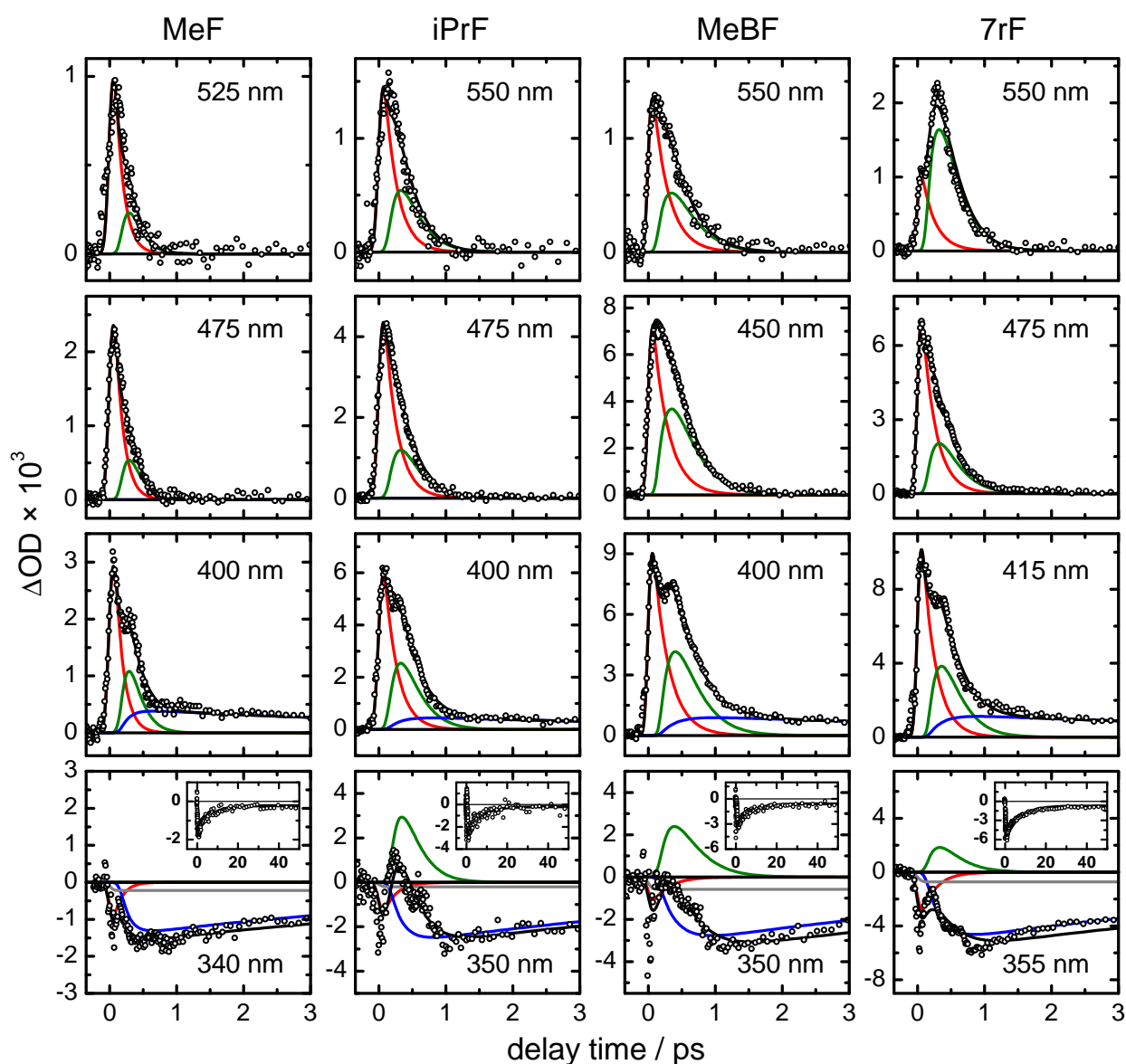
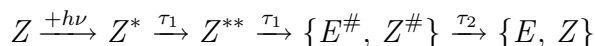


Figure 6.4: Transient absorption traces at selected probe wavelengths following excitation of the Z -forms of MeF, iPrF, MeBF and 7rF at $\lambda_{\text{pump}} = 350$ nm. Open circles represent the data points, black lines the overall fits, colored lines the underlying contributions: ESA₁ (red), ESA₂ (green), HGSA (blue), GSB (gray).

(ESA₂, green line) are required to describe the data. The need for the latter component becomes even more evident in the time profiles at $\lambda_{\text{probe}} = 400$ nm. These are again dominated by the two-component ESA decay, but also show a small positive HGSA (blue line) that is related to the vibrational cooling of the *E*- and *Z*-isomers, which decays to $\Delta\text{OD}=0$ within $\Delta t \approx 15$ ps (cf. Fig. 6.3). The fast decay of ESA₁ (red line) and the delayed appearance of ESA₂ results in a local minimum of the transient absorption in the time profiles at this probe wavelength. Although this minimum resembles the behaviour caused by a critically damped oscillation, attempts to describe the data by just one ESA component with superimposed oscillation failed. The vibrational cooling in the electronic ground states monitored by HGSA was observed with comparable decay times of $\tau_2 \approx 6.6$ ps for all four fulgides.

The time profiles around $\lambda_{\text{probe}} \approx 345$ nm are dominated by the negative GSB and exhibit a fairly complex temporal behaviour, in particular at early delay times, and show a maximum after $\approx 250 - 300$ femtoseconds. This behaviour is caused by the overlapping contributions of the initial GSB, the two ESA components, and HGSA of the *Z*- and *E*-isomers. The apparent refilling of the initial GSB at later delay times is due to slower spectral blue-shifting and narrowing of the *E*- and *Z*-isomer ground-state absorptions (cf. Fig. 6.2) by vibrational energy transfer processes. The fairly small final negative offsets reflect the *E*-*Z* difference spectra at these wavelengths.

The quantitative analysis of the time profiles was carried out by non-linear least squares fitting using a kinetic scheme for isomerisation/deactivation of photoexcited *Z*-isomers with two time constants:



The temporal behaviour of the two ESA components suggests a model with two excited-state species Z^* and Z^{**} , where Z^* represents the initially photo-excited *Z*-isomers in the Franck-Condon (FC) region. The ensuing molecular dynamics lead to the formation of Z^{**} molecules presumably located in a different region of the excited-state potential energy surface (PES) with different ESA behaviour. $E^\#$ and $Z^\#$ represent “vibrationally hot” *E*- or *Z*-molecules returned to the electronic ground state. Within the above scheme, electronic isomerisation and deactivation yielding $E^\#$ or $Z^\#$ are assumed to occur exclusively via the Z^{**} species. At present, we have chosen to restrict the time constants for the excited-state dynamics and isomerisation/deactivation processes to be identical (τ_1) in order to achieve the numerical stability of the fit. While this could miss some details of the molecular dynamics, the assumption seems justified since a model with two independent time constants yielded fluctuating fit results due to the strong correlation between the time constants. Time-resolved fluorescence measurements might provide independent

data that might help to fix this problem, but such data are not available at this time. Finally, the vibrational relaxation that leads to E - and Z -molecules in their electronic and vibrational ground states is described by the time constant τ_2 for $E^\#$ and $Z^\#$. The complete model function is given by a superposition of all contributions with wavelength-dependent amplitudes, convoluted with the Gaussian IRF to account for the limited temporal resolution of the experiment:

$$\text{IRF}(t) = \frac{1}{\sigma\sqrt{2\pi}} \exp\left[-\frac{t^2}{2\sigma^2}\right] \quad (19)$$

$$Z^*(t) = a_1 \cdot \exp\left[-\frac{t}{\tau_1}\right] \otimes \text{IRF}(t) \quad (20)$$

$$Z^{**}(t) = a_2 \cdot \frac{t}{\tau_1} \cdot \exp\left[-\frac{t}{\tau_1}\right] \otimes \text{IRF}(t + \Delta) \quad (21)$$

$$\{E^\#(t), Z^\#(t)\} = b \cdot \left(\exp\left[-\frac{t}{\tau_2}\right] - \exp\left[-\frac{t}{\tau_1}\right] \right) \otimes \text{IRF}(t + \Delta) \quad (22)$$

$$\{E(t), Z(t)\} = p \cdot \left(1 - \exp\left[-\frac{t}{\tau_2}\right] \right) \otimes \text{IRF}(t + \Delta) \quad (23)$$

An additional parameter Δ was included in order to account for the delayed appearance of the second ESA component and consequently also the subsequent HGSA and product absorption contributions. The time constants and shift parameters obtained by the fits are listed in Table 6.1.

The life time τ_{av} given in Table 6.1 were obtained from a single exponential fit of the ESA decay for the transient absorption time profiles at $\lambda_{\text{probe}} \approx 400$ nm and represent a good estimate of the overall excited-state lifetime. The delay time Δ slightly increases from $\Delta \approx 0.12$ to ≈ 0.15 ps towards shorter wavelength for all fulgides, but this is within the error range of Δ . For the fitting of the time profiles at $\lambda = 350$ nm the fixed parameters τ_1 , τ_2 , and Δ were used to model the data.

Table 6.1: Time constants and time shift parameters from fits of the transient absorption time profiles (2σ error limits with respect to last digits in parentheses). τ_{av} was determined from a single exponential fit of the ESA from the time profiles at $\lambda \approx 400$ nm. For details see text.

	τ_1 / ps	Δ / ps ^a	τ_{av} ^a	τ_2 / ps ^a
Z-MeF	0.12(6)	0.15(5)	0.33(3)	6.5(20)
Z-iPrF	0.19(7)	0.12 (6)	0.48(3)	7.0(32)
Z-7rF	0.21(9)	0.12(7)	0.52(4)	6.9(10)
Z-MeBF	0.24(9)	0.15(4)	0.73(6)	6.0(14)

^a At probe wavelengths of $\lambda \approx 400$ nm.

6.4 Discussion

The transient absorption results described in the previous section provide detailed information on the photo-induced dynamics of the *Z*-isomers for the fulgides MeF, iPrF, 7rF, and MeBF on excitation in their first absorption band at $\lambda = 350$ nm.

Observed Ultrafast Dynamics

The spectro-temporal absorption maps and the transient decay curves show clearly that the studied fulgides exhibit very similar photo-induced dynamics with similar distinctive ESA features. In particular, two ESA components can be described by a sequential model with two time constants and an additional time delay between them. The only apparent effect of the structural modifications is a moderate slow-down of the excited-state dynamics, with time constants τ_1 ranging from $\tau_1 = 0.12$ ps for MeF to $\tau_1 = 0.24$ ps in the case of MeBF, and an increase of the respective isomerisation/deactivation times from $\tau_{av} = 0.33$ ps to 0.73 ps. These changes appear not to be related to a change of the respective isomerisation/deactivation routes. A possible explanation of the slow-down of the overall excited-state lifetime could be larger solvent friction due to the bulkier substituents.

The present results agree well with the observed behaviour in our previous study^[20] of *Z*-MeF with excitation at $\lambda = 387$ nm in the red wing of the first absorption band, but with a limited probe wavelength range ($\lambda_{probe} > 410$ nm). In the earlier work, the temporal evolution had been described by a model consisting of a single ESA decay component and a superimposed oscillation. Given that a similar oscillatory behaviour had been obtained and interpreted in the same way in time-resolved studies of other *E/Z* photoisomerisation reactions,^[28,29] an interpretation as a vibrational coherence involving a low-frequency torsional motion probably of the furyl unit seemed reasonable at that time. On the other hand, the present comparative study of four different *Z*-furylfulgides, which were acquired with improved temporal resolution (≈ 30 fs compared to ≥ 50 fs in Ref. [20]) and with a spectral range extending ≈ 100 nm further into the UV, suggests that the ESA behaviour is not reasonably described by an oscillation superimposed on a mono-exponential decay, but rather arises from a genuine second ESA component. This appears to indicate that the isomerisation/deactivation does not proceed on a direct pathway. The new interpretation is corroborated by successful application of the present sequential model (Eq. (20)-(23)) to the data of Ref. [20].

Photoisomerisation Pathways

The favoured scenario for photo-induced E/Z isomerisations involves conical intersections (CIs) acting as efficient photochemical funnels for rapid internal conversions between different electronic states.^[30,31] The observed overall excited-state lifetimes of $\tau < 1$ ps indicate that the isomerisation and electronic deactivation of the photo-excited Z -isomers of the investigated furylfulgides also involve reaction pathways without significant energy barriers.

Taking into account the nice description of the acquired experimental data by the sequential reaction model with a second excited-state species (Z^{**}), the observed ESA behaviour suggests an involvement of an intermediate state. This conclusion is in agreement with the scenario of the photo-induced E/Z isomerisations in hexatriene (HT) and other E/Z photoisomerising systems.^[32–41]

For HT, the spectroscopically bright $1B$ state, a lower lying dark $2A$ state, and the $1A$ electronic ground state are assumed to play a role. Accordingly, the observed transient absorption changes can be interpreted as sketched in Fig. 6.5: The initial photoexcitation prepares a wavepacket in the FC region of the $1B$ state (species Z^*) which is responsible for the first ESA component (ESA_1). This is followed by a rapid internal conversion to the $2A$ state (species Z^{**}) via a CI (CI_1) that leads to the decay of ESA_1 . The $2A$ state is assumed to be optically dark and is therefore not initially excited. Its population causes the rise of the second ESA component (ESA_2). The additional time delay of $\Delta \approx 0.14$ ps describes the rise of ESA_2 and is probably due to a spectroscopically dark window associated with the passage through CI_1 . A similar picture has recently been suggested for the case of the $Z \rightarrow E$ isomerisation of a biomimetic dipolar photoswitch.^[42] Finally, a fast and effective deactivation to the electronic ground state of the E - and Z -isomers via a

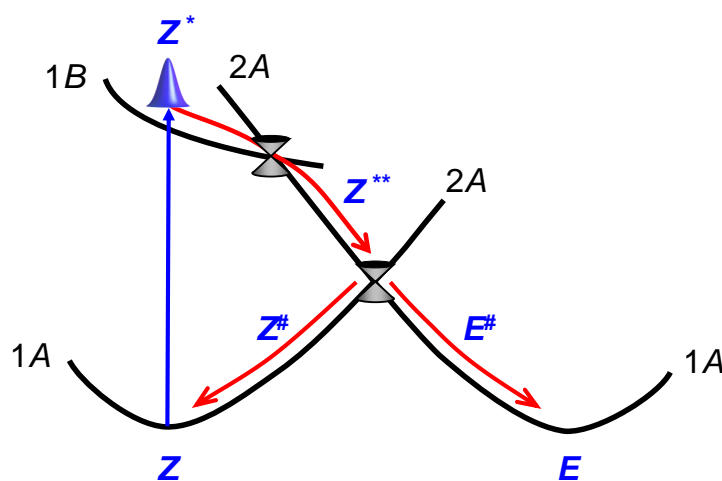


Figure 6.5: Schematic picture of the two-state model for the isomerisation and deactivation of photoexcited Z -fulgides via an intermediate excited state (for details see text).

second CI (CI_2) is responsible for the sub-picosecond decay of ESA_2 .

The sequential model with an intermediate dark state appears to provide a conclusive explanation for the observed transient absorption changes and is also plausible by analogy with HT and other E/Z reactions.^[32-41] We cannot rule out alternative scenarios involving only a single optically excited state, but considering the required specific changes of the Franck-Condon factors of the probed transitions and the previous discussion, a one-state model seems much less plausible. To obtain further evidence, it would be of interest to pursue time-resolved emission experiments, where single exponential decays would be expected due to the optically dark nature of the 2A state.

Effects of structural modifications on the dynamics of furylfulgides

The present results indicate that neither the steric constraints by the large substituent at the C^4 position (iPrF), the internal bridging (7rF), nor the electronic changes by the benzannulation (MeBF) lead to fundamental changes of the $Z \rightarrow E$ isomerisation reaction mechanism. This is in contrast to the pronounced steric effects seen in case of the previously studied isomerisation reactions of the photoexcited E -isomers of the four fulgides^[21] and the remarkable influence of the electronic effect on the dynamics of the respective photoexcited C -isomers.^[22]

The steric effects in E -iPrF and E -7rF led to an acceleration of the $E \rightarrow C$ ring closure reaction by a factor of ≈ 2 ($\tau = 0.05$ ps) compared with MeF and MeBF. This effect was accompanied by strongly improved photochemical properties, such as increased $E \rightarrow C$ ring closure isomerisation quantum yield by a factor of ≈ 3 and inhibition of the unwanted $E \rightarrow Z$ isomerisation.^[17,21] Furthermore, the $E \rightarrow Z$ reaction was found to be a conformer-specific reaction, depending on the ground-state populations of two E -conformers (E_α and E_β), also strongly affected by steric constraints. For MeF and MeBF, similar $E \rightarrow Z$ isomerisation times of $\tau \approx 0.34$ ps were observed. Regarding the ring closure reaction both favorable kinetic competition and conformer populations contribute to the improved photochemical properties of iPrF and 7rF compared with MeF and MeBF.

In agreement with the dynamics of the E -isomers, the qualitatively similar dynamics of all investigated Z -fulgides indicate that any additional electronic states or changes in the excited-state topography that might arise from benzannulation do not play a role for the E/Z isomerisation.

On the other hand, considering the dynamics of photoexcited C -isomers of the four fulgides, strongly increased excited-state lifetimes of C -MeBF with $\tau = 16.9$ ps (up to ≈ 25 times longer than for C -MeF) were explained by the involvement of excited-state energy barriers in the photo-dynamics of benzannulated fulgides.^[22] Surprisingly, longer excited-state lifetimes of MeBF were accompanied by increased $C \rightarrow E$ ring opening

quantum yields,^[17,22] rationalized by an energy barrier along excited-state pathways that lead predominantly to photophysical deactivation of the photoexcited C -MeBF molecules.

6.5 Conclusion

In conclusion, we have studied the ultrafast photo-induced dynamics of the Z -isomers of four structurally modified furylfulgides in solution in n -hexane by femtosecond time-resolved transient absorption spectroscopy. The obtained results complement our previous studies on the effects of increased steric hindrance due to a bulky isopropyl group at the central HT unit or intramolecular bridging and benzannulation of the furyl ring on the switching properties and excited-state dynamics of E - and C -furylfulgides. The excited-state dynamics of the Z -isomers was found to be surprisingly unaltered by both structural effects. All photo-excited Z -isomers showed similar excited-state dynamics, which was interpreted by involvement of an intermediate dark state. The lifetimes of the initial Franck-Condon state range from $\tau_1 = 0.12$ ps for MeF to $\tau_1 = 0.24$ ps in the case of MeBF. The overall excited-state decay times $\tau_{av} = 0.33$ ps to 0.73 ps suggest that the internal conversion to the intermediate state and subsequently to the electronic ground state of the E - and Z -isomers involve distinctive conical intersections, in agreement with the picture for the HT system. The slight increase of the respective time constants can be treated back to the increased moments of inertia. The results indicate that steric and electronic structural modifications can be used to selectively improve the photochromic $E \rightarrow C$ ring closure and the reverse $C \rightarrow E$ ring opening reaction, respectively, without prevention of the $Z \rightarrow E$ back isomerisation. This is very important for applications of fulgides in multiple switching cycles in order to prevent accumulation of the unwanted Z -isomers.

Acknowledgments

This work has been supported by the Deutsche Forschungsgemeinschaft through sub-project A1 of the SFB 677 "Function by Switching" (RS, FR, FT) and by the Biophotonics Initiative (Grant no. 13N9234) of the German Ministry of Research and Education (FS, JM).

References

- [1] H. G. Heller, S. Oliver, *J. Chem. Soc., Perkin Trans. 1* **1981**, 197–201.
- [2] P. J. Darcy, H. G. Heller, P. J. Strydom, J. Whittall, *J. Chem. Soc., Perkin Trans. 1* **1981**, 202–205.
- [3] Y. Yokoyama, *Chem. Rev.* **2000**, *100*, 1717–1739.
- [4] J. A. Delaire, K. Nakatani, *Chem. Rev.* **2000**, *100*, 1817–1845.
- [5] P. Seal, S. Chakrabarti, *J. Phys. Chem. A* **2010**, *114*, 673–679.
- [6] Y. C. Liang, A. S. Dvornikov, P. M. Rentzepis, *Proc. Natl. Acad. Sci. U. S. A.* **2003**, *100*, 8109–8112.
- [7] A. S. Dvornikov, E. P. Walker, P. M. Rentzepis, *J. Phys. Chem. A* **2009**, *113*, 13633–13644.
- [8] S. Rath, M. Heilig, H. Port, J. Wrachtrup, *Nano Lett.* **2007**, *7*, 3845–3848.
- [9] S. Z. Janicki, G. B. Schuster, *J. Am. Chem. Soc.* **1995**, *117*, 8524–8527.
- [10] M. L. Bossi, J. B. Rodríguez, P. F. Aramendía, *J. Photochem. Photobiol., A* **2006**, *179*, 35–41.
- [11] I. B. Ramsteiner, A. Hartschuh, H. Port, *Chem. Phys. Lett.* **2001**, *343*, 83–90.
- [12] F. M. Raymo, M. Tomasulo, *J. Phys. Chem. A* **2005**, *109*, 7343–7352.
- [13] J. Cusido, E. Deniz, F. M. Raymo, *Eur. J. Org. Chem.* **2009**, 2031–2045.
- [14] I. Willner, S. Rubin, *Angew. Chem. Int. Ed.* **1996**, *35*, 367–385.
- [15] E. Uhlmann, G. Gauglitz, *J. Photochem. Photobiol., A* **1996**, *98*, 45–49.
- [16] R. Siewertsen, F. Renth, F. Temps, F. Sönnichsen, *Phys. Chem. Chem. Phys.* **2009**, *11*, 5952–5961.
- [17] F. Strübe, R. Siewertsen, F. D. Sönnichsen, F. Renth, F. Temps, J. Mattay, *Eur. J. Org. Chem.* **2011**, 1947–1955.
- [18] M. Handschuh, M. Seibold, H. Port, H. C. Wolf, *J. Phys. Chem. A* **1997**, *101*, 502–506.
- [19] H. Port, P. Gärtner, M. Hennrich, I. Ramsteiner, T. Schöck, *Mol. Cryst. Liq. Cryst.* **2005**, *430*, 15–21.
- [20] F. Renth, M. Foca, A. Petter, F. Temps, *Chem. Phys. Lett.* **2006**, *428*, 62–67.
- [21] R. Siewertsen, F. Renth, F. Strübe, J. Mattay, F. Temps, *Phys. Chem. Chem. Phys.* **2011**, *13*, 3800–3808.
- [22] R. Siewertsen, F. Renth, F. Strübe, J. Mattay, F. Temps, *unpublished results* **2011**.
- [23] Y. Yokoyama, T. Goto, T. Inoue, M. Yokoyama, Y. Kurita, *Chem. Lett.* **1988**, *17*, 1049–1052.
- [24] A. Kaneko, A. Tomoda, M. Ishizuka, H. Suzuki, R. Matsushima, *Bull. Chem. Soc. Jpn.* **1988**, *61*, 3569–3573.

- [25] Y. Yokoyama, T. Tanaka, T. Yamane, Y. Kurita, *Chem. Lett.* **1991**, *20*, 1125–1128.
- [26] A. Tomoda, A. Kaneko, H. Tsuboi, R. Matsushima, *Bull. Chem. Soc. Jpn.* **1993**, *66*, 330–333.
- [27] To display the transient absorption maps with optimal dynamic ranges, they are plotted using a logarithmic scale by taking $\log(1 + \Delta t/\text{ps})$. The plot scale was then relabelled to correctly range from $\Delta t = -0.2$ to 30 ps.
- [28] S. Takeuchi, T. Tahara, *Chem. Phys. Lett.* **2000**, *326*, 430–438.
- [29] B. Hou, N. Friedman, M. Ottolenghi, M. Sheves, S. Ruhman, *Chem. Phys. Lett.* **2003**, *381*, 549–555.
- [30] B. G. Levine, T. J. Martínez, *Annu. Rev. Phys. Chem.* **2007**, *58*, 613–634.
- [31] W. Domcke, D. R. Yarkony, H. Köppel, eds., *Conical Intersections: Electronic Structure, Dynamics & Spectroscopy*, World Scientific, Singapore **2004**.
- [32] D. R. Cyr, C. C. Hayden, *J. Chem. Phys.* **1996**, *104*, 771–774.
- [33] P. Celani, F. Bernardi, M. A. Robb, M. Olivucci, *J. Phys. Chem.* **1996**, *100*, 19364–19366.
- [34] S. Lochbrunner, W. Fuß, K.-L. Kompa, W. E. Schmid, *Chem. Phys. Lett.* **1997**, *274*, 491–498.
- [35] K. Ohta, Y. Naitoh, K. Tominaga, N. Hirota, Y. Keitaro, *J. Phys. Chem. A* **1998**, *102*, 35–44.
- [36] S. Lochbrunner, W. Fuß, W. E. Schmid, K.-L. Kompa, *J. Phys. Chem. A* **1998**, *102*, 9334–9344.
- [37] M. Boggio-Pasqua, M. J. Bearpark, M. Klene, M. A. Robb, *J. Chem. Phys.* **2004**, *120*, 7849–7860.
- [38] J. Catalán, J. L. G. de Paz, *J. Chem. Phys.* **2006**, *124*, 034306/1–034306/11.
- [39] A. Nenov, T. Cordes, T. T. Herzog, W. Zinth, R. de Vivie-Riedle, *J. Phys. Chem. A* **2010**, *114*, 13016–13030.
- [40] F. Bernardi, M. Olivucci, M. A. Robb, *Chem. Soc. Rev.* **1996**, *25*, 321–328.
- [41] W. Fuß, Y. Haas, S. Zilberg, *Chem. Phys.* **2000**, *259*, 273–295.
- [42] J. Briand, O. Bräm, J. Réhault, J. Léonard, A. Cannizzo, M. Chergui, V. Zanirato, M. Olivucci, J. Helbing, S. Haacke, *Phys. Chem. Chem. Phys.* **2010**, *12*, 3178–3187.

7 Photochromism of Rotation-Hindered Furylfulgides Influenced by Steric Modifications

Frank Strübe^a, Ron Siewertsen^b, Frank D. Sönnichsen^c, Falk Renth^b,
Friedrich Temps^b, Jochen Mattay^{*a}

^a Organische Chemie I, Fakultät für Chemie, Universität Bielefeld, Postfach 100131,
D-33501 Bielefeld, Germany

^b Institut für Physikalische Chemie, Christian-Albrechts-Universität zu Kiel,
Olshausenstr. 40, D-24098 Kiel, Germany

^c Otto-Diels-Institut für Organische Chemie, Christian-Albrechts-Universität zu Kiel,
Otto-Hahn-Platz 4, D-24098 Kiel, Germany.

Reproduced with permission of the John Wiley & Sons Ltd.

Eur. J. Org. Chem. **2011**, 1947-1955

Copyright 2011

- **Own contributions presented in the paper:**
 - Determination of isomerization quantum yields
 - Static UV/VIS spectroscopic investigations
 - Quantum chemical calculations
- **Synthesis:** Frank Strübe in the group of Prof. J. Mattay
- **NMR spectroscopy:** Prof. F. D. Sönnichsen,
Frank Strübe in the group of Prof. J. Mattay
- **Single crystal X-ray structure:** Frank Strübe in the group of Prof. J. Mattay

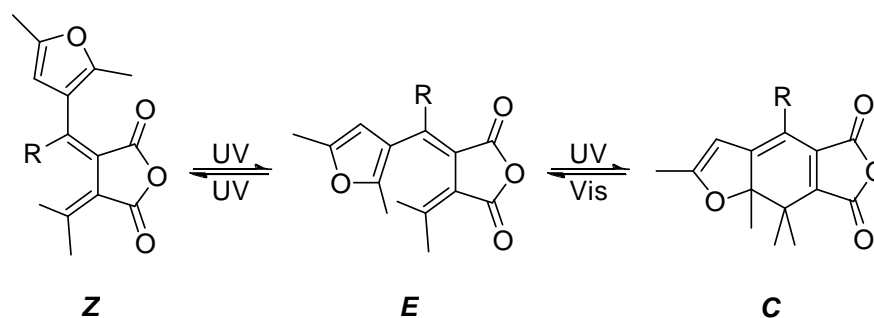
*To whom correspondence should be addressed. E-mail: mattay@uni-bielefeld.de

Abstract

The syntheses of a bicyclic furylfulgide **14** and a (benzofuryl)fulgide **15** with increased steric constraints are described. Their photochromic behaviors were analyzed by means of UV/Vis spectroscopic measurements, X-ray crystallography and NMR experiments, and the results were compared to those of the furyl(methyl)fulgide **12** and the furyl(isopropyl)fulgide **13**. Compounds **13E** and **14E** exhibit large quantum yields of 0.57 and 0.53 for the coloration reaction $E \rightarrow C$ compared with **12E** and **15E** (0.23 and 0.17). After irradiation with 350 nm light, **13E** and **14E** are transformed into the closed (C) forms almost quantitatively, whereas **12E** and **15E** result in a photostationary state with mixtures of the (E), (Z), and (C) forms. The crystal structures obtained for **13E**, **14E**, and **15E** show that the fulgides adopt cyclizable helical (P)- E_α conformations with no significant differences in atomic distances in the hexatriene unit. 2D- and temperature-dependent NMR experiments showed that the enantio- and diastereotopomerization processes were suppressed in a fulgide for the first time. Compound **14E** populates only the E_α conformational state. In contrast, **13E** and **15E** both exist in the cyclizable E_α and the non-cyclizable E_β conformations in solution. Due to the annulated benzene ring, **15E** exhibits a higher thermodynamic barrier than **13E**, so the “belly roll” process was reduced for **15**, but the $E \rightarrow Z$ isomerization could not be suppressed. The structural modification of **14** successfully suppressed the $E \rightarrow Z$ isomerization as well as the belly roll process. The way in which the isomerization reaction is suppressed by sterical hindrance could not be fully elucidated by using these methods.

7.1 Introduction

Fulgides^[1,2] are an important class of photoswitches that complement diarylethenes^[3] and spiropyrans.^[4] Upon wavelength-specific illumination, they undergo reversible color changes and are thus of great interest of a range of applications.^[5–10] The first fulgides were synthesized by Stobbe in the early 20th century.^[11–13] Like diarylethenes, they contain a hexatriene system with at least one phenylic or heterocyclic part as the central photochromic unit for the electrocyclic reaction. There are three different forms of fulgides, two mainly colorless, open forms, (E) and (Z), and a colored, closed form, (C). The photochromic behavior is depicted in Scheme 7.1. The photochromism can be monitored by UV/Vis spectroscopic methods, because there is a considerable change in the absorption spectra. Variation of the substituents at the photochromic center causes a remarkable change in the electronic state of the fulgides and therefore affects the absorption spectra of the compounds. Electron-withdrawing groups lead to a bathochromic shift of the absorption maximum, whereas electron-donating substituents cause a hypsochromic shift.^[14–16] Furthermore,

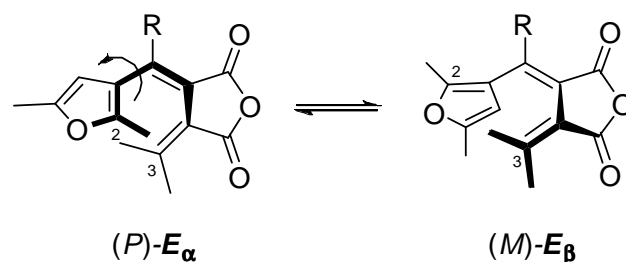


Scheme 7.1: Photochromic reaction of furylfulgides with variable substituents R at the photochromic core unit.

heterocyclic moieties have a large influence on the spectroscopic quality. The open form of furylfulgides exhibits an absorption maximum at about 340 nm, whereas electron-rich indolylfulgides show a remarkable bathochromically shifted absorption maximum at about 400 nm.^[17–19]

The fulgides of the first generation described by Stobbe had limited thermal stability, and the photochromic mechanism was intensively investigated only in the 1970s to 1980s.^[20–24] A milestone in the history of fulgides was achieved by Heller and co-workers in 1981 with the development of a thermally stable fulgide.^[25] The replacement of the hydrogen atoms at the cyclohexatriene unit by methyl groups and the introduction of a heterocyclic furyl moiety afforded fulgides that are stable towards both oxidation and hydrogen transfer. This formed the basis for current applications of fulgides, where high thermal and photochemical stability are essential.

Nevertheless, the efficiency of the photochromic reaction is limited by the photoisomerization of the open forms. The photochemical equilibrium between the (*E*)- and the (*Z*)-form is an unfavorable process that competes with the desired ring closing reaction from the (*E*) to the (*C*) form. Therefore, the quantum yields for the coloration reaction are low, which is a significant disadvantage for potential applications. New results derived from femtosecond time-resolved measurements and DFT calculations show that besides the $E \rightarrow Z$ isomerization, there are other deactivation processes that reduce the quantum efficiency.^[26] In addition to the mentioned electronic substituent effects, steric modifications have great influence on the photochromism.^[16,27] In 1988, Yokoyama et al. investigated the effects of bulky substituents R at the cyclohexatriene moiety on the photochromic reaction of a furylfulgide.^[28] The results showed that the quantum yield for $E \rightarrow Z$ isomerization becomes smaller, and the quantum yield for the $E \rightarrow C$ coloration process increases with the bulkiness of the substituents. In the case of an isopropyl substituent, no $E \rightarrow Z$ isomerization was observed, and a quantum yield for the coloration reaction of 0.58 was found. In comparison, the $E \rightarrow C$ quantum yield of the methyl compound



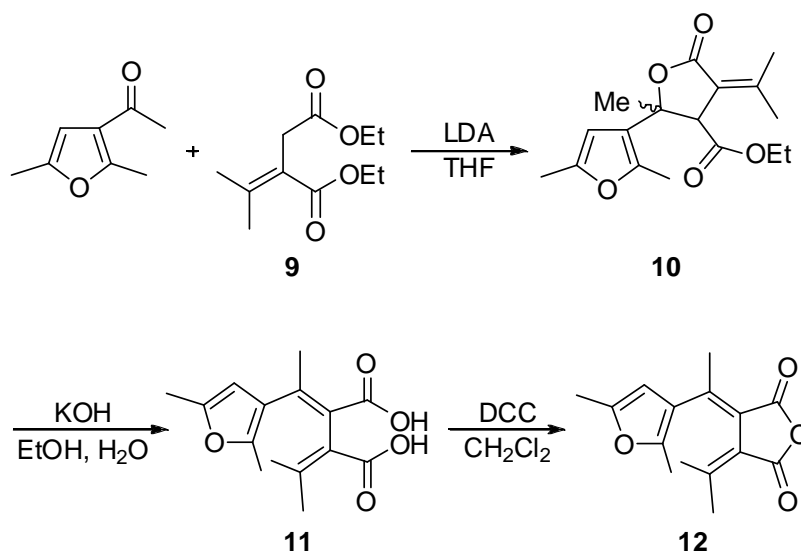
Scheme 7.2: Possible rotameric isomers of a furylfulgide. Due to the geometric constitution, $(M)-E_\beta$ cannot undergo cyclization, whereas $(P)-E_\alpha$ is the cyclizable isomer.

12 was determined to be only 0.19. Later, the influence of a *tert*-butyl substituent was described, which led to a quantum yield for the coloration process of 0.79.^[29] For this reason, sterically hindered fulgides should be even more viable photochromic compounds for high-quality applications. Furthermore, Yokoyama indicated that, in addition to $E \rightarrow Z$ isomerization, the open (E) forms of furylfulgides undergo a diastereotopomerization of the helical structure between the $(P)-E_\alpha$ and $(M)-E_\beta$ conformation.^[30,31] The conversion between these two states occurs by a rotation of the furyl subunit, which Yokoyama called a “belly roll” process (Scheme 7.2).

It is clear that only molecules in the E_α conformation, wherein C-2 faces C-3, are in the correct geometric form to undergo the cyclization to the closed (C) isomer. If the rotation can be suppressed by structural manipulation of the fulgide backbone, all molecules will be available in the cyclizable E_α conformation, and the enantiotopomerization [$(P) - E_\alpha \rightarrow (M) - E_\alpha$] and diastereotopomerization ($E_\alpha \rightarrow E_\beta$) processes would be blocked. Furthermore, the steric hindrance caused by the modification would be large enough to avoid the $E \rightarrow Z$ double bond isomerization. Herein, we report the synthesis of new furylfulgides that implement this concept. In (benzofuryl)fulgide **15** the formal benzannulation of the furyl unit should limit its rotation to a minimal degree. To entirely eliminate the belly roll, a fulgide with a bicyclic framework **14** was designed and synthesized. Here, the rotation of the furyl ring is restrained by an alkyl chain connection between C-10 of the furyl moiety and C-6 of the hexatriene unit.

7.2 Results and Discussion

The furylfulgides **12** - **14** were synthesized by starting from commercially available 2,5-dimethylfuran and the appropriate acyl chloride (Scheme 7.3). The acylated compounds were obtained from a Friedel-Crafts reaction with AlCl_3 as catalyst. To minimize side reactions, the acylation was carried out at 0 °C under argon. Although it is known that furans polymerize in the presence of Lewis acids, the reactions gave moderate yields (49-62%).^[32]



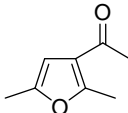
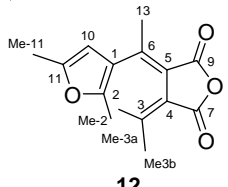
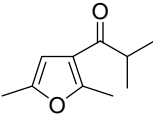
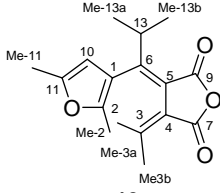
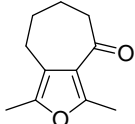
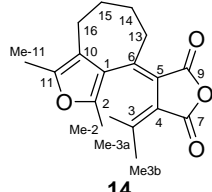
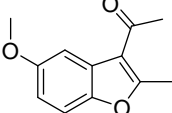
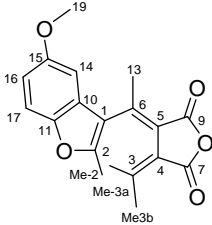
Scheme 7.5: Synthesis of **12** by Stobbe condensation. Saponification of lactone mixture **10** gave diacid **11** as a mixture of (*E*)/(*Z*) isomers, followed by dehydration to give a mixture of **12E** and **12Z**.

Treatment of **9** with lithium diisopropylamide (LDA) at $-78\text{ }^{\circ}\text{C}$ and addition of the heterocyclic compound gave a mixture of isomeric lactones **10**. These intermediate products were only detected by analytical methods (TLC, GCMS, and ^1H NMR spectroscopy). After aqueous workup, the reaction mixture was filtered through silica gel. The crude product was dissolved in ethanol and treated with saturated aqueous KOH solution at $70\text{ }^{\circ}\text{C}$ to give the diacid **11** as a mixture of (*E*)/(*Z*) isomers. For the anhydride formation, the crude diacid was dissolved in dichloromethane, and *N,N'*-dicyclohexylcarbodiimide (DCC) was added. After stirring for 24 h at room temperature, the fulgides were obtained as a mixture of (*E*) and (*Z*) isomers. The isomers were separated by column chromatography with different mixtures of cyclohexane and ethyl acetate as eluent. A slight excess of the (*E*) isomer over the (*Z*)-isomer was obtained (ratio of 1.2-1.5:1). The two isomers of **12-15** can easily be distinguished by their ^1H NMR spectra. Whereas the (*E*) forms show an intense methyl group signal arising from the isopropylidene group ($\text{CH}_3\text{-3a}$; $\delta \approx 1.3$ ppm) in CDCl_3 , the corresponding signal of the (*Z*) isomer is shifted downfield ($\delta = 2.1\text{-}2.3$ ppm). Furthermore, all (*Z*) forms exhibit lower R_f values than the corresponding (*E*) isomers by approximately 10%.

Fulgides **12 - 15** exhibit the expected photochromic behavior of furylfulgides. The absorption maxima (λ_{max}) of the open (*E*) isomers show a strong absorption band at about 330 – 350 nm in the near-UV region. The λ_{max} values of the (*Z*) isomers are shifted by around 20 nm to longer wavelengths. The closed (*C*) isomers have an absorption maximum near 470 – 490 nm (Table 7.1).

Figure 7.1 shows the evolution of the absorption spectrum of **14E** upon successive

Table 7.1: List of the synthesized fulgides **12-15** and precursors, together with their UV/Vis spectroscopic data $\{\lambda_{max}$ [nm], $(\epsilon_{max}$ [L mol⁻¹cm⁻¹]).

ketone	fulgide ^[a]	E ^[b]	Z ^[b]	C ^[b]
		336 (6615)	350 (8906)	472 (9328)
		336 (4125)	352 (4560)	476 (9038)
		344(4715)	364(8145)	491(9560)
		329(6790)	345(8680)	485(9623)

[a] The atom numbering of each fulgide is arbitrary. [b] 10⁻⁴ M solution in *n*-hexane at room temp.

irradiation with 350 nm light. The absorption band near 350 nm decreases to a minimal amount, while the strong band near 500 nm belonging to the (*C*) isomer increases. Irradiation with 500 nm light leads back to the initial spectrum of the (*E*) isomer. A similar behavior can be observed for **13E**. However, solutions of **12E** and **15E** exhibit different characteristics upon irradiation with 350 nm light. The (*C*)/(*Z*)/(*E*) ratios in the photostationary states were analyzed by NMR spectroscopy. A solution of each (*E*) isomer in CDCl₃ was successively irradiated with 350 nm light. The results show that, for **13** and **14**, after an irradiation time of 90 min, the fulgides were almost quantitatively transformed into the closed (*C*) forms. As for **13E**, the (*E*)→(*Z*) isomerization is suppressed in **14E** due to the steric hindrance at C-6. In the cases of **12** and **15**, an equilibrium is established between all three isomers in the photostationary states after an irradiation time of 90 min. For **12**, the conformation ratio (*C*)/(*Z*)/(*E*) is 1:0.15:0.15, and for **15** the ratio is 1:0.65:0.83.

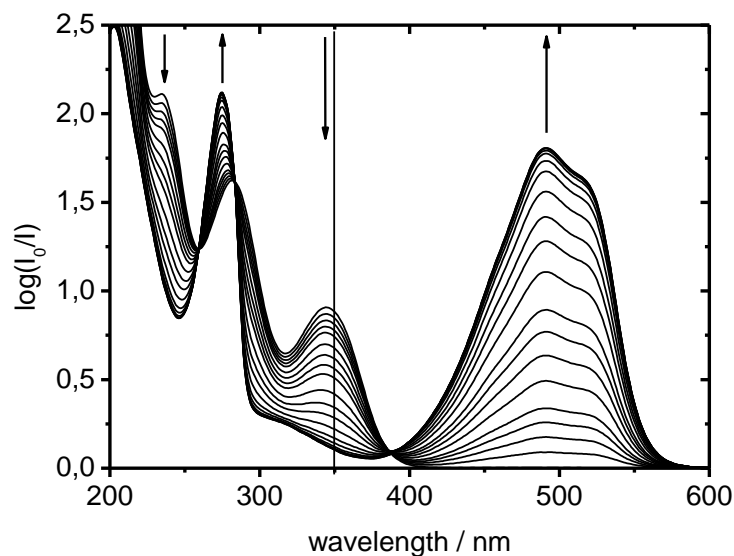


Figure 7.1: . Irradiation of **14E** with 350 nm light ($I = 1.10 \times 10^{-6} \text{ mol}\cdot\text{s}^{-1}\cdot\text{L}^{-1}$; time: 0, 0.25, 0.5, 0.75, 1, 1.5, 2, 2.5, 3, 4, 5, 6, 7.5, 9.5, 11.5, 14.5, 18.5, 23.5, 28.5, 33.5 min).

These results show that the structural modification in **15** does not suppress the (*E*)→(*Z*) isomerization. An explanation for these different photochemical properties caused by steric or electronic differences can be derived from femtosecond time-resolved transient absorption spectroscopy.^[26] In particular, the time-resolved measurements revealed that the photo-induced ring closure reactions are considerably faster in the cases of **13** and **14** ($\tau \approx 50$ fs) compared to **12** and **15** ($\tau \approx 110$ and 140 fs, respectively). Thus, the molecule-specific dynamics in the excited electronic states appear to play decisive roles.

The quantum yields for the photoisomerization reactions of fulgides **12** - **15** in *n*-hexane were determined by using the methods described by Uhlmann and Gauglitz^[37] or Maafi^[38] and are given in Table 7.2. For the known compounds **12** and **13**, the results are in good agreement with the data reported in the literature. Some differences can be found for the value of ϕ_{CE} at 335/365 nm of **12**. However, a range from 0.00 (ϕ_{CE}) up to 0.12 (ϕ_{CE}) is given in the literature, which can be rationalized by the low absorption coefficients of the (*C*) forms at 365 nm.^[37,39] In practice, only an irradiation wavelength around 500 nm appears to be suitable for the (*C*)→(*E*) isomerization and for the determination of ϕ_{CE} .

Table 7.2: Isomerization quantum yields of fulgides **12** - **15**.

compound	ϕ_{EC}^a	ϕ_{EZ}^a	ϕ_{CE}^a	ϕ_{ZE}^a
12	0.23 ₍₃₃₅₎	0.13 ₍₃₃₅₎	0.06 ₍₃₃₅₎ ; 0.10 ₍₅₀₀₎	0.10 ₍₃₃₅₎
13	0.57 ₍₃₃₅₎	0.00	0.12 ₍₃₃₅₎ ; 0.09 ₍₅₀₀₎	- ^[b]
14	0.53 ₍₃₅₀₎	0.00	0.13 ₍₃₅₀₎ ; 0.07 ₍₅₀₀₎	- ^[b]
15	0.17 ₍₃₃₀₎	0.15 ₍₃₃₀₎	0.21 ₍₃₃₀₎ ; 0.16 ₍₅₀₀₎	0.11 ₍₃₃₀₎

^a Irradiation wavelengths [nm] are given as subscripts in parentheses. ^b Not determined.

For fulgides **13E**, **14E**, and **15E**, X-ray crystallographic analysis gave structural information in the solid state (Table 7.3). All (*E*) isomers adopt the (*P*)- E_α conformation in a helical structure in the crystal, and the bond lengths inside the hexatriene units of the fulgides show no significant differences. Compared to the distance between the two ring closing atoms C(2) and C(3) of **12E** [0.3445(4) nm],^[30] only a small deviation is observed for **13E** [0.3426(2) nm], **14E** [0.3559(2) nm], and **15E** [0.3663(2) nm]. Therefore, the interatomic distances do not provide an explanation for the different photochemical properties. The dihedral angles C(9)-C(5)-C(4)-C(3) are also comparable [148.82(11)° for **13E**, 144.83(11)° for **14E**, and 146.29(13)° for **15E**]. Compound **14E** has a strained geometry due to the cycloheptyl ring, which leads to an extension of the dihedral angle C(5)-C(6)-C(1)-C(10) to 151.11(11)° compared with 138.14(10)° for **13E** and 136.83(13)° for **15E**. The complete crystallographic data for **14** and **15** will be published elsewhere.^[40]

NMR experiments were carried out to assess the conformational properties of the furyl-fulgides **13E**, **14E**, and **15E**. The assignments were made by comparison with previously assigned furylfulgides,^[41] and on the basis of correlations in two-dimensional gCOSY, HSQC, and HMBC experiments. Specifically for **14E**, C-7 and C-9 were distinguished in the HMBC experiments by the presence of a 4J coupling between H(Me-3a/b) and C-7, whereas C-4 and C-5 were established by strong 3J correlations to H(Me-3a/b) and 16a/b-H, respectively. The former correlations also distinguish 13a/b-H from 16a/b-H, because the latter in turn shows correlations to C-11 of the furyl ring. These correlations distinguish C-11 from C-2, allowing for the assignments of C(Me-11) and C(Me-2) from 2J cross peaks. The 3J cross peaks of H(Me-11) and H(Me-2) then unambiguously identify C-10 and C-1, respectively.

NMR experiments at variable temperature were utilized to detect chemical-exchange processes such as rotational barriers in the fulgides. At room temperature, the spectrum of **14E** is characterized by one set of resonances for all methyl groups, indicating the presence of only one rotamer (or fast conversion between the conformers).

Table 7.3: Selected interatomic distances and dihedral angles of X-ray structures of **13E**, **14E**, and **15E**.

compound	distance[nm]	dihedral angle [°]	dihedral angle [°]
	C(2)-C(3)	C(9)-C(5)-C(4)-C(3)	C(5)-C(6)-C(1)-C(10)
13E	0.3426(2)	148.82(11)	138.14(10)
14E	0.3559(2)	146.29(13)	151.11(11)
15E ^a	0.3663(2)	146.29(13)	136.83(13)
	0.3540(2)	152.36(13)	129.36(13)

^a Two molecules are present in the elementary cell, one of which showing strained angles due to packing effects.

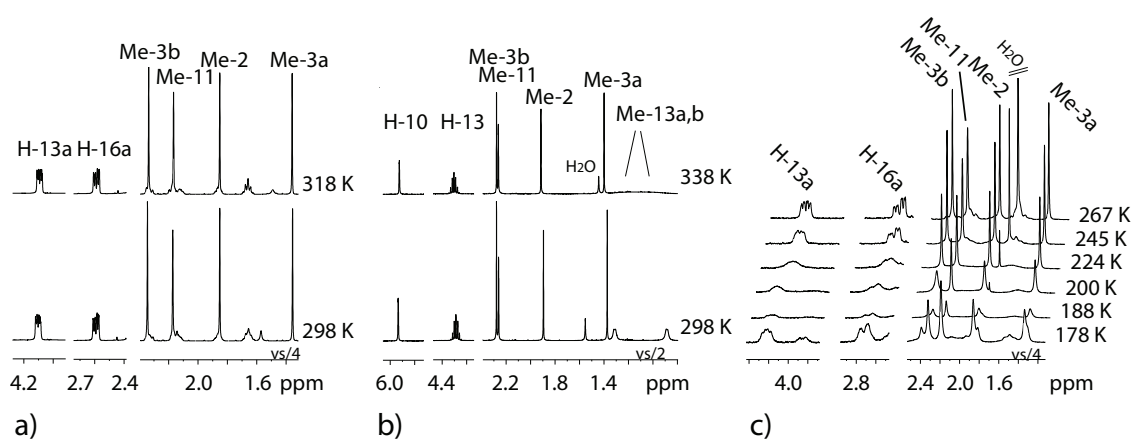


Figure 7.2: (a) 1D ^1H NMR spectra of **14E** at 298 and 318 K. Neither linewidth nor chemical shift change appreciably for any line, including the strongly diastereotopic 13a-H or 16a-H (at $\delta = 4.10$ and 2.60 ppm, respectively). (b) 1D ^1H NMR spectra of **13E** at elevated temperatures from 298 to 338 K. (c) Expanded regions of 1D ^1H NMR spectra of **14E** (200 MHz, CD_2Cl_2) at variable temperatures. The vertical scale of the 13a-H and 16a-H protons (left panel) is increased four-fold versus the upfield region (right panel).

The prochiral methylene ring protons in the cycloheptyl ring, however, lead to sharp, well-separated resonances with clear coupling patterns that are very similar to those of the clearly distinguishable prochiral methyl groups in furyl(isopropyl)fulgide **13E**.

Thus, NMR spectra of **14E** were acquired at elevated temperatures up to 318 K and compared to those of **13E** (Figure 7.2). For **13E**, it had been shown that the methyl groups exchange frequencies at elevated temperatures, with a coalescence temperature of approximately 338 K (Figure 7.2b).^[31,41] In contrast, the spectra of **14E** were devoid of any line broadening, even at the highest achievable temperature, suggesting the absence of any racemization. This was confirmed by NOESY/EXSY experiments at 323 K, which were void of any negative exchange cross peak contributions.

To detect additional rotation barriers, the temperature of the NMR probe was lowered from room temperature to 178 K. In the data for **13E**, subtle chemical-shift changes were observed throughout the fulgide spectra (Figure 7.3a). All resonance line widths changed almost imperceptibly and uniformly, consistent with an increase due only to solvent viscosity changes (and increasing difficulties attaining a homogenous magnetic field through shimming). No further barrier was detected. For **14E**, a kinetic barrier with a coalescence temperature of about 210 K (Figure 7.2c) was observed. Below this transition, two sets of signals are present in a ratio of 1:2.5. Most noticeable is the resonance doubling for 13a-H, with two resonances of similar multiplicities at $\delta = 4.20$ and 3.82 ppm at 178 K. The signal of 16a-H also splits, but the upfield-shifted second resonance is superimposed by those of the methyl groups. For the methyl groups, the doubling is best seen for H(Me-3b) and H(Me-2) owing to the larger shift difference between the peaks.

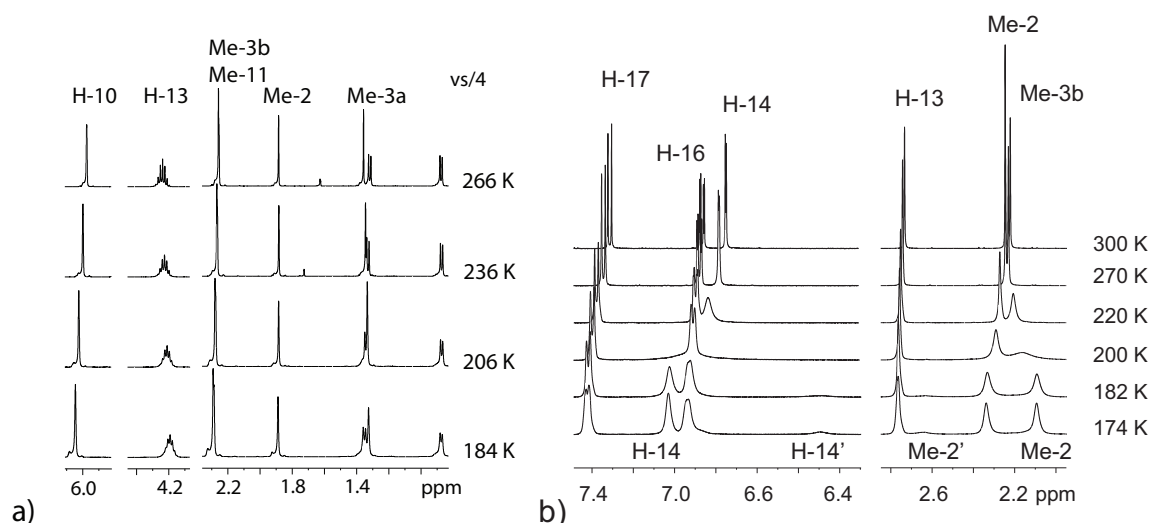


Figure 7.3: (a) Low-temperature 1D ¹H NMR spectra of **13E** (500 MHz, CD₂Cl₂). (b) 1D ¹H NMR spectra of **15E** at variable temperature (200 MHz, CD₂Cl₂).

Racemization of fulgides has been suggested to occur through a three-step process, because the (*P*)- $E_{\alpha} \rightarrow$ (*M*)- E_{α} enantiotopomerization/helical chirality inversion is prohibited by steric overlap.^[30] For **13E**, the belly roll process ($E_{\alpha} \rightarrow E_{\beta}$) converts the helical chirality in concert with the rotation around the C-1–C-6 bond. The enantiotopomerization [(*P*)- $E_{\beta} \rightarrow$ (*M*)- E_{β}] has the higher barrier of 53 kJmol⁻¹ and is responsible for the coalescence observable at high temperature (Figure 7.2b).^[30,31] The barrier for the equivalent process in **14E** can only be similar or higher, owing to larger steric hindrance in **14E**. Most importantly, the cyclic analogue **14E** does not show this coalescence, indicating that the E_{β} - E_{β} conversion was successfully prevented (the respective coalescence temperature raised beyond detection), thus indicating that a non-racemizing fulgide was synthesized.

Interestingly, a low-temperature transition was observed for **14E**, which, in principle, could originate either from the belly roll or from an alternative rotational barrier. Energy calculations for favorable ring conformations of **14E** suggest that the E_{β} conformation is 35 kJ/mol less stable than the E_{α} conformation. An interconversion between these rotamers would thus be expected to have a rotational barrier much higher than 35 kJ/mol, and thus lead to a chemical exchange process above room temperature. Furthermore, an energy difference of 35 kJ/mol results in a population fraction of 100% of the E_{α} conformer using Boltzmann's distribution, whereas the ratio determined from NMR spectroscopic measurements was 1:2.5. It is far more likely instead that the low-temperature interconversion stems from two favorable, energetically nearly equal conformations of the cycloheptyl moiety (Figure 7.4). This agrees well with the observed chemical shift difference between the respective rotamer resonances, with the largest shift differences being observed for 13-H and 16-H, and with typical coalescence temperatures for ring

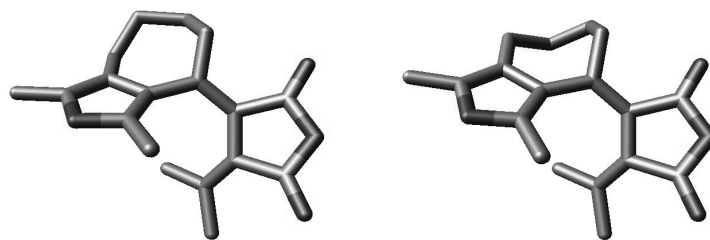


Figure 7.4: Calculated conformers of $14E_\alpha$. Ground-state geometry optimizations were performed at the DFT/B3LYP/6-31+G(d,p) level using Gaussian09.^[43] The calculated energy difference is approx. 6 kJ/mol, which results in a population fraction of approximately 0.9 of the more stable conformer (right) at room temperature by using Boltzmann's distribution. The left conformer matches the experimental X-ray crystallographic structure (carbon atoms grey, oxygen atoms dark grey).^[40]

inversion.^[42] Furthermore, the signals of the isopropylidene methyl groups H(Me-3a/b) shift noticeably, because their location beneath the furyl ring makes them particularly sensitive to furyl ring rotation owing to the ring current effect.

Due to the absence of any diastereotopic groups in (benzofuryl)fulgide $15E$, the enantiotopomerization at high temperature cannot be detected. As expected, the compound exhibits only one set of resonances at room temperature. At low temperatures, however, a rotational barrier is detectable (Figure 7.3b). In dichloromethane the NMR analysis at 500 MHz reveals that the coalescence is clearly observable for 14-H (ca. 200 K) in the benzylic ring and the furyl methyl group H(Me-2) (ca. 190 K), leading to an estimate for the rotational energy barrier of 37 kJ/mol. The corresponding proton chemical shifts for the two rotamers at low temperatures were established by a 2D-EXSY experiment. The ratio between rotamers is approximately 6:1, which is in excellent agreement with the calculated fraction of the E_α -conformer of 82% and 18% of the E_β -conformer.^[26] Based on the knowledge of rotational barriers in the furylfulgide, it is likely that the $E_\alpha \rightarrow E_\beta$ conversion, which becomes visible in this furylfulgide analogue, is due to increased steric hindrance.

7.3 Conclusion

The synthesis of furylfulgides with different structural modifications, which greatly influence the isomerization processes of the photochromic compounds, has been developed. The modification at C-6/C-10 of the furyl backbone strongly affected the belly roll process, or even eliminates it completely. Whereas benzannulation (**15**) reduced the belly roll process (P)- $E_\alpha \rightarrow (M)$ - E_β , and introduction of an isopropyl group (**13**) reduced the (E) \rightarrow (Z) isomerization, both processes and enantiotopomerization are suppressed for the bicyclic furylfulgide **14**.

7.4 Experimental

General: All commercially available compounds, including 2,5-dimethylfuran and LDA (2M in THF/*n*-heptane/ethylbenzene) were purchased from Acros, Alfa Aesar, or Sigma Aldrich and were used without further purification. Solvents were dried according to standard procedures. Column chromatography was performed with silica gel (0.040-0.063 mm, Macherey-Nagel). All NMR data were acquired with Bruker Avance 600, DRX500 or Avance 200 MHz spectrometers. 1D ^1H NMR, ^{13}C NMR, ^{13}C -cpd, DEPT135, gCOSY, HSQC, and HMBC were used for spectroscopic analysis. Samples were dissolved in CDCl_3 , $[\text{D}_6]\text{DMSO}$, or in CD_2Cl_2 with TMS added as internal standard. Spectra were referenced to TMS or solvent lines [CDCl_3 : $\delta = 7.24$ ppm (^1H), 77.0 ppm (^{13}C); $[\text{D}_6]\text{DMSO}$: $\delta = 2.49$ ppm (^1H), 39.5 ppm (^{13}C); CD_2Cl_2 : $\delta = 5.30$ ppm (^1H), 53.52 ppm (^{13}C)]. EI mass spectra were recorded with a VG Autospec X (Micromass CO. UK Ltd.) and HR mass spectra were performed with a Fourier Transform Ion Cyclotron Resonance (FT-ICR) mass spectrometer APEX III (Bruker Daltonik GmbH, Bremen, Germany). The quantum yields of the photoisomerization reactions of fulgides **12–15** in *n*-hexane were determined by monitoring the evolution of the absorption spectra during irradiation of stirred solutions of the (*E*) isomers using a 150 W xenon lamp as light source and a monochromator for wavelength selection (typical spectral width $\Delta\lambda = 5 - 10$ nm). All measurements were performed in a quartz cuvette with $d = 1$ cm pathlength for irradiation and absorption measurements. The irradiation intensities were determined with a power meter (Coherent, 3 Σ , PS19Q), and the accuracy of the intensity measurements was checked by ferrioxalate actinometry.^[44] Absorption spectra were measured with a Shimadzu UV-2401 desktop spectrometer.

General preparation of 3-acyl-2,5-dimethylfurans 1-3: The appropriate acyl chloride (47 mmol) was added to a suspension of AlCl_3 (6.67 g, 50 mmol) in dichloromethane (150 mL) under argon at 0 °C. After stirring for 1 h 2,5-dimethylfuran (5.00 mL, 47 mmol) was added, and the solution immediately turned dark-red. After 30 min, the reaction mixture was cautiously hydrolyzed by addition of aqueous HCl (2 M), and the organic layer was separated. The aqueous layer was extracted with dichloromethane (3×100 mL), and the combined organic layers were washed with saturated aqueous NaCl solution, dried over MgSO_4 , and the solvent was removed in vacuo. The residue was purified by column chromatography.

1-(2,5-Dimethylfuran-3-yl)ethanone (1): Yield 53%; $R_f = 0.36$ (cyclohexane/ethyl acetate 9:1). ^1H NMR (500 MHz, CDCl_3 , 25 °C): $\delta = 6.13$ (s, 1H; Ar-H), 2.47 (s, 3H; CH_3), 2.30 (s, 3H; CH_3), 2.19 (s, 3H; CH_3) ppm. ^{13}C NMR (126 MHz, CDCl_3 , 25 °C): $\delta = 194.2, 156.7, 149.8, 122.0, 106.0, 29.0, 14.2, 13.0$ ppm. MS (70 eV): m/z (%)=138 (55) [M^+], 123 (100) [$\text{M} - \text{CH}_3^+$], 81 (21), 43 (82).

1-(2,5-Dimethylfuran-3-yl)-2-methylpropan-1-one (2): Yield 56%; $R_f = 0.61$ (cyclohexane/ethyl acetate 9:1). $^1\text{H NMR}$ (500 MHz, CDCl_3 , 25 °C): $\delta = 6.16$ (s, 1H; Ar-H), 3.01 (sept, $^3J(\text{H,H}) = 6.6$ Hz, 1H; CH), 2.52 (s, 3H; CH_3), 2.22 (s, 3H; CH_3), 1.11 (d, $^3J(\text{H,H}) = 6.6$ Hz, 6H; CH_3) ppm. $^{13}\text{C NMR}$ (126 MHz, CDCl_3 , 25 °C): $\delta = 201.0, 157.5, 149.7, 120.5, 105.7, 38.1, 18.6, 14.3, 13.2$ ppm. MS (70 eV): m/z (%)=166 (18) [M^+], 123 (100), 43 (28).

Ethyl 5-(2,5-Dimethylfuran-3-yl)-5-oxopentanoate (3): Yield 62%; $R_f = 0.23$ (cyclohexane/ethyl acetate 7:3). $^1\text{H NMR}$ (500 MHz, CDCl_3 , 25 °C): $\delta = 6.14$ (s, 1H; Ar-H), 4.07 (q, $^3J(\text{H,H}) = 6.9$ Hz, 2H; CH_2), 2.67 (t, $^3J(\text{H,H}) = 7.2$ Hz, 2H; CH_2), 2.47 (s, 3H; CH_3), 2.32 (t, $^3J(\text{H,H}) = 7.2$ Hz, 2H; CH_2), 2.18 (s, 3H; CH_3), 1.92 (m, 2H; CH_2), 1.19 (t, $^3J(\text{H,H}) = 6.9$ Hz, 3H; CH_3) ppm. $^{13}\text{C NMR}$ (126 MHz, CDCl_3 , 25 °C): $\delta = 195.7, 173.2, 156.9, 149.8, 121.4, 105.5, 60.2, 39.9, 33.3, 19.1, 14.2, 14.1, 13.1$ ppm. MS (70 eV): m/z (%)=238 (19) [M^+], 193 (23) [$\text{M} - \text{OC}_2\text{H}_5^+$], 192 (23), 123 (100), 43 (38).

5-(2,5-Dimethylfuran-3-yl)pentanoic acid (4): Ester **3** (5.80 g, 24 mmol), KOH (6.86 g, 122 mmol), and hydrazine (3.54 mL, 73 mmol, 98% aq. sol.) were dissolved in diethylene glycol (150 mL) and refluxed at 160 °C. After 1 h, the residual hydrazine and water was distilled off, and the reaction mixture was heated to 195 °C for 4 h. The reaction mixture was neutralized with aqueous HCl (2 M) and extracted with ethyl acetate (4 × 75 mL). The combined organic layers were washed with saturated aqueous NaCl solution, dried with MgSO_4 , and the solvent was removed in vacuo. The product **4** (4.50 g, 23 mmol, 96%) was used without further purification, but can be purified by column chromatography. $R_f = 0.59$ (cyclohexane/ethyl acetate 7:3). $^1\text{H NMR}$ (500 MHz, CDCl_3 , 25 °C): $\delta = 11.08$ (br. s, 1H; COOH), 5.74 (s, 1H; Ar-H), 2.34 (t, $^3J(\text{H,H}) = 7.5$ Hz, 2H; CH_2), 2.27 (t, $^3J(\text{H,H}) = 7.4$ Hz, 2H; CH_2), 2.19 (s, 3H; CH_3), 2.14 (s, 3H; CH_3), 1.60-1.66 (m, 2H; CH_2), 1.48-1.54 (m, 2H; CH_2) ppm. $^{13}\text{C NMR}$ (126 MHz, CDCl_3 , 25 °C): $\delta = 180.2, 149.1, 145.1, 118.9, 107.2, 33.9, 29.7, 24.4, 24.2, 13.4, 11.3$ ppm. MS (70 eV): m/z (%)=196 (34) [M^+], 123 (12), 110 (37), 109 (100), 95 (18), 43 (82).

1,3-Dimethyl-5,6,7,8-tetrahydrocyclohepta[c]furan-4-one (5): Polyphosphoric acid (14 g) was warmed to 80 °C, and **4** (4.50 g, 23 mmol) was added. After stirring for 15 min, the reaction mixture was hydrolyzed with water (120 mL) and extracted with ethyl acetate (4 × 75 mL). The combined organic layers were washed with saturated aqueous NaCl solution, dried with MgSO_4 , and the solvent was removed in vacuo. Purification by column chromatography (cyclohexane/ethyl acetate, 9:1) gave the product **5** (3.74 g, 21 mmol, 93%) as a slight yellow liquid. $R_f = 0.31$ (cyclohexane/ethyl acetate 9:1). $^1\text{H NMR}$ (500 MHz, CDCl_3 , 25 °C): $\delta = 2.55$ (m, 2H; CH_2), 2.51 (m, 2H; CH_2), 2.39 (s, 3H; CH_3), 2.11 (s, 3H; CH_3), 1.71-1.79 (m, 4H; CH_2) ppm. $^{13}\text{C NMR}$ (126 MHz, CDCl_3 , 25 °C):

$\delta = 199.5, 155.8, 144.5, 122.5, 117.7, 42.3, 25.5, 22.4, 22.1, 13.6, 10.9$ ppm. HRMS: m/z calcd. for $C_{11}H_{14}O_2$ [M^+] 178.09938; found 178.09900.

(Z)-4-Methylaminopent-3-en-2-one (6): Methyl amine (10 mL, 0.12 mol, 40% aq. sol.) was added to acetyl acetone (10.30 mL, 0.10 mol) and stirred at room temperature for 2 h. After the exothermic reaction had ended, the layers were separated, and the aqueous layer was extracted with diethyl ether (2×30 mL). The combined organic layers were washed with water and with saturated aqueous NaCl solution, and dried with $MgSO_4$. All volatile compounds were removed in vacuo, and the product was recrystallized from diethyl ether. Compound **6** was obtained as colorless needles (10.52 g, 0.09 mol, 90%), which sublimed in high vacuum. 1H NMR (500 MHz, $CDCl_3$, 25 °C): $\delta = 10.67$ (br. s, 1H; NH), 4.95 (s, 1H; CH), 2.89 (d, $^3J(H,H) = 5.1$ Hz, 3H; NCH_3), 1.96 (s, 3H; CH_3), 1.88 (s, 3H; CH_3) ppm. ^{13}C NMR (126 MHz, $CDCl_3$, 25 °C): $\delta = 194.6, 164.0, 95.0, 29.3, 28.6, 18.5$ ppm. MS (70 eV): m/z (%)=113 (50) [M^+], 98 (100) [$M - CH_3^+$], 56 (65), 43 (16), 40 (14).

1-(5-Hydroxy-2-methylbenzofuran-3-yl)ethanone (7):^[34] To a solution of *p*-benzoquinone (2.13 g, 20 mmol) in glacial acetic acid (80 mL), compound **6** (2.33 g, 21 mmol), dissolved in glacial acetic acid (30 mL), was added. In an exothermic reaction, a colorless precipitate formed after a few minutes. After stirring for 2 h, the precipitate was filtered off, washed with water and a small amount of diethyl ether, and dried in vacuo. The product **7** (2.19 g, 12 mmol, 58%) was used without further purification but can be recrystallized from glacial acetic acid. 1H NMR (500 MHz, $[D_6]DMSO$, 25 °C): $\delta = 9.31$ (s, 1H; OH), 7.35 (m, 2H; Ar-H), 6.73 (dd, $^3J(H,H) = 8.8$ Hz, $^4J(H,H) = 2.5$ Hz, 1H; Ar-H), 2.72 (s, 3H; CH_3), 2.53 (s, 3H; CH_3) ppm. ^{13}C NMR (126 MHz, $[D_6]DMSO$, 25 °C): $\delta = 193.8, 163.2, 154.3, 146.9, 126.7, 117.1, 112.9, 111.1, 106.4, 30.8, 15.4$ ppm. MS (70 eV): m/z (%)=190 (51) [M^+], 176 (11), 175 (100), 147 (13), 43 (20).

1-(5-Methoxy-2-methylbenzofuran-3-yl)ethanone (8): **7** (1.20 g, 6 mmol) was dissolved in dimethyl formamide (40 mL), and sodium hydride (0.30 g, 7 mmol, 60% susp.) was added at 0 °C under argon. After stirring for 1 h, methyl iodide (0.47 mL, 7 mmol) was added, and the reaction mixture was stirred at room temperature for an additional 2 h. The reaction was quenched by addition of aqueous HCl (50 mL, 2 M), and the aqueous layer was extracted with ethyl acetate (3×75 mL). The combined organic layers were washed with saturated aqueous NaCl solution, dried with $MgSO_4$, and the solvent was removed in vacuo. The product was purified by flash column chromatography (cyclohexane/ethyl acetate, 7:3) and recrystallization from cyclohexane. **8** (1.00 g, 5 mmol, 82%) was obtained as yellow crystals. $R_f = 0.64$ (cyclohexane/ethyl acetate 7:3). 1H NMR (500 MHz, $CDCl_3$, 25 °C): $\delta = 7.46$ (d, $^4J(H,H) = 2.5$ Hz, 1H; Ar-H), 7.31 (d, $^3J(H,H) = 8.8$ Hz, 1H; Ar-H),

6.86 (dd, $^3J(\text{H,H}) = 8.8$ Hz, $^4J(\text{H,H}) = 2.5$ Hz, 1H; Ar-H), 3.86 (s, 3H; CH₃), 2.75 (s, 3H; CH₃), 2.60 (s, 3H; CH₃) ppm. ¹³C NMR (126 MHz, CDCl₃, 25 °C): $\delta = 194.0, 163.3, 156.8, 148.4, 126.8, 117.9, 112.7, 111.2, 104.5, 55.9, 30.9, 15.6$ ppm. MS (70 eV): m/z (%) = 205 (11), 204 (74) [M⁺], 190 (17), 189.0 (100) [M - CH₃⁺], 174 (9) [M - 2CH₃⁺], 161 (10), 147 (7), 118 (7), 90 (6), 82 (6), 63 (8).

Diethyl 2-Isopropylidenesuccinate (9):^[45] Diethylsuccinate (9.62 mL, 57.40 mmol) was added to a solution of potassium *tert*-butoxide (6.78 g, 0.06 mmol) in *tert*-butyl alcohol (75 mL). After stirring for 1 h, acetone (4.20 mL, 57.40 mmol) was added, and the reaction mixture was heated to reflux for 20 h. The reaction mixture was acidified with aqueous HCl (2 M) and extracted with diethyl ether (4 × 70 mL). The combined organic layers were washed with saturated aqueous NaCl solution, dried with MgSO₄, and all volatile compounds were removed in vacuo. The dark residue was dissolved in ethanol (140 mL) and acidified with concd. HCl (7 mL). After stirring at room temperature for 48 h, the reaction mixture was neutralized with saturated aqueous NaHCO₃ solution and extracted with diethyl ether (3 × 100 mL). The combined organic layers were washed with water, saturated aqueous NaCl solution, dried with MgSO₄, and all volatile compounds were removed in vacuo. Distillation at 0.07 mbar gave **9** as a colorless liquid (2.63 g, 8.94 mmol, 60%). B.p. 67 – 70 °C (0.07 mbar). ¹H NMR (500 MHz, CDCl₃, 25 °C): $\delta = 4.09$ (q, $^3J(\text{H,H}) = 6.91$ Hz, 2H; CH₂), 4.05 (q, $^3J(\text{H,H}) = 6.91$ Hz, 2H; CH₂), 3.28 (s, 2H; CH₂), 2.06 (s, 3H; CH₃), 1.78 (s, 3H; CH₃), 1.19 (t, $^3J(\text{H,H}) = 6.91$ Hz, 3H; CH₃), 1.16 (t, $^3J(\text{H,H}) = 6.91$ Hz, 3H; CH₃) ppm. ¹³C NMR (126 MHz, CDCl₃, 25 °C): $\delta = 171.3, 167.7, 148.7, 120.6, 60.5, 60.1, 35.3, 23.1, 23.1$ ppm. MS (70 eV): m/z (%) = 214 (2) [M⁺], 169 (55), 168 (76), 141 (14), 140 (28), 113 (23), 112 (100), 96 (13), 95 (52), 68 (19), 67 (58), 59 (14), 53 (16).

General preparation of fulgides 12-15:^[35,36] A solution of **9** (15 mmol) in THF (15 mL) was cooled to -78 °C, and LDA (7.5 mL, 15 mmol; 2 M, THF/*n*-heptane/ethylbenzene) was added under argon. After stirring for 1 h, the appropriate ketone (10 mmol), dissolved in THF (30 mL), was added by using a syringe. The reaction mixture was warmed to room temperature over night and stirred for an additional 24 h. The progress of the reaction was monitored by TLC. Upon completion, the reaction mixture was acidified with aqueous HCl (2 M), and the aqueous layer was extracted with ethyl acetate (3 × 50 mL). The combined organic layers were washed with saturated aqueous NaCl solution, dried with MgSO₄, and the solvent was removed in vacuo. The residue was dissolved in cyclohexane/ethyl acetate (7:3), filtered through silica gel and the solvent removed in vacuo. The residue was dissolved in ethanol (60 mL), and a saturated aqueous solution of KOH (5 mL) was added. After stirring at 70 °C for 20 h, the reaction mixture was poured onto ice and acidified

with aqueous HCl (2 M). The aqueous layer was extracted with ethyl acetate (3 × 50 mL), and the combined organic layers were washed with saturated aqueous NaCl, dried with MgSO₄, and the solvent was removed in vacuo. The dark-brown residue was dissolved in dichloromethane (50 mL), and DCC (4.13 g, 20 mmol) was added. After stirring for 48 h, the reaction mixture was filtered through silica gel, and the solvent was removed in vacuo. The products were purified by column chromatography and recrystallization from adapted solvents.

Fulgide 12-E:^[25] Yield: 8%; $R_f = 0.31$ (cyclohexane/ethyl acetate 9:1). ¹H NMR (500 MHz, CDCl₃, 25 °C): $\delta = 5.90$ (s, 3H; Ar-H), 2.55 (s, 3H; CH₃), 2.32 (s, 3H; CH₃), 2.22 (s, 3H; CH₃), 1.97 (s, 3H; CH₃), 1.33 (s, 3H; CH₃) ppm. ¹³C NMR (126 MHz, CDCl₃, 25 °C): $\delta = 163.8, 163.3, 153.7, 151.3, 148.3, 146.8, 124.2, 120.9, 119.1, 105.8, 26.8, 22.6, 22.2, 13.9, 13.3$ ppm. MS (70 eV): m/z (%)=260 (49) [M⁺], 246 (16), 245 (100) [M - CH₃⁺], 217 (21), 201 (17), 173 (24), 145 (16), 128 (14), 115 (12), 91 (12), 77 (12), 43 (66). HRMS: m/z calcd. for C₁₅H₁₆O₄ [M⁺] 260.10486; found 260.10260.

Fulgide 12-Z:^[25] Yield: 6%; $R_f = 0.17$ (cyclohexane/ethyl acetate 9:1). ¹H NMR (500 MHz, CDCl₃, 25 °C): $\delta = 5.96$ (s, 1H; Ar-H), 2.40 (s, 3H; CH₃), 2.24 (s, 3H; CH₃), 2.18 (s, 3H; CH₃), 2.06 (s, 3H; CH₃), 1.93 (s, 3H; CH₃) ppm. ¹³C NMR (126 MHz, CDCl₃, 25 °C): $\delta = 163.7, 160.9, 153.8, 153.1, 150.3, 145.6, 121.8, 120.1, 119.4, 105.6, 26.8, 25.3, 22.3, 13.7, 13.3$ ppm. MS (70 eV): m/z (%)=260 (45) [M⁺], 246 (16), 245 (100) [M - CH₃⁺], 217 (23), 201 (21), 199 (16), 173 (29), 145 (19), 129 (15), 128 (17), 115 (15), 91 (14), 77 (15), 43 (79). HRMS: m/z calcd. for C₁₅H₁₆O₄ [M⁺] 260.10486; found 260.10310.

Fulgide 13-E:^[39] Yield: 7%; $R_f = 0.45$ (cyclohexane/ethyl acetate 7:3). ¹H NMR (500 MHz, CDCl₃, 25 °C): $\delta = 5.01$ (s, 1H; 10-H), 4.26 (sept, ³ J (H,H) = 6.9 Hz, 1H; 13-H), 2.23 (s, 3H; Me-11), 2.25 (s, 3H; Me-3b), 1.87 (s, 3H; Me-2), 1.34 (s, 3H; Me-3a), 1.28 (d, ³ J (H,H) = 6.9 Hz, 3H; Me-13a), 0.85 (d, ³ J (H,H) = 6.9 Hz, 3H; Me-13b) ppm. ¹³C NMR (126 MHz, CDCl₃, 25 °C): $\delta = 163.2$ (s, C-9), 163.1 (s, C-7), 157.9 (s, C-6), 154.1 (s, C-3), 150.6 (s, C-11), 147.0 (s, C-2), 120.7 (s, C-4), 120.1 (s, C-5), 119.2 (s, C-1), 105.6 (d, C-10), 30.8 (d, C-13), 27.1 (q, Me-3a), 22.6 (q, Me-13b), 22.6 (q, Me-3b), 20.5 (q, Me-13a), 13.3 (q, Me-11), 12.8 (q, Me-2) ppm. MS (70 eV): m/z (%)=289 (15), 288 (74) [M⁺], 274 (14), 273 (74) [M - CH₃⁺], 245 (41), 217 (15), 201 (27), 199 (26), 173 (17), 128 (16), 115 (17), 96 (23), 91 (17), 77 (15), 43 (100). HRMS: m/z calcd. for C₁₇H₂₀O₄ [M⁺] : 288.13616; found 288.13440.

Fulgide 13-Z:^[39] Yield: 5%; $R_f = 0.32$ (cyclohexane/ethyl acetate 7:3). ¹H NMR (500 MHz, CDCl₃, 25 °C): $R_f = 5.86$ (s, 1H; Ar-H), 2.81 (sept, ³ J (H,H) = 6.9 Hz, 1H; CH), 2.38 (s, 3H; CH₃), 2.25 (s, 3H; CH₃), 2.12 (s, 3H; CH₃), 2.03 (s, 3H; CH₃), 1.16

(d, $^3J(\text{H,H}) = 6.9$ Hz, 3H; CH_3), 0.97 (d, $^3J(\text{H,H}) = 6.9$ Hz, 3H; CH_3) ppm. ^{13}C NMR (126 MHz, CDCl_3 , 25 °C): $\delta = 163.4, 161.3, 155.7, 153.3, 151.8, 149.8, 121.1, 120.0, 115.2, 106.3, 34.2, 26.6, 22.1, 21.8, 19.1, 13.4, 12.6$ ppm. MS (70 eV): m/z (%)=289 (15), 288 (78) $[\text{M}^+]$, 273 (76) $[\text{M} - \text{CH}_3^+]$, 245 (44), 227 (39), 217 (19), 201 (31), 199 (26), 173 (20), 128 (15), 115 (17), 96 (23), 91 (16), 43 (100).

Fulgide 14-E: Yield: 6%; $R_f = 0.75$ (cyclohexane/ethyl acetate 7:3). ^1H NMR (500 MHz, CD_2Cl_2 , 25 °C, TMS): $\delta = 4.10$ (ddd, $^3J(\text{H,H}) = 13$ Hz, $^3J(\text{H,H}) = 6$ Hz, $^2J(\text{H,H}) = 3$ Hz, 1H; 13a-H), 2.60 (ddd, $^3J(\text{H,H}) = 15$ Hz, $^3J(\text{H,H}) = 7$ Hz, $^2J(\text{H,H}) = 2$ Hz, 1H; 16a-H), 2.35 (m, 1H; 16b-H), 2.32 (s, 3H; Me-3b-H), 2.20-2.08 (m, 2H; 13b-H, 14a-H), 2.16 (s, 3H; Me-11-H), 1.91-1.82 (m, 1H; 15a-H), 1.84 (s, 3H; Me-2-H), 1.70-1.60 (m, 2H; 15b-H, 14b-H), 1.35 (s, 3H; Me-3a-H) ppm. ^{13}C -NMR (125 MHz, CD_2Cl_2 , 25 °C TMS): $\delta = 163.8$ (s, C-9), 163.4 (s, C-7), 153.9 (s, C-3), 152.8 (s, C-6), 146.0 (s, C-11), 145.2 (s, C-2), 125.3 (s, C-1), 121.1 (s, C-4), 118.5 (s, C-5), 117.6 (s, C-10), 34.0 (t, C-13), 29.2 (t, C-14), 28.0 (t, C-15), 26.7 (q, C-Me-3a), 24.2 (t, C-16), 22.4 (t, C-Me-3b), 13.3 (q, C-Me-2), 11.0 (q, C-Me-11) ppm. MS (70 eV): m/z (%)=301 (20), 300 (100) $[\text{M}^+]$, 285 (14) $[\text{M} - \text{CH}_3^+]$, 257 (30), 243 (14), 241 (21), 213 (18), 128 (13), 115 (13), 43 (84). HRMS: m/z calcd. for $\text{C}_{18}\text{H}_{20}\text{O}_4$ $[\text{M}^+]$ 300.13616; found 300.13550.

Fulgide 14-Z: Yield: 5%; $R_f = 0.65$ (cyclohexane/ethyl acetate 7:3). ^1H NMR (500 MHz, CDCl_3 , 25 °C): $\delta = 2.55 - 2.62$ (m, 2H; CH_2), 2.38 (s, 3H; CH_3), 2.24 (m, 1H; CH_2), 2.18 (m, 1H; CH_2), 2.16 (s, 3H; CH_3), 2.13 (s, 3H; CH_3), 2.04 (m, 1H; CH_2), 1.94 (s, 3H; CH_3), 1.90 (m, 1H; CH_2), 1.41-1.55 (m, 2H; CH_2) ppm. ^{13}C NMR (126 MHz, CDCl_3 , 25 °C): $\delta = 163.8, 161.1, 153.4, 152.2, 151.2, 145.0, 121.8, 121.3, 118.2, 117.8, 37.6, 29.8, 28.4, 26.5, 25.2, 22.1, 13.3, 11.2$ ppm. MS (70 eV): m/z (%)=301 (21), 300 (100) $[\text{M}^+]$, 285 (17) $[\text{M} - \text{CH}_3^+]$, 257 (35), 255 (16), 243 (16), 241 (23), 239 (18), 229 (15), 213 (25), 211 (18), 185 (16), 128 (16), 115 (16), 43 (92). HRMS: m/z calcd. for $\text{C}_{18}\text{H}_{20}\text{O}_4$ $[\text{M}^+]$ 300.13616; found 300.13330.

Fulgide 15-E: Yield: 7%; $R_f = 0.26$ (cyclohexane/ethyl acetate 9:1). ^1H -NMR (500 MHz, CDCl_3 , 25 °C, TMS): $\delta = 7.31$ (d, $^3J(\text{H,H}) = 9$ Hz, 1H; 17-H), 6.88 (dd, $^3J(\text{H,H}) = 9.3$ Hz, 1H; 16-H), 6.73 (d, $^3J(\text{H,H}) = 3$ Hz, 1H; 14-H), 3.82 (s, 3H; 19-H), 2.75 (s, 3H; 13-H), 2.25 (s, 6H; Me-3b-H, Me-2-H), 1.15 (s, 3H; Me-3a-H) ppm. ^{13}C -NMR (CDCl_3 , 125 MHz, 25 °C): $\delta = 163.6$ (s, C-9), 163.0 (s, C-7), 156.2 (s, C-15), 155.5 (s, C-3), 153.5 (s, C-2), 148.8 (s, C-11), 145.0 (s, C-6), 126.5 (s, C-10), 121.5 (s, C-5), 120.8 (s, C-4), 119.6 (s, C-1), 112.9 (d, C-16), 111.6 (d, C-17), 102.8 (d, C-14), 55.9 (q, C-19), 26.7 (q, C-Me-3a), 22.7 (q, C-Me-3b), 22.0 (q, C-13), 14.0 (q, C-Me-2) ppm. MS (70 eV): m/z (%)=327.2 (22), 326.2 (100) $[\text{M}^+]$, 311.2 (43), 309.2 (12), 283.2 (20), 281.2 (12), 267.2 (41), 265.2 (15), 253.2 (13), 239.2 (17), 223.2 (11), 204.1 (11), 165.1 (11), 162.1 (21), 152.1 (12), 115.1 (13),

106.1 (12), 91.1 (12), 77.1 (10), 44.0 (12), 43.0 (16). HRMS: m/z calcd. for $C_{19}H_{18}O_5Na^+$ $[M^+]$ 349.10464; found 349.10480; calcd. for $(C_{19}H_{18}O_5)_2Na^+$ 675.22026; found 675.22007.

Fulgide 15-Z: Yield: 5%; $R_f = 0.11$ (cyclohexane/ethyl acetate 9:1). 1H NMR (500 MHz, $CDCl_3$, 25 °C): $\delta = 7.31$ (d, $^3J(H,H) = 8.8$ Hz, 1H, Ar-H), 6.83 (m, 2H, Ar-H), 3.80 (s, 3H, CH₃), 2.46 (s, 3H, CH₃), 2.36 (s, 3H, CH₃), 2.28 (s, 3H, CH₃), 2.04 (s, 3H; CH₃) ppm. ^{13}C NMR (126 MHz, $CDCl_3$, 25 °C): $\delta = 163.2, 160.9, 157.2, 156.0, 154.3, 148.9, 143.8, 127.6, 122.8, 121.3, 114.9, 111.7, 111.6, 103.0, 66.0, 27.2, 24.0, 22.4, 13.6$ ppm. MS (70 eV): m/z (%)=327 (21), 326 (100) $[M^+]$, 311 (37) $[M-CH_3^+]$, 309 (11), 283 (18), 281 (10), 267 (67), 265 (12), 253 (12) 239 (20), 227 (15), 204 (10), 162 (19), 152 (10), 115 (10). HRMS: m/z calcd. for $C_{19}H_{18}O_5$ $[M^+]$ 326.11542; found 326.11390.

Supporting Information: Detailed evaluation of the quantum yields and evolution of 1H NMR spectra of **12-15** upon successive irradiation.

Acknowledgments

This work was supported by the Biophotonics Initiative of the German Ministry of Research and Education (BMBF, grants 13N9234) (FS, JM) and by the SFB 677 "Function by Switching" funded by the Deutsche Forschungsgemeinschaft (RS, FR, FT).

References

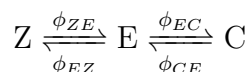
- [1] Y. Yokoyama, *Chem. Rev.* **2000**, *100*, 1717–1739.
- [2] Y. Yokoyama, In B. L. Feringa, ed., *Molecular Switches*. Wiley-VCH, Weinheim **2001**.
- [3] M. Irie, *Chem. Rev.* **2000**, *100*, 1685–1716.
- [4] G. Berkovic, V. Krongauz, V. Weiss, *Chem. Rev.* **2000**, *100*, 1741–1753.
- [5] S. Kawata, Y. Kawata, *Chem. Rev.* **2000**, *100*, 1777–1788.
- [6] B. Yao, Y. Wang, N. Menke, M. Lei, Y. Zheng, L. Ren, G. Chen, Y. Chen, M. Fan, *Mol. Cryst. Liq. Cryst.* **2005**, *430*, 211–219.
- [7] S. Malkmus, F. O. Koller, S. Draxler, T. E. Schrader, W. J. Schreier, T. Brust, J. A. DiGirolamo, W. J. Lees, W. Zinth, M. Braun, *Adv. Funct. Mater.* **2007**, *17*, 3657–3662.
- [8] A. S. Dvornikov, E. P. Walker, P. M. Rentzepis, *J. Phys. Chem. A* **2009**, *113*, 13633–13644.
- [9] F. M. Raymo, M. Tomasulo, *Chem. Soc. Rev.* **2005**, *34*, 327–336.
- [10] J. Cusido, E. Deniz, F. M. Raymo, *Eur. J. Org. Chem.* **2009**, 2031–2045.
- [11] H. Stobbe, *Ber. Dtsch. Chem. Ges.* **1905**, *38*, 3673–3682.
- [12] H. Stobbe, *Ann. Chem.* **1911**, *380*, 1–129.
- [13] H. Stobbe, *Ber. Dtsch. Chem. Ges.* **1907**, *40*, 3372–3382.
- [14] Y. Yokoyama, T. Tanaka, T. Yamane, Y. Kurita, *Chem. Lett.* **1991**, *20*, 1125–1128.
- [15] Y. Yokoyama, T. Sagisaka, Y. Mizuno, Y. Yokoyama, *Chem. Lett.* **1996**, *25*, 587–588.
- [16] A. P. Glaze, H. G. Heller, J. Whittall, *J. Chem. Soc. Perkin Trans. 2* **1992**, 591–594.
- [17] A. Kaneko, A. Tomoda, M. Ishizuka, H. Suzuki, R. Matsushima, *Bull. Chem. Soc. Jpn.* **1988**, *61*, 3569–3573.
- [18] W. Zhao, Y. Ming, Z. Zhu, M. Fan, *J. Photochem. Photobiol., A* **1992**, *63*, 235–240.
- [19] L. Yu, Y. Ming, W. Zhao, M. Fan, *J. Photochem. Photobiol., A* **1992**, *68*, 309–317.
- [20] O. Crescente, H. G. Heller, S. Oliver, *J. Chem. Soc. Perkin Trans. 1* **1979**, 150–153.
- [21] H. G. Heller, S. Oliver, M. Shawe, *J. Chem. Soc. Perkin Trans. 1* **1979**, 154–157.
- [22] H. G. Heller, S. Oliver, *J. Chem. Soc., Perkin Trans. 1* **1981**, 197–201.
- [23] A. Santiago, R. S. Becker, *J. Am. Chem. Soc.* **1968**, *90*, 3654–3658.
- [24] M. Kaftory, *Acta Crystallogr., Sect. C* **1984**, *40*, 1015–1019.
- [25] P. J. Darcy, H. G. Heller, P. J. Strydom, J. Whittall, *J. Chem. Soc., Perkin Trans. 1* **1981**, 202–205.
- [26] R. Siewertsen, F. Renth, F. Strübe, J. Mattay, F. Temps, *Phys. Chem. Chem. Phys.* **2011**, *13*, 3800–3808.
- [27] Y. Yokoyama, T. Iwai, N. Kera, I. Hitomi, Y. Kurita, *Chem. Lett.* **1990**, *19*, 263–264.

- [28] Y. Yokoyama, T. Goto, T. Inoue, M. Yokoyama, Y. Kurita, *Chem. Lett.* **1988**, *17*, 1049–1052.
- [29] J. Kiji, T. Okano, H. Kitamura, Y. Yakoyama, S. Kubota, Y. Kurita, *Bull. Chem. Soc. Jpn.* **1995**, *68*, 616–619.
- [30] Y. Yokoyama, K. Ogawa, T. Iwai, K. Shimazaki, Y. Kajihara, T. Goto, Y. Yokoyama, Y. Kurita, *Bull. Chem. Soc. Jpn.* **1996**, *69*, 1605–1612.
- [31] Y. Yokoyama, T. Iwai, Y. Yokoyama, Y. Kurita, *Chem. Lett.* **1994**, *23*, 225–226.
- [32] T. Reichstein, *Helv. Chim. Acta* **1930**, *13*, 356–360.
- [33] A. Thurkauf, X. Chen, S. Zhang, Y. Gao, A. Kieltyka, J. W. F. Wasley, R. Brodbeck, W. Greenlee, A. Ganguly, H. Zhao, *Bioorg. Med. Chem. Lett.* **2003**, *13*, 2921–2924.
- [34] T. I. Mukhanova, L. M. Alekseeva, E. F. Kuleshova, Y. N. Sheinker, V. G. Granik, *Pharm. Chem. J.* **1993**, *27*, 136–142.
- [35] C. J. Thomas, M. A. Wolak, R. R. Birge, W. J. Lees, *J. Org. Chem.* **2001**, *66*, 1914–1918.
- [36] M. L. Bossi, J. B. Rodríguez, P. F. Aramendía, *J. Photochem. Photobiol., A* **2006**, *179*, 35–41.
- [37] E. Uhlmann, G. Gauglitz, *J. Photochem. Photobiol., A* **1996**, *98*, 45–49.
- [38] M. Maafi, R. G. Brown, *Photochem. Photobiol. Sci.* **2008**, *7*, 1360–1372.
- [39] Y. Yokoyama, T. Inoue, M. Yokoyama, T. Goto, T. Iwai, N. Kera, I. Hitomi, Y. Kurita, *Bull. Chem. Soc. Jpn.* **1994**, *67*, 3297–3303.
- [40] F. Strübe, J. Mattay, B. Neumann, H. G. Stammer, *Acta. Cryst., Sect. C* **2011**, *67*, o33–o36.
- [41] R. Siewertsen, F. Renth, F. Temps, F. Sönnichsen, *Phys. Chem. Chem. Phys.* **2009**, *11*, 5952–5961.
- [42] R. K. Harris, R. A. Spragg, *J. Chem. Soc. (B)* **1968**, 684–691.
- [43] M. J. Frisch, G. W. Trucks, H. B. Schlegel, G. E. Scuseria, M. A. Robb, J. R. Cheeseman, G. Scalmani, V. Barone, B. Mennucci, G. A. Petersson, H. Nakatsuji, M. Caricato, X. Li, H. P. Hratchian, A. F. Izmaylov, J. Bloino, G. Zheng, J. L. Sonnenberg, M. Hada, M. Ehara, K. Toyota, R. Fukuda, J. Hasegawa, M. Ishida, T. Nakajima, Y. Honda, O. Kitao, H. Nakai, T. Vreven, J. A. Montgomery, Jr., J. E. Peralta, F. Ogliaro, M. Bearpark, J. J. Heyd, E. Brothers, K. N. Kudin, V. N. Staroverov, R. Kobayashi, J. Normand, K. Raghavachari, A. Rendell, J. C. Burant, S. S. Iyengar, J. Tomasi, M. Cossi, N. Rega, J. M. Millam, M. Klene, J. E. Knox, J. B. Cross, V. Bakken, C. Adamo, J. Jaramillo, R. Gomperts, R. E. Stratmann, O. Yazyev, A. J. Austin, R. Cammi, C. Pomelli, J. W. Ochterski, R. L. Martin, K. Morokuma, V. G. Zakrzewski, G. A. Voth, P. Salvador, J. J. Dannenberg, S. Dapprich, A. D. Daniels, O. Farkas, J. B. Foresman, J. V. Ortiz, J. Cioslowski, D. J. Fox, Gaussian09 Revision A.02, Gaussian Inc. Wallingford CT 2009.
- [44] C. G. Hatchard, C. A. Parker, *Proc. R. Soc. London, A* **1956**, *235*, 518–536.
- [45] C. G. Overberger, C. W. Roberts, *J. Am. Chem. Soc.* **1949**, *71*, 3618–3621.

Supporting Information

UV/Vis Spectroscopy

Fulgides **12** and **15** show $E \rightarrow Z$ and $Z \rightarrow E$ photoisomerizations and thus react according to A-B-C photokinetics:



The corresponding quantum yields ϕ were determined using the method described by Uhlmann and Gauglitz.^[1] This method requires the molar absorption coefficients of the three isomers and the measurement of absorption time profiles $A^{irr/obs}(t)$ during irradiation at λ_{irr} at three different observation wavelengths λ_{obs} to determine concentration-time profiles of the three isomers. A fourth absorption time profile $A^{irr/irr}(t)$ at the irradiation wavelength is needed for the determination of the photokinetic factors $F^{irr}(t)$. From the concentration-time profiles and the time-dependent photokinetic factors, the quantum yields can be determined. The pure (C) isomer of **15** was obtained by irradiation of a solution of **15E** with 350 nm light and subsequent HPLC (cyclohexane/ethyl acetate 9:1).

The kinetic equations for the three concentrations are given by

$$\begin{aligned} \frac{dc_Z}{dt} &= F^{irr} I_0 d \cdot \left(-\epsilon_Z^{irr} c_Z \phi_{ZE} + \epsilon_E^{irr} c_E \phi_{EZ} \right) \\ \frac{dc_E}{dt} &= F^{irr} I_0 d \cdot \left(-\epsilon_E^{irr} c_E \phi_{EZ} - \epsilon_E^{irr} c_E \phi_{EC} + \epsilon_Z^{irr} c_Z \phi_{ZE} + \epsilon_C^{irr} c_C \phi_{CE} \right) \\ \frac{dc_C}{dt} &= F^{irr} I_0 d \cdot \left(-\epsilon_C^{irr} c_C \phi_{CE} + \epsilon_E^{irr} c_E \phi_{EC} \right) \end{aligned} \quad (24)$$

where I_0^{irr} is the light intensity [$\text{mol s}^{-1} \text{L}^{-1}$], $\epsilon_{Z/E/C}^{irr}$ are the molar absorption coefficients [$\text{L mol}^{-1} \text{cm}^{-1}$] of the (Z), (E) and (C) isomers at λ_{irr} , d is the path length [cm] of the cuvette, $c_{Z/E/C}$ are the concentrations [mol L^{-1}] of the three isomers and $F^{irr}(t) = (1 - 10^{-A^{irr/irr}(t)})/A^{irr/irr}(t)$ is the photokinetic factor of the sample.

Integration of Eqn. (24) with indifferent integration intervals $\Delta t = l$ and $\Delta t = m$ starting at the time i leads to the following expressions for the isomerization quantum yields:

$$\phi_{EC} = \frac{C_{i,m} \Delta c_{C,i,l} - C_{i,l} \Delta c_{C,i,m}}{\epsilon_E^{irr} I_0 \cdot (C_{i,m} E_{i,l} - C_{i,l} E_{i,m})} \quad (25)$$

$$\phi_{EZ} = \frac{Z_{i,l} \Delta c_{Z,i,m} - Z_{i,m} \Delta c_{Z,i,l}}{\epsilon_E^{irr} I_0 \cdot (E_{i,m} Z_{i,l} - E_{i,l} Z_{i,m})} \quad (26)$$

$$\phi_{CE} = \frac{E_{i,m} \Delta c_{C,i,l} - E_{i,l} \Delta c_{C,i,m}}{\epsilon_C^{irr} I_0 \cdot (C_{i,m} E_{i,l} - C_{i,l} E_{i,m})} \quad (27)$$

$$\phi_{ZE} = \frac{E_{i,l} \Delta c_{Z,i,m} - E_{i,m} \Delta c_{Z,i,l}}{\epsilon_Z^{irr} I_0 \cdot (E_{i,m} Z_{i,l} - E_{i,l} Z_{i,m})} \quad (28)$$

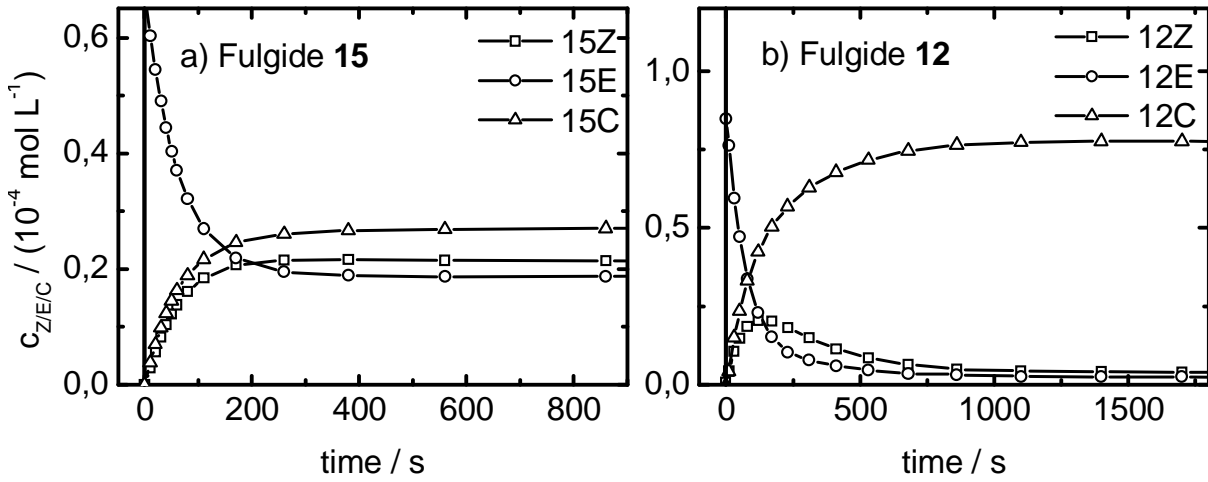


Figure S1: Plot of the concentrations of the three isomers $c_{E/Z/C}(t)$ vs irradiation time a) for fulgide **15** during irradiation at $\lambda_{irr} = 330$ nm and b) for fulgide **12** during irradiation at $\lambda_{irr} = 335$ nm.

with

$$\Delta c_{Z/E/Ci,\Delta t} = c_{Z/E/C}(i + \Delta t) - c_{Z/E/C}(i) \quad (29)$$

$$Z/E/Ci,\Delta t = \int_i^{i+\Delta t} c_{Z/E/C}(t) \cdot F^{irr}(t) dt \quad (30)$$

The numerical integration requires the concentrations $c_{Z/E/C}(t)$ and the photokinetic factors. From the absorption time profiles $A^{irr/obs}(t)$ at the three observation wavelengths $\lambda_{obs,1/2/3}$ and the known molar absorption coefficients of the three isomers the concentrations at all irradiation times and consequently values for $\Delta c_{Z/E/Ci,\Delta t}$ according to Eqn. (29) can be determined from a set of linear equations describing the absorbance of the sample:

$$A^{irr/obs,1/2/3} = \epsilon_Z^{obs,1/2/3} c_Z(t)d + \epsilon_E^{obs,1/2/3} c_E(t)d + \epsilon_C^{obs,1/2/3} c_C(t)d \quad (31)$$

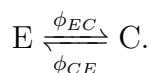
The photokinetic factors $F^{irr}(t)$ can be determined experimentally. The product of $c_{Z/E/C}(t)$ and $F^{irr}(t)$ can be fitted by any functions which can be integrated in order to determine $Z_{i,\Delta t}$, $E_{i,\Delta t}$ and $C_{i,\Delta t}$ according to Eqn. (30). Finally, the isomerization quantum yields can be calculated according to Eqn. (25)-(28). Measurements were carried out at $\lambda_{irr} = 330$ nm for **15** and at $\lambda_{irr} = 335$ nm for **12**. Figure S1 shows the evolution of the concentrations of the (Z), (E) and (C) isomers during irradiation.

The experimental details of the measurement and the determined quantum yields are given in Table S1. For fulgide **15** the results are $\phi_{EC} = 0.17$, $\phi_{EZ} = 0.15$, $\phi_{CE} = 0.21$ and $\phi_{ZE} = 0.11$. A good agreement with literature values was found for fulgide **12**.^[1]

Table S1: Experimental conditions and results for the determination of the isomerization quantum yields of fulgides **12** and **15**.

	λ_{irr} [nm]	I_0^{irr} [mol s ⁻¹ L ⁻¹]	$\lambda_{obs,1}$	$\lambda_{obs,2}$ [nm]	$\lambda_{obs,3}$	c_0 [mol L ⁻¹]	ϕ_{EC}	ϕ_{EZ}	ϕ_{CE}	ϕ_{ZE}
12	335	$3.75 \cdot 10^{-6}$	308	362	475	$0.84 \cdot 10^{-4}$	0.23	0.13	0.06	0.10
15	330	$3.65 \cdot 10^{-6}$	310	365	485	$0.67 \cdot 10^{-4}$	0.17	0.15	0.21	0.11

Fulgides **13** and **14** follow simple A-B photokinetics of the type



The isomerization quantum yields of these photoreactions were determined using the method of Maafl.^[2] Furthermore, this method yields the unknown molar absorption coefficients of the (*C*) isomers of fulgides **13** and **14** in *n*-hexane. Two absorption time profiles $A^{irr/obs}(t)$ are required, measured under isosbestic irradiation ($\lambda_{irr} = \lambda_{isos}$) and non-isosbestic irradiation ($\lambda_{irr} = \lambda_{obs}$) and monitoring the absorption of the sample at the observation wavelength λ_{obs} . For both absorption time profiles ($A^{isos/obs}(t)$ and $A^{obs/obs}(t)$), the observation wavelength is identical to the non-isosbestic irradiation wavelength. The kinetic equation for the (*E*) isomer is given by

$$\frac{dc_E}{dt} = F^{irr} I_0^{irr} d \cdot \left(-\phi_{EC} \epsilon_E^{irr} c_E + \phi_{CE} \epsilon_C^{irr} c_C \right). \quad (32)$$

Equation (32) can be integrated in closed form if F^{irr} is constant, which is true for irradiation at the isosbestic point. The isosbestic absorption time-profile can be described using the general model for the variation of the absorbance of the sample during isosbestic irradiation:^[2]

$$A^{isos/obs}(t) = A_0^{isos/obs} + \frac{m_0^{isos/obs}}{a} \cdot (e^{a \cdot t} - 1) \quad (33)$$

where $m_0^{isos/obs}$ is the initial rate of the reaction, a represents the overall rate coefficient for the reaction and $A_0^{isos/obs}$ is the absorbance of the sample of the pure (*E*) isomer. From fitting of the parameters a and $m_0^{isos/obs}$ of Eqn. (33) to the isosbestic data, and from the final absorbance $A_\infty^{obs/obs}$ of the non-isosbestic absorption time-profile in the photostationary state, the molar absorption coefficient of the (*E*) isomer can be determined

$$\epsilon_C^{obs} = \frac{-A_\infty^{obs/obs} \cdot m_0^{isos/obs}}{\left(A_\infty^{obs/obs} - c_0 \cdot d \cdot \epsilon_E^{obs} \right) \cdot a \cdot c_0 \cdot d}. \quad (34)$$

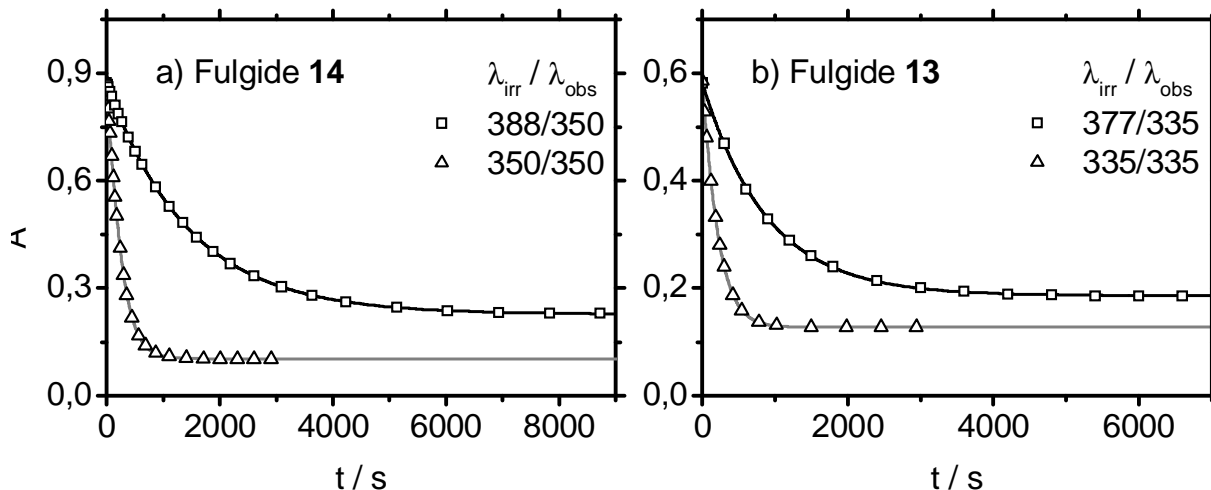


Figure S2: Absorption time profiles of (a) fulgide **14** and (b) fulgide **13** for isosbestic irradiation ($\lambda_{isos}/\lambda_{obs}$, squares) and non-isosbestic irradiation ($\lambda_{obs}/\lambda_{obs}$, triangles). The black lines represent the best fit to the isosbestic traces according to Eqn. (33). The grey line is the exponential fit to the non-isosbestic trace.

In a second step, the isomerization quantum yields can be calculated:

$$\phi_{EC} = \frac{m_0^{isos/obs}}{I_0^{isos} F^{isos} c_0 d^2 \epsilon_E^{isos} \cdot (\epsilon_C^{obs} - \epsilon_E^{obs})} \quad (35)$$

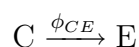
$$\phi_{CE} = -\phi_{EC} - \frac{a}{I_0^{isos} \cdot d \cdot \epsilon_E^{isos} \cdot F^{isos}} \quad (36)$$

Measurements were carried out at $\lambda_{isos} = 388$ nm and $\lambda_{obs} = 350$ nm for **14** and at $\lambda_{isos} = 377$ nm and $\lambda_{obs} = 335$ nm for **13**. Figure S2 shows the absorption time profiles of fulgide **13** and **14** for isosbestic and non-isosbestic irradiation. The experimental details about the measurement and the determined quantum yields are given in Table S2. For **14** the results are $\phi_{EC} = 0.53$ and $\phi_{CE} = 0.12$. A good agreement with literature isomerization quantum yields for fulgide **13** could be found.^[3]

Table S2: Quantum yields and experimental conditions of the photoreactions of fulgides **13** and **14**.

	λ_{obs} [nm]	λ_{isos} [nm]	I_0^{obs} [mol s ⁻¹ L ⁻¹]	I_0^{isos} [mol s ⁻¹ L ⁻¹]	c_0 [mol L ⁻¹]	ϕ_{EC}	ϕ_{CE}
13	335	377	$1.03 \cdot 10^{-6}$	$1.52 \cdot 10^{-6}$	$1.39 \cdot 10^{-4}$	0.57	0.12
14	350	388	$1.10 \cdot 10^{-6}$	$1.31 \cdot 10^{-6}$	$1.93 \cdot 10^{-4}$	0.53	0.13

For all compounds the ϕ_{CE} at 500 nm irradiation wavelength was determined using the method by Uhlmann and Gauglitz.^[1] Since the photokinetic simplifies to



the quantum yield can easily determined by

$$\phi_{CE} = \frac{c_C(t_{i+\Delta t}) - c_C(t_i)}{I_0^{irr} \cdot \int_i^{i+\Delta t} F^{irr} \cdot A^{irr/irr} dt}$$

NMR irradiation experiments

A sample of each fulgide **12E-15E** dissolved in $CDCl_3$ was irradiated successively with 350 nm light. 1H NMR spectra were recorded before irradiation and after 15 min, 30 min and 90 min irradiation time. The evolution of the spectra are shown in Figures S3-S6.

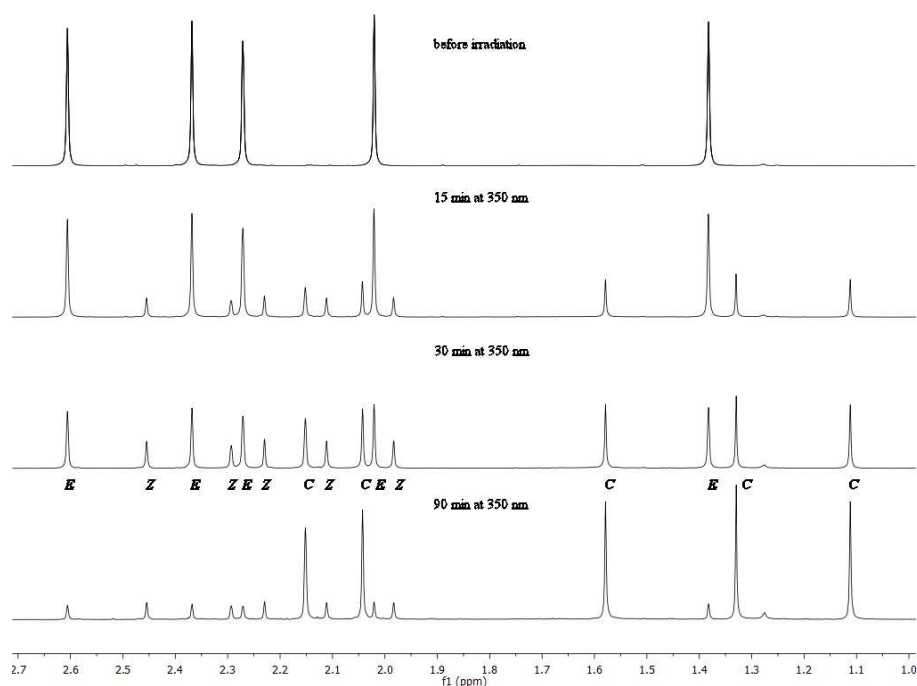


Figure S3: Evolution of the 1H NMR spectra upon successive irradiation of **12E** in $CDCl_3$. The photostationary state after 90 min irradiation time yields in a C/Z/E ratio of 1:0.15:0.15. The isomerization process is illustrated by the evolution of the methyl group signals in the range from 1.0 up to 2.7 ppm.

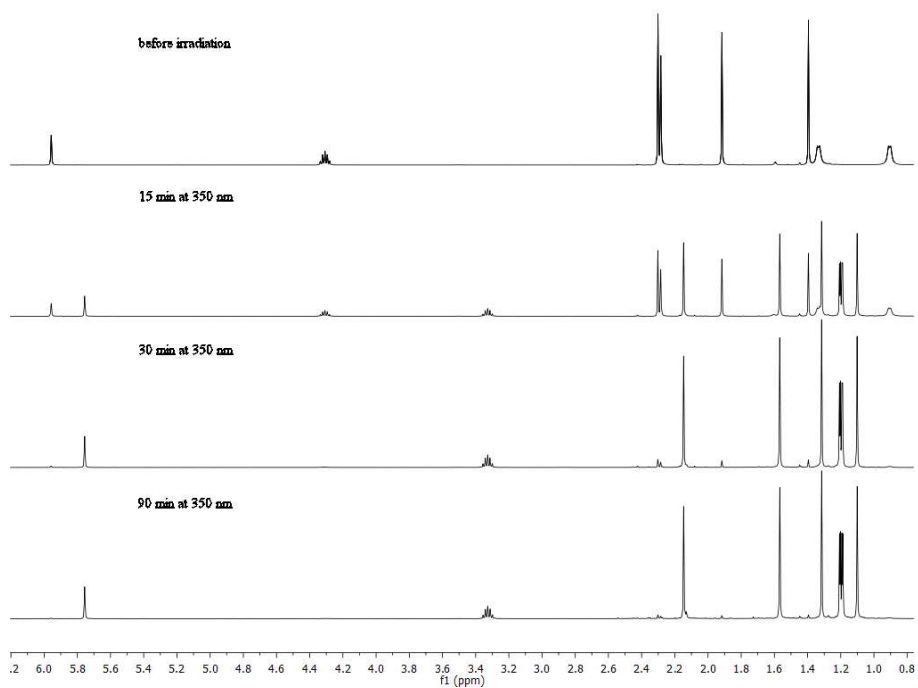


Figure S4: Evolution of the ^1H NMR spectra upon successive irradiation of **13E** in CDCl_3 . Nearly all molecules are transformed to the (*C*) isomer even after 30 min irradiation time. Details are shown from 0.8 up to 6.2 ppm of the ^1H NMR spectra.

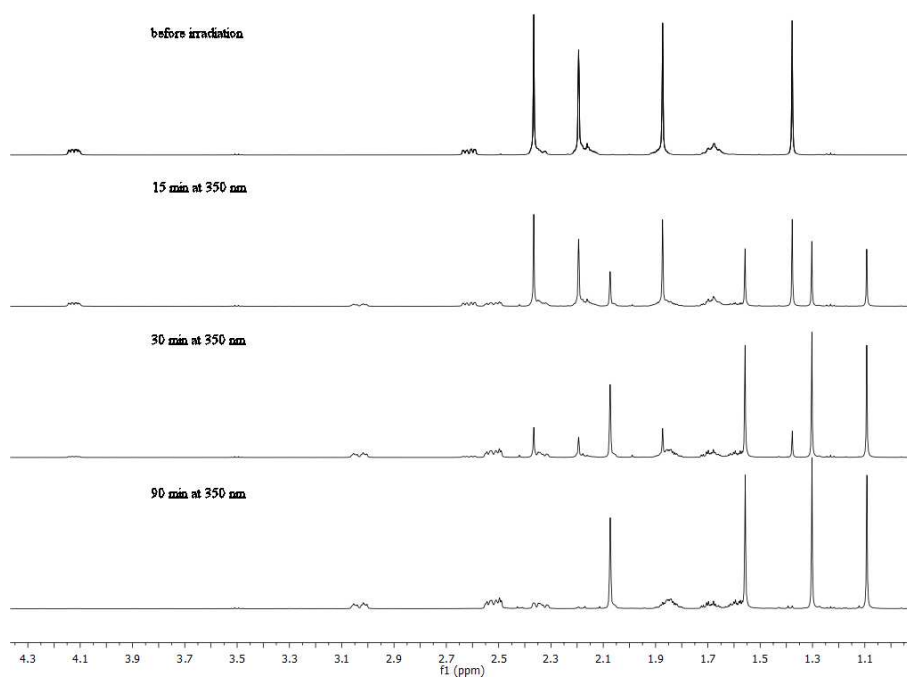


Figure S5: Evolution of the ^1H NMR spectra upon successive irradiation of **14E** in CDCl_3 . Nearly all molecules are transformed to the (*C*) isomer after 90 min irradiation time. Details are shown from 1.0 up to 4.3 ppm of the ^1H NMR spectra.

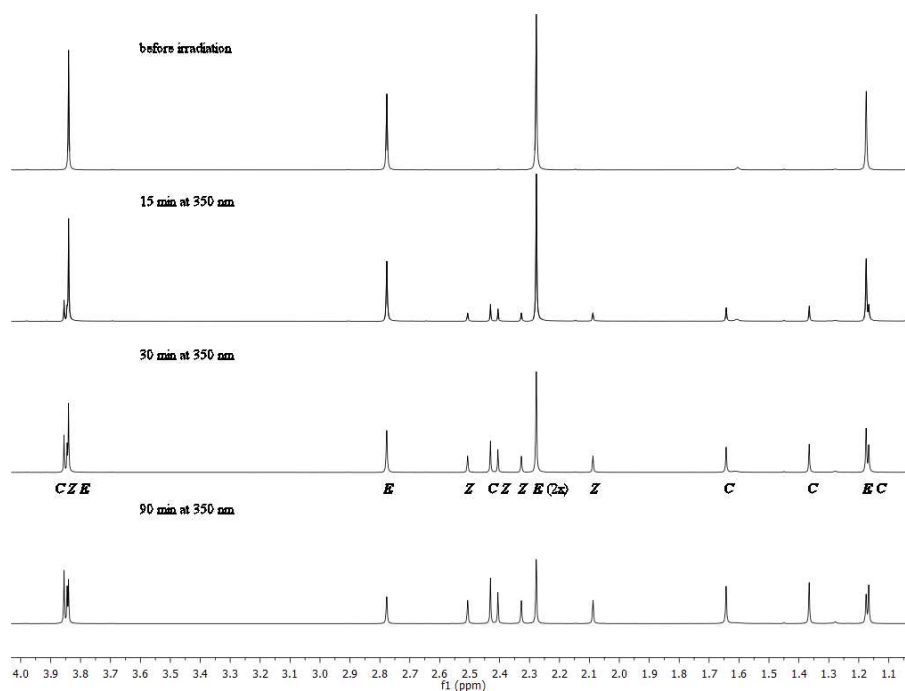


Figure S6: Evolution of the ^1H NMR spectra upon successive irradiation of **14E** in CDCl_3 . The photostationary state yields in a C/Z/E ratio of 1:0.65:0.83. The isomerization process is illustrated by the evolution of the methyl group signals in the range from 1.1 up to 4.0 ppm. Aromatic proton signals are left out for clarity.

References

- [1] E. Uhlmann, G. Gauglitz, *J. Photochem. Photobiol., A* **1996**, *98*, 45–49.
- [2] M. Maafi, R. G. Brown, *Photochem. Photobiol. Sci.* **2008**, *7*, 1360–1372.
- [3] Y. Yokoyama, T. Inoue, M. Yokoyama, T. Goto, T. Iwai, N. Kera, I. Hitomi, Y. Kurita, *Bull. Chem. Soc. Jpn.* **1994**, *67*, 3297–3303.

8 Highly Efficient Reversible $Z \rightleftharpoons E$ Photoisomerization of a Bridged Azobenzene with Visible Light through Resolved $S_1(n\pi^*)$ Absorption Bands

Ron Siewertsen,[†] Hendrikje Neumann,[†] Bengt Buchheim-Stehn,[‡] Rainer Herges,^{*†} Christian Näther,[§] Falk Renth,^{*†} and Friedrich Temps^{*†}

[†] Institut für Physikalische Chemie, Christian-Albrechts-Universität zu Kiel,
Olshausenstr. 40, D-24098 Kiel, Germany

[‡] Otto Diels-Institut für Organische Chemie, Christian-Albrechts-Universität zu Kiel,
Otto-Hahn-Platz 4, D-24098 Kiel, Germany

[§] Institut für Anorganische Chemie, Christian-Albrechts-Universität zu Kiel,
Otto-Hahn-Platz 6-7, D-24098 Kiel, Germany.

Reproduced with permission of the American Chemical Society
J. Am. Chem. Soc. **2009**, *131*, 15594-15595
Copyright 2009 American Chemical Society

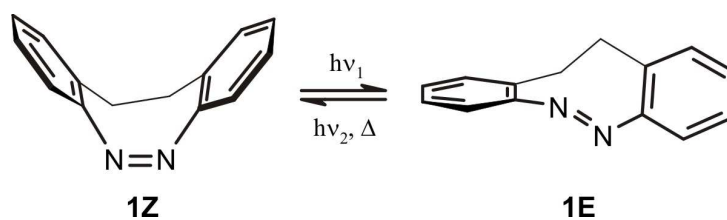
- **Own contributions presented in the paper:**
 - Determination of isomerization quantum yields
 - Static UV/VIS spectroscopic investigations
 - Quantum chemical calculations
- **Synthesis:** Bengt Buchheim-Stehn in the group of Prof. R. Herges,
Hendrikje Neumann in the group of Prof. F. Temps
- **Single crystal X-ray structure:** Prof. C. Näther

*To whom correspondence should be addressed. E-mail: temps@phc.uni-kiel.de, renth@phc.uni-kiel.de, rherges@oc.uni-kiel.de

8.1 Reprint of the Publication

Photochromic molecules, which can be reversibly switched between two isomeric forms with different colors, structures, or functional properties by light at distinctive wavelengths, attract ubiquitous attention for applications as optical memory and logic devices, or as molecular motors, machines, or manipulators.^[1,2] Azobenzene (AB) and its derivatives enjoy particular interest because of the large-amplitude structural changes between their elongated (*E*) and more compact (*Z*) forms, the reversibility of their transformations, and the high photostabilities which guarantee large numbers of switching cycles. The photochromic properties of AB are, however, far from ideal, because the $S_1(n\pi^*)$ electronic absorption bands of its (*E*) and (*Z*) isomers peak at practically the same wavelength ($\lambda = 450 - 440$ nm) and differ essentially only in their oscillator strengths. Switching AB forth and back therefore requires cycling between irradiation in the $S_1(n\pi^*)$ and the $S_2(\pi\pi^*)$ bands, although the latter is located in the less easily accessible UV region, where other molecular moieties attached to the AB unit may suffer photodamage. Here, we report on the photoswitching behavior of 5,6-dihydrodibenzo[*c,g*][1,2]diazocine (**1**). Although **1** has been first prepared quite some time ago,^[3-5] its high potential as a molecular photoswitch has not previously been recognized and studied in detail to our knowledge.

Considering its basic functional unit, **1** is a bridged azobenzene derivative, but has much more favorable photochromic properties than plain AB. The reversible photoconversion between its **1Z** and **1E** isomers is illustrated in Scheme 8.1. We show that **1Z** can be switched to **1E** with an efficiency >90 % by using blue light at $\lambda \approx 370 - 400$ nm, and **1E** can be switched back to **1Z** with ≈ 100 % efficiency by green light with $\lambda \approx 480 - 550$ nm. The calculated ground state structures of both isomers obtained with the B3LYP/def2-TZVP method are displayed in Fig. 8.1a.



Scheme 8.1

We synthesized **1Z** in several batches following a modification of the protocol of Paudler and Zeiler (see Supporting Information).^[4] The product was checked by ^1H NMR spectroscopy and thin layer chromatography, and no traces of impurities were found. The single crystal X-ray diffraction structure (Supporting Information) confirms the calculated slightly disturbed (*Z*) conformation of the central CNNC moiety, which is almost coplanar with a CNNC dihedral angle of only 6.4° and NNC angles of 121° just slightly larger than

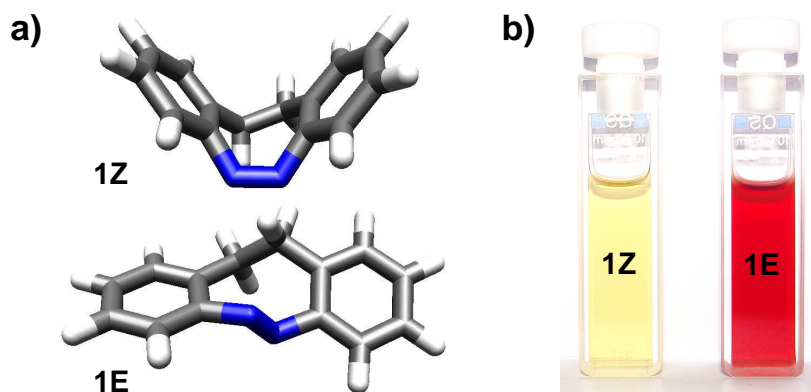


Figure 8.1: a) Equilibrium structures of **1Z** and **1E** in the electronic ground states from quantum chemical calculations at the B3LYP/def2-TZVP level of theory using the TURBOMOLE program.^[6] b) Colors of **1Z** (before irradiation) and **1E** (after irradiation at $\lambda = 385$ nm) in *n*-hexane.

the ideal sp^2 angle. The ethylenic bridge shows some conformational flexibility. Due to the ring strain, **1Z** and not **1E** is the thermodynamically stable form at room temperature, in complete contrast to normal ABs.

The photoisomerization between **1Z** and **1E** was studied using dilute sample solutions in neat dry *n*-hexane. The UV/VIS absorption spectra were monitored on a Shimadzu UV-2401 desktop spectrometer. Conversion of the (*Z*) to the (*E*) isomer was accomplished by irradiating the **1Z** solution using either a broadband UV lamp equipped with a Schott WG360 filter, giving a spectrum with a peak at $\lambda = 370$ nm and width $\Delta\lambda = 33$ nm (fwhm), a 400 mW light-emitting diode at $\lambda = 385$ nm ($\Delta\lambda = 11$ nm), or attenuated second harmonic light pulses at $\lambda = 387$ nm from a 170 fs (fwhm) Ti:Sa laser ($\Delta\lambda = 3$ nm). The (*E*) to (*Z*) back reaction was actively driven using a light emitting diode at $\lambda = 520$ nm or followed under thermal conditions. The solution of **1Z** stored in the dark before irradiation is light yellow (Fig. 8.1b). On irradiation at $\lambda = 385$ nm, however, the color turns to bright red, due to the photoisomerization to **1E**. The evident photochromic effect is underscored by a corresponding change in the measured near-UV/VIS absorption spectrum displayed in Fig. 8.2. As can be seen, **1Z** exhibits a distinctive absorption band with peak at $\lambda = 404$ nm, which we can assign to its $n\pi^*$ excitation. By irradiation at $\lambda = 385$ nm, this band almost disappears, while a new, slightly stronger, and significantly red-shifted absorption grows in. The new band, which is due to the $n\pi^*$ transition of the **1E** isomer, has its peak absorption at $\lambda = 490$ nm. Additional spectral changes are seen in the regions of the $\pi\pi^*$ transitions of both isomers at $\lambda < 350$ nm, where the absorption by the (*E*) isomer is again stronger than that of the (*Z*) isomer.

In the observed photostationary state at $\lambda = 385$ nm (PSS385), the (*E*) isomer is clearly predominant. By monitoring the absorption in the dark, its thermal lifetime was found to

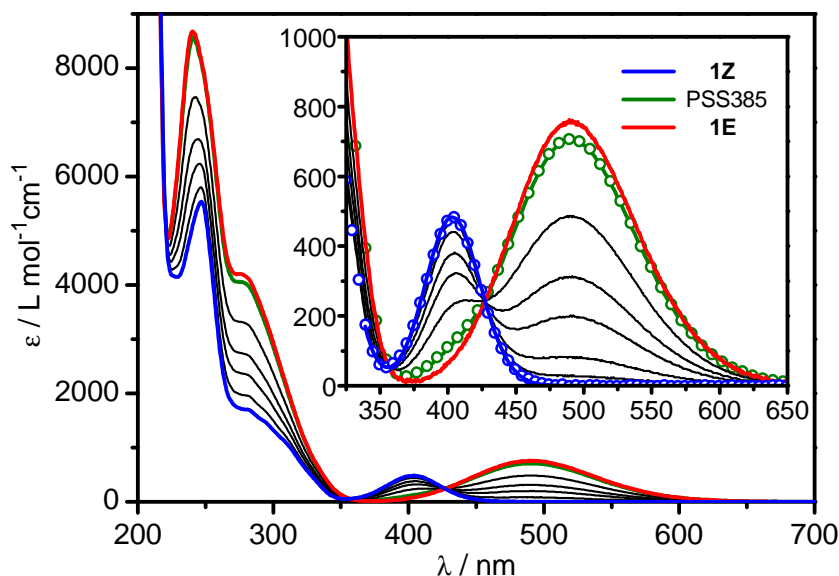


Figure 8.2: UV/VIS absorption spectra of **1Z**, **1E**, and the photostationary state (PSS385) in *n*-hexane (blue, red, and green, respectively). The inset shows the $S_1(n\pi^*)$ region on an enlarged scale, with the recorded spectra (blue and green circles), the fitted log-normal spectra (blue and green lines), and the extracted (*E*) isomer spectrum (red line). The thin black lines show the evolution of the spectrum in the course of the thermal back-isomerization from the PSS385 after $\Delta t = 2, 4, 6, 10,$ and 15 h.

be $\tau = (4.5 \pm 0.1)$ h at 28.5 °C. To elucidate the spectrum for pure **1E** and to determine the quantitative (*Z*) to (*E*) conversion yield, we fitted the **1Z** spectrum using an appropriate log-normal model function (see Fig. 8.2).^[7] We then fitted the spectrum of the PSS385 using a superposition of the suitably scaled **1Z** spectrum and a second log-normal model function for the **1E** absorption. The resulting spectrum for the pure **1E** isomer is displayed in Fig. 8.2. From the absorption coefficients in the PSS385 compared to the pure isomers, the (*Z*) to (*E*) conversion was derived to be $\Gamma = (92 \pm 3)$ %. Conversely, using light at $\lambda = 520$ nm, the (*E*) isomer was quantitatively (≈ 100 %) switched back to the (*Z*) isomer. Moreover, the photoisomerization quantum yields in the forward and back directions, which we investigated using the method of Rau et al.,^[8] are $\Phi_{Z \rightarrow E} = (72 \pm 4)$ % and $\Phi_{E \rightarrow Z} = (50 \pm 10)$ %. The severe constraints by the ethylenic bridge of our title compound do not appear to hinder its (*E*) \rightleftharpoons (*Z*) photoisomerization. For a sustainable application as a molecular photoswitch, a compound must have low photochemical fatigue to allow for large numbers of switching cycles. Monitoring the UV/VIS absorptions of **1** after many repeated alternating irradiation cycles at $\lambda = 385$ and at $\lambda = 520$ nm, respectively, we were unable to detect any signs for photodegradation (Fig. 8.3). The excellent photostability of the compound is vividly demonstrated moreover by the fact that we could use one and the same batch for all our photoswitching experiments made in the course of a half a year.

In conclusion, the bridged AB derivative **1** has much superior spectroscopic properties

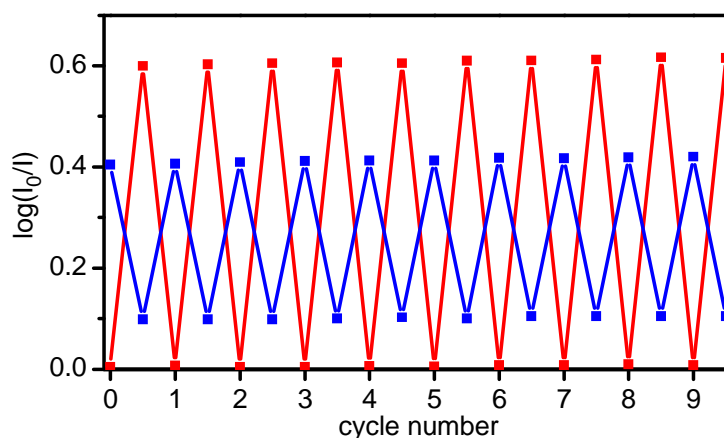


Figure 8.3: Measured absorbances of a solution of **1** at $\lambda_1 = 400$ nm (blue) and $\lambda_2 = 490$ nm (red) in the photostationary states after alternating irradiation at $\lambda = 385$ and $\lambda = 520$ nm in repeated switching cycles.

compared to the parent AB molecule and other commonly used AB derivatives. Most importantly, the respective $S_1(n\pi^*)$ bands of **1Z** and **1E** are well resolved (peak absorptions at $\lambda_Z = 404$ and $\lambda_E = 490$ nm), in striking contrast to AB, where the (*Z*) and (*E*) $n\pi^*$ bands are practically coincident. Efficient switching of **1** in the (*Z*) \rightarrow (*E*) and (*E*) \rightarrow (*Z*) directions can therefore be accomplished with visible light via one or the other $n\pi$ band, whereas conversion between the (*E*) and (*Z*) isomers of AB requires irradiation in the $n\pi^*$ band in the visible in one direction and in the $\pi\pi^*$ band in the UV in the other. The photoisomerization quantum yields of **1** are substantially higher in both directions than in the case of AB, where $\Phi_{Z \rightarrow E} = 53\%$ and $\Phi_{E \rightarrow Z} = 24\%$.^[9] Moreover, a $> 90\%$ photoconversion yield cannot be achieved in the case of AB to our knowledge. Unlike AB, the $n\pi^*$ absorption of the (*E*) isomer of **1** is stronger than that of the (*Z*) isomer; this was reconciled by time-dependent density functional calculations on the excited states. The 4.5 h thermal lifetime of **1E** at room temperature is not a drawback especially for applications involving fast repeated forward and backward switching cycles or at lower temperatures.

Cyclic ABs, which attract much attention as shape-switchable molecules,^[10] show a tendency for unconventional properties when subject to strain. The ring structures alter the quantum yields,^[11] and distorted nonplanar geometries shift the $n\pi^*$ bands of the isomers.^[12] Except for **1**, however, we are aware of only one cyclic (*Z*)-AB that is thermodynamically favored over its (*E*) isomer without a badly compromised photoresponse, a highly constrained azobenzenophane.^[13] Considering its distinctive structural change and the favorable properties of its $n\pi^*$ states, **1** appears to be an ideal functional unit for a molecular tweezer,^[14] which would be closed in its off-form (*Z*), opened by photoconversion to the (*E*) isomer, and returned to closed by the reverse photoconversion.

Acknowledgment.

This work has been supported by the Deutsche Forschungsgemeinschaft within the Sonderforschungsbereich 677 “Function by Switching” (subproject A1).

References

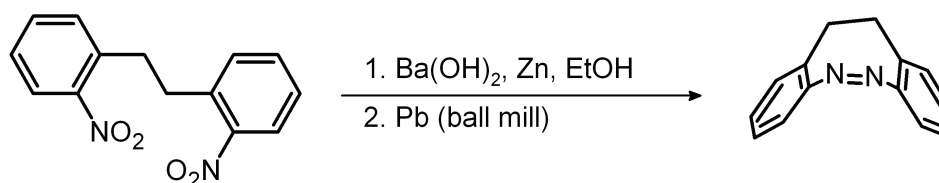
- [1] B. L. Feringa, *Molecular Switches*, Wiley-VCH, Weinheim **2001**.
- [2] V. Balzani, A. Credi, M. Venturi, *Molecular Devices and Machines: Concepts and Perspectives for the Nanoworld*, Wiley-VCH, Weinheim **2008**.
- [3] H. Duval, *Bull. Soc. Chim. Fr.* **1910**, *7*, 727–732.
- [4] W. W. Paudler, A. G. Zeiler, *J. Org. Chem.* **1969**, *34*, 3237–3239.
- [5] E. Tauer, R. Machinek, *Liebigs Ann.* **1996**, 1213–1216.
- [6] R. Ahlrichs, M. Bär, M. Häser, H. Horn, C. Kölmel, *Chem. Phys. Lett.* **1989**, *162*, 165–169.
- [7] D. B. Siano, D. E. Metzler, *J. Chem. Phys.* **1969**, *51*, 1856–1861.
- [8] H. Rau, G. Greiner, G. Gauglitz, H. Meier, *J. Phys. Chem.* **1990**, *94*, 6523–6524.
- [9] H. Rau, *J. Photochem.* **1984**, *26*, 221–225.
- [10] M. Müri, K. C. Schuermann, L. De Cola, M. Mayor, *Eur. J. Org. Chem.* **2009**, 2562–2575.
- [11] Y. Norikane, N. Tamaoki, *Eur. J. Org. Chem.* **2006**, 1296–1302.
- [12] K. Janus, J. Sworakowski, *J. Phys. Chem. B* **2005**, *109*, 93–101.
- [13] Y. Norikane, R. Katoh, N. Tamaoki, *Chem. Commun.* **2008**, 1898–1900.
- [14] F.-G. Klärner, B. Kahlert, *Acc. Chem. Res.* **2003**, *36*, 919–932.

Supporting Information

Synthesis of (*Z*)-5,6-dihydrodibenzo[*c,g*][1,2]diazocine (**1Z**)

The synthesis of **1Z** was performed following a modification of the procedure of Paudler and Zeiler (see Scheme S1).^[1]

Scheme S1: Reaction scheme for the synthesis of **1Z**.



A solution of 2.0 g (7.4 mmol) 2,2'-dinitrodibenzyl in 131 ml ethanol was heated to boiling in a three-necked flask. A suspension of 4.31 g (13.7 mmol) barium hydroxide octahydrate in 33 ml hot *aqua dest.* was added to the solution. The mixture was stirred continuously while heating for another 2 h to the reflux, then allowed to cool to room temperature for 2 h, and finally 7 g of dry ice were added carefully. The solution was stirred for another 10 min and filtered afterwards. After the solvent was removed *in vacuo*, the residue was washed with a hot mixture of cyclohexane/dichloromethane (5:2) and filtered again to obtain 842 mg of an orange to brown solid, which contained considerable amounts of the azoxy compound. Since recrystallization from carbon tetrachloride did not prove successful, the solid obtained in step 1 was used without further purification for the reaction with 3.8 g of lead in a ball mill at 50 Hz over a period of 4 h. After extraction with dichloromethane, a yellow to orange solution was obtained. The solvent was removed *in vacuo*, and the residue was purified by column chromatography on silica gel (3 – 5 μm) with a 5:2 mixture of chloroform and dichloromethane ($R_f = 0.25$). After removal of the eluent and vacuum drying for one week, the product was obtained as yellow crystals. Yield: 64.2 mg (4%).

¹H-NMR (200 MHz, CDCl₃, 25 °C, TMS): δ /[ppm] = 7.1 (dd, 2H, H₂, H_{2'}), 6.99 (2dd, 4H, H_{3,4}, H_{3',4'}), 6.82 (dd, 2H, H₅, H_{5'}), 2.88 (msym, 4H, H₇, H_{7'});

UV/VIS (*n*-hexane, $c = 10^{-4}$ mol/l): λ /[nm] ($\lg I_0/I$) = 247 (0.35), 277 (0.109), 402 (0.03)

Single crystal X-ray structure determination of compound 1Z

The data were measured using an IPDS-1 from STOE. Structure solutions were done with direct methods using SHELXS-97, and structure refinement was performed against F² using SHELXL-97. All non-hydrogen atoms were refined using anisotropic displacement parameters. The hydrogen atoms were positioned with idealised geometry and refined with fixed isotropic displacement parameters using a riding model. Two carbon atoms were disordered and were refined using a split model. Details of the structure determination are given in Tables S1-S5, the structure is displayed in Fig. S1.

Table S1: Crystal data and structure refinement for compound **1Z**.

Identification code	compound 1Z / herges18
Empirical formula	C ₁₄ H ₁₂ N ₂
Formula weight	208.26 g/mol
Temperature	170(2) K
Wavelength	0.71073 Å
Crystal system	monoclinic
Space group	P2 ₁ /n
Unit cell dimensions	a = 8.5090(6) Å α = 90° b = 13.1425(7) Å β = 92.759(8)° c = 9.9040(6) Å γ = 90°
Volume	1106.28(12) Å ³
Z	4
Density (calculated)	1.250 Mg/m ³
Absorption coefficient	0.075 mm ⁻¹
F(000)	440
Crystal size	0.4 × 0.3 × 0.3 mm ³
Theta range for data collection	2.58 to 28.07°
Index ranges	-11 ≤ h ≤ 11, -17 ≤ k ≤ 17, -12 ≤ l ≤ 13
Reflections collected	10511
Independent reflections	2666 [R(int) = 0.0432]
Completeness to theta = 28.07°	99.2 %
Refinement method	Full-matrix least-squares on F ²
Data / restraints / parameters	2666 / 0 / 165
Goodness-of-fit on F ²	1.048
Final R indices [I > 2σ(I)]	R1 = 0.0481, wR2 = 0.1251
R indices (all data)	R1 = 0.0682, wR2 = 0.1372
Extinction coefficient	0.15(2)
Largest diff. peak and hole	0.193 and -0.179 e.Å ⁻³

Table S2: Atomic coordinates ($\times 10^4$) and equivalent isotropic displacement parameters ($\text{\AA}^2 \times 10^3$). U(eq) is defined as one third of the trace of the orthogonalized U^{ij} tensor.

	x	y	z	U(eq)
N(1)	4425(1)	6349(1)	609(1)	33(1)
N(2)	5733(1)	6021(1)	1008(1)	37(1)
C(1)	6037(1)	5723(1)	2404(1)	33(1)
C(2)	6338(2)	4700(1)	2636(1)	43(1)
C(3)	6802(2)	4374(1)	3922(2)	50(1)
C(4)	6997(2)	5074(1)	4956(2)	49(1)
C(5)	6702(2)	6082(1)	4710(1)	47(1)
C(6)	6212(2)	6440(1)	3430(1)	39(1)
C(7)	5758(8)	7583(4)	3483(8)	47(1)
C(8)	4497(9)	7953(6)	2468(8)	38(1)
C(7')	6125(6)	7525(3)	2968(6)	45(1)
C(8')	4423(11)	7924(6)	2926(8)	56(2)
C(9)	3105(2)	7221(1)	2466(1)	35(1)
C(10)	1738(2)	7328(1)	3160(2)	49(1)
C(11)	474(2)	6691(2)	2926(2)	58(1)
C(12)	539(2)	5915(1)	1976(2)	54(1)
C(13)	1877(2)	5796(1)	1259(1)	39(1)
C(14)	3149(1)	6438(1)	1517(1)	27(1)

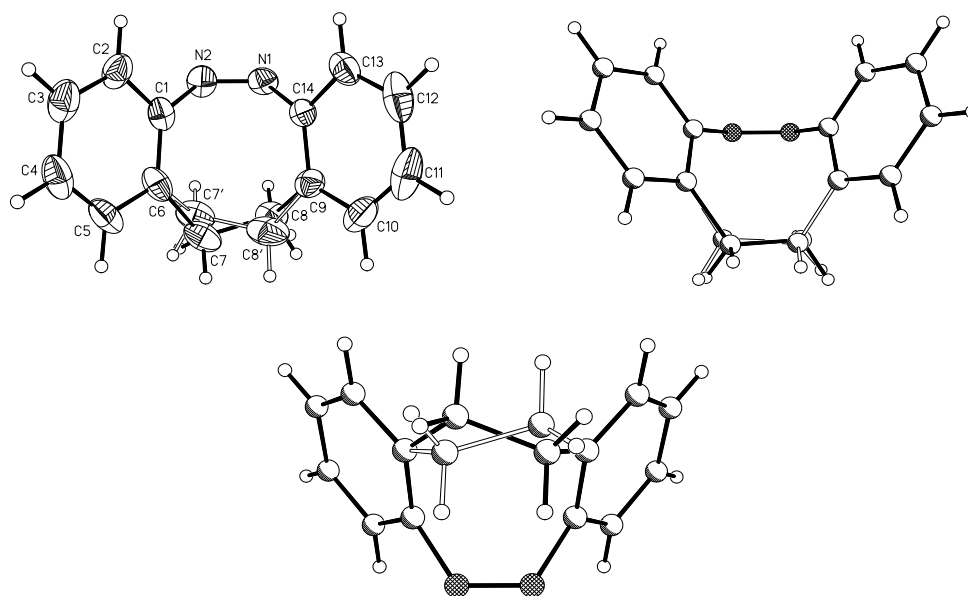
**Figure S1:** Crystal structure of compound **1Z**.

Table S3: Bond lengths [Å] and angles [°].

N(1)-N(2)	1.241(2)	C(7)-C(8)	1.515(10)
N(1)-C(14)	1.448(2)	C(8)-C(9)	1.526(8)
N(2)-C(1)	1.447(2)	C(7')-C(8')	1.539(11)
C(1)-C(2)	1.386(2)	C(8')-C(9)	1.507(8)
C(1)-C(6)	1.389(2)	C(9)-C(10)	1.387(2)
C(2)-C(3)	1.383(2)	C(9)-C(14)	1.395(2)
C(3)-C(4)	1.381(2)	C(10)-C(11)	1.374(3)
C(4)-C(5)	1.368(2)	C(11)-C(12)	1.390(3)
C(5)-C(6)	1.397(2)	C(12)-C(13)	1.380(2)
C(6)-C(7')	1.498(5)	C(13)-C(14)	1.386(2)
C(6)-C(7)	1.552(6)		
N(2)-N(1)-C(14)	121.2(1)	C(7)-C(8)-C(9)	108.8(6)
N(1)-N(2)-C(1)	121.0(1)	C(6)-C(7')-C(8')	111.5(5)
C(2)-C(1)-C(6)	121.6(2)	C(9)-C(8')-C(7')	119.0(6)
C(2)-C(1)-N(2)	116.3(2)	C(10)-C(9)-C(14)	117.3(2)
C(6)-C(1)-N(2)	121.6(2)	C(10)-C(9)-C(8')	114.7(3)
C(3)-C(2)-C(1)	119.7(2)	C(14)-C(9)-C(8')	127.8(4)
C(4)-C(3)-C(2)	119.7(2)	C(10)-C(9)-C(8)	127.2(3)
C(5)-C(4)-C(3)	119.9(2)	C(14)-C(9)-C(8)	114.9(3)
C(4)-C(5)-C(6)	122.2(2)	C(8')-C(9)-C(8)	17.5(3)
C(1)-C(6)-C(5)	116.9(2)	C(11)-C(10)-C(9)	121.5(2)
C(1)-C(6)-C(7')	114.8(3)	C(10)-C(11)-C(12)	120.3(2)
C(5)-C(6)-C(7')	127.3(3)	C(13)-C(12)-C(11)	119.5(2)
C(1)-C(6)-C(7)	131.5(3)	C(12)-C(13)-C(14)	119.5(2)
C(5)-C(6)-C(7)	111.1(3)	C(13)-C(14)-C(9)	121.8(2)
C(7')-C(6)-C(7)	23.2(2)	C(13)-C(14)-N(1)	116.0(2)
C(8)-C(7)-C(6)	117.3(5)	C(9)-C(14)-N(1)	121.5(2)

Table S4: Anisotropic displacement parameters ($\text{\AA}^2 \times 10^3$). The anisotropic displacement factor exponent takes the form: $-2\pi^2[h^2a^{*2}U_{11} + \dots + 2hka^*b^*U_{12}]$

	U_{11}	U_{22}	U_{33}	U_{23}	U_{13}	U_{12}
N(1)	41(1)	38(1)	21(1)	2(1)	4(1)	1(1)
N(2)	38(1)	49(1)	26(1)	6(1)	8(1)	3(1)
C(1)	23(1)	49(1)	25(1)	7(1)	6(1)	0(1)
C(2)	44(1)	52(1)	34(1)	1(1)	8(1)	19(1)
C(3)	51(1)	56(1)	43(1)	13(1)	5(1)	20(1)
C(4)	38(1)	75(1)	33(1)	15(1)	-4(1)	4(1)
C(5)	38(1)	65(1)	36(1)	-4(1)	-11(1)	-10(1)
C(6)	30(1)	45(1)	42(1)	5(1)	-8(1)	-13(1)
C(7)	48(3)	45(2)	48(3)	-7(2)	-5(2)	-21(2)
C(8)	48(2)	24(2)	42(3)	3(3)	-2(2)	-6(1)
C(7')	57(2)	34(2)	45(2)	-1(2)	3(2)	-21(2)
C(8')	91(4)	25(2)	50(3)	-2(3)	-12(3)	-6(2)
C(9)	41(1)	27(1)	35(1)	1(1)	0(1)	6(1)
C(10)	55(1)	51(1)	41(1)	1(1)	9(1)	24(1)
C(11)	39(1)	78(1)	58(1)	27(1)	17(1)	22(1)
C(12)	30(1)	61(1)	70(1)	25(1)	-6(1)	-6(1)
C(13)	39(1)	38(1)	40(1)	4(1)	-11(1)	-4(1)
C(14)	32(1)	28(1)	22(1)	6(1)	-1(1)	2(1)

Table S5: Hydrogen coordinates ($\times 10^4$) and isotropic displacement parameters ($\text{\AA}^2 \times 10^3$).

	x	y	z	U(eq)
H(2)	6225	4225	1915	51
H(3)	6987	3671	4092	60
H(4)	7334	4856	5838	58
H(5)	6836	6554	5433	56
H(7A)	5405	7731	4400	57
H(7B)	6721	7988	3359	57
H(8A)	4921	7983	1556	46
H(8B)	4152	8645	2715	46
H(7C)	6544	7578	2056	54
H(7D)	6788	7952	3591	54
H(8C)	4203	8163	3846	67
H(8D)	4375	8528	2327	67
H(10)	1674	7853	3814	58
H(11)	-450	6781	3414	70
H(12)	-331	5470	1823	64
H(13)	1926	5279	592	47

Quantum Chemical Calculations

The ground state equilibrium structures of **1Z** and **1E** were determined by quantum chemical calculations using the Turbomole program at the B3LYP/def2-TZVP level.^[2] The structural parameters of the equilibrium structures are given in Table S6 and S7.

Table S6. Atomic cartesian coordinates (Å) for the ground state equilibrium structure of **1Z**.

	x	y	z		x	y	z
N	-0.618886	-0.883112	1.731709	C	2.078455	-1.573467	-0.171975
N	0.609782	-1.018485	1.682439	C	1.380794	-0.604192	0.545112
C	-3.149784	0.161082	-1.476635	H	-3.818097	0.403014	-2.292443
C	-3.126067	-1.121614	-0.940862	H	-3.776124	-1.894502	-1.329033
C	-2.268677	-1.401151	0.108970	H	-2.252341	-2.382436	0.564684
C	-1.398180	-0.426127	0.604236	H	-2.346616	2.136199	-1.367177
C	-1.423557	0.881062	0.096547	H	-1.170931	2.520332	1.446423
C	-2.315554	1.135813	-0.952342	H	-0.576530	2.792221	-0.170484
C	-0.617308	2.049069	0.627623	H	0.800661	1.447635	2.155139
C	0.823679	1.776817	1.115925	H	1.367038	2.722747	1.104189
C	1.562257	0.759864	0.289180	H	2.601046	2.172258	-0.939281
C	2.438948	1.120736	-0.733271	H	3.776150	0.465143	-2.277520
C	3.104755	0.160800	-1.485427	H	3.445224	-1.942265	-1.779820
C	2.920865	-1.189857	-1.205541	H	1.950409	-2.616943	0.084059

Table S7: Atomic cartesian coordinates (Å) for the ground state equilibrium structure of **1E**.

	x	y	z		x	y	z
N	-0.367763	-0.503565	-1.012256	C	-0.587112	0.516610	1.579363
N	0.367727	0.501058	-1.014376	C	0.587164	-0.518405	1.578669
C	1.699781	0.196441	-0.639281	H	-3.218763	0.794292	2.208638
C	-1.699892	-0.197832	-0.638447	H	-5.207355	0.363877	0.823612
C	-1.806595	0.262669	0.689143	H	-4.957017	-0.476936	-1.495020
C	-3.094602	0.449760	1.187893	H	-2.678112	-0.883915	-2.413542
C	-4.220566	0.202705	0.407827	H	2.678190	0.883116	-2.414204
C	-4.081481	-0.272253	-0.891820	H	4.956913	0.479713	-1.494616
C	-2.813034	-0.496315	-1.411644	H	5.207413	-0.359883	0.824621
C	2.813048	0.496483	-1.411925	H	3.218988	-0.792080	2.208940
C	4.081485	0.274404	-0.891468	H	-0.184377	1.511396	1.372571
C	4.220598	-0.200188	0.408333	H	-0.964360	0.560324	2.603343
C	3.094632	-0.448481	1.187906	H	0.964632	-0.562884	2.602561
C	1.806541	-0.263003	0.688663	H	0.184731	-1.513104	1.371002

References

- [1] W. W. Paudler, A. G. Zeiler, *J. Org. Chem.* **1969**, *34*, 3237–3239.
- [2] R. Ahlrichs, M. Bär, M. Häser, H. Horn, C. Kölmel, *Chem. Phys. Lett.* **1989**, *162*, 165–169.

Additional Results

In order to obtain first informations about the influence of the length of the alkyl bridge of bridged azobenzenes on their photochromic properties, quantum chemical calculation were performed using the program packet Turbomole^[1] with DFT/TDDFT/B3LYP/def2-TZVP. Ground state structures of the (*E*) and (*Z*) isomers, their energy differences ($\Delta E(Z_{S_0} - E_{S_0})$) and vertical excitation energies $\Delta E(S_1 \leftarrow S_0)$ were calculated for azobenzenes with an ethyl (**1**, brAB), a propyl (**2**) and a butyl bridge (**3**), and for normal azobenzene (**4**) for comparison (see Fig. 8.4). The results are summarized in Table 8.1.

The calculated vertical excitation energies of **1** and **4** nicely reproduce the well resolved $S_1 \leftarrow S_0$ absorption bands for **1E** and **1Z** and the almost indistinguishable energies of the $S_1 \leftarrow S_0$ transition of **4E** and **4Z**. Furthermore, the reverse thermodynamic stability of **1** and **4** could be calculated from the relative ground state energies of the two isomers. As mentioned above, in contrast to normal AB, the (*Z*) isomer of **1** is the thermodynamic stable form.

To the best of the author's knowledge, compounds **2** and **3** have not been synthesized so far and no experimental or theoretical data is available. The quantum chemical calculations of these azobenzenes show that with increasing length of the alkyl bridge the thermodynamic stability of bridged ABs can be tuned regarding their relative energy differences $\Delta E(Z_{S_0} - E_{S_0})$. For the propyl-bridged AB **2**, the (*E*) isomer is the more stable form. The butyl-bridged derivative exhibits even a higher value of $\Delta E(Z_{S_0} - E_{S_0})$ compared to **2** with similar values as for normal AB. Interestingly, TDDFT calculations showed that all bridged compounds have spectrally separated $S_1 \leftarrow S_0$ transitions in

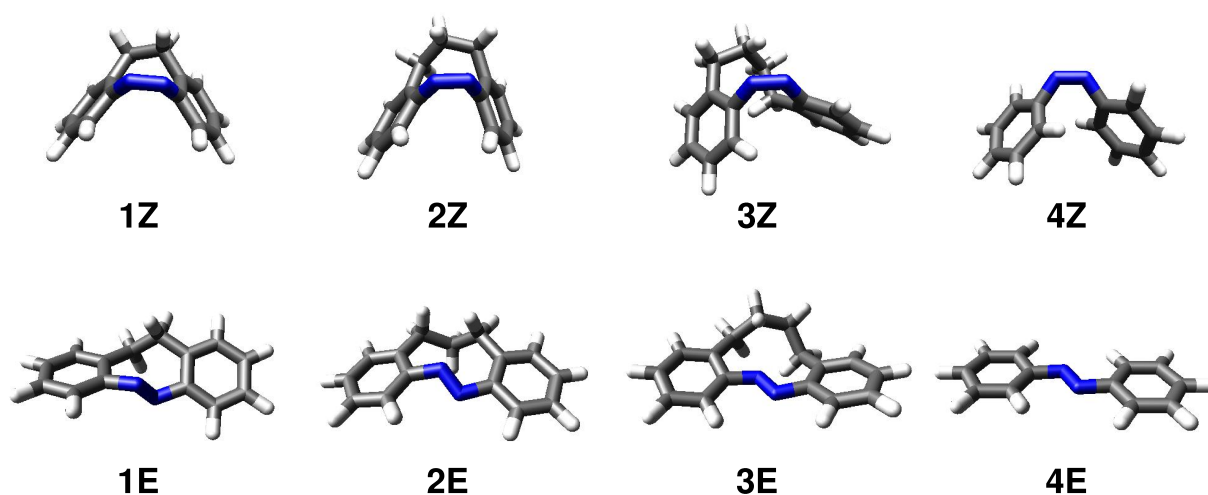


Figure 8.4: Calculated (*E*) and (*Z*) structures of bridged azobenzenes with different length of the bridge (**1-3**) and of normal AB (**4**) for comparison.

contrast to AB. Therefore, the length of the alkyl bridge might be used to control the thermodynamic stability of azobenzenes with improved photochromic properties.

The ultrafast dynamics and photoisomerization quantum yields of these compounds would be of great interest regarding a new class of photochromic ABs with selectable thermodynamic stability for the (*E*) and the (*Z*) isomer, excellent photochromic properties and high isomerization quantum yields.

Table 8.1: Calculated (TDDFT) and experimental (λ_{max}) vertical $S_1 \leftarrow S_0$ excitation energies $\Delta E(S_1 \leftarrow S_0)$ of the (*E*) and (*Z*) isomers of the ABs **1-4** and calculated electronic ground state energy difference $\Delta E(Z_{S_0} - E_{S_0})$ of their two isomers.

	$\Delta E(S_1 \leftarrow S_0)$ / nm				$\Delta E(Z_{S_0} - E_{S_0})$ / eV
	(<i>Z</i>) TDDFT	(<i>Z</i>) λ_{max}	(<i>E</i>) TDDFT	(<i>E</i>) λ_{max}	
1	434	404 ^a	528	490 ^a	-0.3
2	432	-	482	-	+0.3
3	471	-	518	-	+0.7
4	485	440 ^b	486	450 ^b	+0.6

^a This work, solvent *n*-hexane. ^b Ref. [2], solvent *n*-hexane.

References

- [1] R. Ahlrichs, M. Bär, M. Häser, H. Horn, C. Kölmel, *Chem. Phys. Lett.* **1989**, *162*, 165–169.
- [2] H. H. Perkampus, *UV-VIS Atlas of Organic Compounds*, Wiley-VCH, Weinheim **1992**.

9 Superior $Z \rightarrow E$ and $E \rightarrow Z$ photoswitching dynamics of dihydrodibenzodiazocine, a bridged azobenzene, by $S_1(n\pi^*)$ excitation at $\lambda = 387$ and 490 nm

Ron Siewertsen, Jan Boyke Schönborn, Bernd Hartke, Falk Renth,*
Friedrich Temps*

^a Institut für Physikalische Chemie, Christian-Albrechts-Universität zu Kiel,
Olshausenstr. 40, D-24098 Kiel, Germany

Reproduced with permission of the PCCP Owner Societies

Phys. Chem. Chem. Phys. **2011**, *13*, 1054-1063

Copyright 2011

- **Own contributions presented in the paper:**
 - Femtosecond time-resolved transient absorption spectroscopy
 - Femtosecond time-resolved fluorescence up-conversion spectroscopy
 - Data analysis and writing of the data analysis software
 - Determination of isomerisation quantum yields
 - Static UV/VIS spectroscopic investigations

- **CASPT2/CASSCF calculations:** Jan Boyke Schönborn in the group of Prof. B. Hartke

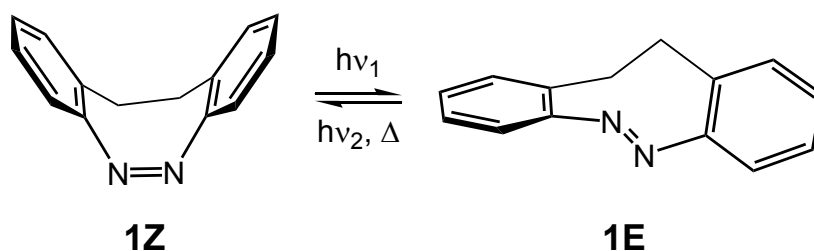
*To whom correspondence should be addressed. E-mail: temps@phc.uni-kiel.de, renth@phc.uni-kiel.de

Abstract

The ultrafast $Z \rightarrow E$ and $E \rightarrow Z$ photoisomerisation dynamics of 5,6-dihydrodibenzo[*c,g*]-[1,2]diazocine (**1**), the parent compound of a class of bridged azobenzene-based photochromic molecular switches with a severely constrained eight-membered heterocyclic ring as central unit, have been studied by femtosecond time-resolved spectroscopy in *n*-hexane as solvent and by quantum chemical calculations. The diazocine contrasts with azobenzene (AB) in that its Z rather than E isomer is the energetically more stable form. Moreover, it stands out compared to AB for the spectrally well separated $S_1(n\pi^*)$ absorption bands of its two isomers. The Z isomer absorbs at around $\lambda = 404$ nm, the E form has its absorption maximum around $\lambda = 490$ nm. The observed transient spectra following $S_1(n\pi^*)$ photoexcitation show ultrafast excited-state decays with time constants $\tau_1 = 70$ fs for the Z and < 50 fs for the E isomer reflecting very fast departures of the excited wave packets from the S_1 Franck-Condon regions and $\tau_2 = 270$ fs (320 fs) related to the $Z \rightarrow E$ (resp. $E \rightarrow Z$) isomerisations. Slower transient absorption changes on the time scale of $\tau_3 = 5$ ps are due to vibrational cooling of the reaction products. The results show that the unique steric constraints in the diazocine do not hinder, but accelerate the molecular isomerisation dynamics and increase the photoswitching efficiencies, contrary to chemical intuition. The observed isomerisation times and quantum yields are rationalised on the basis of CASPT2//CASSCF calculations by a S_1/S_0 conical intersection seam at a CNNC dihedral angle of $\approx 96^\circ$ involving twisting and torsion of the central CNNC moiety. With improved photochromism, high quantum yields, short reaction times and good photostability, diazocine **1** and its derivatives constitute outstanding candidates for photoswitchable molecular tweezers and other applications.

9.1 Introduction

A detailed understanding of the ensuing dynamics of photochromic molecular switches is a *sine qua non* for exploiting their full application potential as, *e.g.*, tiny light-driven machines or manipulators,^[1-3] for high-density optical data storage,^[4-8] as non-linear optical devices,^[9] for photoregulation of biomolecules,^[10-14] dendrimers,^[15,16] polymers^[17-20] or emulsions,^[21] for innovative photoresponsive surfaces,^[22] or in superresolution imaging.^[23-26] Azobenzene (AB) and its derivatives play particularly important roles in these fields because of the large change in molecular size, shape and dipole moment between the thermodynamically favoured, stretched E isomer and the energetically higher, more compact Z isomer, which can be interconverted through reversible $E \rightarrow Z$ and $Z \rightarrow E$ photoisomerisation reactions on irradiation with visible (VIS) or ultraviolet (UV) light. In addition, AB stands out for its low photochemical fatigue, which guarantees high numbers



Scheme 9.1

of switching cycles. For many applications, however, the photoswitching properties of AB are far from ideal. In the first place, the UV/VIS absorption spectra of the *E* and *Z* forms of AB are very similar — the two isomers absorb at almost the same wavelengths in the VIS and in the near UV and differ essentially only in their respective oscillator strengths. Switching AB back and forth in practice thus requires photo-excitation to the $S_2(\pi\pi^*)$ state at $\lambda \approx 350 - 360$ nm to drive the isomerisation in the $E \rightarrow Z$ direction and excitation to the $S_1(n\pi^*)$ state at $\lambda \approx 445$ nm for the reverse $Z \rightarrow E$ direction. Both reactions take place on sub-picosecond time scales,^[27–35] but the respective reverse reactions at the same wavelengths limit the attainable conversion efficiencies. Moreover, excitation in the UV may not always be feasible in applications, and has to be avoided when attached other molecular moieties can be photodamaged.

Recently, we reported on the unique photoswitching properties of 5,6-dihydrodibenzo-*[c,g][1,2]*diazocine (**1**), the parent compound of a class of bridged, AB-related photochromic molecules with an eight-membered heterocyclic ring as central unit (Scheme 9.1).^[36] Diazocine **1** turned out to have superior photochromic properties compared to AB. In particular, the severe conformational constraints brought by the central ring raise the *E* isomer in energy above the *Z* isomer, resulting in a reversed thermodynamic stability of **1Z** and **1E** compared to normal AB. The reason is that the latter may no longer adopt the planar equilibrium structure of *E*-AB. The structure of **1Z** as the more stable isomer has been determined by single crystal X-ray diffraction.^[36] Moreover, as shown by Fig. 9.1, the $S_1(n\pi^*)$ absorption bands of both isomers of **1** are spectrally well separated. The respective absorptions peak at $\lambda = 404$ nm (**1Z**) and $\lambda = 490$ nm (**1E**), in striking contrast to AB, where they appear at virtually identical wavelengths (≈ 440 nm). As a result of these extraordinary spectral properties and the ensuing special molecular dynamics, the achieved photoconversion yields ($> 90\%$) are remarkably higher than for AB.^[36] Furthermore, large numbers of switching cycles are attainable with compound **1** as well.^[36] The ≈ 4.5 h room temperature thermal lifetime of **1E** is more than sufficient for applications involving fast repeated forward and backward switching cycles or at lower temperatures.

Intrigued by the drastic changes of the UV/VIS spectrum and the observed excellent photoswitching properties, we investigated the $Z \rightarrow E$ and $E \rightarrow Z$ isomerisation dynamics

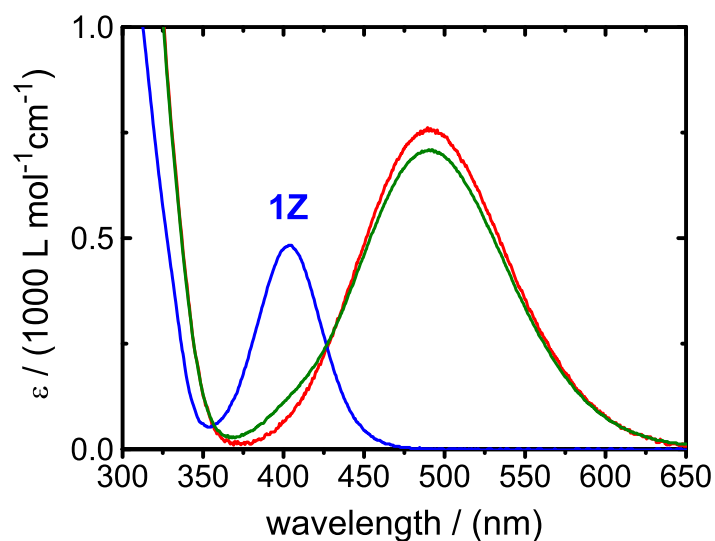


Figure 9.1: UV/VIS absorption spectra of **1Z** (blue) and **1E** (red) in *n*-hexane as solvent. Also shown is the spectrum in the photostationary state by irradiation at $\lambda = 385$ nm (green line).

of **1** in *n*-hexane following S_1 excitation by means of femtosecond broadband transient absorption and fluorescence up-conversion spectroscopy and by quantum chemical calculations. The results which we present in this paper reveal how the severe constraints in the diazocine lead to a favourable acceleration of the molecular dynamics and higher quantum yields with respect to AB.

9.2 Experimental and computational methods

1Z was synthesised following a modification of the protocol of Paudler^[37] as described previously.^[36] The purity of the product (> 98 %) was checked by $^1\text{H-NMR}$ spectroscopy. Isomer **1E** was prepared from **1Z** by irradiation to the photostationary state (PSS) in *n*-hexane (Uvasol, Merck) at $\lambda = 385$ nm using a 400 mW light-emitting diode (LED; Nichia NCSU034A, 11 nm spectral width).^[36] The *Z*-to-*E* conversion yield was 92 %. No further purification was attempted since **1Z** does not absorb at the wavelength used to excite **1E**.

The photoisomerisation quantum yields of **1Z** and **1E** were determined following the method of Rau et al.,^[38] which analyses the irradiation intensity dependence of the concentrations in the PSS *via* the UV/VIS absorbances. The measurement used 2 mL of a dilute, continuously stirred solution of **1Z** ($c_0 = 0.31$ mM) in *n*-hexane in a 1 cm cuvette, which was irradiated by the 385 nm LED. The incident light intensity was attenuated by means of neutral density filters and a variable aperture to values between 0.25 and 1.50 mW and measured with a power meter (Coherent, OP-2 UV) calibrated

by ferrioxalate actinometry.^[39] The UV/VIS spectra were taken on a Shimadzu UV-2401 desktop spectrometer.

The femtosecond time-resolved measurements were made in flow cells of 1 mm optical path length with 0.2 mm fused silica windows. The optical densities were adjusted to $OD \approx 0.5$ at the applied excitation wavelengths. A peristaltic pump exchanged the excited volumes between successive laser pulses. Furthermore, the sample reservoirs were continuously irradiated at the appropriate wavelengths driving the back-reactions to avoid accumulation of photoproducts. All measurements were done at room temperature in *n*-hexane as solvent.

The transient absorption and fluorescence up-conversion setups have been described before.^[40,41] Briefly, a Ti:Sa laser (Clark MXR CPA-2001) supplied pulses at $\lambda = 775$ nm with ≈ 150 fs duration (Gaussian fwhm) at 1 kHz repetition rate. The required excitation pulses ($0.4 \mu\text{J}$) at $\lambda_{\text{pump}} = 387$ nm for **1Z** were generated by second harmonic generation (SHG). Isomer **1E** was excited at $\lambda_{\text{pump}} = 490$ nm delivered by a non-collinear optical parametric amplifier (NOPA). Supercontinuum white light pulses for the broadband transient absorption measurements were generated in a CaF_2 plate and then split into a probe and a reference beam. The resulting spectra were detected as function of pump-probe delay using an imaging spectrograph equipped with a 1024×127 pixel CCD camera (LOT, MS260i and DB401-UV). The intense near-IR part of the supercontinuum was removed by a BG18 filter before the spectrograph. The pump-probe delay was controlled using a linear translation stage (PI M-126). The cross-phase modulation (XPM) and stimulated Raman scattering (SRS) contributions from independent measurements in pure *n*-hexane were used for time-zero correction of the supercontinuum, to optimize experimental settings and to determine the instrument response function (IRF). Both contributions were subtracted from the time-corrected sample signals with suitable weights accounting for the pump pulse absorptions to obtain the two-dimensional experimental spectro-temporal absorption maps. The observed XPM shape was included as input in non-linear least-squares fits to the observed absorption-time profiles. The measured IRF widths were 160 fs and 50 – 70 fs (Gaussian fwhm) for SHG and NOPA excitation, respectively. These values allow for time resolutions of the measurements after deconvolution of ≈ 70 fs and ≈ 35 fs, respectively.

Fluorescence-time profiles of the excited sample molecules at wavelengths of $\lambda_{\text{fl}} = 600 - 675$ nm were recorded using the up-conversion technique. A pair of off-axis parabolic mirrors ($f = 119$ mm) was used to focus the emitted light into a BBO crystal for type II sum frequency generation (SFG) with the 775 nm gate pulses from the Ti:Sa laser. The SFG radiation was monitored through a double monochromator (Jobin-Yvon HR 10) by a photomultiplier (Hamamatsu R1527P) connected to a preamplifier and a gated photon counter (Stanford Research SR 400). A band pass filter (UG11, Schott) was placed

before the monochromator to remove background intensity from unwanted other non-linear optical processes. Cross correlation of scattered pump light with the gate pulses gave an IRF width of ≈ 230 fs, corresponding to an estimated experimental time resolution (taking into account the widths of the pump and gate pulses and the difficulties in measuring the very low fluorescence intensities of the molecules) of ≈ 150 fs.

Quantum chemical calculations were carried out using the programs TURBOMOLE^[42] for density functional and time-dependent density functional theory (DFT, TDDFT) and MOLCAS^[43] for multi-reference (CASSCF, CASPT2) calculations. The structures and vibrational frequencies of the molecules in their electronic ground states were calculated at the B3LYP/def2-TZVP and at the CASSCF(14,12) level. The active space for the CASSCF calculations consisted of the π and π^* orbitals of the N=N bond, the n and n^* orbitals of the two N atoms in an additive and a subtractive linear combination, and ten orbitals from the aromatic phenyl rings, five of π and five of π^* character. Starting from the ground-state equilibrium structures, state-averaged CASSCF(14,12)^[44,45] geometry optimisations of the first excited state were performed using a mixed basis with different treatments for the various atoms as follows: Dunning's aug-cc-pVTZ basis was assigned to the N atoms, cc-pVDZ functions were used for all C atoms, and the STO-3G description, which was shown to result in errors in the excitation energies of only 1% compared to a double zeta basis, was assigned to the H atoms. The obtained energies were re-evaluated using the CASPT2 method with a mixed basis resulting in an approximate doubling in size compared to the basis used for the geometry optimisation and Cholesky decomposition with a threshold of 0.1×10^{-3} , as implemented in MOLCAS. Vertical $S_0 \rightarrow S_1$ excitation energies were also calculated for the DFT equilibrium structures by using the TDDFT method at the B3LYP/def2-TZVP level.

9.3 Results

Photoisomerisation quantum yields

The photoisomerisation quantum yields $\phi_{Z \rightarrow E}$ and $\phi_{E \rightarrow Z}$ of **1Z** and **1E** were derived from the dependence of the PSS on the irradiation intensity.^[38] The ensuing reactions are described by the kinetic equation

$$\frac{dc_E}{dt} = I_0^* F^* l (\phi_{Z \rightarrow E} \epsilon_Z^* c_Z - \phi_{E \rightarrow Z} \epsilon_E^* c_E) - k_{E \rightarrow Z}^{\text{th}} c_E,$$

where ϵ_Z^* and ϵ_E^* are the respective molar absorption coefficients of the two isomers at the irradiation wavelength λ^* , c_Z and c_E are the respective concentrations (with $c_Z + c_E = c_0$), l is the optical path length, I_0^* the irradiation intensity (in $\text{mol L}^{-1} \text{s}^{-1}$) in the sample cuvette at λ^* , $F^* = (1 - 10^{-A^*})/A^*$ the photokinetic factor at λ^* , $A^* = (\epsilon_Z^* c_Z + \epsilon_E^* c_E) l$

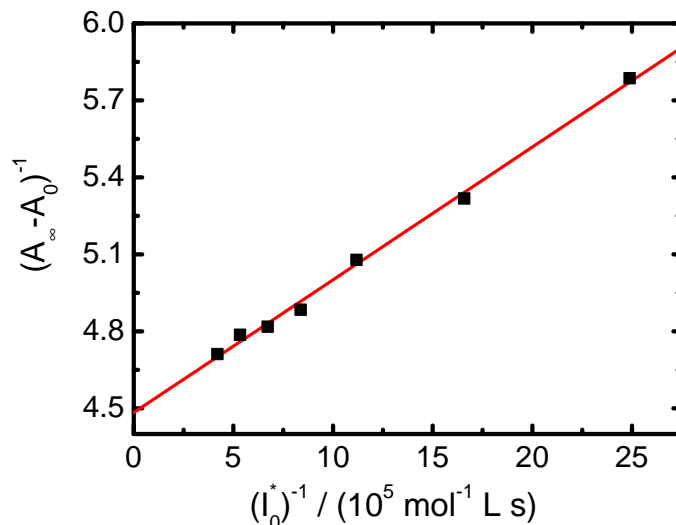


Figure 9.2: Plot of $(A_\infty - A_0)^{-1}$ at $\lambda = 490$ nm *vs.* $(I_0^*)^{-1}$ for the determination of the quantum yields $\phi_{Z \rightarrow E}$ and $\phi_{E \rightarrow Z}$.

the absorbance at λ^* , and $k_{E \rightarrow Z}^{\text{th}}$ is the rate coefficient for the thermal back reaction. In the PSS at the irradiation wavelength ($\lambda^* = 385$ nm), $dc_E/dt = -dc_Z/dt = 0$. Starting with a solution of pure Z isomer, and monitoring the PSS at the selected observation wavelength ($\lambda = 490$ nm, *cf.* Fig. 9.1), $\phi_{Z \rightarrow E}$ and $\phi_{E \rightarrow Z}$ were thus determined from the slope and intercept of a plot of $(A_\infty - A_0)^{-1}$ *vs.* $(I_0^*)^{-1}$, which is described as detailed by Rau et al.^[38] by the equation

$$\frac{1}{(A_\infty - A_0)} = \frac{\phi_{Z \rightarrow E} \epsilon_Z^* + \phi_{E \rightarrow Z} \epsilon_E^*}{(\epsilon_E - \epsilon_Z) c_0 l \phi_{Z \rightarrow E} \epsilon_Z^*} + \frac{k_{E \rightarrow Z}^{\text{th}}}{(\epsilon_E - \epsilon_Z) c_0 l^2 \phi_{Z \rightarrow E} \epsilon_Z^* F_\infty^*} \times \frac{1}{I_0^*}.$$

A_0 and A_∞ are the measured absorbances at the observation wavelength λ , where the formation of the E product is monitored, at time $t = 0$ (*i.e.*, immediately before the irradiation) and in the PSS (determined by extrapolation to $t \rightarrow \infty$), F_∞^* is the photokinetic factor at λ^* in the PSS, and ϵ_E and ϵ_Z are the respective molar absorption coefficients of the E and Z isomers at that wavelength.

The obtained plot of $(A_\infty - A_0)^{-1}$ *vs.* $(I_0^*)^{-1}$ with the linear regression to the data points is given in Fig. 9.2. Using the independently determined value for the rate coefficient for the thermal back reaction under the experimental conditions ($k_{E \rightarrow Z}^{\text{th}} = 6.16 \times 10^{-5} \text{ s}^{-1}$)^[36] and the molar absorption coefficients of the Z and E isomers at $\lambda = 490$ nm from the UV/VIS spectrum (Fig. 9.1), the derived values for the photoisomerisation quantum yields (with 2σ error limits) are

$$\phi_{Z \rightarrow E} = 0.72 \pm 0.04 \quad \text{and} \quad \phi_{E \rightarrow Z} = 0.50 \pm 0.10.$$

Time-resolved $Z \rightarrow E$ photoisomerisation

The recorded two-dimensional spectro-temporal transient absorption map following excitation of **1Z** at $\lambda_{\text{pump}} = 387$ nm for probe wavelengths between $355 \text{ nm} \leq \lambda_{\text{probe}} \leq 650$ nm and delay times of $-0.2 \text{ ps} \leq \Delta t \leq 2.1$ ps is shown in Fig. 9.3. The measurements were continued up to $\Delta t = 30$ ps, but the changes at longer times were small. As can be seen, the absorption map features a negative signal from ground state bleaching (GSB) at probe wavelengths between 355 – 440 nm, which mirrors the static absorption spectrum of **1Z**. At early times ($\Delta t \leq 0.25$ ps), excited-state absorption (ESA) leads to a positive transient absorption over the entire probe wavelength range despite the spectrally overlapping GSB. The ESA amplitude is largest at $\lambda_{\text{probe}} < 400$ nm and decays within the first few hundred femtoseconds. A positive band is left between $450 \text{ nm} \leq \lambda_{\text{probe}} \leq 600$ nm, where hot product absorption (HPA) occurs from vibrationally excited *E* molecules in the electronic

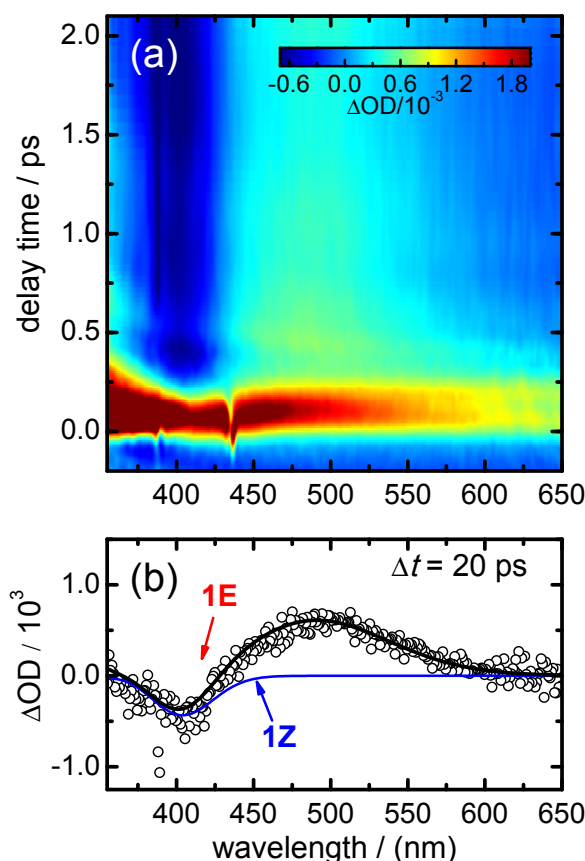


Figure 9.3: (a) Two-dimensional transient absorption map showing the change of optical density ΔOD for probe wavelengths λ_{probe} between 355 and 650 nm and delay times Δt from -0.2 to 2.1 ps following excitation of **1Z** at $\lambda_{\text{pump}} = 387$ nm. (b) Spectrum at $\Delta t = 20$ ps (open circles) and fit (solid lines) by a weighted sum of the static UV/VIS absorption spectra of the *Z* and *E* isomers to the data (see text). The small irregularities at $\Delta t \approx 0$ and $\lambda_{\text{probe}} = 387$ and 439 nm are artefacts due to imperfect subtraction of scattered pump light and the stimulated Raman scattering (SRS) signal of the solvent.

ground state. The rise of the HPA band on the time scale of the ESA decay confirms the sub-picosecond time scale of the $Z \rightarrow E$ isomerisation.

The following slower spectral blue-shift and narrowing of the product band reflects subsequent vibrational cooling of the molecules. Spectral changes beyond $\Delta t \approx 10$ ps are negligible. The final spectrum at $\Delta t = 20$ ps, which is displayed in Fig. 9.3b, is well described by a sum of the static UV/VIS spectra of **1Z** and **1E** with equal concentrations but opposite signs (positive for E , negative for Z), confirming the absence of side reactions.

Figure 9.4 displays the absorption-time profiles after excitation of **1Z** at 387 nm at three selected probe wavelengths. All three graphs show that the temporal behavior is dominated by an immediate rise followed by a fast decay. A global fit to the data required two sub-picosecond decay components, these can be discerned best at $\lambda_{\text{probe}} = 550$ nm. Subsequent slower and much weaker changes lead to the final negative and positive offsets

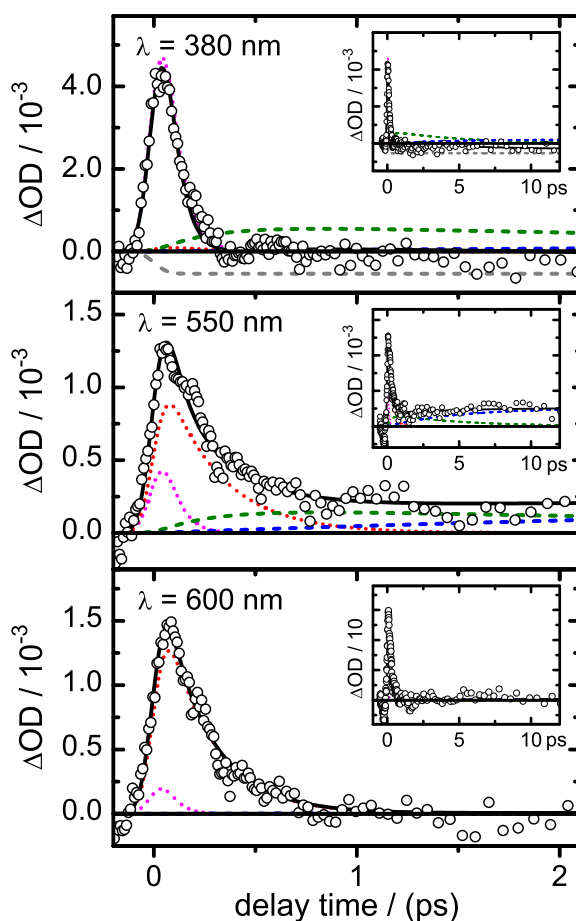


Figure 9.4: Absorption-time profiles after excitation of **1Z** at $\lambda_{\text{pump}} = 387$ nm at three selected probe wavelengths for delay times between -0.2 and 2.1 ps. Data points are represented by open circles, the global non-linear least-squares fit results to the data are indicated by black lines, and the individual fit components are shown as dotted (ESA) and dashed (grey: GSB, green: HPA, blue: PA) lines. The insets show the time profiles on a longer time scale.

resulting from the GSB and product absorption (PA) bands.

A quantitative analysis of the time profiles was performed by a global non-linear least-squares fit to the data using a consecutive kinetic scheme with three time constants ($\tau_1 - \tau_3$). The slow components were disentangled by fixing the amplitudes of the permanent GSB and the PA using the known steady-state UV/VIS spectra and the determined values for the photoisomerisation quantum yields. The best-fit time constants (with 2σ error limits) are

$$\tau_{1,Z} = 0.07 \pm 0.01 \text{ ps,}$$

$$\tau_{2,Z} = 0.27 \pm 0.06 \text{ ps,}$$

$$\tau_{3,Z} = 5.00 \pm 0.30 \text{ ps.}$$

These direct experimental results were complemented by a time-resolved fluorescence measurement, which revealed a decay of the fluorescence of **1Z** with a lifetime $\tau_{\text{fl}} < 0.15$ ps, *i.e.*, faster than the ≈ 150 fs time resolution of our up-conversion setup. This observation is consistent with an ultrashort lifetime of the initially excited Franck-Condon (FC) state in S_1 of the order of $\tau_{1,Z}$ (≈ 0.07 ps). The time constants are discussed in more detail Section 9.4.

Time-resolved $E \rightarrow Z$ photoisomerisation

The measured spectro-temporal transient absorption map up to $\Delta t = 2.1$ ps following excitation of **1E** at $\lambda_{\text{pump}} = 490$ nm is given in Fig. 9.5. Although the data look dissimilar to those for **1Z** (Fig. 9.3) at first glance, they reflect essentially the same steps. However, the processes light up at different wavelengths now because of the exchange of reactant and product. The broad negative GSB band between $\lambda_{\text{probe}} = 425$ and 600 nm thus mirrors the static **1E** absorption spectrum. The positive transients at the earliest delay times ($\Delta t \leq 0.2$ ps) are due to ESA, which has its largest amplitude at $\lambda_{\text{probe}} < 400$ nm and decays within < 0.5 ps. A superimposed damped oscillatory modulation can be discerned at < 420 nm. The HPA from vibrationally hot Z molecules at $\lambda_{\text{probe}} \approx 400$ nm rises simultaneously with the ESA decay and confirms the sub-picosecond time scale of the $E \rightarrow Z$ isomerisation, but is difficult to discern because of partial spectral overlap with the GSB. The much smaller spectral changes after the first ≈ 0.5 ps again reflect slower vibrational cooling. The final spectrum at $\Delta t = 10$ ps (Fig. 9.5b) corresponds to the **1Z-1E** difference spectrum and clearly shows the photoisomerisation.

Selected absorption-time profiles after excitation of **1E** at $\lambda_{\text{pump}} = 490$ nm at three representative probe wavelengths are given in Fig. 9.6. The curves show an instantaneous rise and fast (sub-picosecond) subsequent decays. The minor changes at longer times lead

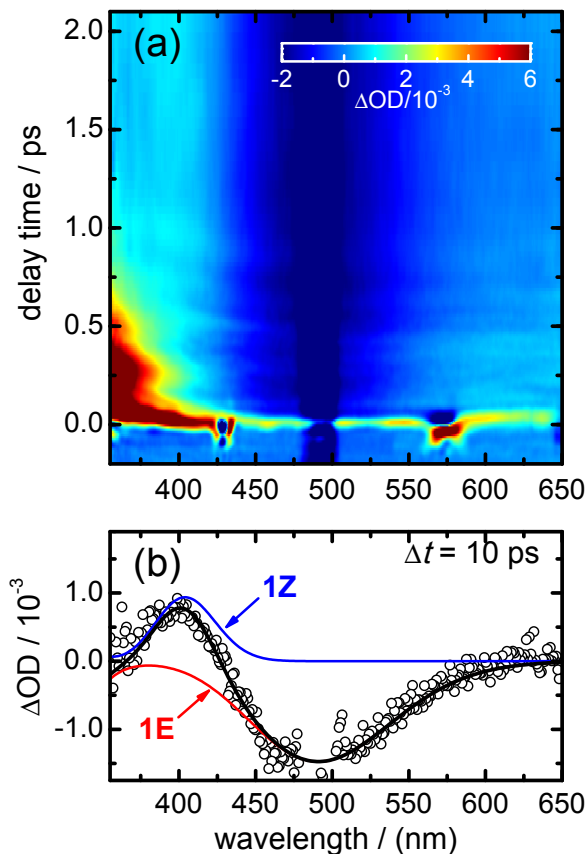


Figure 9.5: (a) Two-dimensional transient absorption map showing the change of optical density ΔOD following excitation of **1E** at $\lambda_{\text{pump}} = 490$ nm for probe wavelengths λ_{probe} from 355 to 650 nm and delay times Δt between -0.2 and 2.1 ps. The small features at $\Delta t \approx 0$ and $\lambda_{\text{probe}} = 430$, 490 , and 575 nm are experimental artefacts. (b) Spectrum at $\Delta t = 10$ ps (open circles) and fit (solid lines) by a weighted sum of the static UV/VIS absorption spectra of **1Z** and **1E**.

to the final negative and positive offsets by permanent GSB and PA. A global quantitative analysis of the time profiles performed as above required three time constants with values (2σ error limits) of

$$\begin{aligned}\tau_{1,E} &= 0.05 \text{ ps (fixed)}, \\ \tau_{2,E} &= 0.32 \pm 0.10 \text{ ps}, \\ \tau_{3,E} &= 5.0 \text{ ps (fixed equal to } \tau_{3,Z}),\end{aligned}$$

plus an oscillatory component with frequency of $113 \pm 12 \text{ cm}^{-1}$ and damping time $\tau_d = 0.13 \pm 0.07$ ps. As for **1Z**, an up-conversion measurement of **1E** showed that the observable fluorescence decays faster than our available experimental time resolution (≈ 150 fs).

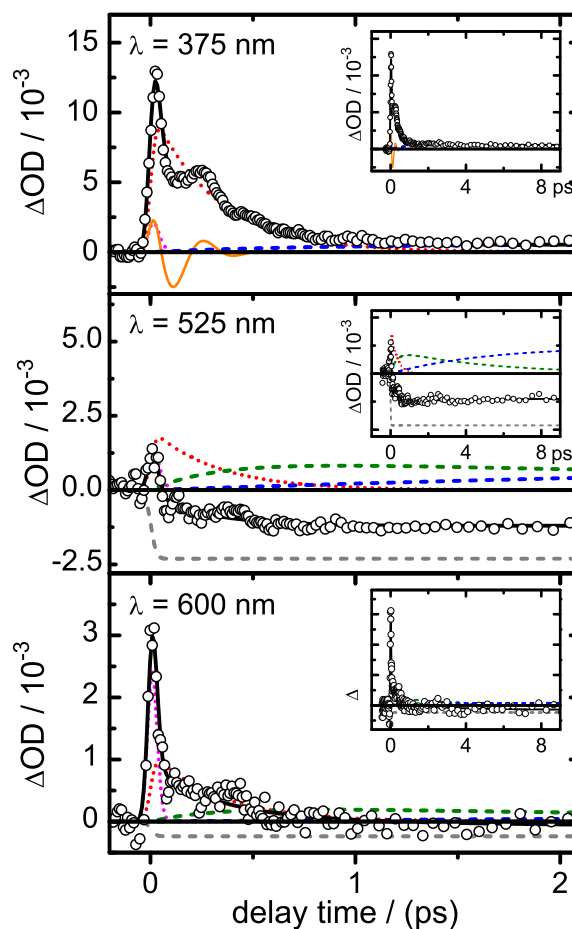


Figure 9.6: Time profiles of the transient absorption at selected probe wavelengths after excitation of **1E** at $\lambda_{\text{pump}} = 490$ nm for delay times between -0.2 and 2.1 ps. Open circles represent data points, solid black lines are the global non-linear least-squares fits. The thin (orange) line indicates the oscillating component, and other components are shown as dotted (ESA) and dashed (grey: GSB, green: HPA, blue: PA) lines. The insets show the time profiles on an extended scale.

Computational results

Table 9.1 lists important ground state structural parameters for diazocines **1Z** and **1E** and their AB counterparts. The equilibrium structures of the molecules were calculated using the DFT and the CASSCF methods. Since both gave almost identical results, only the CASSCF values are listed. The calculated structure of **1Z** agrees well with the experimental single crystal X-ray diffraction structure.^[36] This confirms that the chosen quantum chemical methods are well-suited and should also correctly predict the structure of **1E**. The largest structural effect with respect to AB is seen in the CNNC dihedral angle, which is 147° in diazocine **1E** compared to 180° in *E*-AB. The calculated energy difference between the two diazocine isomers is 0.3 eV in favour of **1Z**.

Taking the calculated ground state structures, TDDFT and state-averaged three-state

Table 9.1: Calculated and experimental (X-ray diffraction) azo group bond angles for **1Z**, **1E**, and the respective AB isomers in their electronic ground states.

bond angle	1Z _{eq} ^a	1Z _{expt} ^b	Z-AB ^c	1E _{eq} ^a	E-AB ^d
CNNC / °	5.0	-0.7	8.0	147.0	180.0
CNN / °	120.9	121.2	121.9	111.9	113.6
NNC / °	120.4	121.0	121.9	111.9	113.6

^aCalculated CASSCF results. ^bExperimental X-ray diffraction values from Ref. [36]. ^cRef. [46]. ^dRef. [47].

CASPT2 energy calculations on the CASSCF(14,12) wave functions yielded the vertical $S_1 \leftarrow S_0$ excitation energies for both diazocine isomers. The results are listed in Table 9.2 next to the experimental excitation energies from the maxima of the respective UV/VIS absorption bands in Fig. 9.1. The observed energies (wavelengths) are 3.07 eV (404 nm) for **1Z** and 2.53 eV (490 nm) for **1E**. As shown, the TDDFT (2.85 and 2.35 eV for **1Z** and **1E**) and CASPT2 excitation energies (2.87 and 2.43 eV, respectively) agree very well. The calculations confirmed the $n\pi^*$ character of the transitions.

The actual isomerisation reactions of the photo-excited **1Z** and **1E** molecules were explored by unrestrained state-averaged two-state CASSCF(14,12) structure optimisations of the first excited states. The S_0 equilibrium structures determined by the same method and basis provided the two starting points for these calculations. As seen above, the vertical CASPT2 excitation energies are in excellent agreement with the experimental values. The CASSCF energies from the excited-state structure optimisations were thus re-evaluated at the CASPT2 level. To rule out confusion, we stress that these calculations, as they were set up, essentially give simple but straightforward series of snapshots of local structures from separate optimisations for each isomer, *i.e.*, they were not designed to yield fully optimised minimum energy reaction pathways. The calculations nevertheless provide a useful picture of the shape of the excited-state potential energy hypersurface (PEHS) between the two FC points. The structures, which are given in Tables S1-S6 in the electronic supplementary information (ESI), and the energies determined in the course of the excited-state optimisations are depicted as function of the CNNC dihedral angle Φ in Fig. 9.7. The picture obtained in this way shows a crossing between the S_1 and S_0 states at a twisted structure with Φ slightly larger than 96° that suggests the existence of a

Table 9.2: Calculated and experimental vertical $S_1 \leftarrow S_0$ excitation energies ΔE .

method	UV/VIS		TDDFT		CASPT2	
	eV	nm	eV	nm	eV	nm
$\Delta E(\mathbf{1Z})$	3.07	404	2.85	434	2.87	432
$\Delta E(\mathbf{1E})$	2.53	490	2.35	528	2.43	511

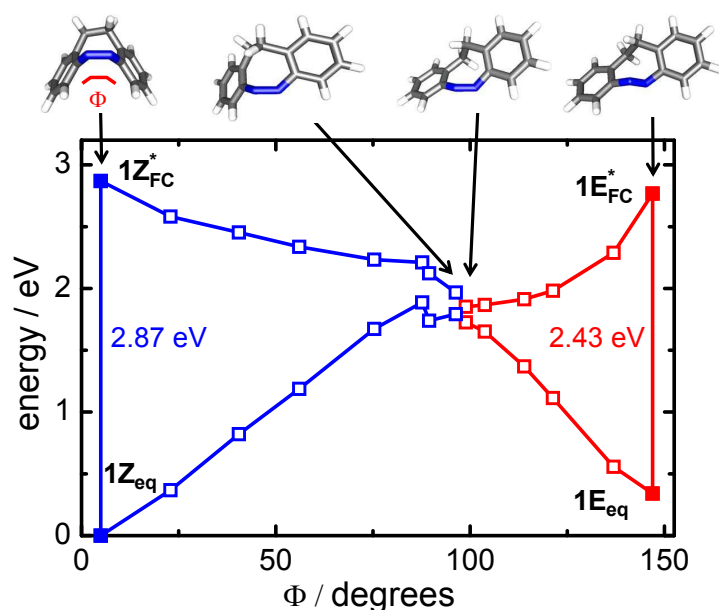


Figure 9.7: Calculated energies and structures from the CASPT2//CASSCF excited-state optimisations as function of the CNNC dihedral angle (Φ) starting at the FC excited states $1Z_{\text{FC}}^*$ (solid blue squares, left) and $1E_{\text{FC}}^*$ (solid red squares, right). The open blue (red) squares indicate the calculated $Z \rightarrow E$ ($E \rightarrow Z$) pathways. All energies are relative to $1Z_{\text{eq}}$.

conical intersection (CI) in that region. The crossing region appears to be accessible along essentially barrierless pathways following steep downhill gradients on the excited-state PEHS from $1Z$ (increasing Φ angles) or $1E$ (decreasing Φ angles). As can be seen from the structures displayed at the top of Fig. 9.7, the torsion and twisting of the central CNNC unit is accompanied by simultaneous changes of other coordinates. The conclusions which we can draw from these calculations are discussed in Section 9.4.

9.4 Discussion

The results described in the preceding section give comprehensive insight into the photoisomerisation reactions of diazocine **1**, the parent compound of a class of molecules that, although first prepared a long time ago,^[37,48,49] have only recently been fully recognized as interesting photochromic molecular switches with high application potential.^[36] Compared to plain azobenzene, the ethylenic bridge between the two phenyl rings reverses the thermodynamic stabilities of the Z and E isomers in the diazocine. It is this feature that distinguishes the diazocines from azobenzenes. The performed time-resolved experiments and quantum chemical calculations help us to rationalize, why the tight structural constraints due to the bridge also lead to significantly enhanced photochromic properties.

Observed time constants and dynamics

The transient ESA decay curves extracted from the spectro-temporal absorption maps reveal biphasic molecular dynamics with time constants of $\tau_1 < 0.1$ ps and $\tau_2 \approx 0.3$ ps for both isomers. The physical bearings and underlying chemical mechanisms revealed by these two time constants are of main interest.

Although the extracted ultra-short first value of $\tau_{1,Z} = 0.07 \pm 0.01$ ps for **1Z** is close to the time resolution of the measurements, it is still determined with good precision and confidence. For **1E**, however, the respective result of $\tau_{1,E} \approx 0.05$ ps should be taken as an upper limit. It needed to be included in the fitting procedure to the data with a fixed value to mirror the observed short-time behaviour, but a shorter value could have been adopted for that purpose as well. The molecular dynamics reflected by $\tau_{1,E}$ thus appear to be faster than the available experimental time resolution. Since the fluorescence-time profiles match with τ_1 within the limits of experimental resolution, it is suggested in line with previous arguments for AB^[29,30] that the fast decay times (τ_1) for both molecular isomers describe the initial departures of the prepared wave packets from their S_1 FC regions. Conversely, the longer lifetimes (τ_2) reflect the excited-state population decays through S_1/S_0 CIs along the isomerisation reaction coordinate. The reaction times for the Z and E isomers were found to be similar within their error limits ($\tau_{2,Z} = 0.27 \pm 0.06$ ps, $\tau_{2,E} = 0.32 \pm 0.10$ ps).

The short τ_1 values suggest steep gradients of the S_1 PEHS in the FC regions for both isomers that induce fast directed wave packet motions. This should result in ultrafast spectral red-shifts of the fluorescence out of the observation window, so that we may rationalize why the slower ESA decay component (τ_2) cannot be observed in emission. With the present experimental time resolution, it was not possible to directly observe the supposed fluorescence red-shifts, but it is of interest to note that the expected corresponding transient absorption blue-shifts can be seen in the spectro-temporal absorption maps for both molecules at short wavelengths (*cf.* Figs. 9.3 and 9.5). As noted, the absorption maps have the better time resolutions.

The “photochemical funnel” at a CI between the S_1 and S_0 electronic states returns the excited wavepackets to the ground state, where they are directed either to the respective reactant minima or to the product minima of the PEHS. This interpretation agrees with the corresponding HGSA and HPA rise times. The observed kinetics show that the transformations through the supposed CI take place within ≈ 0.3 ps after the excitation. This suggests practically barrierless excited-state reaction pathways to the CI. The large photoisomerisation quantum yields ($\phi_{Z \rightarrow E} = 0.72$, $\phi_{E \rightarrow Z} = 0.50$) showcase the extraordinary efficiencies of the transformations of the molecules on the S_1 PEHS and through the S_1/S_0 CI.

The superimposed weak damped ESA modulation in the absorption map for **1E** at early times featuring a frequency of 113 cm^{-1} is the signature of collective low-frequency molecular motions accompanying the major structural reorganisation of the molecules moving along the minimum energy isomerisation pathway en route to the S_1/S_0 CI. Similar behaviour has been observed in previous time-resolved studies of $E \rightarrow Z$ photoisomerisation and excited-state relaxation dynamics.^[50–54] Considering the multi-dimensionality of the chemical transformations, we refrain from assigning the observed modulation frequency to a specific vibrational mode and note only that **1E** in the ground state does possess low-frequency normal mode vibrations in the range of interest.

The photo-induced reactions eventually terminate on the S_0 PEHS by slower vibrational cooling processes of the reactant and product molecules in about 5 ps (τ_3).

Ground state structures

The calculated ground-state equilibrium structures (Table 9.1) show that the steric constraints in the central eight-membered ring affect the Z and E isomers of diazocine **1** completely differently. As revealed by the X-ray and the calculated structures of **1Z**, its central ring is hardly affected by ring strain. In particular, the CNNC dihedral angle indicates that its CNNC moiety has an almost undisturbed coplanar Z configuration with NNC angles of $\approx 121^\circ$ close to the ideal sp^2 angle and quite similar to Z -AB.^[46]

The calculated structure of the E isomer has a CNNC torsional angle of 147.0° and is non-planar due to the restrictions by the ethylenic bridge between the two phenyl rings, in strong contrast to the unconstrained planar structure of E -AB.^[47] It is the constrained CNNC torsional angle that is responsible for the stability reversal of the two diazocine isomers compared to AB. The ethylenic bridge itself has some configurational flexibility in both isomers.

Vertical excitation energies

As shown by the data in Table 9.2, the calculated vertical $S_1 \leftarrow S_0$ excitation energies of 2.87 eV (432 nm) for **1Z_{eq}** and 2.43 eV (511 nm) in the case of **1E_{eq}** are in excellent agreement with the experimental values of 3.07 and 2.53 eV derived from the absorption maxima in the UV/VIS spectrum at $\lambda = 404$ and 490 nm, respectively.

Photoisomerisation mechanisms

The actual chemical transformations of both isomers of diazocine **1** in the S_1 state starting from the vertically excited FC states **1Z_{FC}*** and **1E_{FC}*** can be assessed with the help of Fig. 9.7. The performed excited-state optimisations from the Z and from the E side

indicate isomerisation routes for the photo-excited molecules through crossings of the S_1 and S_0 states at a CNNC dihedral angle slightly larger than 96° with a twisted and slightly distorted CNNC structure that can be reached by the reactants via essentially barrierless pathways. Although further investigations beyond the displayed snapshots, namely fully optimised minimum energy pathway calculations and CI optimisations, were not carried out in this work due to serious computational difficulties, probably caused by the high steric demands of the ethylenic bridge and by the multi-dimensionality of the dynamics, it is tempting to identify the state crossings with respective CIs. The steep potential energy gradients leading to the photochemical funnel(s) from either side and the resulting very direct wave packet motions towards the CI without unnecessary detours allow us to rationalise the ultrashort isomerisation times (≈ 0.3 ps) and the observed large quantum yields. The high momenta acquired by the atoms during their downhill move may play decisive roles to drive the molecules through the S_1/S_0 intersection with extraordinary efficiencies such that the resulting isomerisation quantum yields reach values of 50 % and more. Another factor explaining the high quantum yields is the favourable pre-orientation of the phenyl rings in the reactant. This has also been concluded by Böckmann *et al.*^[55] from the pathways of the reactive trajectories in direct dynamics calculations.

The coordinate featured in Fig. 9.7 on the abscissa can be roughly described as a torsion of the central CNNC unit about its dihedral angle. It resembles the “hula-twist” motion proposed by Liu *et al.* for the $E \rightarrow Z$ isomerisation of retinal in confined environments^[56] and later invoked in many other cases, including the photoisomerisation of stilbene.^[57] Similar “torsional” motions have been conjectured in the recent direct dynamics simulation studies of diazocine **1** by Böckmann *et al.*^[55] and by Carstensen *et al.*^[58] One has to keep in mind, nevertheless, that any one-dimensional plot as in Fig. 9.7 has to be an oversimplification. As can be seen from the structures displayed above Fig. 9.7, the central CNNC torsion is accompanied by structural changes of other coordinates. In particular, it can be discerned that the two middle structures in Fig. 9.7 around $\Phi = 96^\circ$ differ significantly in other structural measures, especially considering the ethylenic bridge and the relative orientations of the phenyl rings. In agreement with the dynamics simulations by Carstensen *et al.*,^[58] this suggests two different local minima along the S_1/S_0 intersection seam for differing configurations of the azo- and ethylenic bridges. Although more sophisticated investigations of the PEHS were not yet carried out for the reasons noted above, the geometry optimisations allow for the given interpretation on the basis that they collapse at nearly degenerate S_1/S_0 energies and do not encounter any stable minima from between the FC regions to these points. Furthermore, it was confirmed by trial calculations that the ethylenic bridge exhibits high flexibility so that it can easily flip into its proper configuration. Figure 9.7 thus forms at least a good starting

point for more thorough future work.

In the ground state at $\Phi \approx 88^\circ$, close to the supposed intersection region at $\Phi = 96^\circ$, Fig. 9.7 seems to indicate a small energy barrier. This may be an artefact, since the depicted ground state points are only the energies for the respective excited-state structures, and the true minimum energy pathways in the electronic ground state may differ. The direct dynamics-surface hopping calculations by Carstensen *et al.*^[58] did, however, also suggest the presence of a ground-state barrier that can interfere with the $E \rightarrow Z$ isomerisation. The putative barrier may induce a temporary return of the molecule to the S_1 state.^[58] That scenario offers an interesting alternative explanation for the superimposed very weak ESA modulation with a frequency of $\approx 113 \text{ cm}^{-1}$ in the transient absorption-time profile (see Figs. 9.5 and 9.6) of excited **1E** at $\lambda_{\text{probe}} < 425 \text{ nm}$ different from the collective low-frequency modes en route to the CI which were referred to in the discussion above as traditional explanation for the observed modulation. The short ESA lifetime hampers a further analysis here.

Comparison to azobenzene

Irrespective of their different equilibrium structures, it is interesting to compare the excited-state dynamics of diazocine **1** with that of azobenzene (AB), which has attracted much attention for its prototypical character and fundamental importance.

ABs exist in the E form in the ground state in thermodynamic equilibrium, and can isomerise to the less stable Z structure only after energetic activation, *e.g.*, by absorption of a photon. The only exception to this rule that we are aware of is the cyclic “AB dimer” [0.0](3,3′)-azobenzenophane,^[59] which adopts the (Z, Z) structure in the ground state due to different steric restrictions. Experimental^[27–34,60–62] and theoretical^[63–68] studies of AB have shown that the isomerisation quantum yields and the molecular dynamics are closely related. Femtosecond spectroscopy of E -AB after $S_1(n\pi^*)$ excitation yielded time constants of $\approx 0.3 \text{ ps}$ and $\approx 2 - 3 \text{ ps}$, which were assigned to the initial motion out of the excited-state FC region and the actual isomerisation time, respectively.^[27–30,32] For Z -AB, characteristic times of roughly ≈ 0.1 and $\approx 1 \text{ ps}$ indicate even faster isomerisation.^[27,29] The respective quantum yields of AB^[61] of $\Phi_{E \rightarrow Z} = 0.24$ and $\Phi_{Z \rightarrow E} = 0.53$ on S_1 excitation reflect those times.

Time-resolved fluorescence anisotropy measurements of E -AB in n -hexane as solvent provided evidence for a rotational isomerisation pathway through a S_1/S_0 CI as the preferred reaction mechanism in the S_1 state.^[30] Theoretical calculations supported a barrierless rotational route, whereas an energy barrier was found on the inversion coordinate.^[45,69–71] A concerted inversion channel involving the in-plane symmetric CNN-bending mode has been proposed as well.^[71] $S_2(\pi\pi^*)$ excitation of AB eventually also results in isomerisation

via the rotational route through the S_1/S_0 CI because of an ultrafast S_2/S_1 internal conversion, but with a lower quantum yield owing to the different initial structure in S_1 reached by the internal conversion than by direct optical excitation.^[31–35,65–67,72,73]

For rotationally hindered azobenzophanes^[74] and an azobenzene capped with a crown ether^[75] excited to the S_1 state, significantly longer isomerisation times by up to a factor of 10 were observed. This has been attributed to structural restrictions of the rotational reaction channel and to increased solvent friction.^[74,75] For the capped AB, an isomerisation involving free rotation of the phenyl rings was ruled out because of similar decay times of the capped AB crown ether and a chemically similar open derivative.^[75] Calculations did, however, indicate that the rotational constraints in these molecules are not rigid and only impede the large-amplitude rotation of the phenyl rings, but not the torsion of the CNNC dihedral angle.^[63,76] It was also suggested that a restriction of the opening of the NNC angle rather than a hindering of the rotation would lead to AB molecular switches with higher quantum yields.^[63,66,76]

As shown by the present results, the photoreaction of diazocine **1Z** occurs with a comparable rate as the fast, direct dynamics in Z -AB. There are no indications for a slower indirect isomerisation, claimed in the case of Z -AB to explain the observed^[27,29] additional ≈ 1 ps time constant. This is quite a notable effect. The photoisomerisation of **1E** is even accelerated by a factor of $\approx 6 - 9$ compared to E -AB. This is in remarkable contrast to the significant slowdown of the photoisomerisation in the mentioned rotation-restricted E -ABs. It appears that the twisted conformation of the E isomer of **1** with its strongly reduced CNNC dihedral angle of 147° promotes the $E \rightarrow Z$ isomerisation by torsional motion of the CNNC moiety. The increased $E \rightarrow Z$ isomerisation rate and quantum yield of **1E** can thus be traced back to the favourable pre-orientation of the CNNC unit due to the bridge. The direct dynamics simulations of photo-excited **1E** and **1Z** support this assertion.^[55,58]

9.5 Conclusions

In conclusion, we have studied the $Z \rightarrow E$ and $E \rightarrow Z$ photoisomerisations of the prototypical diazocine **1**, a severely constrained azobenzene-based cyclic photoswitch, following excitation to the $S_1(n\pi^*)$ state in n -hexane as solvent by femtosecond time-resolved spectroscopy and by quantum chemical calculations. For both isomers, the observed excited-state dynamics suggest a very fast initial motion on the S_1 PEHS away from the FC region in only ≈ 0.1 ps and show that both photoreactions take place in only ≈ 0.3 ps. The severe structural constraints in **1** thus lead to an accelerated $E \rightarrow Z$ photoisomerisation compared to plain AB, but hardly affect the $Z \rightarrow E$ reaction. CASPT2//CASSCF calculations indicate reaction mechanisms involving torsion of the

central CNNC unit of the molecule towards a S_1/S_0 intersection seam at a dihedral angle of $\approx 96^\circ$. The pathways to the CI region(s) appear to be barrierless with steep downhill gradients from photo-excited **1Z** and **1E** alike. The efficient photochemical funnel by the intersection seam, along with the forces caused by the steep potential energy gradients, explain the experimentally observed high quantum yields and short isomerisation times. Taking into account the calculated equilibrium structure of the *E* isomer, the increased quantum yield and speed of the $E \rightarrow Z$ photoreaction can be ascribed to the significantly twisted conformation of **1E** that corresponds to a favourable pre-orientation of the central CNNC unit and facilitates the photoreaction. The dynamics help us to rationalize why the severe constraints by the bridging lead to improved photoswitching. The efficient ultrafast reactions, excellent photochromic properties, high quantum yields and good photostability make diazocine **1** a promising candidate for application as molecular optical switch, especially when its fairly rigid conformation can be an additional benefit.

Acknowledgments

This work has been performed as part of project A1 of the Sonderforschungsbereich 677 “Function by Switching” supported by the Deutsche Forschungsgemeinschaft.

References

- [1] B. L. Feringa, *Molecular Switches*, Wiley-VCH, Weinheim **2001**.
- [2] V. Balzani, A. Credi, B. Ferrer, S. Silvi, M. Venturi, *Top. Curr. Chem.* **2005**, *262*, 1–27.
- [3] V. Balzani, A. Credi, M. Venturi, *Molecular Devices and Machines: Concepts and Perspectives for the Nanoworld*, Wiley-VCH, Weinheim **2008**.
- [4] Z. F. Liu, K. Hashimoto, A. Fujishima, *Nature* **1990**, *347*, 658–660.
- [5] T. Ikeda, O. Tsutsumi, *Science* **1995**, *268*, 1873–1875.
- [6] S. Kawata, Y. Kawata, *Chem. Rev.* **2000**, *100*, 1777–1788.
- [7] Y. C. Liang, A. S. Dvornikov, P. M. Rentzepis, *Proc. Natl. Acad. Sci. U. S. A.* **2003**, *100*, 8109–8112.
- [8] A. S. Dvornikov, E. P. Walker, P. M. Rentzepis, *J. Phys. Chem. A* **2009**, *113*, 13633–13644.
- [9] J. A. Delaire, K. Nakatani, *Chem. Rev.* **2000**, *100*, 1817–1845.
- [10] I. Willner, S. Rubin, *Angew. Chem. Int. Ed.* **1996**, *35*, 367–385.
- [11] I. Willner, *Acc. Chem. Res.* **1997**, *30*, 347–356.
- [12] L. Ulysse, J. Cubillos, J. Chmielewski, *J. Am. Chem. Soc.* **1995**, *117*, 8466–8467.
- [13] S. Spörlein, H. Carstens, H. Satzger, C. Renner, R. Behrendt, L. Moroder, P. Tavan, W. Zinth, J. Wachtveitl, *Proc. Natl. Acad. Sci. U. S. A.* **2002**, *99*, 7998–8002.
- [14] X. Liang, H. Asanuma, M. Komiyama, *J. Am. Chem. Soc.* **2002**, *124*, 1877–1883.
- [15] A. Archut, F. Vögtle, L. De, Cola, G. C. Azzellini, V. Balzani, P. S. Ramanujam, R. H. Berg, *Chem. Eur. J.* **1998**, *4*, 699–706.
- [16] F. Vögtle, M. Gorka, R. Hesse, P. Ceroni, M. Maestri, V. Balzani, *Photochem. Photobiol. Sci.* **2002**, *1*, 45–51.
- [17] G. S. Kumar, D. C. Neckers, *Chem. Rev.* **1989**, *89*, 1915–1925.
- [18] A. Natansohn, P. Rochon, *Chem. Rev.* **2002**, *102*, 4139–4175.
- [19] T. Hugel, N. B. Holland, A. Cattani, L. Moroder, M. Seitz, H. E. Gaub, *Science* **2002**, *296*, 1103–1106.
- [20] N. B. Holland, T. Hugel, G. Neuert, A. Cattani-Scholz, C. Renner, D. Oesterhelt, L. Moroder, M. Seitz, H. E. Gaub, *Macromolecules* **2003**, *36*, 2015–2023.
- [21] I. Porcar, P. Perrin, C. Tribet, *Langmuir* **2001**, *17*, 6905–6909.
- [22] B. Baisch, D. Raffa, U. Jung, O. M. Magnussen, C. Nicolas, J. Lacour, J. Kubitschke, R. Herges, *J. Am. Chem. Soc.* **2009**, *131*, 442–443.
- [23] M. Sauer, *Proc. Natl. Acad. Sci. U. S. A.* **2005**, *102*, 9433–9434.
- [24] S. W. Hell, *Science* **2007**, *316*, 1153–1158.
- [25] S. W. Hell, *Nat. Methods* **2009**, *6*, 24–32.
- [26] B. Huang, M. Bates, X. Zhuang, *Annu. Rev. Biochem.* **2009**, *78*, 993–1016.

- [27] T. Nägele, R. Hoche, W. Zinth, J. Wachtveitl, *Chem. Phys. Lett.* **1997**, *272*, 489–495.
- [28] Y.-C. Lu, C.-W. Chang, E. W.-G. Diao, *J. Chin. Chem. Soc.* **2002**, *49*, 693–701.
- [29] H. Satzger, S. Spörlein, C. Root, J. Wachtveitl, W. Zinth, P. Gilch, *Chem. Phys. Lett.* **2003**, *372*, 216–223.
- [30] C.-W. Chang, Y.-C. Lu, T.-T. Wang, E. W.-G. Diao, *J. Am. Chem. Soc.* **2004**, *126*, 10109–10118.
- [31] I. K. Lednev, T.-Q. Ye, R. E. Hester, J. N. Moore, *J. Phys. Chem.* **1996**, *100*, 13338–13341.
- [32] I. K. Lednev, T. Q. Ye, P. Matousek, M. Towrie, P. Foggi, F. V. R. Neuwahl, S. Umaphathy, R. E. Hester, J. N. Moore, *Chem. Phys. Lett.* **1998**, *290*, 68–74.
- [33] T. Fujino, S. Y. Arzhantsev, T. Tahara, *J. Phys. Chem. A* **2001**, *105*, 8123–8129.
- [34] T. Fujino, S. Y. Arzhantsev, T. Tahara, *Bull. Chem. Soc. Jpn.* **2002**, *75*, 1031–1040.
- [35] H. Satzger, C. Root, M. Braun, *J. Phys. Chem. A* **2004**, *108*, 6265–6271.
- [36] R. Siewertsen, H. Neumann, B. Buchheim-Stehn, R. Herges, C. Näther, F. Renth, F. Temps, *J. Am. Chem. Soc.* **2009**, *131*, 15594–15595.
- [37] W. W. Paudler, A. G. Zeiler, *J. Org. Chem.* **1969**, *34*, 3237–3239.
- [38] H. Rau, G. Greiner, G. Gauglitz, H. Meier, *J. Phys. Chem.* **1990**, *94*, 6523–6524.
- [39] C. G. Hatchard, C. A. Parker, *Proc. R. Soc. London, A* **1956**, *235*, 518–536.
- [40] T. Pancur, N. K. Schwalb, F. Renth, F. Temps, *Chem. Phys.* **2005**, *313*, 199–212.
- [41] F. Renth, M. Foca, A. Petter, F. Temps, *Chem. Phys. Lett.* **2006**, *428*, 62–67.
- [42] R. Ahlrichs, M. Bär, M. Häser, H. Horn, C. Kölmel, *Chem. Phys. Lett.* **1989**, *162*, 165–169.
- [43] G. Karlström, R. Lindh, P.-A. Malmqvist, B. O. Roos, U. Ryde, V. Veryazov, P.-O. Widmark, M. Cossi, B. Schimmelpfennig, P. Neogrady, L. Seijo, *Comput. Mat. Sci.* **2003**, *28*, 222–239.
- [44] J. Dunning, Thom H., *J. Chem. Phys.* **1989**, *90*, 1007–1023.
- [45] A. Cembran, F. Bernardi, M. Garavelli, L. Gagliardi, G. Orlandi, *J. Am. Chem. Soc.* **2004**, *126*, 3234–3243.
- [46] A. Mostad, C. Rømming, *Acta Chem. Scand.* **1971**, *25*, 3561–3568.
- [47] T. Tsuji, H. Takashima, H. Takeuchi, T. Egawa, S. Konaka, *J. Phys. Chem. A* **2001**, *105*, 9347–9353.
- [48] H. Duval, *Bull. Soc. Chim. Fr.* **1910**, *7*, 727–732.
- [49] E. Tauer, R. Machinek, *Liebigs Ann.* **1996**, 1213–1216.
- [50] S. Takeuchi, T. Tahara, *Chem. Phys. Lett.* **2000**, *326*, 430–438.
- [51] B. Hou, N. Friedman, M. Ottolenghi, M. Sheves, S. Ruhman, *Chem. Phys. Lett.* **2003**, *381*, 549–555.
- [52] R. Siewertsen, F. Renth, F. Temps, F. Sönnichsen, *Phys. Chem. Chem. Phys.* **2009**,

- 11, 5952–5961.
- [53] J. Briand, O. Bräm, J. Réhault, J. Léonard, A. Cannizzo, M. Chergui, V. Zanirato, M. Olivucci, J. Helbing, S. Haacke, *Phys. Chem. Chem. Phys.* **2010**, *12*, 3178–3187.
- [54] A. J. Wurzer, T. Wilhelm, J. Piel, E. Riedle, *Chem. Phys. Lett.* **1999**, *299*, 296–302.
- [55] M. Böckmann, N. L. Doltsinis, D. Marx, *J. Phys. Chem. A* **2010**, *114*, 745–754.
- [56] R. S. H. Liu, D. T. Browne, *Acc. Chem. Res.* **1986**, *19*, 42–48.
- [57] W. Fuß, C. Kosmidis, W. E. Schmid, S. A. Trushin, *Chem. Phys. Lett.* **2004**, *385*, 423–430.
- [58] O. Carstensen, J. Sielk, J. B. Schönborn, G. Granucci, B. Hartke, *J. Chem. Phys.* **2010**, *133*, 124305/1–124305/12.
- [59] Y. Norikane, R. Katoh, N. Tamaoki, *Chem. Commun.* **2008**, 1898–1900.
- [60] H. Rau, E. Lüddecke, *J. Am. Chem. Soc.* **1982**, *104*, 1616–1620.
- [61] H. Rau, *J. Photochem.* **1984**, *26*, 221–225.
- [62] H. Rau, In H. Dürr, H. Bouas-Laurent, eds., *Photochromism: Molecules and Systems*. Elsevier, Amsterdam **2003**.
- [63] C. Nonnenberg, H. Gaub, I. Frank, *ChemPhysChem* **2006**, *7*, 1455–1461.
- [64] G. Granucci, M. Persico, *Theor. Chem. Acc.* **2007**, *117*, 1131–1143.
- [65] S. Yuan, Y. Dou, W. Wu, Y. Hu, J. Zhao, *J. Phys. Chem. A* **2008**, *112*, 13326–13334.
- [66] I. Conti, M. Garavelli, G. Orlandi, *J. Am. Chem. Soc.* **2008**, *130*, 5216–5230.
- [67] L. Wang, W. Xu, C. Yi, X. Wang, *J. Mol. Graph. Model.* **2009**, *27*, 792–796.
- [68] Y. Ootani, K. Satoh, A. Nakayama, T. Noro, T. Taketsugu, *J. Chem. Phys.* **2009**, *131*, 194306/1–194306/10.
- [69] T. Ishikawa, T. Noro, T. Shoda, *J. Chem. Phys.* **2001**, *115*, 7503–7512.
- [70] C. Ciminelli, G. Granucci, M. Persico, *Chem. Eur. J.* **2004**, *10*, 2327–2341.
- [71] E. W.-G. Diao, *J. Phys. Chem. A* **2004**, *108*, 950–956.
- [72] I. K. Lednev, T.-Q. Ye, L. C. Abbott, R. E. Hester, J. N. Moore, *J. Phys. Chem. A* **1998**, *102*, 9161–9166.
- [73] T. Schultz, J. Quenneville, B. Levine, A. Toniolo, T. J. Martinez, S. Lochbrunner, M. Schmitt, J. P. Shaffer, M. Z. Zgierski, A. Stolow, *J. Am. Chem. Soc.* **2003**, *125*, 8098–8099.
- [74] Y.-C. Lu, E. W.-G. Diao, H. Rau, *J. Phys. Chem. A* **2005**, *109*, 2090–2099.
- [75] T. Pancur, F. Renth, F. Temps, B. Harbaum, A. Krüger, R. Herges, C. Näther, *Phys. Chem. Chem. Phys.* **2005**, *7*, 1985–1989.
- [76] C. Ciminelli, G. Granucci, M. Persico, *J. Chem. Phys.* **2005**, *123*, 174317/1–174317/10.

Supporting Information

Table S1: Atomic cartesian coordinates (Å) of the calculated ground state equilibrium structures of **1Z** (**1Z_{eq}**, **1Z_{FC}***) calculated by DFT.

	x	y	z		x	y	z
N	-0.618886	-0.883112	1.731709	C	2.078455	-1.573467	-0.171975
N	0.609782	-1.018485	1.682439	C	1.380794	-0.604192	0.545112
C	-3.149784	0.161082	-1.476635	H	-3.818097	0.403014	-2.292443
C	-3.126067	-1.121614	-0.940862	H	-3.776124	-1.894502	-1.329033
C	-2.268677	-1.401151	0.108970	H	-2.252341	-2.382436	0.564684
C	-1.398180	-0.426127	0.604236	H	-2.346616	2.136199	-1.367177
C	-1.423557	0.881062	0.096547	H	-1.170931	2.520332	1.446423
C	-2.315554	1.135813	-0.952342	H	-0.576530	2.792221	-0.170484
C	-0.617308	2.049069	0.627623	H	0.800661	1.447635	2.155139
C	0.823679	1.776817	1.115925	H	1.367038	2.722747	1.104189
C	1.562257	0.759864	0.289180	H	2.601046	2.172258	-0.939281
C	2.438948	1.120736	-0.733271	H	3.776150	0.465143	-2.277520
C	3.104755	0.160800	-1.485427	H	3.445224	-1.942265	-1.779820
C	2.920865	-1.189857	-1.205541	H	1.950409	-2.616943	0.084059

Table S2: Atomic cartesian coordinates (Å) of the ground state equilibrium structures of **1E** (**1E_{eq}**, **1E_{FC}***) calculated by DFT.

	x	y	z		x	y	z
N	-0.367763	-0.503565	-1.012256	C	-0.587112	0.516610	1.579363
N	0.367727	0.501058	-1.014376	C	0.587164	-0.518405	1.578669
C	1.699781	0.196441	-0.639281	H	-3.218763	0.794292	2.208638
C	-1.699892	-0.197832	-0.638447	H	-5.207355	0.363877	0.823612
C	-1.806595	0.262669	0.689143	H	-4.957017	-0.476936	-1.495020
C	-3.094602	0.449760	1.187893	H	-2.678112	-0.883915	-2.413542
C	-4.220566	0.202705	0.407827	H	2.678190	0.883116	-2.414204
C	-4.081481	-0.272253	-0.891820	H	4.956913	0.479713	-1.494616
C	-2.813034	-0.496315	-1.411644	H	5.207413	-0.359883	0.824621
C	2.813048	0.496483	-1.411925	H	3.218988	-0.792080	2.208940
C	4.081485	0.274404	-0.891468	H	-0.184377	1.511396	1.372571
C	4.220598	-0.200188	0.408333	H	-0.964360	0.560324	2.603343
C	3.094632	-0.448481	1.187906	H	0.964632	-0.562884	2.602561
C	1.806541	-0.263003	0.688663	H	0.184731	-1.513104	1.371002

Table S3: Atomic cartesian coordinates (\AA) of the ground state equilibrium structures of **1Z** ($\mathbf{1Z}_{eq}$, $\mathbf{1Z}_{FC}^*$) calculated by CASSCF.

	x	y	z		x	y	z
N	-0.618886	-0.883112	1.731709	C	2.078455	-1.573467	-0.171975
N	0.609782	-1.018485	1.682439	C	1.380794	-0.604192	0.545112
C	-3.149784	0.161082	-1.476635	H	-3.818097	0.403014	-2.292443
C	-3.126067	-1.121614	-0.940862	H	-3.776124	-1.894502	-1.329033
C	-2.268677	-1.401151	0.108970	H	-2.252341	-2.382436	0.564684
C	-1.398180	-0.426127	0.604236	H	-2.346616	2.136199	-1.367177
C	-1.423557	0.881062	0.096547	H	-1.170931	2.520332	1.446423
C	-2.315554	1.135813	-0.952342	H	-0.576530	2.792221	-0.170484
C	-0.617308	2.049069	0.627623	H	0.800661	1.447635	2.155139
C	0.823679	1.776817	1.115925	H	1.367038	2.722747	1.104189
C	1.562257	0.759864	0.289180	H	2.601046	2.172258	-0.939281
C	2.438948	1.120736	-0.733271	H	3.776150	0.465143	-2.277520
C	3.104755	0.160800	-1.485427	H	3.445224	-1.942265	-1.779820
C	2.920865	-1.189857	-1.205541	H	1.950409	-2.616943	0.084059

Table S4: Atomic cartesian coordinates (\AA) of the ground state equilibrium structures of **1E** ($\mathbf{1E}_{eq}$, $\mathbf{1E}_{FC}^*$) calculated by CASSCF.

	x	y	z		x	y	z
N	-0.367763	-0.503565	-1.012256	C	-0.587112	0.516610	1.579363
N	0.367727	0.501058	-1.014376	C	0.587164	-0.518405	1.578669
C	1.699781	0.196441	-0.639281	H	-3.218763	0.794292	2.208638
C	-1.699892	-0.197832	-0.638447	H	-5.207355	0.363877	0.823612
C	-1.806595	0.262669	0.689143	H	-4.957017	-0.476936	-1.495020
C	-3.094602	0.449760	1.187893	H	-2.678112	-0.883915	-2.413542
C	-4.220566	0.202705	0.407827	H	2.678190	0.883116	-2.414204
C	-4.081481	-0.272253	-0.891820	H	4.956913	0.479713	-1.494616
C	-2.813034	-0.496315	-1.411644	H	5.207413	-0.359883	0.824621
C	2.813048	0.496483	-1.411925	H	3.218988	-0.792080	2.208940
C	4.081485	0.274404	-0.891468	H	-0.184377	1.511396	1.372571
C	4.220598	-0.200188	0.408333	H	-0.964360	0.560324	2.603343
C	3.094632	-0.448481	1.187906	H	0.964632	-0.562884	2.602561
C	1.806541	-0.263003	0.688663	H	0.184731	-1.513104	1.371002

Table S5: Atomic cartesian coordinates (\AA) of the excited state structure $1\mathbf{Z}_{CI}^*$ calculated by CASSCF.

	x	y	z		x	y	z
C	0.248346	-0.075023	-0.005539	H	-2.807651	3.430141	-1.352715
C	0.205767	-0.199785	1.380506	H	-2.715392	5.611438	-0.236188
C	1.320843	-0.537075	2.121971	H	-1.910083	5.770417	2.096408
C	2.528369	-0.752634	1.480537	H	-1.188507	3.727627	3.286789
C	2.608225	-0.615937	0.105546	H	1.560022	-0.157747	-1.691271
C	1.481210	-0.275333	-0.621611	H	3.547132	-0.767489	-0.402079
C	-1.602254	2.437642	1.637681	H	3.401158	-1.015031	2.055940
C	-1.553073	3.677735	2.274650	H	1.236810	-0.625349	3.192974
C	-1.955024	4.814228	1.600361	H	-0.571032	0.772549	-1.759149
C	-2.397383	4.726820	0.291106	H	-1.327272	-0.719061	-1.255465
C	-2.446006	3.491827	-0.338470	H	-2.824321	1.115414	-1.238061
C	-2.049413	2.330499	0.305764	H	-2.759499	0.322617	0.307204
N	-1.045146	0.105583	2.055660	C	-2.198295	0.977066	-0.356440
N	-1.114448	1.354009	2.326270	C	-0.945303	0.237561	-0.888736

Table S6: Atomic cartesian coordinates (\AA) of the excited state structure $1\mathbf{E}_{CI}^*$ calculated by CASSCF.

	x	y	z		x	y	z
C	0.027654	-0.044299	0.032537	H	-0.104360	3.400860	1.818324
C	-0.137491	0.044053	1.417018	H	-0.265826	1.304246	3.123820
C	-0.163342	1.278726	2.052264	H	0.253567	1.095466	-1.752934
C	-0.062619	2.447031	1.318055	H	0.184202	3.279195	-0.640238
C	0.089703	2.378010	-0.056055	H	-0.905588	-4.240957	3.633962
C	0.130606	1.142559	-0.682652	H	-1.016232	-4.857610	-1.234834
C	-0.974143	-3.287316	1.735923	H	-0.801706	-6.525811	2.685419
C	-1.023636	-3.432792	0.349841	H	-0.814967	-6.818428	0.224892
C	-0.971464	-4.722671	-0.165726	H	0.974561	-1.934292	-0.277747
C	-0.868959	-5.832410	0.657563	H	0.351638	-1.186790	-1.721433
C	-0.851867	-5.669608	2.032508	H	-1.417566	-2.614664	-1.564122
C	-0.909327	-4.395154	2.567926	H	-1.992947	-1.623144	-0.254790
N	-0.214103	-1.094696	2.253323	C	-1.157697	-2.245667	-0.574294
N	-1.083361	-2.016860	2.387056	C	0.127565	-1.374611	-0.673645

10 Summary

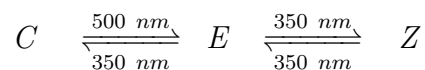
This Thesis dealt with the influence of intramolecular structural modifications on the ultrafast excited-state dynamics and isomerization quantum yields of structurally modified derivatives of the furylfulgide 2-[1-(2,5-dimethyl-3-furyl)-ethylidene]-3-isopropylidene succinic anhydride and the ethylene-bridged azobenzene (fsTAS) derivative 5,6-dihydro-dibenzo[*c,g*][1,2]diazocine (brAB). These investigated compounds represent two important classes of photochromic switches. The structural restriction of degrees of freedom in these molecular photochemical switches and their investigation with femtosecond time-resolved absorption spectroscopy (fsTAS) and quantum chemical calculations turned out to be a promising strategy for the systematic optimization of photochromic switches.

Selective acceleration of the desired pathways and restraint of unwanted excited-state pathways by the structural modifications could be observed and identified for both classes of switches. The steric constraints appear to cause suitable pre-orientations of the molecules for the wanted reactions, thus leading to the observed increased photoisomerization quantum yields by way of favorable kinetic competition.

Furylfulgides

For the present comparative study of furylfulgides, the parent compound methyl-furylfulgide (MeF for short), carrying a methyl substituent at the central hexatriene/cyclohexadiene chromophore unit at C⁴, was systematically modified by steric constraints. This was done by replacing the methyl group by an isopropyl substituent (iPrF) or by intramolecular bridging (7rF). Furthermore, in MeBF the conjugated π -system of MeF was enlarged by benzannulation of the furyl unit as an electronic effect.

The photochromism of furylfulgides is based on the electrocyclic $C \rightarrow E$ ring opening on irradiation with visible light and the reverse $E \rightarrow C$ ring closure with UV light. The parallel photochemical $E \rightarrow Z$ isomerization at the C⁴ – C⁵ double bond is an unwanted side reaction that can compete with the desired photochromic $E \rightarrow C$ ring closure pathway:



For the four furylfulgides the full reactive cycle was investigated. Steric and electronic effects were found to selectively affect the $E \rightarrow C$ ring closure and $C \rightarrow E$ ring opening dynamics, respectively. The $Z \rightarrow E$ dynamics was almost unaffected by both effects.

The photoreactions of the E -isomers of the four fulgides were found to be determined by the competition between several possible photo-induced isomerization/deactivation

channels. These are (i) the desired $E \rightarrow C$ ring closure reaction, (ii) the unwanted $E \rightarrow Z$ reaction, and (iii) the photo-induced *cis/trans* (Z/E) isomerization at the isopropylidene group. The latter process is a pure deactivation process which exclusively leads back to the E -reactant and therefore potentially lowers the isomerization quantum yields. Derivatives with increased sterical hindrance by larger substituents (iPrF) or intramolecular bridging (7rF) at C^4 showed inhibition of the $E \rightarrow Z$ side reaction and an increase of the $E \rightarrow C$ isomerization quantum yield by a factor of ≈ 3 compared to MeF and MeBF. From a direct combination of femtosecond time-resolved transient absorption spectroscopy and quantum chemical calculations the reason for this strong improvement of photochemical properties induced by steric restraints could be elucidated. The results indicate that two major effects are responsible for the favorable changes of the photoreactive properties:

First, the increased $E \rightarrow C$ quantum yields of iPrF and 7rF could be traced back to a suitable pre-orientation of the furyl moiety with respect to the isopropylidene group caused by the steric effects. This pre-orientation leads to an accelerated conrotatory $E \rightarrow C$ reaction with isomerization time constants of $\tau = 0.05$ ps for iPrF and 7rF compared with $\tau \approx 0.12$ ps for MeF and MeBF, leading to a preference of the desired $E \rightarrow C$ channel through kinetic competition with processes (ii) and (iii) which otherwise lower the $E \rightarrow C$ isomerization quantum yields. Only for MeF and MeBF could the additional slower $E \rightarrow Z$ reaction with $\tau \approx 0.34$ ps be observed by fsTAS measurements, almost not affected by the benzannulation.

Secondly, the undesired $E \rightarrow Z$ reaction was found to be a conformer-specific reaction depending on the ground-state populations of the two E -conformers E_α and E_β and proceeding predominantly from the non-cyclizable E_β conformer. DFT calculations of the conformer populations of E_α and E_β showed a correlation between the population of the E_β -conformer and the $E \rightarrow Z$ isomerization quantum yields of the four fulgides. The steric modifications in iPrF and 7rF caused an increase of the relative energies of the E_β conformers which led to a decrease of the E_β population to 3% for iPrF and practically 0% for 7rF, where both fulgides lack of a observable $E \rightarrow Z$ reaction channel, in contrast to MeF and MeBF with E_β populations 34% and 18%, respectively. With 7rF a fulgide with a completely blocked $E_\alpha \rightleftharpoons E_\beta$ equilibration could be investigated for the first time, specially designed on the basis of the results of femtosecond time-resolved fsTAS measurements of MeF and synthesized in the group of Prof. Mattay.

The fast $E \rightarrow C$ isomerization times and the conformer-specific $E_\beta \rightarrow Z$ and $E_\alpha \rightarrow C$ isomerizations are consistent with TDDFT calculations performed in the course of this Thesis. A minimum on the S_1 potential energy surface for E_β -MeF along a possible $E \rightarrow Z$ reaction coordinate could be found providing a plausible hypothesis to explain the predominantly $E_\beta \rightarrow Z$ reaction. On the other hand, a direct barrierless $E \rightarrow C$ pathway

via a CI was found by excited-state geometry optimizations for E_α -MeF, rationalizing the fast ring closure reaction times.

Further important informations could be obtained from semiclassical dynamics calculations performed in the group of Prof. Hartke. They found a flipping motion of the C^4 -substituent of E -iPrF (isopropyl-substituent) to be the initial step of the $E \rightarrow Z$ isomerization. The larger this C^4 -substituent, the slower the motion of the respective substituent. This supports the theory of favorable kinetic competition to be an important reason for the increased $E \rightarrow C$ isomerization quantum yields and inhibited $E \rightarrow Z$ isomerization of fulgides with steric restraints.

Regarding further applications of fulgides, it is important that the benzannulation in MeBF did not have a strong influence on the $E \rightarrow C$ and $E \rightarrow Z$ dynamics and photochemical properties. This is of great significance, because MeBF can be used for further linking of chromophores in order to obtain, e.g., switchable fluorescence behavior for applications such as far-field fluorescence nanoscopy.

In contrast, the ultrafast dynamics of the reverse $C \rightarrow E$ photoisomerization was found to be dramatically influenced by the benzannulation. For MeF, iPrF and 7rF, with only steric modifications at C^4 , ultrafast dynamics from the Franck-Condon (FC) region with time constants of $\tau = 0.37 - 0.53$ ps followed by a barrierless sub-picosecond internal conversion to the electronic ground state with $\tau = 0.65 - 0.94$ ps could be observed with $C \rightarrow E$ isomerization quantum yields of $\phi \approx 0.09$. For MeBF a comparable fast contribution with $\tau = 0.39$ ps, but a noticeable increase of the excited-state lifetime with $\tau = 4.6$ ps and $\tau = 16.9$ ps could be observed, which is ≈ 25 times longer as found for MeF. This behavior was interpreted as the involvement of excited-state potential energy barriers for MeBF along the reaction/deactivation pathways as a possible consequence of the electronic effect on the excited-state topography of benzannulated fulgides. The remarkably long-lived excited-state absorption contribution with $\tau = 16.5$ ps for MeBF was interpreted as trapping in a local excited-state potential energy minimum. In contrast to the photochemistry of E -fulgides, the increased excited-state lifetime was accompanied by increased isomerization quantum yields of $\phi \approx 0.16$. A plausible hypothesis to explain this improved photochemical efficiency is the location of the excited-state energy barriers along a non-reactive excited-state pathway. This obviously needs further investigation regarding photochemical stability and fluorescence quantum yields.

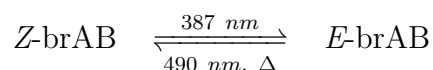
Although the $E \rightarrow Z$ isomerization is an unwanted process in the photoisomerization of fulgides, the reverse $Z \rightarrow E$ reaction is of considerable importance because it avoids photochemical accumulation of the Z -isomer in the course of multiple switching cycles. It could be shown that neither sterically constraining substituents at the C^4 position (in iPrF and 7rF) nor the electronic effect by benzannulation (in MeBF) lead to fundamental

changes of the $Z \rightarrow E$ isomerization/deactivation mechanism. Complex excited-state dynamics were observed and interpreted as a possible involvement of an optically dark intermediate excited state that is populated via a conical intersection (CI) from the initially excited Franck-Condon (FC) state. Averaged lifetimes of the excited state from $\tau_{\text{av}} = 0.33$ ps for MeF and $\tau_{\text{av}} = 0.73$ ps for MeBF were found for the four fulgides. The increased lifetimes with increasing molecular size of the structural modifications point to an inertial effect.

The results show that steric and electronic modifications of fulgides affect the $C \rightarrow E$ ring opening and the $E \rightarrow C$ ring closure reaction of furylfulgides separately. This allows for a selective tuning of these reaction channels. Steric modifications could be used to improve the $E \rightarrow C$ photoisomerization without a noticeable influence on the $C \rightarrow E$ dynamics. The introduction of electronic effects via benzannulation hardly affected the $E \rightarrow C$ ring closure reaction, but led to strongly increased isomerization times and excited-state energy barriers which surprisingly improve the photochemical properties of fulgides. The important restoring $Z \rightarrow E$ channel was not inhibited by structural modifications. The results in this Thesis provide guidelines for the synthesis of new fulgides with improved photochemical properties.

Bridged azobenzene

In the second part of this Thesis, the photo-induced $E \rightarrow Z$ and $Z \rightarrow E$ isomerizations of the ethylene-bridged azobenzene derivative brAB with a severely constrained eight-membered heterocyclic ring as central unit were studied by determination of isomerization quantum yields, femtosecond time-resolved transient absorption spectroscopy, and quantum chemical calculations:



It could be shown that the investigated bridged azobenzene has the potential to become the parent molecule of a new class of improved photochromic switches because of well separated $S_1(n\pi^*)$ absorption bands of the E - and Z -isomers in contrast to AB, higher isomerization quantum yields, and very effective $E \rightarrow Z$ (100 %) and $Z \rightarrow E$ (> 90 %) photo-switching at wavelengths $\gtrsim 400$ nm. Furthermore, the steric constraints due to the ethylene bridge in brAB led to a reversed thermodynamic stability of the two isomers with the Z -isomer as the thermodynamic stable form. TDDFT/DFT calculation of bridged AB with different length of the alkyl bridge suggest that the thermodynamic stability of ABs can be controlled by the length of the bridge, while preserving the excellent photochromic properties.

The photoisomerization reactions after S_1 excitation were found to be much faster compared to AB. For the $E \rightarrow Z$ reaction, motion from the initially excited FC region of the S_1 state with a time constant $\tau < 50$ fs and an isomerization time of $\tau = 0.32$ ps were determined for E -brAB after photo-excitation at $\lambda = 490$ nm. For the $Z \rightarrow E$ reaction after excitation at $\lambda = 387$ nm, departure from the FC region in $\tau = 0.07$ ps and an isomerization time of $\tau = 0.27$ ps were observed. The accelerated $E \rightarrow Z$ isomerization goes along with an increase of the respective isomerization quantum yield to $\phi_{E \rightarrow Z}^{S_1} = 0.50$, while the $Z \rightarrow E$ isomerization quantum yield was $\phi_{Z \rightarrow E}^{S_1} = 0.72$. This improvement of photochemical properties could be explained by a pre-orientation of the central CNNC dihedral angle due to the steric restraints of the ethylenic bridge, which results in an accelerated and more efficient molecular isomerisation dynamics, similar to the effect of steric pre-orientation in the investigated fulgides.

In the case of brAB, the structural restraints block a full rotational motion of the phenyl rings and inhibit a symmetric concerted inversion, which would predominantly lead back to the reactant and might therefore lower photochemical efficiency of normal AB. CASPT2//CASSCF calculations of brAB performed in the group of Prof. Hartke found two distinctive conical intersection regions at a common CNNC dihedral angle of $\approx 96^\circ$ for the $E \rightarrow Z$ and the $Z \rightarrow E$ isomerizations. The reaction coordinate resembles a hula-twist like isomerization mechanism.

The bridged azobenzene brAB allows for photochromic reversible switching of an AB derivative at wavelength $\gtrsim 400$ nm with extraordinary high quantum yields. Femtosecond time-resolved spectroscopy and quantum chemical calculations helped to rationalize why steric constraints by the intramolecular bridging led to its improved photoswitching properties compared with AB. Azobenzenes with variable lengths of the alkyl bridge will have high potential to become a new class of photochromic switches with improved photochromic properties for several applications.

Acknowledgment

An dieser Stelle möchte ich mich bei allen bedanken, die mich bei meiner Arbeit unterstützt haben. Mein besonderer Dank gilt:

- Herrn Prof. Dr. Friedrich Temps für die Möglichkeit, innerhalb eines so interessanten Gebiets forschen und meine Doktorarbeit in seinem Arbeitskreis anfertigen zu dürfen, sowie für die gute Betreuung während meiner ganzen Doktorandenzeit und die wertvolle Hilfe bei allen Fragen und Problemen.
- Dr. Falk Renth für zahlreiche Diskussionen und besonders für die Unterstützung beim Erreichen der Publikationsreife der im Rahmen dieser Arbeit entstandenen Veröffentlichungen.
- Meinen ehemaligen Laborkollegen Nina Schwalb und Harald Studzinski, die mir in meiner Anfangszeit alles über die Arbeit im Femtolabor beigebracht haben.
- Boyke Schönborn und Ole Carstensen aus dem Arbeitskreis von Prof. B. Hartke für die hervorragende Zusammenarbeit zwischen Experiment und Theorie. Ihre Arbeiten haben maßgeblich zum Verständnis der experimentellen Ergebnisse beigetragen.
- Frank Strübe aus dem Arbeitskreis von Prof. J. Mattay aus Bielefeld für die außerordentlich hervorragende Zusammenarbeit. Seine Synthesen der verschiedenen Furylfulgide haben große Teile meiner Arbeit erst ermöglicht. Außerdem danke ich für die Führung durch das schöne Bielefeld.
- Bengt Buchheim-Stehn aus dem Arbeitskreis von Prof. R. Herges und Hendrikje Neumann danke ich sehr für die Synthese des verbrückten Azobenzols.
- Herrn Prof. Frank Sönnichsen für die NMR-Untersuchungen und für die gute Zusammenarbeit, sowie für die netten Gespräche und hilfreichen Diskussionen.
- Großer Dank gilt auch meinen lieben Laborkolleginnen Mayra Stuhldreier, Julia Bahrenburg und Katharina Röttger für die hervorragende Stimmung im Labor und außerhalb. Ohne Euch wäre ich bestimmt dem Wahnsinn verfallen. Vielen Dank außerdem für das konstruktive Korrekturlesen meiner Arbeit, hierbei ein besonderer Dank an Mayra! Insgesamt: EHL: EgD!
- 在此,我想对 Zhang Rongrong 女士在此次合作中的鼎力相助表示最诚挚的谢意!

- Meinem Freund Johannes Dammeier danke ich für die nette Gesellschaft bei etwa 1000 Mittagspausen und für die schönen Schwedenreisen.
 - Dr. Joachim Gripp, der bei jedem technischen Problem – vom Gaschromatographen bis zur Rotlichtlampe – immer hilfreiche und praktische Lösungen parat hatte.
 - Uwe Eggers für die Hilfe bei allen Computer- und Lebensfragen.
 - Dem gesamten AK Temps und AK Friedrichs danke ich für die gute Arbeitsatmosphäre und die netten Grillfeste! Insbesondere Carsten Fehling, der bisher (fast!) jede Frage beantworten konnte und auch zu später Stunde immer gerne zu einem Gespräch bereit war, Alexander Thrun für die Lösung eigentlich unlösbarer LaTeX2Lyx Probleme und Hauke und Thomas für den Hinweis, dass ich sie hier fast vergessen hätte.
 - Ganz besonderer Dank gilt den Mitarbeitern unserer Werkstatt Frank Herzog, Frank Laasch, Andreas Sievers, Olaf Wendt und Klaus-Dieter Will sowie Michael Karstens und Klaus Warns für die zahlreichen Spezialanfertigungen, die den TA-Aufbau maßgeblich verbessert haben.
 - Nicht zuletzt möchte ich mich ganz herzlich bei meinen Eltern bedanken, die mir das Chemiestudium ermöglicht und mich stets unterstützt haben.
 - Schließlich bedanke ich mich sehr bei meiner Freundin Ameli, die mich stets umsorgt hat.
-
- Diese Arbeit wurden durch die Deutsche Forschungsgemeinschaft (DFG) im Sonderforschungsbereich 677 – Funktion durch Schalten – gefördert.

Curriculum Vitae

Personal Data

Name: Ron Siewertsen
Nationality: German
Date of birth: 20/01/1980
Place of birth: Kiel
Address: Preußerstr. 16, 24105 Kiel

Education

since 10/2006 **Doctoral candidate** on the topic *Femtosecond Spectroscopy, Dynamics of Molecular Switches* in the group of Prof. Dr. F. Temps, Physical Chemistry, Christian-Albrechts-Universität zu Kiel
Thesis title: *Ultrafast Photochromic Reactions of Structurally Modified Furylfulgides and a Bridged Azobenzene*

10/2001–09/2006 **Chemistry studies** (Diploma) at the Christian-Albrechts-Universität zu Kiel
Diploma Thesis: *Femtosekunden-Fluoreszenzspektroskopie der Photoisomerisierung eines verbrückten Azobenzols und eines Furylfulgids* in the group of Prof. Dr. F. Temps, Christian-Albrechts-Universität zu Kiel, Final grade (Dipl. Chem.): 1.3

10/2000–08/2001 “**Zivildienst**” Servicehaus der Arbeiterwohlfahrt, Kiel

08/1990–06/2000 **Abitur** (university-entrance diploma), Gymnasium Wellingdorf, Kiel

Publications

- R. Siewertsen, H. Neumann, B. Buchheim-Stehn, R. Herges, C. Näther, F. Renth, and F. Temps. “*Highly Efficient Reversible $Z \rightleftharpoons E$ Photoisomerization of a Bridged Azobenzene with Visible Light through Resolved $S_1(n\pi^*)$ Absorption Bands*”, **J. Am. Chem. Soc.**, 131:15594–15595, 2009.
- R. Siewertsen, F. Renth, F. Temps, and F. Sönnichsen: “*Parallel Ultrafast E-C Ring Closure and E-Z Isomerisation in a Photochromic Furylfulgide Studied by Femtosecond Time-Resolved Spectroscopy*”, **Phys. Chem. Chem. Phys.**, 11:5952–5961, 2009.

- F. Renth, N. K. Schwalb, R. Siewertsen, and F. Temps: “*Pump-Probe Spectroscopy of Ultrafast Vibronic Dynamics in Organic Chromophores*”, In **Conical Intersections**, volume 2. World Scientific, Singapore, 2011. in press.
- R. Siewertsen, J. B. Schönborn, B. Hartke, F. Renth, and F. Temps: “*Superior $Z \rightarrow E$ and $E \rightarrow Z$ photoswitching dynamics of dihydrodibenzodiazocine, a bridged azobenzene, by $S_1(n\pi^*)$ excitation at $\lambda = 387$ and 490 nm*”, **Phys. Chem. Chem. Phys.**, 13:1054–1063, 2011.
- R. Siewertsen, F. Renth, F. Strübe, J. Mattay, and F. Temps: “*Tuning of Switching Properties and Excited-State Dynamics of Fulgides by Structural Modifications*”, **Phys. Chem. Chem. Phys.**, 13:3800–3808, 2011.
- F. Strübe, R. Siewertsen, F. D. Sönnichsen, F. Renth, F. Temps, and J. Mattay: “*Photochromism of Rotation-Hindered Furyl Fulgides Influenced by Steric Modifications*”, **Eur. J. Org. Chem.**, 1947–1955, 2011.

In preparation:

- R. Siewertsen, F. Renth, F. Strübe, J. Mattay, and F. Temps: “*Electronic and Steric Effects on the Ultrafast $C \rightarrow E$ Ring-Opening of Structurally Modified Furylfulgides*”, see Chapter 5, 2011.
- R. Siewertsen, F. Renth, F. Strübe, J. Mattay, and F. Temps: “*Ultrafast $Z \rightarrow E$ Photoisomerisation of Structurally Modified Furylfulgides*”, see Chapter 6, 2011.

Talks and Posters

- R. Siewertsen: “*Transient Absorption Spectroscopy of the Ultrafast Photoinduced Dynamics of a Furylfulgide Switch*”, Talk at the **SFB677 Seminar**, Kiel 2007.
- R. Siewertsen: “*Femtosecond Broad-Band Absorption Spectroscopy of a Motionally Constrained Azobenzene*”, Talk at the **SFB677 Seminar**, Kiel 2008.
- R. Siewertsen, F. Renth, B. Buchheim-Stehn, R. Herges and F. Temps: “*Ultrafast photo-induced Z - E and E - Z isomerizations of a severely constrained azobenzene with improved photochromic properties*”, Poster at the **Vortragstagung der GDCh-Fachgruppe Photochemie**, Bielefeld 2008.
- F. Renth, R. Siewertsen, and F. Temps: “*Competing ultrafast photo-induced ring closure and E - Z isomerization of a photochromic furylfulgide*”, Poster at the **Vortragstagung der GDCh-Fachgruppe Photochemie**, Bielefeld 2008 (Poster prize).
- R. Siewertsen, F. Renth and F. Temps: “*Wellenpaketaufspaltung bei der ultraschnellen Photoisomerisierungsdynamik eines Furylfulgids*”, Talk at the **Bunsentagung**, Saarbrücken 2008.

-
- R. Siewertsen, F. Renth, and F. Temps: “*Competing ultrafast photo-induced ring closure and E-Z isomerization of a photochromic furylfulgide*“, Poster at the **DPG Frühjahrstagung**, Hamburg 2009.
 - F. Renth, R. Siewertsen, R. Herges, B. Buchheim-Stehn, F. Temps: “*Ultrafast Photoisomerization despite Severe Constraints in a Bridged Azobenzene with Enhanced Photochromic Properties Studied by Femtosecond Time-Resolved Spectroscopy*“, Talk at the **DPG Frühjahrstagung**, Hamburg 2009.
 - F. Renth, R. Siewertsen, F. Temps, F. Sönnichsen, F. Strübe, J. Mattay: “*Ultrafast Conformer-specific Photochemistry and Effects of Steric Constraints in Photochromic Furylfulgides*“, Talk at the **XXIV International Conference on Photochemistry**, Toledo, Spain 2009.
 - J. Bahrenburg, K. Röttger, R. Siewertsen, F. Renth and F. Temps: “*Ultrafast Photo-Induced Isomerization of a Push-Pull Azobenzene Covalently Linked to Polymeric Micronetworks*“, Poster at the **International Bunsen Discussion Meeting**, Leipzig 2009.
 - J. Bahrenburg, K. Röttger, R. Siewertsen, F. Renth, F. Temps : “*Ultrafast Photo-Induced Isomerization Azobenzene in Polymeric Micronetworks*“, Talk at the **International Bunsen Discussion Meeting**, Leipzig 2009.
 - R. Siewertsen, F. Renth, F. Temps, B. Buchheim-Stehn and R. Herges: “*Ultrafast photoisomerization despite severe constraints in an azobenzene with improved photochromic properties*“, Talk at the **Bunsentagung**, Köln 2009.
 - R. Siewertsen, F. Renth, F. Temps, F. Sönnichsen, F. Strübe and J. Mattay: “*Effects of steric constraints and ultrafast conformer-specific photochemistry in photochromic furylfulgides*“, Poster at the **Femtochemistry IX**, Beijing, China 2009.
 - R. Siewertsen, F. Renth, F. Temps, J. B. Schönborn, B. Hartke, F. Sönnichsen, B. Buchheim-Stehn, R. Herges, F. Strübe, J. Mattay: “*Ultrafast Dynamics of Molecular Switches: Conformer-specific Photochemistry and Effects of Intramolecular Constraints*“, Poster at the **SFB677 Conference**, Salzgau 2009.
 - R. Siewertsen: “*Ultrafast Dynamics of Photochromic Furylfulgides: Conformer-specific Photochemistry and Effects of Intramolecular Constraints*“, **Invited talk, Prof. J. Mattay**, Bielefeld 2009.
 - R. Siewertsen: “*Femtosecond Spectroscopy of Photochemical Switches*“, **Invited talk, Prof. B. Hartke**, Kiel 2009.
 - F. Renth, R. Siewertsen, J. B. Schönborn, B. Hartke, F. Sönnichsen, F. Strübe, J. Mattay: “*Comparative study of the ultrafast photochemistry of photochromic furylfulgides tuned by structural modifications*“, Talk at the **Bunsentagung**, Bielefeld 2010.

- F. Renth, R. Siewertsen, F. Strübe, J. Mattay, J. B. Schönborn, B. Hartke, F. Temps: “*Ultrafast Photochemistry of Photochromic Furylfulgides: Tuning by Structural Modifications*”, Poster at the **XXIII IUPAC Symposium on Photochemistry**, Ferrara, Italy 2010.
- J. Bahrenburg, K. Röttger, R. Siewertsen, F. Renth and F. Temps: “*Photoisomerization of a Push-Pull Azobenzene in Solution and in Polymer Colloids via a Sequential Relaxation Pathway*”, Poster at the **XXIII IUPAC Symposium on Photochemistry**, Ferrara, Italy 2010.
- R. Siewertsen, F. Renth, F. Temps, F. Strübe, J. Mattay: “*Steric and Electronic Effects on the Ultrafast Photoisomerization of Structurally Modified Fulgides*“, Talk at the **Vortragstagung der GDCh-Fachgruppe Photochemie**, Erlangen 2010.